
Electronic Thesis and Dissertation Repository

5-1-2024 4:30 PM

An Analysis of Primary Stability of Stemless Humeral Implants in Shoulder Arthroplasty

David Cunningham, *The University of Western Ontario*

Supervisor: Johnson, James A., *The University of Western Ontario*

Co-Supervisor: Athwal, George S., *The Roth McFarlane Hand and Upper Limb Centre, St. Joseph's Hospital*

A thesis submitted in partial fulfillment of the requirements for the Doctor of Philosophy degree in Mechanical and Materials Engineering

© David Cunningham 2024

Follow this and additional works at: <https://ir.lib.uwo.ca/etd>



Part of the Biomechanical Engineering Commons

Recommended Citation

Cunningham, David, "An Analysis of Primary Stability of Stemless Humeral Implants in Shoulder Arthroplasty" (2024). *Electronic Thesis and Dissertation Repository*. 10095.

<https://ir.lib.uwo.ca/etd/10095>

This Dissertation/Thesis is brought to you for free and open access by Scholarship@Western. It has been accepted for inclusion in Electronic Thesis and Dissertation Repository by an authorized administrator of Scholarship@Western. For more information, please contact wlsadmin@uwo.ca.

Abstract

There is a scarcity of literature on the performance of the stemless humeral components. This present work describes the development of a novel loading simulator for the quantification of implant performance, as well as its use in the evaluation of implant parametric design and surgical protocol decision variables.

Interface fixation of humeral components was first evaluated using computational methods to determine the optimal metric to quantify implant fixation. Distractive micromotion was found to be the defining micromotion direction in two different designs of humeral implants.

A loading simulator capable of replicating 3D physiological loads, and comprehensive loading and digital image acquisition program were successfully developed. High resolution digital tracking methods were commissioned to quantify implant fixation.

The novel apparatus was used to compare the use of bone specimens to polyurethane bone surrogate materials using the clinically relevant variable of the degree of press-fit. It was found that the polyurethane analogue materials commonly utilized for the evaluation of implant performance did not accurately replicate the results as were collected in the biological specimens, and that fixation does not linearly increase with press-fit. Moving forward, it was concluded that only bone would be employed for the fixation studies herein.

One of the most important clinical variables with respect to the fixation of stemless implants is neck shaft angle. This was evaluated in terms of primary fixation in a clinically available stemless reversed implant. This was also assessed using a computational framework for a larger range of inclinations. The results of both works were in agreement; finding that decreasing neck-shaft angle resulted in decreased fixation of the implant evaluated.

This present work represents an advancement of knowledge regarding the performance of shoulder arthroplasty humeral components and provides a more thorough evaluation methodology than has been previously utilized during studies of the same nature.

Decreasing neck shaft angle to increase range-of-motion comes at the cost of implant primary fixation, and over-increasing implant press-fit may compromise the fixation of stemless implants. Moreover, the relevance of focusing on normal micromotion due to its prominence for the stemless implant designs was shown to be a key outcome.

Keywords

reverse total shoulder arthroplasty, glenohumeral joint, humerus, implant fixation, bone analogue, ASTM F1839-08, ASTM F2028-17, stemless, neck shaft angle, implant press-fit

Summary

Shoulder replacement surgeries are a common medical intervention for patients with damaged or diseased shoulders. This surgical intervention is designed to replace the anatomic shoulder joint with an artificial substitute and has been proven to help patients regain their pre-injury independence and quality of life. Recently, there have been advancements to the design of shoulder implants that have not been thoroughly investigated. This dissertation is directed towards the evaluation of the novel stemless reversed shoulder implant variant, with focus on the fixation properties of the bone-implant interface. This work evaluated implant fixation using both computational and experimental methodologies.

Initially, implant fixation phenomena were investigated using computer simulation approaches in order to identify the best method to quantify implant stability. It was found that bone-implant gapping motion was the most effective value to measure for the implant geometry under investigation. Second, a novel implant evaluation apparatus was created to replicate the forces that an implant would realistically experience after surgery. A high-resolution camera system was used to measure bone-implant gapping during loading. This loading system was then used in an experimental study to investigate how using foam surrogate materials in the place of bone specimens influences the results of those analyses. It was found that foam surrogates do not replicate the results obtained with bone specimens. Subsequently, this work evaluated the effect of the surgical implantation variable of “neck shaft angle” both computationally and experimentally. These two studies both showed that increasing neck shaft angle resulted in increased fixation, and the latter work additionally revealed that increasing neck shaft angle also favourably increased implant survivorship during loading.

Overall, this work developed an effective strategy to thoroughly evaluate the fixation behaviour of stemless implants after surgery by replicating realistic load magnitudes that implants might experience during use. This is important, as there are a limited number of methods for implant evaluation that exhibit acceptable mimicry of the real implant loading environment.

Co-Authorship Statement

Without my collaborators, the completion of this graduate thesis would not be possible. I would like to acknowledge the following:

Chapter 1: Not Submitted for Publication.

Sole Author: David Cunningham

Manuscript Revisions: Jim Johnson, George Athwal

Chapter 2: Not Submitted for Publication.

Study Design: David Cunningham, Jim Johnson, George Athwal

Model Development: David Cunningham, Jim Johnson, George Athwal

FEA Analysis: David Cunningham, Jim Johnson

Data Analysis: David Cunningham

Statistical Analysis: David Cunningham

Manuscript Preparations: David Cunningham

Manuscript Revisions: Jim Johnson, George Athwal

Chapter 3: Not Submitted for Publication.

Apparatus Design: David Cunningham, Jim Johnson

Model Development: David Cunningham, Jim Johnson

Data Analysis: David Cunningham

Statistical Analysis: David Cunningham

Manuscript Preparations: David Cunningham

Manuscript Revisions: Jim Johnson

Chapter 4: Not Submitted for Publication.

Study Design: David Cunningham, Jim Johnson, George Athwal

Specimen Preparation: David Cunningham, Alexander Gilchrist

Experimental Testing: David Cunningham

Data Analysis: David Cunningham, Jim Johnson

Statistical Analysis: David Cunningham

Manuscript Preparations: David Cunningham

Manuscript Revisions: Jim Johnson

Chapter 5: Published.

Journal of Shoulder and Elbow Surgery Intl. – 2024/04/18

DOI: <https://doi.org/10.1016/j.jseint.2024.04.001>

Study Design: David Cunningham, Jim Johnson, George Athwal

Specimen Preparation: David Cunningham, Ahmed Habis, Fares Uddin, Maria Murcia, Vivian Oparin, Elizabeth Cunningham

Experimental Testing: David Cunningham, Ahmed Habis, Fares Uddin

Data Analysis: David Cunningham

Statistical Analysis: David Cunningham

Manuscript Preparations: David Cunningham

Manuscript Revisions: David Cunningham, Jim Johnson, Ahmed Habis, Fares Uddin, George Athwal

- Chapter 6:** Published.
Journal of Shoulder and Elbow Surgery – 2023/07/26
DOI: <https://doi.org/10.1016/j.jse.2023.06.035>
Study Design: David Cunningham, Jim Johnson, George Athwal
Model Development: David Cunningham, Gregory Spangenberg, Daniel Langohr, Jim Johnson
FEA Analysis: David Cunningham, Daniel Langohr, Jim Johnson
Data Analysis: David Cunningham
Statistical Analysis: David Cunningham
Manuscript Preparations: David Cunningham
Manuscript Revisions: David Cunningham, Jim Johnson, George Athwal, Gregory Spangenberg, Daniel Langohr
- Chapter 7:** Not Submitted for Publication.
Sole Author: David Cunningham
Manuscript Revisions: Jim Johnson, George Athwal

Dedication

To my family.

Acknowledgements

First, I would like to thank my primary supervisor and mentor, Dr. James A. Johnson, for your outstanding direction and support. Your patient and exceptional guidance has been instrumental throughout this work, and your expertise and insightful feedback has not only shaped the trajectory of my research but has also played a pivotal role in my academic and personal growth. You have provided me with countless opportunities to contribute to the research of fascinating topics, and I am truly grateful.

Additionally, I would like to thank my co-supervisor, Dr. George S. Athwal. Your passion for research and your enthusiastic support of new ideas is inspiring. I have no doubt that your positive leadership is one of the many qualities that motivates all those who have the pleasure of working with you – including myself. Your acumen for translating seamlessly between medicine and engineering design is remarkable.

Thank you, Dr. Ahmed Habis and Dr. Fares Uddin, for your hard work and dedication to the projects on which we collaborated. I truly appreciate you adapting your busy schedules in order to provide support to our testing. I wish you all the best with your future as orthopaedic surgeons.

I would also like to thank those people who have continuously supported me throughout my education. To my family, who have been the foundation on which I have always relied, and who have always been there to support me in every step of my educational journey. Your steadfast encouragement and understanding have been a constant source of inspiration. And to Rick and Linda McMullin, who have similarly been instrumental in my stability and have taught me so much more than just how to repair vehicles. Your kindness is unparalleled. And of course, thank you Lisa Vanderpas for your unwavering support, your tireless reassurance, and your perpetual inspiration.

Thank you also to all my past and current lab mates at the HULC laboratory, all of whom have created such an incredible and supportive work environment. Thank you, Cole Fleet, for being a constant support and positivity both in research and during our TA appointments, and thank you, Gregory Spangenberg, for your mentorship in coding and data analysis. This was truly not a solitary journey but a collective triumph.

Table of Contents

Abstract	ii
Summary	iv
Co-Authorship Statement.....	v
Dedication	vii
Acknowledgements.....	viii
Table of Contents	ix
List of Figures	xii
List of Tables	xiii
List of Appendices	xiv
Chapter 1	1
1 Introduction.....	1
1.1 Shoulder Anatomy	2
1.1.1 Osseous Anatomy	3
1.1.2 Soft Tissue Anatomy.....	11
1.2 Osseous Structures	15
1.2.1 Mechanical Properties of Bone.....	18
1.2.2 Stress Shielding and “Wolff’s Law”	19
1.3 Anatomical Shoulder Arthroplasty	19
1.3.1 Anatomical Shoulder Arthroplasty Components	21
1.3.2 Anatomical Shoulder Arthroplasty Procedure.....	23
1.3.3 Fixation Methods	24
1.3.4 Complications	26
1.4 Reverse Shoulder Arthroplasty	27
1.4.1 Reverse Shoulder Arthroplasty Components.....	32
1.4.2 Reverse Shoulder Arthroplasty Procedure.....	32
1.4.3 Implant Design and Fixation.....	34
1.5 Biomechanical Analyses.....	41
1.5.1 Humeral Stem Testing Standards.....	42
1.5.2 Finite Element Methods	43
1.5.3 Digital Tracking Methods	45
1.6 Motivation.....	49
1.7 Objectives and Hypotheses	51
1.8 Thesis Overview	52
1.9 References.....	53
Chapter 2	61

2	Orthogonal vs Tangential Interface Micromotion in Stemless Shoulder Implants: A Technical Note	61
2.1	Introduction.....	62
2.2	Methods.....	64
2.3	Outcome Variables and Analysis.....	66
2.4	Results.....	67
2.5	Discussion	67
2.6	Conclusion	70
2.7	References.....	71
	Chapter 3	74
3	Developing a System for the Evaluation of Novel Shoulder Implant Designs	74
3.1	Introduction.....	75
3.2	Methods.....	76
3.2.1	Design Problem and Requirements.....	76
3.2.2	Three-Dimensional Force Application	77
3.2.3	Digital Micromotion Tracking	82
3.2.4	Apparatus Control and Digital Image Collection	83
3.3	Outcome Variables and Statistical Analysis	84
3.3.1	Apparatus Design Evaluation	84
3.4	Results.....	86
3.5	Discussion	92
3.6	Conclusion	93
3.7	References.....	94
	Chapter 4	97
4	An Assessment of Cadaveric vs Synthetic Cancellous Bone Models for the Quantification of Normal Micromotion using Press-Fit as a Clinical Variable	97
4.1	Introduction.....	98
4.2	Methods.....	99
4.3	Outcome Variables and Analysis.....	104
4.5	Discussion	106
4.6	Conclusion	107
4.7	References.....	109
	Chapter 5	111
5	Stemless Reverse Shoulder Arthroplasty Neck-Shaft Angle Influences Humeral Component Time-Zero Fixation and Survivorship: A Cadaveric Biomechanical Assessment.....	111
5.1	Introduction.....	112
5.2	Methods.....	113

5.2.1	Specimen Preparation.....	113
5.2.2	<i>In-Vitro</i> Loading Protocol	115
5.2.3	Measurement of Implant Stability.....	119
5.3	Outcome Variables and Analysis.....	121
5.4	Results.....	121
5.5	Discussion	124
5.6	Conclusion	129
5.7	References.....	130
Chapter 6		133
6	Stemless Reverse Humeral Component Neck-Shaft Angle has an Influence on Initial Fixation.....	133
6.1	Introduction.....	134
6.2	Methods.....	135
6.2.1	Developing 3D Models using Computed Tomography	135
6.2.2	Implant Development and Positioning	138
6.2.3	Finite Element Model Generation	140
6.3	Outcome Variables and Analysis.....	142
6.4	Results.....	143
6.5	Discussion	148
6.6	Conclusion	153
6.7	References.....	154
Chapter 7		158
7	Thesis Closure.....	158
7.1	Summary	159
7.2	Strengths and Limitations	162
7.3	Future Investigations.....	164
7.4	Significance and Conclusions	165
7.5	References.....	167
Appendices.....		168
Curriculum Vitae		219

List of Figures

Figure 1-1: Bony Structures of the Right Shoulder Joint (Langohr, 2015)	3
Figure 1-2: Osseous Anatomy of the Right Humerus (Langohr, 2015)	5
Figure 1-3: Anterior View of the Right Scapula and Clavicle (Langohr, 2015)	8
Figure 1-4: Significant Scapulohumeral Shoulder Muscles (Langohr, 2015)	14
Figure 1-5: Humeral Separation of Cortical and Trabecular Bone (Langohr, 2015)....	17
Figure 1-6: Major Shoulder Arthroplasty Variations (Soltanmohammadi, 2019).....	20
Figure 1-7: Anatomical Shoulder Arthroplasty Components (West, 2017)	22
Figure 1-8: Reverse Total Shoulder Arthroplasty Components (Langohr, 2015)	29
Figure 1-9: Biomechanical Advantage of Reverse Total Shoulder Arthroplasty (Langohr, 2015)	30
Figure 1-10: Generic Humeral Component Geometries of Total Shoulder Arthroplasty (Razfar, 2014)	37
Figure 1-11: Finite Element Discretization of Humerus (Razfar, 2014)	44
Figure 2-1: Orthogonal vs Tangential Micromotion in a Stemless Humeral Implant .	63
Figure 2-2: Perform and Simpliciti Implants Positioned in a Humeral Model.....	65
Figure 2-3: The Tornier Simpliciti® Implant Split into Regions of Interest	66
Figure 2-4: Tangential and Orthogonal Micromotion in Tornier Perform and Tornier Simpliciti Implants.....	69
Figure 3-1: Rocking Horse Phenomenon Depicted on a Reversed Total Shoulder Arthroplasty	78
Figure 3-2: Vector Representation of all Relevant Loading Conditions available in OrthoLoad	79
Figure 3-3: Reverse Total Shoulder Arthroplasty Glenosphere Reaction Force	80
Figure 3-4: Triaxial Loading Apparatus and Polished Force Application Pad Detail.	81
Figure 3-5: Custom 3D-Printed Calibration Fixture	85
Figure 3-6: Cyclical Loading of a CERBERUS Actuator, Increasing Load from 100 [N] to 350 [N]	88
Figure 3-7: Macro Digital Tracking Calibration Curve	89
Figure 3-8: Micro Digital Tracking Calibration Curve.....	90
Figure 3-9: Comparison Between LVDT and Digital Tracking Measurements as a Function of Load.....	91
Figure 4-1: BMD and Young's Modulus of Bone Slices at Interface	100

Figure 4-2: Modular Generic Press-Fit Implant.....	102
Figure 4-3: High Resolution Digital Image Tracking.....	103
Figure 4-4: Porcine vs Polyurethane Foam Micromotion.....	105
Figure 5-1: NSA Cut Guide	114
Figure 5-2: CERBERUS Apparatus with a Potted Humeral Specimen Positioned...	116
Figure 5-3: OrthoLoad Boundary Load Vectors.....	117
Figure 5-4: Boundary Loads on a Humeral Model	118
Figure 5-5: High Resolution Image of the Bone-Implant Interface.....	120
Figure 5-6: Micromotions in Stemless Implants based on Neck Shaft Angle	122
Figure 5-7: Implant Survivability at 135° and 145° NSA	123
Figure 5-8: A 3D Plot of "Safe" OrthoLoad Activities.....	126
Figure 6-1: Development of 3D Solid SolidWorks Humeral Model with Trabecular and Cortical Regions from CT Scan Data.....	137
Figure 6-2: A Generic Stemless Reversed Humeral Component Inserted into a Proximal Humerus (Left).....	139
Figure 6-3: Force Vectors for Four Activities of Daily Living and Projected onto a Humeral Model (Left).....	142
Figure 6-4: Heatmaps of Bone-Implant Distraction, Projected onto a Left Humerus	144
Figure 6-5: Heatmaps of Implant-Bone Distraction Micromotion for Four Activities of Daily Living at Five NSAs	145
Figure 6-6: Maximum Micromotion (mean \pm 1 SD) Levels for the Four Simulated Activities at Five Neck Shaft Angles.....	147
Figure 6-7: Depiction of a Wedge of High-Quality Bone, Removed by a 135° NSA Resection.....	151
Figure 6-8: Interface BMD of 135° NSA and 145° NSA Stemless Humeral Implants	152

List of Tables

Table 5-1: Micromotion Data during Increasing Cyclical Load Tests	121
Table 6-1: Summary of Micromotions Developed During Activities of Daily Living at Varied NSAs	146

List of Appendices

Appendices.....	168
Appendix A: Glossary of Medical and Engineering Terminology.....	168
Appendix B: Loading Apparatus Design and Control.....	170
B.1 Introduction	170
B.2 Physical Design	170
B.3 Software Design	184
Appendix C: Mimics Bone Model Generation	187
C.1 Introduction	187
C.2 Bone Model Isolation	188
Appendix D: SolidWorks Bone Reaming and Implant Positioning	192
D.1 Introduction	192
D.2 <i>In-Silico</i> Humeral Head Reaming	193
D.2 Implant Positioning	195
Appendix E: Material Property Assignment using Mimics 2021	198
E.1 Introduction	198
E.2 Material Property Assignment.....	198
Appendix F: Finite Element Analysis using Abaqus/CAE 2021	203
F.1 Introduction.....	203
F.2 Implant/Bone Contact.....	203
Appendix G: Bone Mineral Density Analysis of Peri-Prosthetic Bone.....	206
G.1 Introduction	206
G.2 Methods.....	207
G.3 Outcome Variables and Analysis	209
G.4 Results.....	209
G.5 Discussion	214
G.6 Conclusion	216
Appendix References	217

Chapter 1

1 Introduction

OVERVIEW

Total reverse shoulder replacement is now a very common treatment option for patients with severe arthritis of the glenohumeral joint, as well as rotator cuff tears and complex shoulder joint fractures. The survival of the reverse total shoulder arthroplasty prosthetic is dependent on several key engineering failure modes including instability and humeral component loosening. The humeral component is an important feature of the shoulder implant and has been the subject of numerous studies. However, recent advances in the design of the humeral component have not yet been thoroughly studied. For this dissertation, a dynamic loading apparatus was designed, and both experimental and computational evaluations were conducted to determine the effect of implant design and surgical implantation variables during testing of the fixation of the humeral component under clinically relevant loads. This primary chapter provides a description of the shoulder anatomy, material properties of bone, the primary total shoulder arthroplasty procedure, the reverse total shoulder arthroplasty procedure, as well as the most common biomechanical experimental testing procedures and technologies used to quantify fixation of the humeral implant component. Descriptions of the hypotheses and motivations regarding these investigations are also inscribed herein.

(Appendix A provides a glossary of the medical and engineering terminology used throughout this thesis)

1.1 Shoulder Anatomy

The shoulder is a complex musculoskeletal structure with numerous components functioning together as an integrated biomechanical mechanism. The shoulder is comprised of a variety of muscular, skeletal, and connective tissue components; including three bones, three joints, one pseudojoint, as well as a complex assortment of muscles, tendons, and ligaments working together to articulate and stabilize the joint (Figure 1-1) [1]. This elaborate arrangement of biomechanical components, and the resulting combined articulations, provide a larger range of motion to the shoulder in three planes than any other joint in the human body [2]. In contrast to the other joints in the human body which are primarily constrained by bony anatomy, the primary constraint on the shoulder joint is provided by local muscle, tendon, and ligament tissues [2], [3]. The resulting dynamic constraint allows this joint to achieve an impressive range of motion with little constraint provided by the surrounding osseous structures [4]. There are multiple contributing factors that affect the mobility and stability of the shoulder joint, including the health of the articular surface and the condition of the muscle-tendon and capsuloligamentous structures housed within the shoulder multipart [1]. Thus, the overall performance of the shoulder relies on the high level of cooperative function of the numerous components involved in the actuation of the shoulder joint. Injury or degradation of a single component can severely diminish the overall functionality of the shoulder, potentially resulting in pain or even pseudoparalysis of the shoulder joint [1], [2], [5].

This work will focus primarily on the function and testing of the glenohumeral joint. However, to better understand the biomechanical contributions of the components of the shoulder, each component must first be well understood. The shoulder multipart is comprised of a variety of different components that can be divided into two main categories: (i) osseous anatomy and (ii) soft tissue constructs [1]. The key anatomical properties of each of these discrete functional groups is described below in detail.

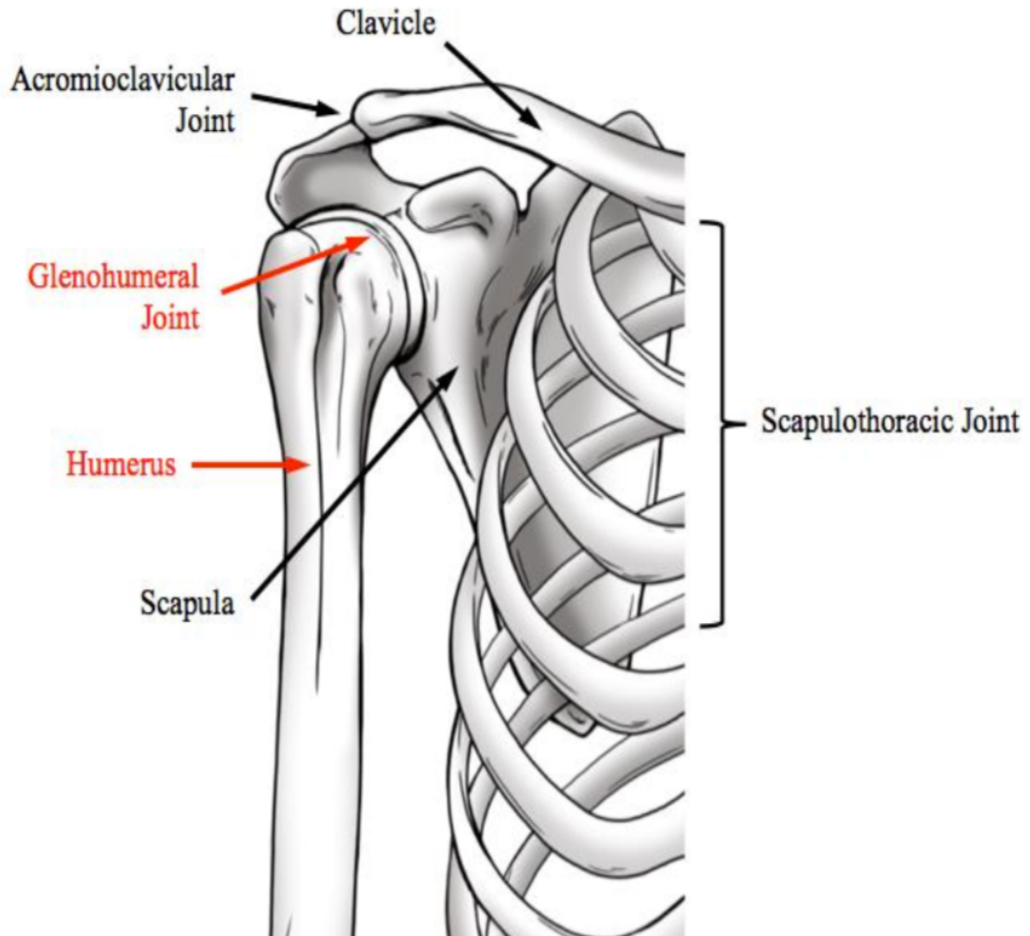


Figure 1-1: Bony Structures of the Right Shoulder Joint (Langohr, 2015)

The glenohumeral joint and humerus are the primary joint and bone of interest, respectively, highlighted alongside the other bony structures of the shoulder.

1.1.1 Osseous Anatomy

The osseous anatomy of the shoulder can be described as the articulations and bony structures directly contributing to joint movement [1]. There are three major bones involved in shoulder movement: the clavicle, the humerus, and the scapula (Figure 1-2). The large range of motion of the shoulder is achieved through the contributions of the glenohumeral joint, the acromioclavicular joint, the sternoclavicular joint, and the scapulothoracic pseudojoint [1]. These four major articulations cooperate to enable the large range of motion exhibited by the shoulder. The glenohumeral joint provides the major relative motion between the humerus and the scapula, while the other three joints provide the

variety of scapular rotations achievable relative to the torso; simultaneously to glenohumeral rotation [2]. The combined articulations of the shoulder and the surrounding musculature therefore permit the shoulder to have the largest range of motion in all three planes than any other joint in the human body [1]. The spherical shaped head of the humerus, when positioned in the concave cavity of the scapula, experiences little constraint from the surrounding osseous structures and is free to achieve a wide range of orientations when healthy [1], [4]. However, the degree of mobility in the shoulder, and the stability of the same, is heavily reliant on the health of the articular surface and the condition of the muscle-tendon units and capsuloligamentous structures involved in the actuation of the shoulder joint [1]. Resultantly, degradation or damage to any component of this complex multi-joint can severely affect the cooperative function of the shoulder [1].

1.1.1.1 Bony Structures

The humerus forms the most proximal aspect of the upper limb. It is the longest and largest bone in the upper limb and is positioned between the scapula, and the radius and ulna [6]. The proximal surface of the humerus is largely spherical and articulates within the concave glenoid cavity while the distal end forms one side of the elbow (Figure 1-2). The proximal aspect of the humerus is referred to as the humeral head and is oriented in the superior-medial-posterior direction, resembling approximately one-third of a sphere. The humeral head is positioned contacting the articular surface of the glenoid cavity, forming the synovial glenohumeral joint. A thin layer of hyaline cartilage covers one half of the glenohumeral articular surface; dissipating and resisting the compressive forces transmitted between the humerus and scapula during the loading of the shoulder [1]. When the humerus is oriented in the superior-medial-posterior position, it optimally transmits load and is the most effective in range of motion and stability of the shoulder [2]. The distal end of the humerus forms one half of the elbow joint, contains both articular and non-articular surfaces, and is transversely wider than the shaft of the humerus [1]. Articular surfaces in the elbow, the capitulum and trochlea, articulate with the radius and the ulna respectively [1]. In comparison to the quadrupedal ancestors of the human, the primate humerus is relatively medially rotated with respect to the humeral head, giving it the characteristically large range of external rotation unique to primates [6].

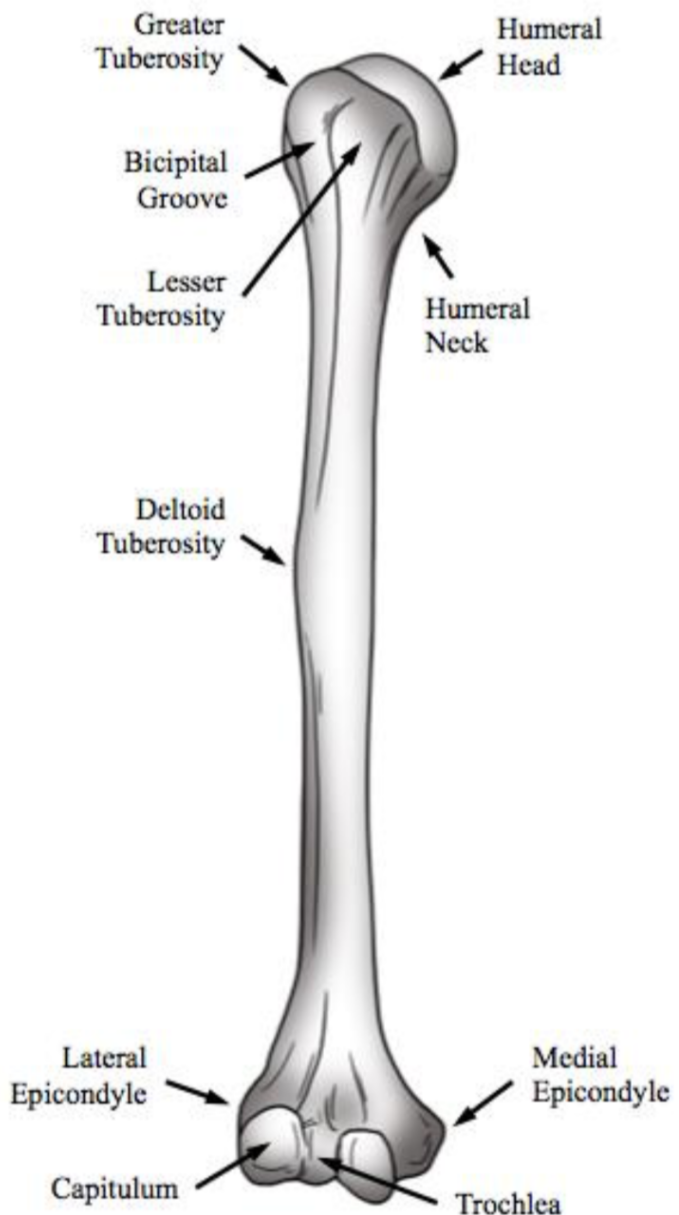


Figure 1-2: Osseous Anatomy of the Right Humerus (Langohr, 2015)

Important landmarks of the humerus contributing to the motion of the shoulder joint. The upper anatomy of the humerus, above the deltoid tuberosity, is the main area of interest.

The greater and lesser tuberosities are location sites for muscles involved in the actuation and stabilization of the shoulder [7]. The greater tuberosity is separated from the lesser tuberosity by the bicipital groove, also known as the intertubercular sulcus, which acts as a

guide for the bicep tendon from its origin, around the glenohumeral joint and to its insertion point [2], [6]. The greater tuberosity is located on the lateral edge of the proximal humerus and is positioned posteriorly to the acromion whereas the lesser tuberosity is located laterally from the articular margin of the humeral head, projecting from the front of the humeral shaft [6]. The greater tuberosity, or greater tubercle, is the most lateral part of the proximal end of the humerus. The posterosuperior aspect of the greater tubercle serves as the attachment point for the supraspinatus, infraspinatus, and teres minor muscles [6], providing stability during the adduction-abduction, and internal-external rotation motions of the humerus [2]. The greater tubercle also performs an important function in the biomechanical advantage of the shoulder joint, increasing the moment arm of the supraspinatus and deltoid muscles during abduction angles of 30 degrees and 60 degrees respectively [1]. This is similar to the method in which the acromion increases the moment arm of the deltoid muscle [2]. The lesser tubercle is located anterior and distal to the humeral neck, laterally to the articular margin of the humeral head [6]. The tendons from the fourth rotator cuff muscle, the subscapularis, attach at the lesser tuberosity [2]. These tendons are responsible for providing stability during the adduction-abduction and internal-external reorientations of the shoulder [2]. It is important to note that the attachments from the teres minor and subscapularis muscles are not confined to their respective tuberosities, instead extending past the tubercle to the adjacent humeral metaphysis [6]. The deltoid tuberosity, located along the anterolateral shaft of the humerus, serves as the insertion point for the deltoid muscle [2].

The scapula is a thin, flat, and triangular bone that is positioned over the posterolateral chest wall [6]. The scapula forms the connection between the torso and the upper limb, acting to transmit forces between the upper limb and torso and vice versa in addition to rotating in conjunction with the humerus, thereby facilitating the large range of motion exhibited by the shoulder [2]. The scapula is located overlying parts of the second to seventh ribs on the posterolateral aspect of the thorax (Figure 1-3) [4], [6]. The scapula and the clavicle together form a strut-like configuration, attaching the scapula to the axial skeleton [1]. The three columns of bone at the neck of the scapula: the lateral spine of the scapula, the lateral border of the scapula, and the coracoid, work together to transmit load from the glenoid

fossa or the coracoid into the scapula [6]. This biomechanically-optimized arrangement provides stability to the shoulder in addition to enabling the large range of motion exhibited by the shoulder, allowing the humerus to swing clear of the body [2].

The clavicle, or collarbone, extends laterally from the sternum to the acromion of the scapula, articulating with both during scapulothoracic rotation [2]. The purpose of the clavicle is to resist the compressive forces across the space over which it spans, thereby increasing the moment arm of the medial deltoid and adding to the biomechanical advantage of the shoulder during actuation of the surrounding musculature [2], [7]. The coracoid process, spine, and acromion are scapular bony projections, serving as origin and insertion sites for the supraspinatus, infraspinatus, and subscapularis muscles [7]. The clavicle acts to transmit part of the weight of the limb to the axial skeleton, and during scapulothoracic rotation, the clavicle articulates at the acromioclavicular joint (between the clavicle and acromion), and the sternoclavicular joint (between the sternum and clavicle), guiding and stabilizing the scapula as it articulates with the thorax [1].

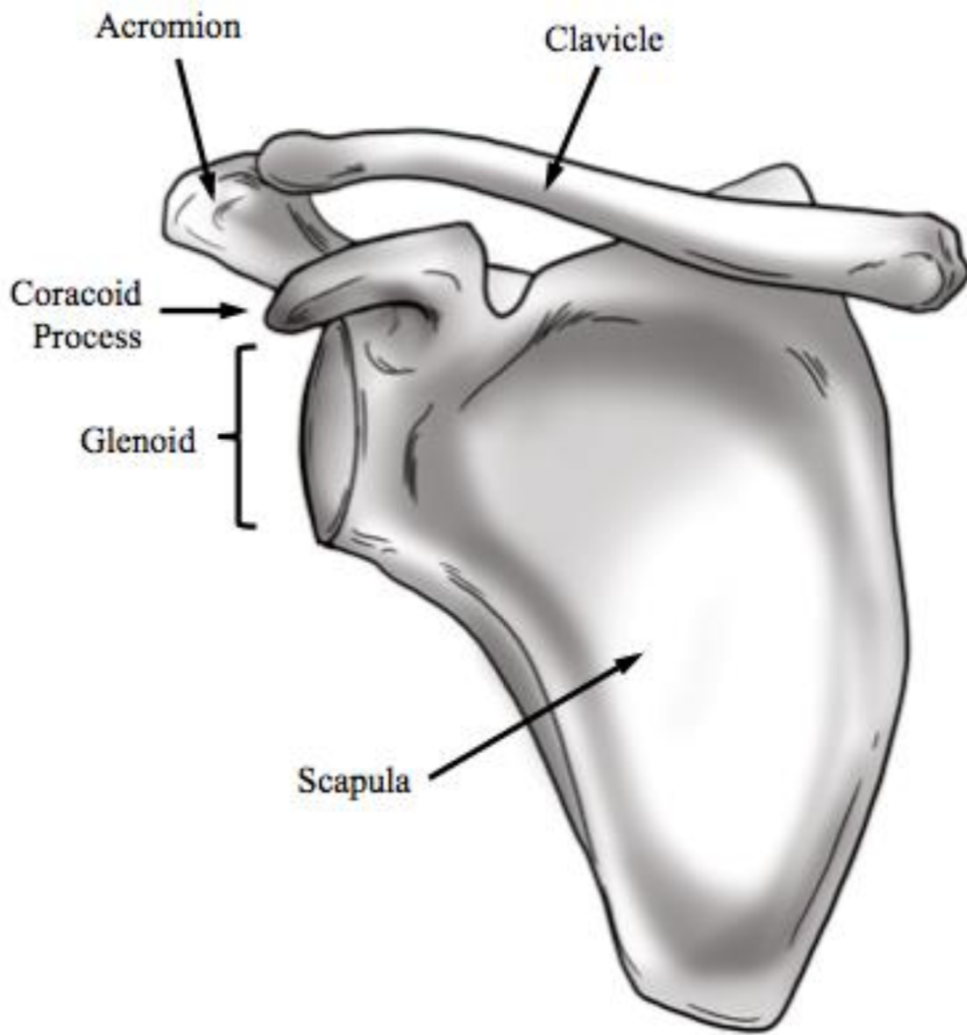


Figure 1-3: Anterior View of the Right Scapula and Clavicle (Langohr, 2015)

Important anatomy of the scapula and clavicle where articulations and muscle origins occur.

1.1.1.2 Articulations

Joints are the bony structures in the skeleton where two or more bones meet, providing motion by facilitating the relative movement of articulating components [2], [6]. The shoulder joint, although versatile, is also the most susceptible to dislocation due to its flexible constraint mechanism [1], [3]. Of the four joints that are involved in the movement of the shoulder, the glenohumeral joint is the largest contributor to the range of motion exhibited by the shoulder; providing three degrees of freedom about the centre of rotation at the humeral head.

The glenohumeral joint is known as a ball-and-socket joint; defined as any multiaxial joint formed at the mating of a globoid head and an opposing concave cup [6]. It is important to note that the humeral head and glenoid are not perfectly spherical shapes, and rather are slightly ovoid [6]. This means that congruence is not perfect at the articulation and optimal mating between the surfaces only occurs when the arm is positioned in the superior-medial-posterior position [2], [6]. The glenohumeral joint is classified as a synovial joint; meaning that the articular surfaces are lubricated with the boundary lubricant lubricin, facilitating motion during slow movements, while the joint cavity is filled with synovial fluid, introducing fluid-film lubrication during rapid movements [6]. The incongruence of the glenohumeral articulating surfaces aids in the initiation of the fluid-film lubrication interaction during less rapid actuations of the shoulder [6].

The glenohumeral joint functions in rotation, flexion/extension, and abduction/adduction modes, providing the three degrees of freedom possible between the humeral head and glenoid fossa [1]. The motions of the shoulder are highly sequence-dependent, meaning that the total range of motion enjoyed by the shoulder is conditional; based on the initial position of the articulating components [1]. The amount of adduction-abduction range of motion of the shoulder is an excellent example of the sequence-dependency of the shoulder. During the abduction motion of the shoulder, the range of motion is limited to 60 degrees to 90 degrees when the humerus is internally rotated at the commencement of abduction due to the constraining geometry of the greater tubercle of the acromion and the tensioning of the glenohumeral ligament [4]. However, if the humerus is rotated externally, the degree

of abduction possible increases to between 90 degrees and 120 degrees as the geometrical tension constraints of the system are reduced [4]. These effects of position-dependent geometrical constraints are necessary to be aware of during design of shoulder implants as they define what are considered as the “normal” operating conditions of the shoulder.

The articular profiles in the glenohumeral joint are the glenoid labrum, the hyaline cartilage-covered glenoid fossa, and the cartilage covered humeral head [1]. The glenoid labrum is a fibrocartilaginous ring that is positioned around the glenoid fossa, helping to effectively deepen the glenoid cavity and thereby increasing the stability of the glenohumeral joint [1]. The labrum increases the contacting surface area between the humeral head and the glenoid fossa by 56% transversally and 75% vertically [4]. This deepening of the glenoid socket decreases the average contact stress at the articulation, reducing cartilage wear and increasing overall articulation strength [2], [3].

The acromioclavicular, sternoclavicular, and scapulothoracic joints permit the relative motion between the scapula and torso [4]. These joints facilitate scapular rotation relative to the torso, stabilizing the scapula during movement [2]. Forces from the upper extremity are transferred through the scapula to the clavicle bone, and then on to the sternum via the sternoclavicular joint [1]. The acromioclavicular and sternoclavicular joints are synovial joints and are positioned between the clavicle and scapula and the clavicle and sternum, respectively [4]. The acromioclavicular joint is a synovial plane joint with a fibrocartilaginous disk; articulating at the acromial end of the clavicle and the medial acromial margin [6]. The acromioclavicular joint is considered to be the main articulation that connects the axial skeleton and the upper arm [1]. The articulating surfaces of both the acromion and clavicle are covered in fibrocartilage, and the intra-articular fibrocartilaginous disk present at the articulation partially separates the contacting surfaces of the acromion and the clavicle [4]. This fibrocartilaginous disk adapts to the contour of the acromioclavicular mating surfaces and, when healthy, serves to distinguish two discrete compartments between the clavicular and acromial surfaces [6].

The sternoclavicular joint is a synovial sellar joint [6]. At this joint, the shallow sternal socket of the first rib is separated from the bulbous sternal end of the clavicle by a fibrocartilaginous disk, similar to that of the acromioclavicular joint [4]. The medial end of the clavicle is convex cephalocaudally and concave anteroposteriorly while the opposing sternal socket is reciprocally shaped [4]. Although the articulating surfaces at the sternoclavicular joint are saddle-shaped, the joint functions as a ball-and-socket joint, maintaining three degrees of freedom during motion of the shoulder [4]. Additionally, similarly to the articulating surfaces of the acromion and clavicle, the articulating component surfaces of the sternoclavicular joint are covered in a layer of fibrocartilage [1]. This layer of fibrocartilage provides strength and elasticity to the contacting surfaces; resisting wear during the cyclical application of force and pressure at the articular surfaces of the sternoclavicular and acromioclavicular joints [1].

The scapulothoracic pseudojoint is the name given to the mechanism responsible for relative movement between the scapula and torso [1]. While not a synovial joint, the scapulothoracic pseudojoint is retained in place by the atmospheric pressure of the axioscapular muscles (levitator scapulae, rhomboid major, rhomboid minor, serratus anterior, and trapezius) [4]. Scapulothoracic relative motion is facilitated by the separation between the concave anterior surface of the scapula and the convex external surface of the thorax [4]. The serratus anterior and subscapularis muscles create a plane for the surfaces of the scapula and thorax to glide past one another, permitting the relative motion between the scapula and the torso [1].

1.1.2 Soft Tissue Anatomy

1.1.2.1 Ligaments

There are numerous passive soft tissue constructs contributing to the motion of the shoulder, statically stabilizing the translation and rotation of the humerus [2]. The several ligaments and joint capsules involved in movement of the shoulder cooperatively tension and loosen during glenohumeral actuation [1], aiding in limiting range of motion at extreme joint angles. The glenohumeral joint capsule possesses a large range of motion and provides

the freedom necessary to permit full functionality of the shoulder joint [1]. However, the passive soft tissues of the shoulder multipart are also sufficiently constrained to serve as constraining limits to glenohumeral motion, restricting joint hypermobility [2]. The fibrous glenoid joint capsule is positioned at the periphery of the glenoid labrum and at the margin of the humeral head, enveloping the joint [6].

The glenoid labrum is the fibrocartilaginous rim of the glenoid cavity, structurally deepening the glenohumeral socket and stabilizing the shoulder [6]. The glenoid labrum also serves to protect the bone as well as aid in the lubrication of the glenohumeral joint [2]. The labrum provides an origin point for a variety of glenohumeral ligaments, different combinations of which contribute to the stabilizing of the shoulder in the superior, anterior, and inferior aspects, tensioning during certain motion configurations [2].

1.1.2.2 Active Musculature

In addition to the stabilizing contributions of passive soft tissue in the shoulder, active musculature provides dynamic stabilization in addition to contributing to the actuation of the shoulder multipart (Figure 1-4). The muscles responsible for shoulder actuation can be categorized based on their respective attachment sites. When categorizing based on origin, the muscles of the shoulder can be grouped into the axiohumeral, axioscapular, and scapulohumeral muscles [2]. For the purposes of this work the scapulothoracic muscles (affecting rotation of the scapula with respect to the torso) will not be explicitly described.

The axiohumeral muscles, also referred to as the humerothoracic muscles, have attachments located laterally to the humerus and medially to the axial skeleton [1]. This muscle group is comprised of the pectoralis major and latissimus dorsi [2]. Although these two muscles are positioned on opposite sides of the trunk, both function to adduct and internally rotate the humerus [2]. The pectoralis major contributes to the flexion and internal rotation of the humerus while the latissimus dorsi generates extension and internal rotation of the humerus and clavicular head [2], [7].

Axioscapular muscles, also referred to as the scapulothoracic muscles, will not be defined explicitly in this work. In the context of shoulder actuation, the axioscapular muscles are responsible for maintaining the ball-and-socket configuration of the glenohumeral joint during reorientation of the humerus [7]. However, the axioscapular muscles also serve to provide relative motion between the scapula and the torso, as well as to elevate the acromion to provide biomechanical advantage during excessive acceleration phases of the humerus [7]. This reorientation of the scapula requires a complex coupling of different scapulothoracic muscles, and as a result, the scapula has an intricate system of muscular activation in order to perform the diverse array of tasks for which it is responsible [7]. For the purposes of this work, it is sufficient to note that the scapulothoracic muscle group includes the trapezius, levator scapulae, rhomboid major and minor, serratus anterior, and the pectoralis major muscles [1].

Scapulohumeral muscles have been categorized as having attachments distally on the humerus and proximally on the scapula. The scapulohumeral muscles include the deltoid, supraspinatus, subscapularis, infraspinatus, teres minor, and coracobrachialis muscles (Figure 1-4). The deltoid is located on the proximal portion of the humerus and converges to an insertion on the lateral aspect of the humeral shaft [7]. The deltoid is the largest muscle that contributes to shoulder motion, and is comprised of three distinct parts, the anterior (clavicular), the lateral (acromial), and the posterior (spinal) components, each of which are separated by fibrous raphes [3]. When all three parts of the deltoid contract simultaneously, the humerus abducts from the trunk, however these highly differentiated components of the deltoid are not solely restricted to abducting the arm [1]. Individual contractions of each deltoid component can affect numerous different humeral orientations. Extension and lateral rotation of the arm can be affected by individual contractions of the anterior and posterior components of the deltoid [1]. Each distinct head of the deltoid occurs unique lines of action, and while working cooperatively, the anterior and posterior deltoids produce flexion-extension and internal-external rotation modes in addition to the abduction-adduction humeral rotations of the humerus [2].

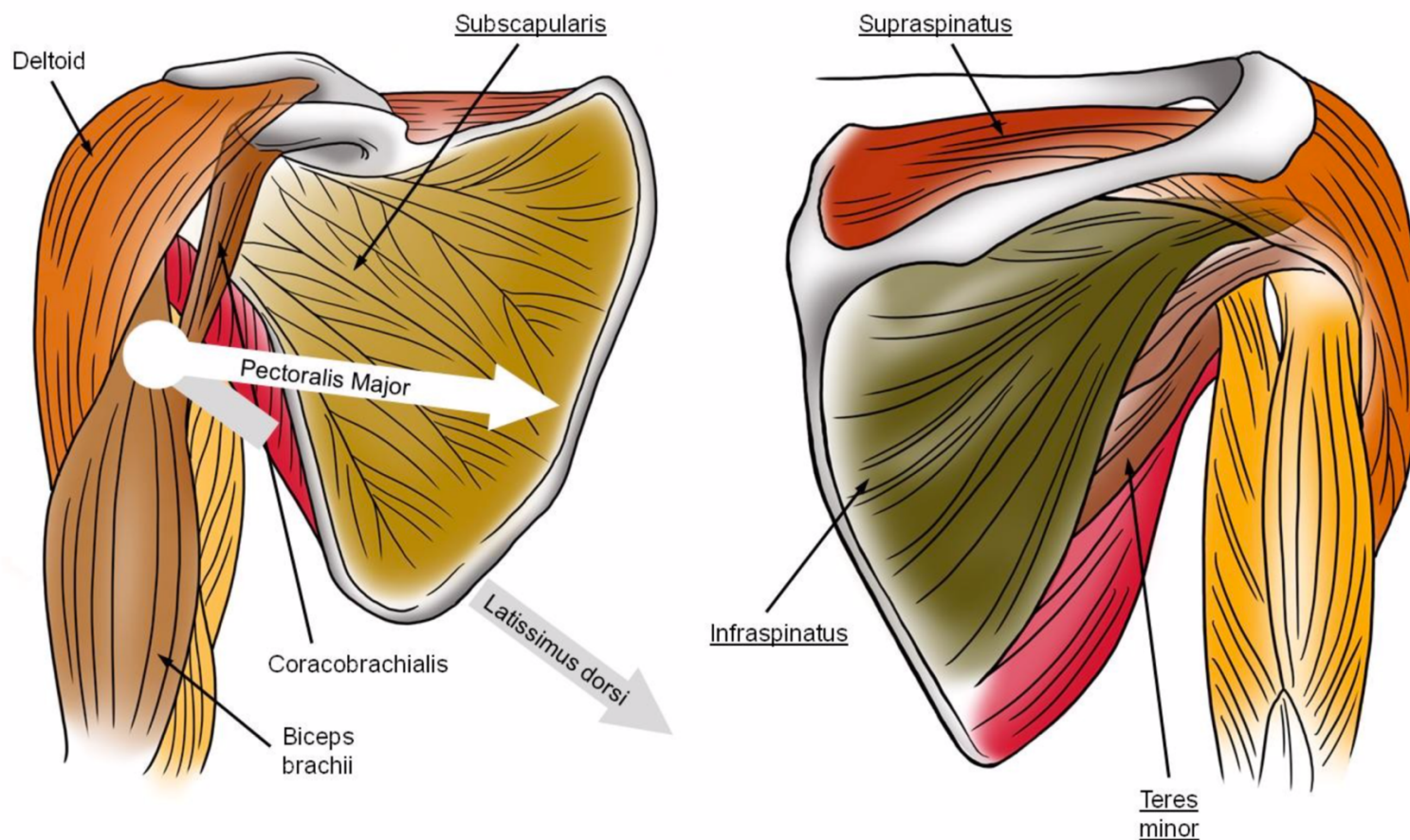


Figure 1-4: Significant Scapulohumeral Shoulder Muscles (Langohr, 2015)

Important scapulohumeral muscles viewed in the right shoulder from anterior (left) and posterior (right) views. Arrows signify the line of action in Pectoralis Major and Latissimus Dorsi muscles.

1.2 Osseous Structures

Bone tissue, or osseous tissue, is one of the most rigid materials to be found in the human body. Osseous tissue is a dense and highly organized composite material, formed by both inorganic phases and organic phases, providing immense structural support and protection to the human body and its organs. Osseous tissue is comprised of organic collagen and inorganic calcium and phosphate minerals which comprise approximately 60% to 70% of the material by weight [8]. Conversely, water comprises approximately 25% to 30% of the material by weight [8]. Bone acts as a strong connective tissue, and has evolved to enable fast terrestrial motion, facilitating the rigid and precise articulations that do not distort under the load needed for the predictable loading and rapid movements of the limbs [6]. However, bone acts in a viscoelastic and anisotropic manner, and the mechanical properties of bone are highly dependent on loading mechanism and rate. The organic collagen fibre content of bone provides the bone the ability to resist loading in tension in addition to its viscoelastic properties, whereas the inorganic components of bone provide the rigidity necessary to support compressive loads [8]. Bone is a highly adaptive material that is very sensitive to loading, changing properties and geometry based on disuse, immobilization, or vigorous activity [8]. In contrast to the cartilaginous components of the body, bone is highly vascular; and this high cellularity of osseous tissue contributes to its high level of adaption and reparation ability in the event of damage [8].

Osseous tissue is a highly anisotropic material; indicating that the mechanical properties of bone will change based on the direction of loading [8]. Generally, in the case of bone tissue, this results in larger load-bearing characteristics when bone is loaded longitudinally [8]. Bone is also considered to be viscoelastic; behaving differently based on speed of load application and length of loading. When bone is loaded rapidly, it can support higher loads before critical failure whereas during slow loading, in some cases, bone can only support loads of approximately half the magnitude [8].

Bones can be categorized into four distinct classifications based on their geometry and internal compositions [1]. These classifications include long bones, short bones, flat bones,

and irregular bones. In the context of the shoulder, the humerus and clavicle are considered to be long bones, whereas the scapula is considered a flat bone. The humerus and clavicle, as long bones, can be subdivided into three sections based on their composition: the epiphysis, the diaphysis, and the metaphysis. The epiphysis is the end and articular surface of the bone, the diaphysis is the central shaft of the bone, and the metaphysis is the mid-region between the epiphysis and diaphysis [1]. Macroscopically, bone can be subdivided into two groups based on its composite properties: trabecular (cancellous) and cortical (compact) bone (Figure 1-5).

Generally, cortical bone is located at the central cortex of long bones and is comprised of osteons or Haversian systems; cylindrical structural units that contain living osteocytes and a mineral matrix [6]. Osteons are oriented parallel to one another. In the case of long bones, this orientation is along the long axis of the bone [6]. The direction of collagen within osteons varies, but in a manner similar to the orientation of osteons in long bones, collagen fibres are generally oriented longitudinally in areas usually subjected to tension, and more obliquely at locations mainly subjected to compressive forces [6]. Due to the regularly oriented structural components in cortical bone, cortical bone structures are more suitable for absorbing compressive and tensile loading stresses and are more stiff and rigid than cancellous bone structures [1]. In the diaphysis of the bone, the entire section is comprised only of cortical bone [1]. Cortical bone is also present in the epiphysis, forming a cortical shell that gradually thickens towards the diaphysis of long bones [1].

Cancellous bone, or trabecular bone, is inhomogeneous, porous [1], and is sometimes referred to as spongy bone due to its highly vascularized structure, resembling a sponge [6]. Cancellous bone is basically lamellar and is comprised of trabeculae surrounding marrow cavities [6]. These trabeculae take the form of branches and curved plates [6]. Cancellous bone is not as strong as cortical bone but is optimally oriented in order to transmit applied stresses to the cortical shell of the epiphysis [1]. Trabecular bone is present in the epiphysis of long bones, gradually phasing out towards the outer edge of the metaphysis [1]. In the diaphysis of long bones, there is instead a “hollow” medullary canal within the cortical shell [1]. The relative proportion of trabecular to cortical bone varies

within bones depending on the predictable loading mechanisms encountered by the osseous tissue and the material properties required to support said loading [1]. Bone tissue is metabolically active, remodelling and adapting geometry in response to the repetitive physiological influences and mechanical forces encountered [1]. Due to the vastly differing mechanical properties of trabecular bone and cortical bone, bone remodelling is highly localized and will vary throughout the cross section of bone depending on the optimal energy absorption criteria [1].

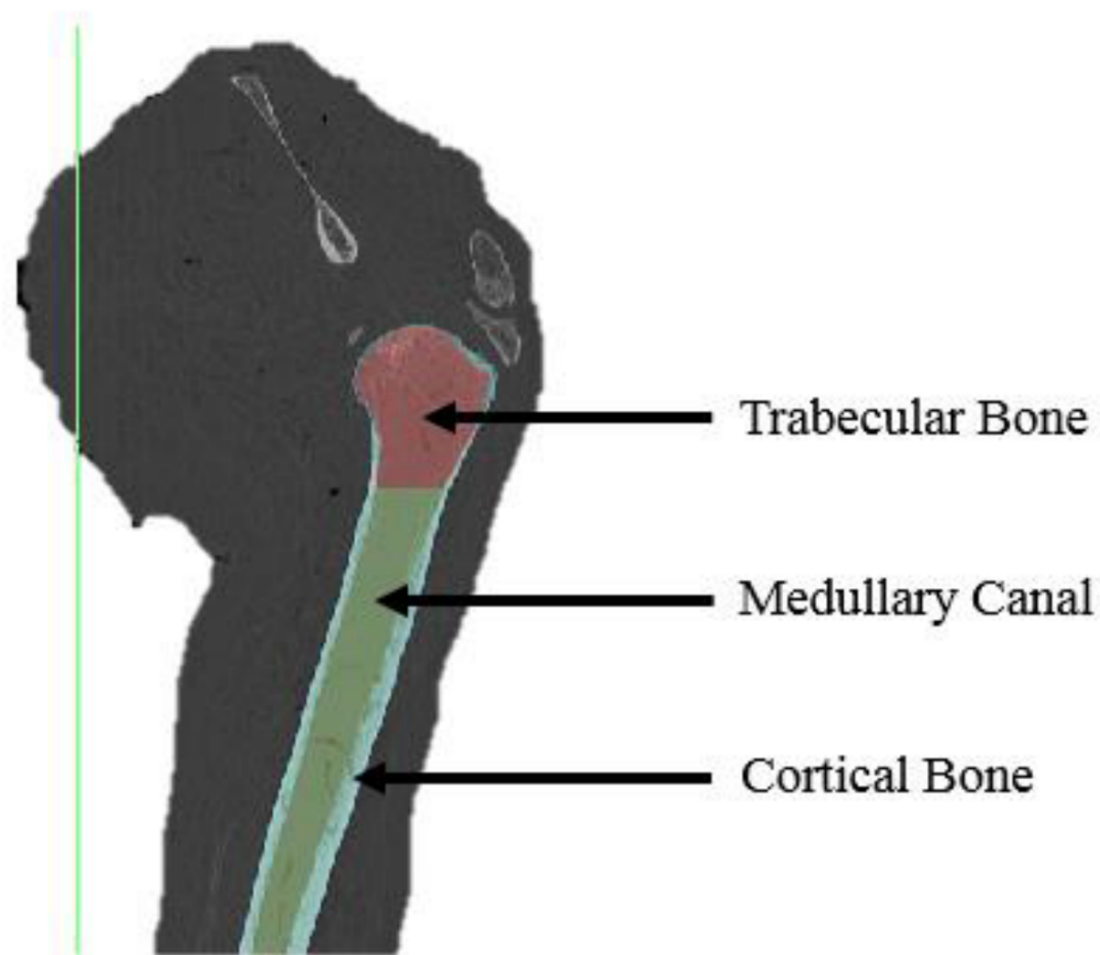


Figure 1-5: Humeral Separation of Cortical and Trabecular Bone (Langohr, 2015)

Internal division of cortical and trabecular bone in the left humerus. Trabecular bone located near the glenohumeral articulation is labeled in red, and the cortical bone is labeled in green.

1.2.1 Mechanical Properties of Bone

Bone is comprised mainly of hydroxyapatite microcrystals and collagen type I [6]. This complex composite material is highly responsive to physiological and mechanical influences and as a result, has location-varying, viscoelastic, and anisotropic properties based on location, loading direction, and loading method encountered [1], [6], [8]. This translates to inconsistent instantaneous material properties in bone which are highly case-dependent, making replication of bone using analogue materials challenging. These unpredictable material properties make performing mechanical testing on prosthetic components difficult and costly [9]. Due to the difficulties of deriving a constant bone material model, there have been several works that have attempted to create a method of isolating location-based mechanical properties using non-invasive methods; the most prevalent relationship accepted in literature today is the Young's modulus-bone density estimation [1], [10]. Using this estimation technique there are again varying outcomes, but for the specific purposes of this work the widely accepted results of a 2003 experimental study focused on the modulus-density relationship of trabecular bone will be used [11]. This relationship facilitates the estimation of modulus across the highly varied densities of trabecular bone, which are extremely dependent on patient morphology and sampling location [11].

Conversely, cortical bone, although still possessing anisotropic and viscoelastic properties, has a more consistent Young's modulus of between 12-14 GPa and 20-22 GPa in the transverse and longitudinal axes, respectively [12]. However, these values can also vary based on patient age, sex, or the pathology present.

To quantify the material properties of bone for 3D modelling and development of bone analogue materials, computerized tomography (CT) scans of bone are obtained and the apparent density of the local bone is quantified in Hounsfield Units (HU) [1]. The modulus-density relationship of trabecular bone to be used in this study was derived in an experimental study completed by Morgan *et al* [11]. The results of this study indicated a strong site-dependency in the relationship between elastic modulus and density, indicating that the mechanical properties of bone are more reliant on trabecular orientation and energy

absorption than on density alone [11]. However, estimations produced by this method are considered acceptable in the context of empirical bone models [1]. There are many alternative methods of approximating Young's modulus of trabecular bone, some of which include computational or Finite Element models, however these methods consistently produce higher values of Young's modulus than those produced by Morgan *et al* [11]. In an effort to maintain engineering conservatism, this paper will use the experimental relationship published by Morgan *et al* [11].

1.2.2 Stress Shielding and “Wolff’s Law”

In the 1890s, a German team observed and documented the relationship between the internal changes of bone and the changes in the external mechanical influences of bone [13], [14]. In understandable terms, the team revealed that external mechanical loads, when applied to bone, cause geometrical and structural changes to bone as the tissue adapts and remodels to absorb the change in loading [14]. This effect was named in recognition of Julius Wolff, a researcher on the German team, and is now referred to as “Wolff’s Law”. This remodelling process occurs over time, optimizing the bone’s structure, composition, and geometry as loads are regularly applied [1], [13]. In the context of orthopaedic implants, the insertion of an alien device can substantially change the distribution of load within the bone, sharing the load and decreasing the mechanical loading demand on the surrounding bone [1]. This is the direct consequence of orthopaedic implants being more rigid than the native bone structures. Unfortunately, the dramatic reduction in stresses in the native bone can result in loss of bone surrounding the implant, as the bone is no longer required to absorb and dissipate the same level of energy [13]. This can lead to implant loosening and failure of the reconstructed joint. This occurrence is referred to as stress shielding, and is a common problem associated with the shoulder arthroplasty procedure [1], [15].

1.3 Anatomical Shoulder Arthroplasty

The shoulder arthroplasty is a surgical procedure that is performed to reduce pain and improve function of the glenohumeral joint. The procedure is frequently prescribed to

patients with infection, trauma, or arthritis of the glenohumeral articulation [16]. The shoulder arthroplasty procedure has evolved over time, with variations in the prosthetic increasing the number of surgical options available to best suit the needs of the patient [17] (Figure 1-6). Early reports of the shoulder arthroplasty are widely reported, however it is generally accepted that Themistocles Gluck, a German physician and surgeon, pioneered and designed the first shoulder arthroplasty in the late 1800s [16]. However, it was not until 1893 when the first record emerged of a shoulder arthroplasty being performed on humans [16]. In 1893, French surgeon Jules Emile Péan was widely credited to have successfully implanted a rubber and platinum prosthetic into the shoulder of a baker [16]. This primary attempt installing a shoulder prosthetic was at first successful, increasing strength and range of motion in the patient, however the implant was removed two years later due to infection [16].

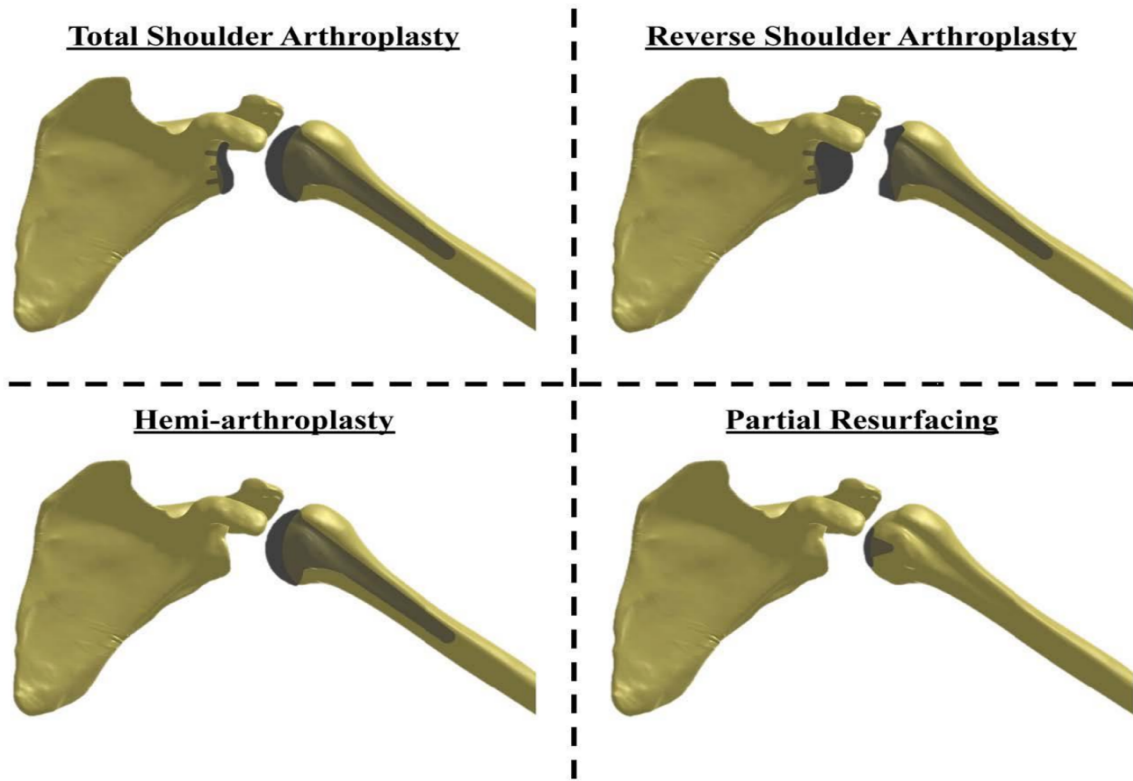


Figure 1-6: Major Shoulder Arthroplasty Variations (Soltanmohammadi, 2019)

Common variations of the shoulder arthroplasty procedure available to treat severe humeral fractures, severe arthritis, and other shoulder deficiencies; each with varying levels of invasiveness and success rates.

The first shoulder arthroplasty procedures were not immediately accepted as a successful method of improving shoulder function. It was not until Charles S. Neer designed the Neer prosthesis that the shoulder arthroplasty became widely regarded as a viable method of treating shoulder deficiencies [16]. In 1955, Neer introduced and began human clinical trials on the partial arthroplasty procedure [18]. His clinical trials reflected positive results, where 11 out of 12 patients who received a proximal humeral arthroplasty reported to be free of pain [16]. In 1974, Neer repeated his clinical trials using his proximal humeral arthroplasty design, this time treating glenohumeral osteoarthritis [16]. Results of this trial were similarly successful [16]. Although pain relief was repeatedly reported during the early Neer proximal humerus arthroplasties, in postoperative inspection of the prostheses, superior humeral head migration was frequently observed [16].

In response to repetitive reports of superior head migration in Neer humeral prostheses, in 1977, twenty years after Neer's introduction of the partial arthroplasty procedure, Marmor proposed the addition of a glenoid component to the shoulder arthroplasty [16]. The glenoid component was introduced in an attempt to promote stability and reduce humeral head migration after five of Marmor's patients who were suffering from rotator cuff tears experienced superior migration [16]. This proposition led to the evolution of the total shoulder arthroplasty procedure, designed with both humeral and glenoid components, which is now the most common treatment option available to patients who suffer severe arthritis of the glenohumeral joint or patients who have occurred massive proximal humeral fractures [1].

1.3.1 Anatomical Shoulder Arthroplasty Components

The common total shoulder arthroplasty procedure has glenoid and humeral components (Figure 1-7), geometrically mimicking the anatomical configuration of the glenohumeral joint [19], [20]. The humeral stem and humeral head components are fitted together using a Morse taper, allowing for minimization of stocking requirements as well as reducing the need for stem removal during revision surgery in both the anatomical and reverse total shoulder arthroplasties [21]. A glenoid baseplate component is mounted to the prepared

glenoid surface, forming a replicated glenohumeral articular surface in place of the damaged glenohumeral articulation [19].

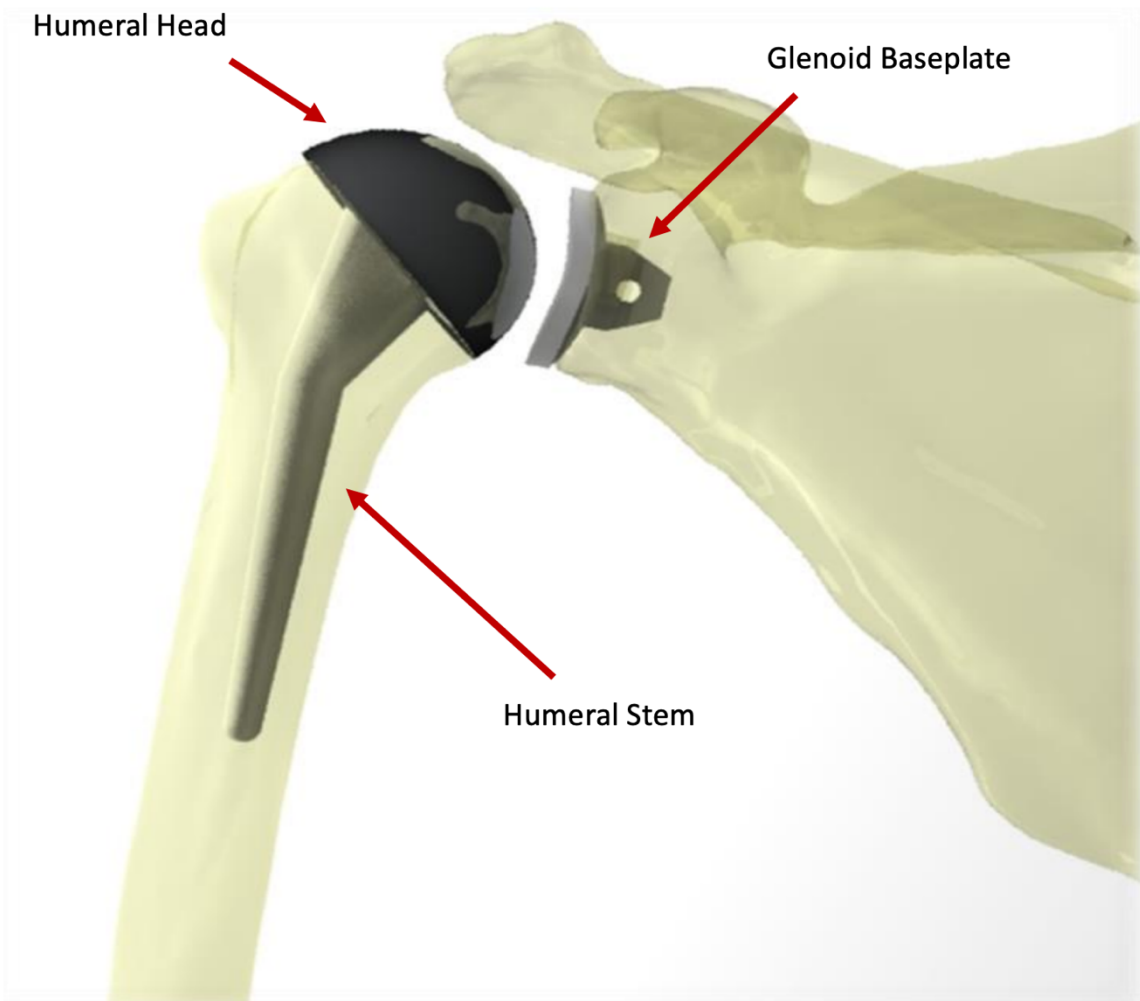


Figure 1-7: Anatomical Shoulder Arthroplasty Components (West, 2017)

Major components of the common anatomical total shoulder arthroplasty, including a glenoid baseplate component installed on the prepared glenoid, a humeral stem component installed in the epiphysis and diaphysis of the humerus, and a humeral head component fitted to the humeral stem using a Morse taper arrangement.

1.3.2 Anatomical Shoulder Arthroplasty Procedure

Anatomical shoulder arthroplasty is a complex surgery that involves invasive navigation of the shoulder. For a routine primary total shoulder arthroplasty procedure with an intact rotator cuff, a deltopectoral approach is used [19]. Once the humeral head has been exposed, osteophytes are removed and the humerus is prepared [19]. All osteophytes that might alter the perception of the true neck of the humerus are excised in order to avoid inaccurate orientation of the reaming process and erroneous cutting of the humeral head; potentially leading to a varus or valgus cut [19]. The humeral head is cut off within 8 mm \pm 3.2 mm cephalad of the superior edge of the greater tuberosity, determined by the insertion of the supraspinatus tendon [19]. The humeral head cut must be in proper retroversion with respect to the transepicondylar axis, normally between 20 and 40 degrees of retroversion in order to ensure appropriate prosthetic stability and range of motion [19]. After cut orientation is confirmed, the humeral head is cut with an oscillating bone saw. A trial implant is then temporarily installed for verification of the cut orientation [19].

Trial humeral heads are positioned on the humerus in order to accurately mate to the geometry of the native glenoid [19]. After the correct size of humeral head prosthetic is identified, a calcar planar is used to level the exposed face of the humeral osteotomy to ensure acceptable contact mating is achieved with the collar of the humeral head component [19]. The humerus is then reamed for insertion of the humeral stem, and temporary humeral stem components are fit-tested for sizing and orientation before the final humeral stem is positioned [19]. The final humeral stem component is typically installed using either a press-fit or cementation fixation method depending on the patient's age, bone quality, or humeral canal type and geometry [19]. In the case of poor bone quality, evidence of osteoporosis, or rheumatoid arthritis, a cemented humeral stem is preferred [19]. The final humeral head component is then installed onto the humeral stem using a Morse taper arrangement and is gently tapped into place to ensure secure fixation [19].

The glenoid component of the total shoulder arthroplasty is installed in a manner similar to that of the humeral components [19]. The glenoid is exposed and any remaining cartilage is removed from the glenoid down to the subchondral bone [19]. For reasons similar to

those driving the process of exposing of the humeral head, osteophytes surrounding the glenoid can distort the shape of the native anatomy, making it difficult to isolate the centre of the glenoid and are therefore removed [19]. The glenoid prosthetic component is chosen to maximize the head size without allowing any overhang to occur. The centre of the glenoid is identified with the aid of a glenoid-centring guide, and the glenoid is visually inspected before a centring hole is drilled and a probe is inserted into the glenoid vault to verify the depth of the guide hole [19]. The glenoid is then reamed using an open-faced reamer to prepare the mating surface, and any posterior glenoid wear is corrected by selectively resecting anterior bone [19]. There are several different glenoid-baseplate fixation mechanisms available, and dependent on the preference of the surgical team and chosen fixation design, a guide is positioned and either three holes are drilled for a pegged glenoid component, or superior and inferior holes are drilled, and a vertical slot is machined for a keeled glenoid baseplate configuration [19].

In a method comparable to the installation of the humeral component of the total shoulder arthroplasty, a trial glenoid baseplate is used to assess stability, validity of positioning, and uniform seating on the prepared surface [19]. Once the sizing and positioning of the trial glenoid baseplate is satisfactory, the final glenoid baseplate is either installed using a cemented method or press-fit into place [19].

1.3.3 Fixation Methods

There are two commonly used methods of glenoid baseplate fixation utilized in the shoulder arthroplasty and reverse shoulder arthroplasty procedures. These common methods include pegged anchoring and keeled anchoring approaches. Other variations and methods of glenoid baseplate anchoring are also in use, including designs making use of a helical blade arrangement or other design microevolutions targeted towards increasing fixation of the prosthesis [22]. The keeled glenoid baseplate was initially introduced in the original Neer glenoid component design in 1973 [23]. Many microevolutions and reiterations of this design have occurred, introducing varying dimensions of keel and iterations of surface profiles; however, the usual design of the keeled glenoid anchoring arrangement still resembles a rectangular and tapered “fin” [23]. The alternative and more common method

of glenoid baseplate anchoring, where fixation is achieved through the use of a variety of different combinations of pegs of varying lengths, is preferred to the keeled approach for proposed reasons of more uniform stress distribution and minimal removal of native glenoid bone [24]. Biomechanical studies have indicated that using a pegged fixation approach may reflect better resistance to the high sheer forces in the shoulder when compared to a keeled design, resulting in a decreased rate of revision surgery due to loosening [23].

Although there have been many studies on the comparative strengths of keeled and pegged glenoid baseplate components, fixation studies have not yet yielded consistent results indicating which method is more effective. In some cases, in patients with glenoid osteoporosis and inadequate space for a pegged baseplate, a keeled component is required for geometrical reasons [24]. However, when there is adequate space for either arrangement, studies have found that there is no statistically significant difference between the clinical results of using keeled or pegged glenoid components [23], [25]. However, as previously introduced, there have been studies that have indicated an increased rate of revision surgeries after installation of a keeled glenoid baseplate [23]. Radiostereometric analysis has similarly previously indicated that keeled baseplate designs have resulted in larger levels of glenoid baseplate migration and radiolucency [26]. Unfortunately, due to the lack of active participants, a large number of isolated variables, and the variety of different subvariations in keeled and pegged glenoid baseplate designs, the conclusiveness of comparative studies involving pegged and keeled glenoid baseplates is harshly limited [23], [25], [26].

Just as there are variations in the design of the glenoid component of the reverse and anatomical shoulder arthroplasty procedures, there are also variations in design of the humeral stem component. Beyond the choice of fixation method, surface profile, and base geometry of the humeral stem, factors of which will be discussed later in this work, the surgical team must decide on a variety of different stem designs [27]. Variables such as humeral offset, acromiohumeral distance, and range of motion must be discussed, particularly in the design case of the reverse shoulder arthroplasty, which will be examined

later in this work [27]. In a clinical context, the Grammont reverse shoulder arthroplasty design has been effective in restoring shoulder function as well as relieving pain; however scapular notching, arm lengthening, and excessive damage to the greater tuberosity are all common complications associated with the Grammont humeral stem design [27]. There are many different designs that have surfaced in order to reduce these adverse effects, however, for the purposes of this work, it is sufficient to understand that there are a variety of patient-specific design choices in relation to the humeral stem component of both the reverse and anatomical shoulder arthroplasties that effect the articular profile and surface impingement of the replacement glenohumeral joint [27].

1.3.4 Complications

Since the rise in popularity of the anatomical shoulder arthroplasty, the success rates of the total shoulder arthroplasty have increased. This has resulted in a larger number of shoulder arthroplasties performed per year, leading to a similarly increasing rate of revision surgeries [19]. Complicating factors increasing revision rates include bone deficiency, muscle atrophy, and contracted or scarring soft tissues of the shoulder, all of which are more common in the rapidly ageing patient base [19]. Between 2006 and 2010 alone, a French study found the rate of shoulder arthroplasty revision surgeries had increased 29% across French hospitals [28]. This increase has been attributed to both a general increase in the number of shoulder arthroplasties performed as well as the expanded indications for the surgery, leading to a larger variety of patient candidates and subsequently a larger variety of potential sources of complication [28]. In 2011, the Mayo Clinic Total Joint Registry reported an 18.6% revision rate in total shoulder arthroplasties [29]. During this statistical analysis it was also reported that males were at significantly higher risk for requiring a revision surgery, reporting twice as many revision surgeries as their female counterparts [29]. Other influences such as BMI, underlying rotator cuff disease, and younger age were also found to be significant factors leading to a higher rate of revision surgery [29].

Unfortunately, there is still a limited number of studies reporting the predictors for immediate revision surgery following the total shoulder arthroplasty. Although there has been an inadequate amount of data collected regarding the revision of the total shoulder

arthroplasty, the statistics available suggest that the rate of immediate revision is between 8% and 11% for the total shoulder arthroplasty procedure [29]. Risk factors of immediate revision surgery include male sex, underlying diagnosis of avascular necrosis, post-traumatic arthritis, presence of a rotator cuff tear, excessive radiolucency adjacent to the flat tray, and metal-backed glenoid baseplate design [29]. However, due to the small sample sizes associated with statistical study of the revision of the total shoulder arthroplasty, these statistical inferences are not currently considered to be powerful [29]. Other common complications such as periprosthetic fracture and loosening, intraoperative fracture, and bone loss due to osteolysis or stress shielding may also result in partial or full revision of the shoulder arthroplasty, further increasing the number of variables leading to revision [1]. Although there are several medical factors that influence the longevity of the total shoulder arthroplasty, there are also a number of reported design failures leading to the need for revision surgery. The most prevalent of these common design risks is the loosening of the glenoid component [30], [31]. In a 2013 clinical study, focusing on aseptic total shoulder arthroplasty failure, it was found that the top two factors influencing the need for revision of the total shoulder arthroplasty were glenoid component loosening and wear and dissociation of the polyethylene liner [30]. Glenoid component loosening alone was reported in 14.3% of some four-thousand and ten anatomical shoulder arthroplasties studied between 2006 and 2010, with humeral loosening, instability, and infection also leading to revision surgery in 14%, 4.6% and 1.1% of said shoulder arthroplasties, respectively [28].

1.4 Reverse Shoulder Arthroplasty

The reverse total shoulder arthroplasty (Figure 1-8) is a surgical method of treating dysfunction and pain of the shoulder associated with a variety of different injuries including complex proximal humeral fractures, glenohumeral arthritis, massive rotator cuff tears, rotator cuff arthropathy, and pseudoparalysis of the shoulder [5], [22], [32]. In contrast to the anatomical shoulder arthroplasty, which mimics the form and function of the native glenohumeral joint, the reverse total shoulder arthroplasty reverses the native articular geometry [1]. The anatomically concave glenoid is removed and replaced with a convex glenosphere, and the anatomically convex humeral head is replaced with a concave humeral

cup; constraining and moving the centre of rotation of the glenohumeral joint to the centre of the glenosphere (Figure 1-9). The reorientation of the centre of rotation medializes and lowers the natural centre of rotation of the glenohumeral joint, fixing and stabilizing the articulation while lengthening the effective moment arm of the deltoid [32]. The glenosphere component of the reverse total shoulder arthroplasty houses the new centre of rotation, and the convex humeral cup, mounted on the metaphyseal element of the humeral stem, mates with the prosthetic glenosphere, creating the reversed glenohumeral articulation [2].

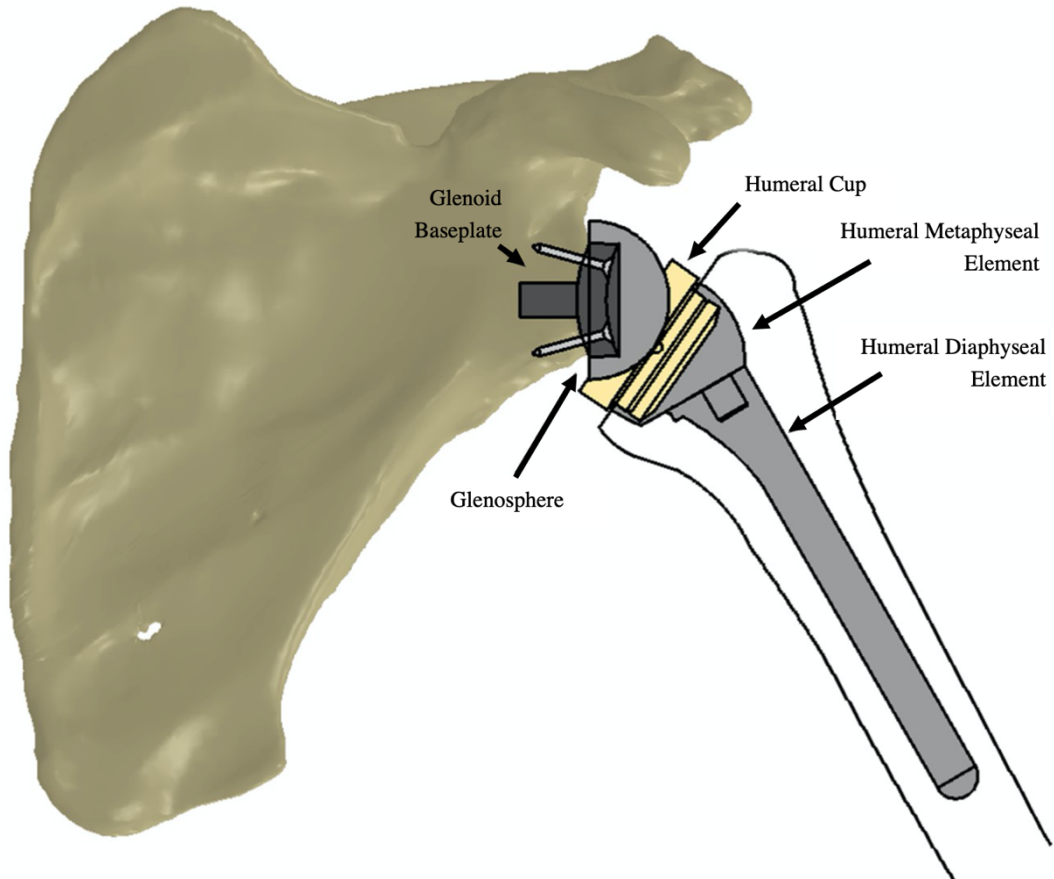


Figure 1-8: Reverse Total Shoulder Arthroplasty Components (Langohr, 2015)

Major components of the reverse total shoulder arthroplasty prosthetic including a glenoid baseplate and mounted glenosphere, and a modular humeral cup with mated metaphyseal and diaphyseal elements.

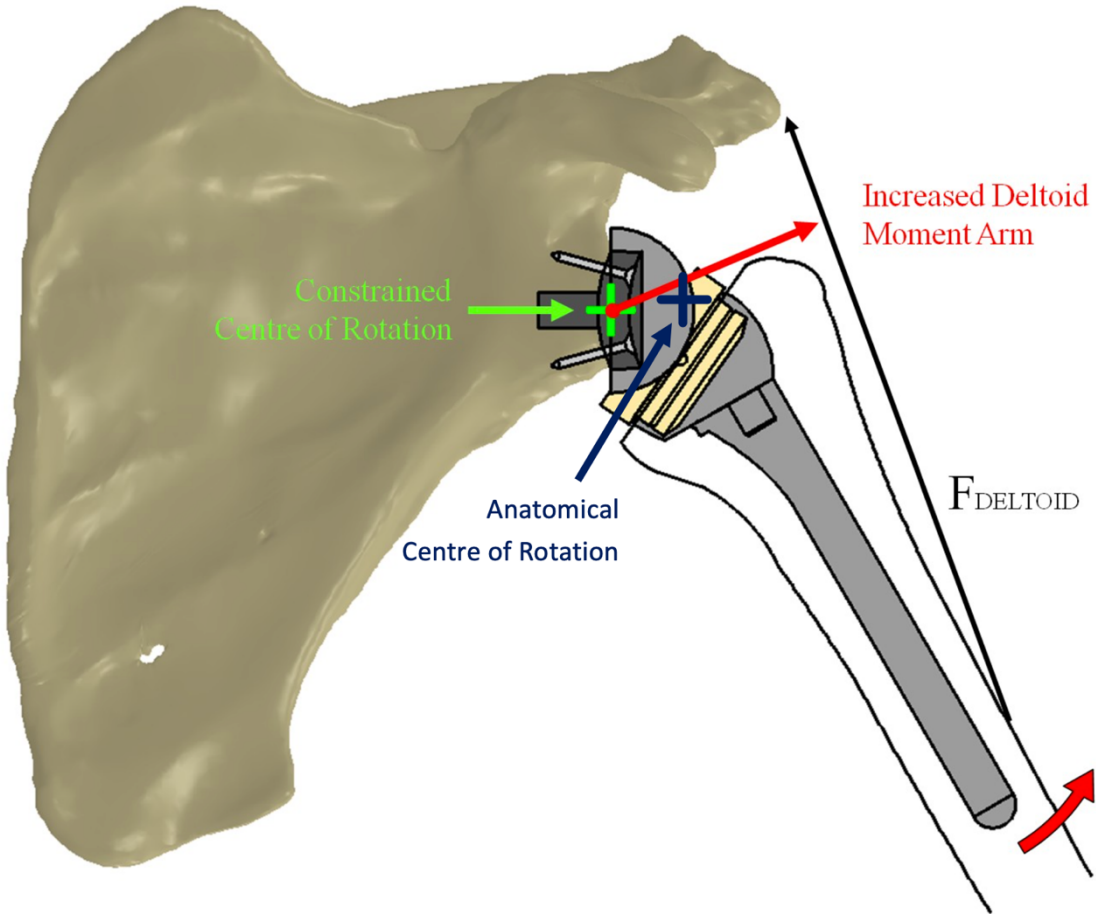


Figure 1-9: Biomechanical Advantage of Reverse Total Shoulder Arthroplasty (Langohr, 2015)

Mechanical effect of the reverse total shoulder arthroplasty: anatomical centre of rotation before RTSA (blue) and modified centre of rotation (green) with respect to new deltoid muscle moment arm (red).

The reversal of the native glenohumeral geometry was first introduced in Neer's Mark I reversed glenohumeral articulation design [16]. After Neer reviewed his series of anatomical shoulder arthroplasties performed between 1973 and 1981, he noted that outcomes were poorer when the rotator cuff was not functional. These clinical outcomes pushed Neer to design a constrained total shoulder replacement; artificially adding stability to the modified glenohumeral articulation [16]. The Neer Mark I reversed shoulder arthroplasty design was successful in constraining the shoulder while increasing range of motion, however, the large spherical glenosphere component did not allow the rotator cuff to be reattached [16]. This led to the design of the Mark II and Mark III Neer reversed shoulder prostheses; each outfitted with a smaller glenosphere to facilitate reattachment of the rotator cuff [16]. The Mark II design suffered from a reduced range of motion and decreased excursion due to the smaller glenosphere, leading to the incorporation of a rotating stem in the Mark III design in an effort to regain motion [16]. Unfortunately, dislocation and scapular fixation were consistent problems amongst the Neer reversed shoulder prostheses, so Neer abandoned further experimentation with a constrained shoulder prosthesis design [16].

In the 1970's, a handful of surgeons continued to pursue fixed-fulcrum designs, however complication rates continued to be high with the major failure modes of loosening (9%), fracture (18%), and severe pain (27%) present in patients at 18 and 39 months postoperatively [16]. Responding to the fixation difficulties experienced with the reverse total shoulder arthroplasty prosthetic design, in 1972, a new design produced by Reeves *et al.* addressed the issue of baseplate loosening through the design and incorporation of the divergent threaded peg glenoid baseplate [16]. The divergent screw design produced higher pullout strengths, and the new design also exhibited a centre of rotation that was closer to the anatomic centre [16].

Between 1972 and 1991, there were numerous advances in the design of the reverse total shoulder arthroplasty [16]. These changes varied from modifications to the geometry of the glenosphere component to attempts to improve fixation at the humeral and glenoid interfaces [16]. Although there were many changes to the reverse total shoulder arthroplasty

prosthetic, likely the most influential of these works was the research performed by Kessel and Bayley in 1979, which noted the cancellous bone of the glenoid as unsuitable for achieving the desired level of fixation [16]. The findings of Kessel and Bayley were likely the initial catalytic force that has driven the numerous following works investigating the fixation of the glenoid baseplate component of the reverse total shoulder arthroplasty.

1.4.1 Reverse Shoulder Arthroplasty Components

There are five major components that comprise the reverse total shoulder arthroplasty prosthetic (Figure 1-8). These components include a two-part, modular humeral component consisting of a metaphyseal element and a diaphyseal element mated with a Morse taper, a polyethylene humeral cup, a glenosphere, and a glenoid baseplate [5]. In the modern reverse total shoulder arthroplasty, the centre of rotation is fixed to the glenoid, positioned at the centre of the glenosphere. This medializes and lowers the centre of rotation from that of the anatomical geometry, thereby lengthening the deltoid moment arm and reducing the required deltoid force for humeral abduction [5]. In the reverse total shoulder arthroplasty, the glenosphere component replaces the anatomically concave glenoid, and the anatomically convex humeral head is replaced by a concave cup, mating with the glenosphere and forming the reversed glenohumeral articulation; constraining the humerus and stabilizing the joint [5].

1.4.2 Reverse Shoulder Arthroplasty Procedure

Analogously to the surgical technique utilized in the anatomical shoulder arthroplasty procedure, in the reverse total shoulder arthroplasty a deltopectoral approach is typically used to preserve the deltoid, although in cases where the subscapularis is to be preserved, an antero-superior trans-deltoid approach may also be used [5]. After the humeral head has been fully exposed, it is dislocated before resection may occur [5]. The humeral head is resected distally to the greater tuberosity at an angle of between 135° and 155°, depending on the design of the humeral prosthetic [5]. At the discretion of the surgical team, the glenoid may be prepared at this point or the humerus can continue to be prepared [5]. If it

is elected that the glenoid be prepared first, a protector is placed over the bone cut to prevent damage during the preparation of the glenoid [5].

Preparation of the glenoid begins with the excision of glenoid osteophytes with a rongeur in order to properly identify and isolate the centre of the glenoid [5]. The piriform articular surface of the glenoid is then fully exposed before the glenoid is reamed in a method similar to that of the anatomical shoulder arthroplasty [5]. A centring hole is first drilled with care, using three-dimensional computerized tomography (CT) scans to ensure that the central peg of the glenoid baseplate is placed in the area where the bone is the thickest [5]. This process requires planning to anticipate whether or not an intercalated bone graft is necessary to compensate for bone loss [5]. The trajectory of the centring hole must be accurately drilled in the same direction as the future central peg of the metaglene [5]. The resulting hole is then probed with a k-wire to ensure that bone contact is achievable along the entire length of the centring post to ensure proper fixation [5]. Reaming of the glenoid is then carefully performed to ensure that full contact between the glenoid baseplate and the glenoid is achieved, while not excessive in order to preserve solid subchondral bone for fixation purposes [5]. Reaming is often performed with a curved open-faced reamer, and any peripheral bone or remaining cartilage that could interfere with later fixation of the glenosphere is removed [5]. The glenoid baseplate is installed to the prepared glenoid using 2 to 4 divergent screw holes based on the requirements of the baseplate [5], [33]. Screw depth is chosen to maximize screw contact with bone in order to achieve optimal fixation [5]. There is some discussion on the optimal arrangement of screws, including angle of divergence and the use of locking or compression screws [5], [33]; however, if geometry allows, it is generally preferred to use divergent inferior and superior screws to obtain primary compression [5].

After the glenoid baseplate has been properly installed, the installation of the humeral component can then be completed. The humeral medullary canal and metaphyseal zone are reamed using two different reamers [5]. The sizes of these reamers are chosen based on the size and geometry of the patient's humerus with the goal to preserve as much native bone as is possible [5]. During the reaming, it is essential that no superior impingement is present

with the acromion, and no antero-medial impingement is present with the coracoid process [5]. If necessary, modifications to the reaming are made after a trial glenosphere and humeral component are installed in order to corroborate that the humeral component can move freely around the glenosphere [5]. Once the correct sizes of humeral component and glenosphere have been identified, the humeral diaphyseal stem is installed, preserving as much native bone as is possible while still maintaining solid fixation [5]. The humeral diaphyseal stem may be affixed using either cemented or press fit methods, depending on a variety of different variables such as the possibility and ease of revision, the allowable operative time, and the quality of the native bone [32], [34]. The glenosphere component, the humeral epiphysio-metaphyseal element, and the humeral cup or liner are then installed or impacted into place, and the incision is closed [5].

1.4.3 Implant Design and Fixation

1.4.3.1 Glenoid Implant Design Variations

There are several different fixation mechanisms that may be used for both the glenoid baseplate and humeral diaphyseal stem element of the reverse total shoulder arthroplasty. For the glenoid component, there are considerations involving bone grafting, screw arrangement and type, screw placement and orientation, and type of baseplate that must be considered [22], [33], [35]–[38].

In order to achieve proper fixation of the glenoid baseplate, healthy bone stock must be available to provide adequate surface interface with the back of the baseplate. In the case where the glenoid has occurred severe erosion, common amongst patients with rotator cuff arthropathy, a bone graft may be used to correct the geometry of the glenoid; providing a contact surface between the bone and the hydroxyapatite surface of the glenoid baseplate [5], [35], [38]. This not only improves fixation of the glenoid baseplate, but also serves to improve the biomechanics of the arthroplasty, providing the opportunity for the surgical team to correct the orientation of the glenosphere in the case of asymmetric glenoid erosion [5]. In patients with severe rotator cuff tear arthropathy this is especially important, as the resultant arthritic changes may cause bone loss on the superior aspect of the glenoid [38].

Fixation of the glenoid baseplate is heavily reliant on bony ingrowth for long-term stability and said osseous integration has been found to occur only when initial tangential micromotion at the baseplate is $< 150 \mu\text{m}$ [33], [38]. Conversely, it is speculated that the tolerable micromotion limit in the orthogonal direction is significantly lower, however, there is no literature available that specifically defines an inhibitory limit to osseointegration in the orthogonal direction. In the case of glenoid bone loss, it is possible for superior glenoid erosion to result in excessive micromotion at the glenoid-baseplate interface, rendering any fixation attempt requiring osseointegration ineffective [38].

Another important consideration for the reverse total shoulder arthroplasty procedure is the use, orientation, and design of peripheral screws. More accepted methods of achieving proper glenoid baseplate fixation involve the use of peripheral screws, however there is no consensus on the most optimal screw design and orientation. Studies have been completed in order to isolate the most optimal screw placement and orientation; however, results have consistently reflected that the quality and quantity of healthy bone stock available for fixation is more important than standardization of the positioning of peripheral screws [39]. A number of additional studies have been performed in order to isolate the optimal screw geometry, and there have been positive results when using longer, larger screws when attempting to maximize the achievable level of fixation [37]. Another common variant of screw fixation involves the use of locking peripheral screws, or compression screws, which provide a higher level of interfacial force between the glenoid baseplate backing and the native bone [33]. However, studies investigating the relative strengths of different combinations of unlocked and locked peripheral screws have reflected no statistically significant difference between their quantified fixations [33]. However, in the context of practical installation, the use of locking screws can limit the detection of indicators that may suggest insufficient screw engagement as there is no tactile resistance to be noticed by the surgical team [39].

Another somewhat novel variable in glenoid baseplate fixation is the use of a helical blade when seating the glenoid baseplate. Using a helically bladed baseplate instead of a straight fin arrangement has been studied in the context of proximal femoral prosthetics, and there

has been some study indicating that the arrangement can be applied to the glenoid baseplate component of the reverse total shoulder arthroplasty prosthetic [22]. A study produced in 2017 by Zilber *et al.* reported that the helical bladed glenoid baseplate design could be used in the place of a pegged or keeled design, and that the design was effective in preserving native glenoidal bone as no mechanical reaming is necessary during installation [22]. This study was performed in a clinical method, wherein forty-four patients underwent a reverse total shoulder arthroplasty using the helically bladed arrangement, with postoperative follow-up at twenty-four months [22]. However, to the author's knowledge, there are few to no additional works that are readily available, focused on investigating the helically bladed glenoid baseplate component design.

1.4.3.2 Humeral Implant Design Variations

Correspondingly to the fixation of the glenoid baseplate, the humeral component must also be chosen while keeping a variety of different variables in mind. In both the reverse total shoulder arthroplasty and the anatomical total shoulder arthroplasty, there are currently three major design iterations of humeral component currently available: the stemmed humeral component, the short-stemmed humeral component, and the novel stemless humeral component designs (Figure 1-10) [40]. Newer humeral prosthetic implants have sought to decrease stem length in an effort to reduce the effects of stress shielding, to preserve bone stock, and to provide easier future revision surgery [40]. Unfortunately, there has been little scientific investigation into the effects of stem length in the context of humeral prosthetics due to the novelty of the shorter and stemless designs [40]. From the information available, when compared to a stemmed geometry, it has been found that reduction of stem length in humeral prosthetic components may result in cortical bone stresses that mimic the stresses found in natural humeral geometry more closely, however shorter stems may also elevate stresses present in the trabecular bone of the humerus [40]. When discussed in the context of stress shielding, this increase in trabecular bone stresses and the mimicry of natural cortical bone stresses may result in less resorption of native bone, thereby increasing long-term fixation of the implant. Although this topic has not been discretely studied in the context of the humeral prosthetic, work completed on the design of the stemless femoral prosthetic has reported higher bone-mineral density when stemless

implants are used in the place of stemmed implants, indicating lower levels of resorption [41]. From the perspective of primary fixation level present in stemless humeral prosthetics, a 2016 study reported that stemless total shoulder arthroplasties provided the same level of primary fixation when compared with a stemless humeral component design, indicating that stemless methods may be a viable alternative to stemmed humeral designs when preservation of healthy bone stock is preferred [15].

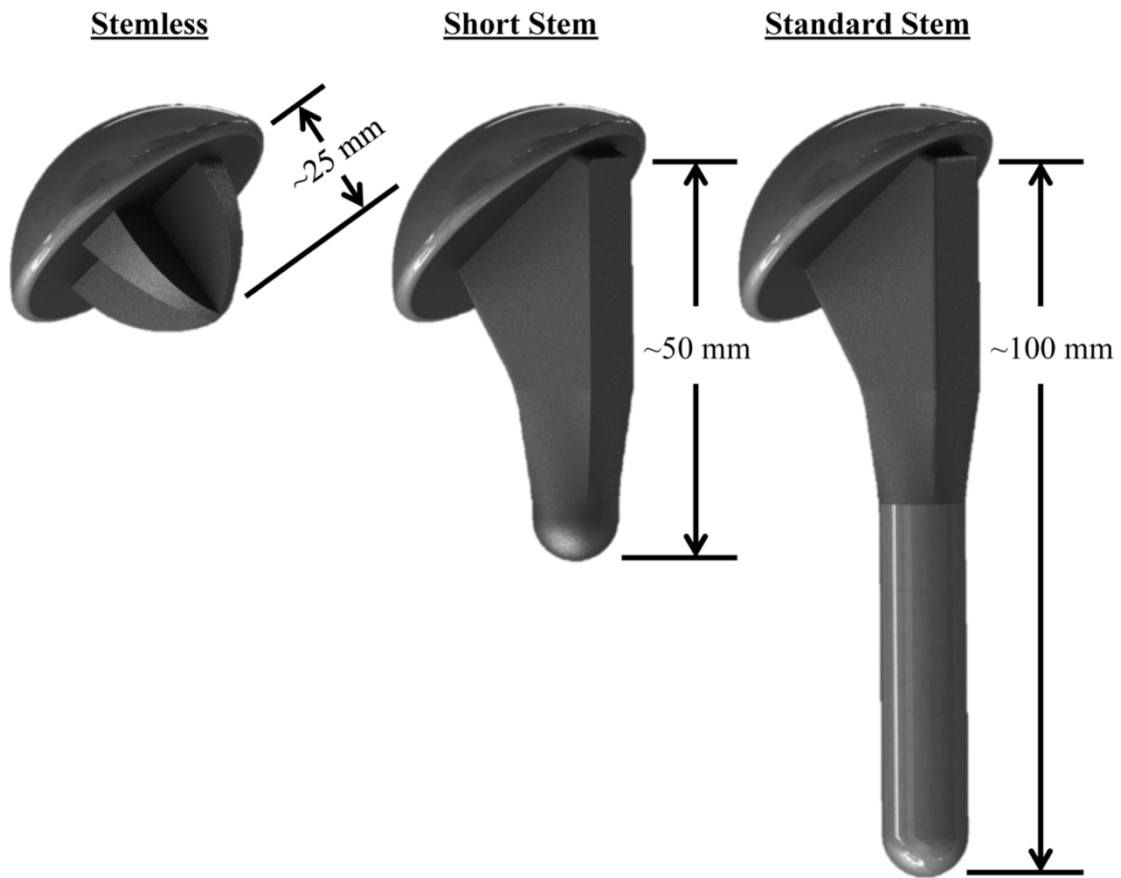


Figure 1-10: Generic Humeral Component Geometries of Total Shoulder Arthroplasty (Razfar, 2014)

Generic stemless, short stem, and standard stem shoulder implant designs. Depicted above are the geometries for the anatomical total shoulder arthroplasty humeral prosthetic, including a prosthetic humeral head, however the same stem geometry may be reapplied to the reverse total shoulder arthroplasty prosthetic.

The secondary decision on stem geometry that must be made when installing the humeral component of the shoulder arthroplasty prosthetic is deciding on the implant girth. The literature available, focused on the influences of humeral stem girth, has previously indicated that stem girth significantly changes the bone to implant contact [1]. This phenomenon is due in part to changes in bone distribution and porosity, differences in the loading conditions between anatomical sites, and the influence of proximal geometry and relative implant location [1]. This effect has been found to be inversely proportional to implant size, with implant-bone contact decreasing as stem girth increases [1]. This is relevant to the fixation of the humeral component, as the degree of contact exhibited by the design of the diaphyseal stem element is proportional the stability and strength of the implant [1]. In addition to providing a higher degree of contact, smaller stem geometries also exhibited lower probabilities of bone resorption, indicating that smaller humeral stem geometries may be beneficial if native bone stock is to be maintained [1].

Another design judgement to be discussed is the decision of inlay versus onlay humeral reverse total shoulder arthroplasty components. Inlay humeral components are the typical design choice and are part of the typical Grammont type humeral prosthetic [42]. The onlay design of humeral stem is a variant design that predominantly medializes the centre of rotation of the reverse total shoulder arthroplasty, thereby further increasing the deltoid moment arm while preserving tuberosity bone stock [43]. The onlay humeral component creates less humeral distalization and more humeral lateralization than the typical Grammont type design, causing changes to the range of motion of the shoulder postoperatively; potentially increasing external rotation, adduction, and extension range of motion [42]. The onlay design may additionally serve to modify stress distribution in the proximal humerus, however, to the author's knowledge, there are no current studies that have investigated the effect of onlay humeral prosthetic components in the reverse total shoulder arthroplasty design.

1.4.3.3 Humeral Implant Surgical Decisions

In the humeral component of the reverse total shoulder arthroplasty, the surgical team must decide between a cemented fixation method, or a press-fit fixation method with bony

ingrowth. Both fixation variants have their own advantages, and the decision to use either must therefore be decided upon using a case-by-case method. Total shoulder arthroplasty procedures have historically been completed using cemented fixation methods. Cemented fixation methods provide higher variability of component positioning and decreases in implant micromotion, thereby reducing postoperative pain [34]. However, cemented components are difficult to revise, as a larger amount of native bone must be removed before a new implant may be installed [34]. Recently, uncemented prosthetics, or press-fit prosthetics, have become more popular due to their potential benefits; including decreased operative time, better bony ingrowth potential, simplified revision due to the preservation of native bone stock, and avoidance of proximal stress shielding [34]. The press-fit design, however, suffers from higher rates of loosening after primary fixation, higher rates of radiolucency during follow-up [32], higher risk of humeral fracture intraoperatively, and increased rotational and axial micromotion when compared with cemented fixation [34]. The topic of press-fit versus cemented fixation methods has been investigated thoroughly as press-fit humeral stems have become more common, and although each fixation method occurs their respective complications, there has been found to be no difference in primary micromotion or revision rate when using press-fit or cementitious methods [32], [34], [44]. However, although comparative studies on press fit vs cementitious methods are available, there still remains a knowledge gap in the influence of different magnitudes and designs of press-fit in osseointegrated implants.

In addition to direct fixation surgical decisions, there are also a number of positioning decisions that a surgical team must make before installation that also effect the performance of implants during use. These include decisions on installation retroversion, installation lateralization, and installation inclination.

Firstly, implant retroversion, or the degree of posterior tilt of the implant relative to the anatomical axis of the humerus, has a recorded effect on the postoperative range of motion, particularly in internal/external rotation. It has previously been found that increasing implant retroversion markedly increases external rotation, while slightly decreasing internal rotation [45]. Additionally, increasing humeral component retroversion can

decrease the risk of inferior impingement [46], thereby decreasing comfort and decreasing the risk of implant dislocation. To the author's knowledge, no works currently report the effect of humeral component retroversion on the primary fixation of humeral components.

Secondly, humeral prosthetic component lateralization, or the degree of lateral shift of the implant relative to the anatomical axis of the humerus, can have an effect on implant performance. In particular, increasing component lateralization can decrease the torque required for shoulder actuation [47]; thereby decreasing the glenohumeral articular loads. Increasing humeral prosthetic lateralization has also been shown to increase overall postoperative range of motion [48].

Lastly, the humeral prosthetic component installation decision of inclination (referenced by the installation term of "neck shaft angle") has not been thoroughly studied. Neck shaft angle (NSA) refers to the relative orthogonal humeral neck inclination between the prosthetic and resection plane [49]. Precedent literature is limited on this topic and focuses mainly on the influence of neck shaft angle in the context of improving impingement-free range of motion and reduction of scapular notching [48]–[50]. It has been previously found that a decrease in anatomic neck-shaft angle results in a reduction in scapular notching, but the effect of neck shaft angle on range of motion is still disputed [49], [50]. In terms of stemless implant performance, there is little to no published information focused on the influence of neck shaft angle, and the effect of this surgical design variable on implant primary fixation remains a mystery.

1.4.3.4 Complications

As in the case of the anatomical shoulder arthroplasty, there are design-associated complications commonly concomitant with the reverse total shoulder arthroplasty. When compared to its anatomical counterpart, the reverse total shoulder arthroplasty procedure has boasted a lower complication rate (39.8% and 24%, respectively), but has also reported higher rates of revision surgeries (11.2% and 13.4%, respectively) [28]. In a 2012 study it was found that in the reversed implant the most common complications are instability (4.7%), infection (3.8%), glenoid component loosening (3.5%), haematoma (2.6%), and

humeral component loosening (1.3%) [28]. The most common of these, instability of the implant, can be the result of a variety of different factors, however the most common of these is the improper seating of the humeral diaphyseal shaft; where the shaft is not inserted fully, resulting in improper restoration of the humerus [28]. The other common design-oriented complications, glenoid and humeral component loosening, are often the result of bone loss and improper implant-bone fixation [28]. Implant loosening is postoperatively assessed with radiographic and computer assisted tomographic imaging, where implant loosening is considered to be significant in cases where radiolucent lines and migration is measured to be greater than 2 mm [28]. Understanding the main failure modes of the reverse total shoulder arthroplasty procedure is essential in the continued optimization of the prosthetic.

Improving the design of the reversed total shoulder arthroplasty prosthetic has been the topic of numerous studies. As reported by Frankle *et al.* in 2005, out of sixty consecutive reverse total shoulder prostheses installed by a single surgeon, ten of said patients experienced complications [51]. In an effort to reduce these unacceptably high complication rates, novel prosthetic designs have continued to surface, revising the fixation method, geometry, and material of the implant. Baseplate positioning [36], [52], screw configuration and orientation [33], [36], bony ingrowth methods [52], humeral stem design [15], [17], and component fixation methods [32], [34] have been researched as new revisions of the reverse total shoulder arthroplasty prosthetic continue to become available.

1.5 Biomechanical Analyses

Optimization of the individual components of the reverse total shoulder arthroplasty procedure has been the topic of numerous experimental, clinical, and computer-assisted studies. Common methods of quantifying the success of reverse total shoulder arthroplasty variant designs include experimental (*in-vitro*) studies [1], wherein the application of load is performed in a controlled environment, clinical (*in-vivo*) studies [15], [43], where the fixation and performance of implant variants are assessed over time, postoperatively in patients, and computer-assisted (*in-silico*) studies [17], where Finite Element Analysis

(FEA) is used to quantify bone-stress, loading, and interface contact in a perfectly controlled environment.

In both experimental and computer-assisted methods of studying implant mechanics, an important topic to discuss is the boundary parameters and simulation requirements necessary to replicate the effects of real-life loading. This is significant, as the strength of any study attempting to evaluate the effectiveness of prosthetic design variation depends on its ability to replicate the real-life scenario. In the context of both humeral and glenoid component design studies, contact pressure mechanics determine the boundary forces required for replication of the anatomical condition [2], [53]. There have been a number of *in-vitro* studies performed in order to determine the contact stress at the prosthetic glenohumeral articulation; predominantly in the context of determining wear rates in the reverse total shoulder arthroplasty prosthetic [2]. Variables such as positioning, size, and geometry of the implant create variations in the total deltoid force affected during actuation of the glenohumeral joint, however, studies investigating the loading of the reverse total shoulder arthroplasty prosthetic have reported experimental loads of between 250 N and 340 N for active glenohumeral abduction [2], [54]. Similar results have been reported in finite element studies, reflecting maximum loads of between 110 N and 313 N present at the reversed glenohumeral articulation [55].

1.5.1 Humeral Stem Testing Standards

Unfortunately, there is little to no standardization in the biomechanical testing of reversed total shoulder arthroplasty prostheses. The most relevant and accepted guidelines for reversed shoulder prosthetic testing are ASTM F1378 [56], ASTM F2028 [57], and ASTM F1839 [58]. The standard specification for testing of shoulder prostheses, ASTM F1378 – 18, indicates the basic metallurgical and performance requirements for the design of new prosthetic implants, however, there is little to no specific information on loading requirements [56]. The ASTM F2028 and ASTM F1839 are standards are written to identify the requirements for glenoid baseplate testing during dynamic motion, and the approved bone analogue materials acceptable in the testing of orthopaedic implants, respectively [57], [58]. However, no existing standard provides guidance on methods of

evaluating the fixation of the humeral component of the reversed total shoulder arthroplasty procedure.

1.5.2 Finite Element Methods

The usage of *in-silico* methods in the context of orthopaedic research has become frequent as computational technology becomes more powerful. Simulation of the anatomy, movement, joint forces, muscle forces, and the range of motion of the human body has become commonplace, and there have been computational studies performed on almost every joint in the human body using finite element models. In the case of the shoulder, there have been a number of studies that have used finite element analysis to evaluate bone stress, bone-implant contact, and strain energy density while simulating natural arm motions [1], [17], [40]. These studies are generally more cost-effective than clinical and experimental methods, as they are non-invasive, and they eliminate equipment and material costs.

The finite element method requires the discretization of a solid continuum into a finite number of elements (Figure 1-11), numerically solving field problems described by a set of partial differential equations [59]. This method creates a means by which the global properties of a system can be described by the local behaviour of each element; mathematically creating a relationship between applied loads, boundary conditions, and material properties to the behaviour of the global model [40]. Displacements of nodes are modelled as functions of nodal forces, and inter-node displacements are approximated using displacement interpolation functions. These displacements are then translated into strain values, and by using the material properties assigned to the global model, the software is then able find values for local stress in the evaluated nodes [59]. Through taking the derivative of the displacement functions, the bending moment and shear forces in the structure can also be derived [59].

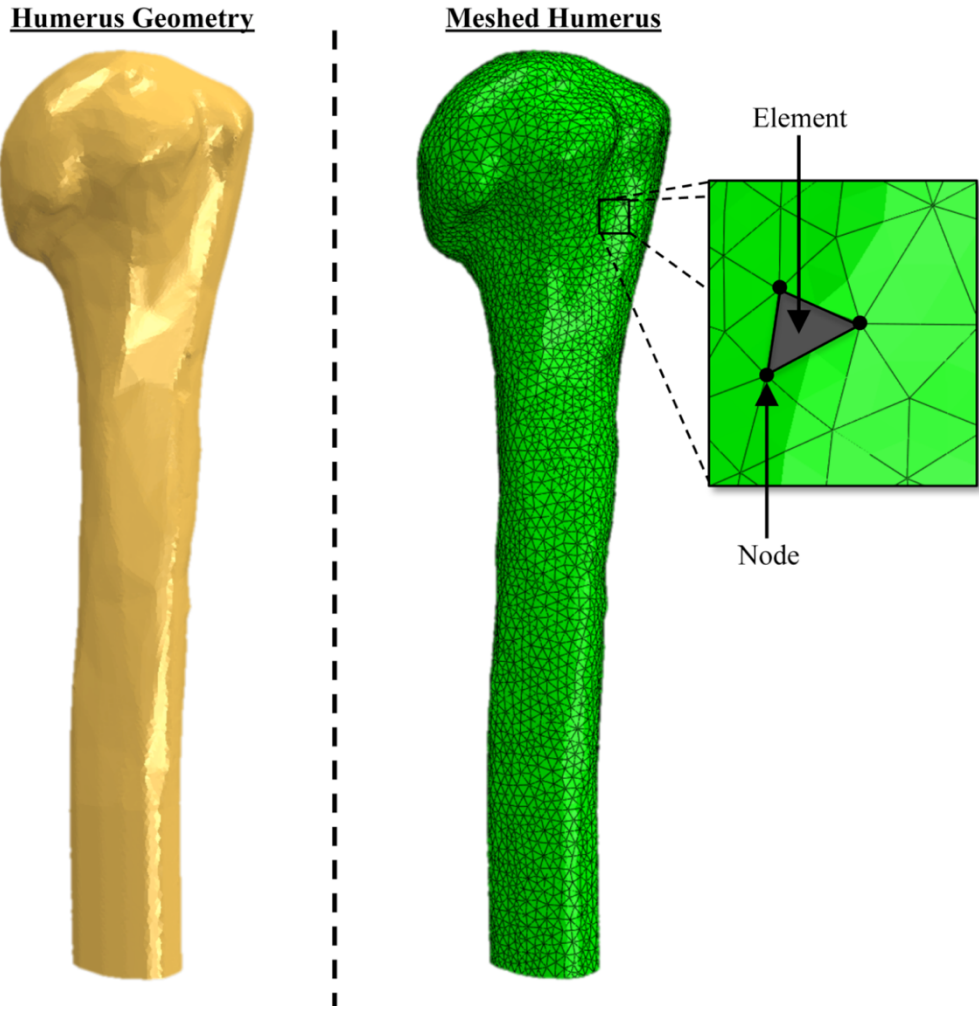


Figure 1-11: Finite Element Discretization of Humerus (Razfar, 2014)

Generic continuous model of the proximal humerus discretized using finite element analysis into a finite number of discrete elements, each of which is comprised of multiple nodes. Pictured above are first order tetrahedral solid elements, used for illustration purposes.

In the context of orthopaedic implant studies, finite element analysis has been instrumental in the acceleration of prosthetic development. However, the accuracy of these studies is paramount to the ongoing optimization of the reverse total shoulder prosthetic [17]. There are several errors associated with the finite element method, which must first be discussed before continuing. The first, and the most severe error in finite element analysis, is modelling error; where the software user creates a dissimilarity in the model and the situation under study, thereby introducing a variable that may produce large inaccuracies

in the analysis [59]. In the context of orthopaedic research, computerized tomography (CT) scans are used to create finite element models, reducing the probability that error may occur [1]. However, during the simulation of loading, accurate boundary conditions and local mesh refinement must be considered in order to reduce the possibility of modelling error [59]. Perfect boundary conditions must therefore be sufficiently far from the locations of interest to ensure that local results are not distorted. The second major error associated with finite element analysis is discretization error. This is the only error specific to finite element software. In order for discretization error to occur, the number of local nodes in the area of interest introduces artificial stiffness to the system, causing the stiffness in the finite element model to be higher than the stiffness of the associated mathematical model [59]. In order to reduce the artificial stiffness present, the number of nodes present may be increased. This process is called h-convergence, where “h” denotes the characteristic length of the finite elements [59]. During analysis, finite element software evaluates the magnitude of the solution difference in the finite element model and mathematical model, remeshing at areas of large error until the two solutions converge [59]. This is what is referred to as the convergence process. The final error accompanying finite element analysis is solution error, caused by the accumulation of round-off errors, however, the magnitude of this error is usually negligible when compared to modelling and discretization error. For the purposes of this work, the software package Abaqus/CAE 2021 (Dessault Systèmes Simulia Corp., Johnston, RI, USA) will be used for all finite element analysis steps.

In the context of orthopaedic evaluations, finite element methods have been regularly used to examine many different variables, from local strain energy density to bone-implant interface behaviours. For the current investigation, the latter will be evaluated, as the interfacial mechanics of bone-implant constructs are more relevant to the primary fixation of humeral implants.

1.5.3 Digital Tracking Methods

Computer-vision-based measurements have become more commonplace as non-contacting methods of measurement have become compulsory in many research applications [60]. Digital image tracking has many different practical applications in two-dimensional, three-

dimensional, and volumetric capacities, providing the opportunity to measure deformation, motion, or changes to shape unhindered by strain gauges or other contacting measurement methods [60].

Image correlation is by no means a new technology given its early history in the 1950s when image positional information was used for the purposes of ground surveying and condition monitoring [60]. However, recent advances in computational technology have vastly expanded the available applications for image correlation as analysis programs and experimental methods have become more refined and reliable [60]. Briefly described, image correlation is the process of dividing an area of interest into an evenly spaced virtual grid, with subsets (pixel sets) assigned for tracking local movement and deformation [60]. Characteristic patterns from subsets are used to extract full-field information during deformation of the subject, which can then be converted into displacement, motion, or deformation measurements for practical use [60]. In recent years, developments in digital image correlation technology have yielded researchers that ability to use computer-vision-based measurements in three dimensional or volumetric studies [60].

In the context of orthopaedics, digital image correlation has been used to evaluate surface strain in composite bone structures prior to and after installation of prosthetic components [61] or during the loading of bone or implant materials [10], [62]. The accuracy of digital measurement methods has been debated, however a 2012 validation study reported that digital image correlation demonstrated close agreement to established strain gauging techniques commonly used in orthopaedic experimental studies, validating its use for orthopaedic implant studies [61]. Other common uses for digital measurement methods in orthopaedics include micromotion measurement at the implant-bone interface [63] or measuring fracture propagation during cyclic loading of implants [64]. For the purposes of this work, the software package ProAnalyst (Xcitex Inc., Woburn, MA, USA) will be used for computer-vision-based image processing.

1.5.3.1 Three-Dimensional Digital Tracking

Optical three-dimensional metrology, or three-dimensional tracking, is the basic method of processing digital data that is used for digital image correlation analysis. “Digital Metrology”, as defined for the purposes of this work, refers to the class of non-contacting methods used to extract full-field shape, deformation, and/or motion measurements [60].

As orthopaedic prosthetics continue to become more optimized for the individual patient; the approval processes for orthopaedic prosthetics must likewise become enhanced. With more innovation comes the need for more accurate testing methodologies, lest scientific investigations into new designs yield no meaningful results. Historically, industry-accepted practices of approving shoulder arthroplasty prosthetics have relied on the ASTM F1378 [56], ASTM F2028 [57], and ASTM F1839 [58] standards for guidance; however, these standard testing methods for measuring the functional minimum requirements for performance of orthopaedic implants have not been updated to reflect the needs of the dynamic orthopaedic prosthetic industry. In studies on the fixation of orthopaedic prosthetic implants, it has been indicated that the use of linear variable differential transformers and differential variable reluctance transformers [57] produce misleading micromotion values, and that optical digital metrology methods are more reliable and accurate [65], [66]. This difference in accuracy is best described by the effective micromotion definitions measured by each method. When using contacting linear variable differential transformers or similar methods of measuring micromotion, the effective metric being measured is the global prosthetic motion whereas the metric measured by digital metrology methods is the relative motion of the prosthetic component to the interfacial bone [65]. As discussed previously in this work, interfacial micromotion must be limited for osseous integration to occur [33], [38]; thereby realizing the importance of accurately assessing interfacial micromotion while avoiding measurement of global displacement.

As with any measurement methodology, it is essential to first understand the sources of error that may influence the accuracy of the work. Digital metrology methods are not immune to uncertainty of measurement, and arguably have more severe sources of error than their contacting counterparts. There are several assumptions that must be considered

when using computer vision tracking. In three-dimensional optical metrology, it is assumed that: (1) one camera is selected arbitrarily as the “master” camera, (2) the orientation and position of the world coordinate system is determined relative to the “master” camera, (3) the orientation and position of all other cameras are defined relative to the “master” camera, and each camera is assumed invariant, and (4) system calibrations of the object are determined relative to the “master” camera.

As exemplified above, the importance of a “perfect” system is paramount when performing optical metrology. This is important, as it stresses the necessity for a closed system, where all environmental influences are minimized [60]. In the context of orthopaedic micromotion studies, it is therefore important to ensure that loading of the specimen is performed in a static coordinate system, and any relative motion between cameras is perfectly constrained.

In practical applications, images are always contaminated by noise of one form or another [60]. In order to account for these signal variations, Gaussian random noise assumptions are incorporated into post-processing of images to reduce the influence of environmental and system noise on the final calculated measurements. Other sources of inaccuracies: intensity noise, camera stability, and mechanical vibrations must also be considered before optical measurement methods may be applied effectively; leading to the topics of hardware selection, system configurations, calibration procedures, and measurement procedures.

When selecting hardware, it is generally suggested to use camera-lens combinations that are identical for multi-camera systems [60]. This reduces the potential for differences in spatial resolution, contrast incompatibilities, and integration issues that could add to uncertainty. In addition, there is importance in maintaining good light transmission in order to reduce non-uniqueness in the image centre for three-dimensional metrology applications [60].

Another major consideration to be discussed when using multi-camera systems is the arrangement and configuration of cameras and lighting for image acquisition [60]. Larger pan angles (stereo angles) will increase depth resolution but will also increase matching

bias [60]. For micromotion measurements, where maximization of in-plane sensitivity is the primary goal, it is beneficial to maintain stereo angle ranges of between 10° and 30° in order to maintain good out-of-plane sensitivity while guaranteeing modest perspective differences [60]. In the context of non-linear sample geometries, similar to those exhibited by the humeral component of the reverse total shoulder arthroplasty prosthetic, it is therefore beneficial to use more than two discrete cameras for image acquisition, thereby maintaining modest stereo angles without sacrificing out-of-plane sensitivity. Similar arrangements of lighting sources are suggested for the purpose of eliminating local bright spots due to reflections [60].

When calibrating optical metrology systems, and when performing measurements on said systems, there are two major methods available for use. First, it is possible to independently calibrate separate cameras; defining a common coordinate system for each camera [60]. Second, it is common to consider both cameras as a single measurement system; determining the relative orientation and position of each camera relative to that of the “master” camera [60]. Both methods of calibration are effective in creating a global coordinate system for analysis, and both use calibration fixtures in order to accommodate for distortion during the parameter estimation process [60]. After calibration, it is then essential to ensure that the camera positions and orientations do not change, or the global coordinate system on which all subsequent displacement measurements are calculated will not provide accurate results [60].

For the purposes of this work, (3) machine vision USB3 cameras (acA4096-30uc, Basler AG, Ahrensburg, SH, Germany) will be used in conjunction with (3) c-mount premium lenses (C11-3520-12M-P f35, Basler AG, Ahrensburg, SH, Germany). A total of (2) 15-watt LED lights (A-LED W15, AOS Technologies AG, Baden, Daettwil, Aargau, Switzerland) will be used to facilitate adequate contrast.

1.6 Motivation

Despite the widespread use of the reverse total shoulder arthroplasty prosthetic, there are design variations that are still not fully understood which require further investigation. Due

to the acceleration in the advancement of prosthetic technologies and the ongoing pressure for new designs with better postoperative lifespan, reductions in complications, and better overall performance, literature has struggled to keep up with the explosion of orthopaedic implant designs. Examination into novel reverse total shoulder arthroplasty designs will yield insight into the future of the prosthetic and will increase the knowledge base available for safe use of the new innovations available in the field of orthopaedics.

For the humeral component of the total shoulder arthroplasty procedure, it has been found that decreasing stem length may produce higher stresses in the proximal bone that better agree with the intact state, suggesting reduced levels of stress shielding [40]. Investigations *in-vivo* have confirmed that bone mineral densities in stemless implants were higher than those in stemmed implants, suggesting that further study is indicated into the design of stemless orthopaedic implants [41]. Although there have been a number of studies completed on the effects of humeral stem geometry to the primary fixation of the reverse total shoulder arthroplasty prosthetic [1], [15], [17], [27], [40], [43], there is still a lack of available literature on the effects of stemless humeral prosthetic designs and their viability as an alternative to the proven stemmed humeral prosthetic components available. It is therefore essential to not only investigate the effects of stemless revisions of the reverse total shoulder arthroplasty humeral component, but to investigate other major design iterations that may influence initial fixation.

Primary fixation of orthopaedic components is essential to the success of surgery. In cases of excessive micromotion, overloading of new implants may lead to fibrous tissue formation at the bone-implant interface, blocking osseous integration and leading to implant loosening [33], [38]. It is therefore essential to evaluate the effects of joint loading on primary fixation of stemless humeral implants in order to evaluate and quantify their susceptibility to loosening, thereby evaluating their risk of requiring revision surgery. In addition, the separate investigation of tangential vs orthogonal micromotion has not been studied in these stemless type humeral implants; an important distinction that has implications on the short and long term fixation potential of these osseointegrating implants.

1.7 Objectives and Hypotheses

The purposes of this dissertation are to create a novel evaluation system capable of quantifying implant fixation during physiological loading and to evaluate the effects of bone analogue models vs biological specimens in fixation studies. Additionally, both computational and experimental methods are used to evaluate load transfer and fixation in stemless reversed shoulder arthroplasty humeral components at varying neck shaft angles.

The objectives and hypotheses are as follows:

1. To quantify both tangential and orthogonal micromotion in stemless humeral component implants. (Chapter 2)
2. To develop a loading apparatus capable of applying a complex array of physiologically relevant loads to investigate the degree of primary fixation in stemless orthopaedic implants. (Chapter 3)
3. To compare the results of fixation analyses using biological vs synthetic bone models while using the effects of press-fit in stemless implants and resultant micromotion as a metric for degree of fixation. (Chapter 4)

Hypotheses (null):

- i) There is no significant difference in the micromotion of implants installed in biological bone tissue vs when installed in polyurethane foam substitute materials.
- ii) Press-fit magnitude does not have a significant effect on the primary fixation of stemless components.
4. To evaluate the performance of 145° and 135° neck shaft angle stemless humeral components using micromotion as a metric for degree of fixation. (Chapter 5)

Hypothesis (null):

- iii) There is no significant difference in micromotion developed at the implant-bone interface between 145° and 135° neck shaft angle in stemless reverse shoulder arthroplasty humeral components *in-vitro*.

5. To develop a three-dimensional finite element model of the proximal humerus to evaluate the comparative degree of fixation of stemless reverse shoulder arthroplasty humeral components at varying neck shaft angles. (Chapter 6)

Hypothesis (null):

- iv) There is no significant difference in micromotion at the implant-bone interface when comparing reverse shoulder arthroplasty stemless humeral components at varying neck shaft angles in silico.

1.8 Thesis Overview

The following chapter, Chapter 2, describes the micromotion phenomena that are present in the stemless humeral implant during loading. The next, Chapter 3, presents the design and development of a novel tri-axis loading apparatus for the *in-vitro* assessment of primary fixation in humeral prosthetics.

The subsequent, Chapter 4, investigates the influence of surrogate bone materials, and their effect on primary fixation analyses of humeral components using *in-vitro* methods. The succeeding chapters, Chapter 5 and Chapter 6, investigate the effects of the surgical implantation variable of neck shaft angle in stemless reverse total shoulder arthroplasty humeral implants. The final chapter, Chapter 7, contains a thesis closure and discussion.

1.9 References

- [1] S. Synnott, “The Effect of Implant Girth and Implant Collar on the Degree of Bone to Implant Contact and Bone Stresses in the Proximal Humerus,” The University of Western Ontario, 2018.
- [2] G. D. Langohr, “Fundamentals of the Biomechanical Characteristics Related to the Loading of Reverse Total Shoulder Arthroplasty Implants and the Development of a Wear Simulation Strategy,” 2015. [Online]. Available: https://ir.lib.uwo.ca/etd/3436/?utm_source=ir.lib.uwo.ca%2Fetd%2F3436&utm_medium=PDF&utm_campaign=PDFCoverPages
- [3] T. Millett, Peter J;van der Meijden, Olivier A.J.; Gaskill, “Surgical Anatomy of the Shoulder,” Instructional Course Lectures, 2012. <https://link-gale-com.proxy1.lib.uwo.ca/apps/doc/A453291476/AONE?u=lond95336&sid=AONE&xid=3ed1353e> (accessed Nov. 09, 2019).
- [4] M. Culham, Elsie; Peat, “Functional Anatomy of the Shoulder Complex,” 1993. doi: 10.2519/jospt.1993.18.1.342.
- [5] C. Nerot and X. Ohl, “Primary shoulder reverse arthroplasty: Surgical technique,” Orthop. Traumatol. Surg. Res., vol. 100, no. 1 S, pp. S181–S190, 2014, doi: 10.1016/j.otsr.2013.06.011.
- [6] S. Standring, Gray’s Anatomy: The Anatomical Basis of Clinical Practice, 41st ed. Elsevier Ltd, 2016.
- [7] A. Giacomo, Giovanni Di; Pouliart, Nicole; Costantini, Alberto; De Vita, Atlas of Functional Shoulder Anatomy, vol. 1. 2015. doi: 10.1017/CBO9781107415324.004.
- [8] A. D. P. Bankoff, “Biomechanical Characteristics of the Bone,” in Human Musculoskeletal Biomechanics, 2012, pp. 61–85. doi: <https://doi.org/10.5772/19690>.
- [9] D. R. Trumble, W. E. McGregor, and J. A. Magovern, “Validation of a bone analog model for studies of sternal closure,” Ann. Thorac. Surg., vol. 74, no. 3, pp. 739–744, 2002, doi: 10.1016/S0003-4975(02)03699-8.
- [10] I. Kalouche, J. Crépin, S. Abdelmoumen, D. Mitton, G. Guillot, and O. Gagey, “Mechanical properties of glenoid cancellous bone,” Clin. Biomech., vol. 25, no. 4,

- pp. 292–298, 2010, doi: 10.1016/j.clinbiomech.2009.12.009.
- [11] E. F. Morgan, H. H. Bayraktar, and T. M. Keaveny, “Trabecular bone modulus-density relationships depend on anatomic site,” *J. Biomech.*, vol. 36, no. 7, pp. 897–904, 2003, doi: 10.1016/S0021-9290(03)00071-X.
 - [12] E. Hamed, E. Novitskaya, J. Li, P. Y. Chen, I. Jasiuk, and J. McKittrick, “Elastic moduli of untreated, demineralized and deproteinized cortical bone: Validation of a theoretical model of bone as an interpenetrating composite material,” *Acta Biomater.*, vol. 8, no. 3, pp. 1080–1092, 2012, doi: 10.1016/j.actbio.2011.11.010.
 - [13] H. M. Frost, “From Wolff’s law to the mechanostat: A new ‘face’ of physiology,” *J. Orthop. Sci.*, vol. 3, no. 5, pp. 282–286, 1998, doi: 10.1007/s007760050054.
 - [14] C. Ruff, B. Holt, and E. Trinkaus, “Who’s Afraid of the Big Bad Wolff?: “Wolff’s Law” and Bone Functional Adaptation,” *Am. J. Phys. Anthropol.*, vol. 129, pp. 484–498, 2006, doi: 10.1002/ajpa.20371.
 - [15] P. Collin, T. Matsukawa, P. Boileau, U. Brunner, and G. Walch, “Is the humeral stem useful in anatomic total shoulder arthroplasty?,” *Int. Orthop.*, vol. 41, no. 5, pp. 1035–1039, 2017, doi: 10.1007/s00264-016-3371-4.
 - [16] E. L. Flatow and A. K. Harrison, “A history of reverse total shoulder arthroplasty,” *Clin. Orthop. Relat. Res.*, vol. 469, no. 9, pp. 2432–2439, 2011, doi: 10.1007/s11999-010-1733-6.
 - [17] P. Soltanmohammadi, “Finite Element Analysis of Hollow-stemmed Shoulder Implants in Different Bone Qualities Derived from a Statistical Shape and Density Model,” 2019.
 - [18] O. Lech, “Charles S. Neer,” *Rev. Bras. Ortop.* (English Ed., vol. 46, no. 2, pp. IFC1–IFC2, 2011, doi: 10.1016/s2255-4971(15)30226-3.
 - [19] L. U. Bigliani and E. L. Flatow, Eds., *Shoulder Arthroplasty*. Springer International Publishing. doi: 10.1017/CBO9781107415324.004.
 - [20] E. West, “Functional Design and Analysis of a Linked Shoulder Prosthesis,” University of Western Ontario, 2017.
 - [21] C. Chuinard, “CORR Insights ® : Conversion of Stemmed Hemi- or Total to Reverse Total Shoulder Arthroplasty: Advantages of a Modular Stem Design,” *Clin. Orthop. Relat. Res.*, vol. 473, no. 2, pp. 661–662, 2015, doi: 10.1007/s11999-

- 014-4043-6.
- [22] S. Zilber, E. Camana, P. Lapner, E. Haritinian, and L. Nove Josserand, “Reverse total shoulder arthroplasty using helical blade to optimize glenoid fixation and bone preservation: preliminary results in thirty five patients with minimum two year follow-up,” *Int. Orthop.*, vol. 42, no. 9, pp. 2159–2164, 2018, doi: 10.1007/s00264-018-3891-1.
 - [23] A. Welsher et al., “A comparison of pegged vs. keeled glenoid components regarding functional and radiographic outcomes in anatomic total shoulder arthroplasty: a systematic review and meta-analysis,” *JSES Open Access*, vol. 3, no. 3, pp. 136-144.e1, 2019, doi: 10.1016/j.jses.2019.04.002.
 - [24] A. S. Ha, J. M. Petsavage, and F. S. Chew, “Current concepts of shoulder arthroplasty for radiologists: Part 2 - Anatomic and reverse total shoulder replacement and nonprosthetic resurfacing,” *Am. J. Roentgenol.*, vol. 199, no. 4, pp. 768–776, 2012, doi: 10.2214/AJR.12.8855.
 - [25] T. W. Throckmorton, P. C. Zarkadas, J. W. Sperling, and R. H. Cofield, “Pegged versus keeled glenoid components in total shoulder arthroplasty,” *J. Shoulder Elb. Surg.*, vol. 19, no. 5, pp. 726–733, 2010, doi: 10.1016/j.jse.2009.10.018.
 - [26] T. C. Gascoyne et al., “Radiostereometric analysis of keeled versus pegged glenoid components in total shoulder arthroplasty: A randomized feasibility study,” *Can. J. Surg.*, vol. 60, no. 4, pp. 273–279, 2017, doi: 10.1503/cjs.001817.
 - [27] A. Lädermann et al., “Effect of humeral stem design on humeral position and range of motion in reverse shoulder arthroplasty,” *Int. Orthop.*, vol. 39, no. 11, pp. 2205–2213, 2015, doi: 10.1007/s00264-015-2984-3.
 - [28] L. Favard, “Revision of total shoulder arthroplasty,” *Orthop. Traumatol. Surg. Res.*, vol. 99, no. 1 Suppl, pp. S12–S21, 2013, doi: 10.1016/j.otsr.2012.11.010.
 - [29] J. A. Singh, J. W. Sperling, and R. H. Cofield, “Revision surgery following total shoulder arthroplasty: Analysis of 2588 shoulders over three decades (1976 to 2008),” *J. Bone Jt. Surg. - Ser. B*, vol. 93 B, no. 11, pp. 1513–1517, 2011, doi: 10.1302/0301-620X.93B11.26938.
 - [30] N. Bonnevialle et al., “Aseptic glenoid loosening or failure in total shoulder arthroplasty: Revision with glenoid reimplantation,” *J. Shoulder Elb. Surg.*, vol.

- 22, no. 6, pp. 745–751, 2013, doi: 10.1016/j.jse.2012.08.009.
- [31] P. Vavken, P. Sadoghi, A. Von Keudell, C. Rosso, V. Valderrabano, and A. M. Müller, “Rates of radiolucency and loosening after total shoulder arthroplasty with pegged or keeled glenoid components,” *J. Bone Jt. Surg. - Ser. A*, vol. 95, no. 3, pp. 215–221, 2013, doi: 10.2106/JBJS.L.00286.
- [32] J. J. King, K. W. Farmer, A. M. Struk, and T. W. Wright, “Uncemented versus cemented humeral stem fixation in reverse shoulder arthroplasty,” *Int. Orthop.*, vol. 39, no. 2, pp. 291–298, 2014, doi: 10.1007/s00264-014-2593-6.
- [33] N. T. Formaini, N. G. Everding, J. C. Levy, B. G. Santoni, A. N. Nayak, and C. Wilson, “Glenoid baseplate fixation using hybrid configurations of locked and unlocked peripheral screws,” *J. Orthop. Traumatol.*, vol. 18, no. 3, pp. 221–228, 2017, doi: 10.1007/s10195-016-0438-3.
- [34] M. Uy et al., “Cemented humeral stem versus press-fit humeral stem in total shoulder arthroplasty: A systematic review and meta-analysis,” *Bone Jt. J.*, vol. 101-B, no. 9, pp. 1107–1114, 2019, doi: 10.1302/0301-620X.101B9.BJJ-2018-1369.R1.
- [35] M. Königshausen et al., “Bone grafting in oblique versus prepared rectangular uncontained glenoid defects in reversed shoulder arthroplasty. A biomechanical comparison,” *Clin. Biomech.*, vol. 50, no. June, pp. 7–15, 2017, doi: 10.1016/j.clinbiomech.2017.09.011.
- [36] B. O. Parsons, K. I. Gruson, K. J. Accounti, R. A. Klug, and E. L. Flatow, “Optimal rotation and screw positioning for initial glenosphere baseplate fixation in reverse shoulder arthroplasty,” *J. Shoulder Elb. Surg.*, vol. 18, no. 6, pp. 886–891, 2009, doi: 10.1016/j.jse.2008.11.002.
- [37] A. R. Hopkins, U. N. Hansen, A. M. J. Bull, R. Emery, and A. A. Amis, “Fixation of the reversed shoulder prosthesis,” *J. Shoulder Elb. Surg.*, vol. 17, no. 6, pp. 974–980, 2008, doi: 10.1016/j.jse.2008.04.012.
- [38] E. J. Martin, T. R. Duquin, and M. T. Ehrensberger, “Reverse total shoulder glenoid baseplate stability with superior glenoid bone loss,” *J. Shoulder Elb. Surg.*, vol. 26, no. 10, pp. 1748–1755, 2017, doi: 10.1016/j.jse.2017.04.020.
- [39] C. Chebli, P. Huber, J. Watling, A. Bertelsen, R. T. Bicknell, and F. Matsen,

- “Factors affecting fixation of the glenoid component of a reverse total shoulder prosthesis,” *J. Shoulder Elb. Surg.*, vol. 17, no. 2, pp. 323–327, 2008, doi: 10.1016/j.jse.2007.07.015.
- [40] N. Razfar, “Finite Element Modeling of the Proximal Humerus to Compare Stemless , Short and Standard Stem Humeral Components of Varying Material Stiffness for Shoulder Arthroplasty,” University of Western Ontario, 2014. [Online]. Available: <https://ir.lib.uwo.ca/etd/2431>
- [41] E. Munting, P. Smitz, N. Van Sante, C. Nagant De Deuxchaisnes, A. Vincent, and J. P. Devogelaer, “Effect of a stemless femoral implant for total hip arthroplasty on the bone mineral density of the proximal femur: A prospective longitudinal study,” *J. Arthroplasty*, vol. 12, no. 4, pp. 373–379, 1997, doi: 10.1016/S0883-5403(97)90192-3.
- [42] A. Beltrame, P. Di Benedetto, C. Cicuto, V. Cainero, R. Gisonni, and A. Causero, “Onlay versus inlay humeral steam in reverse shoulder arthroplasty (Rsa): Clinical and biomechanical study,” *Acta Biomed.*, vol. 90, pp. 54–63, 2019, doi: 10.23750/abm.v90i12-S.8983.
- [43] G. Merolla et al., “Grammont humeral design versus onlay curved-stem reverse shoulder arthroplasty: comparison of clinical and radiographic outcomes with minimum 2-year follow-up,” *J. Shoulder Elb. Surg.*, vol. 27, no. 4, pp. 701–710, 2018, doi: 10.1016/j.jse.2017.10.016.
- [44] P. J. C. Heesterbeek, A. B. Wymenga, and G. G. Van Hellemond, “No difference in implant micromotion between hybrid fixation and fully cemented revision total knee arthroplasty: A randomized controlled trial with radiostereometric analysis of patients with mild-to-moderate bone loss,” *J. Bone Jt. Surg. - Am. Vol.*, vol. 98, no. 16, pp. 1359–1369, 2016, doi: 10.2106/JBJS.15.00909.
- [45] J. Berhouet, P. Garaud, and L. Favard, “Influence of glenoid component design and humeral component retroversion on internal and external rotation in reverse shoulder arthroplasty: A cadaver study,” *Orthop. Traumatol. Surg. Res.*, vol. 99, no. 8, pp. 887–894, 2013, doi: 10.1016/j.otsr.2013.08.008.
- [46] J. Berhouet, P. Garaud, and L. Favard, “Evaluation of the role of glenosphere design and humeral component retroversion in avoiding scapular notching during

- reverse shoulder arthroplasty,” *J. Shoulder Elb. Surg.*, vol. 23, no. 2, pp. 151–158, 2014, doi: 10.1016/j.jse.2013.05.009.
- [47] K. Chan, G. D. G. Langohr, M. Mahaffy, J. A. Johnson, and G. S. Athwal, “Does Humeral Component Lateralization in Reverse Shoulder Arthroplasty Affect Rotator Cuff Torque? Evaluation in a Cadaver Model,” *Clin. Orthop. Relat. Res.*, vol. 475, no. 10, pp. 2564–2571, 2017, doi: 10.1007/s11999-017-5413-7.
- [48] A. Arenas-Miquelez, R. J. Murphy, A. Rosa, D. Caironi, and M. A. Zumstein, “Impact of humeral and glenoid component variations on range of motion in reverse geometry total shoulder arthroplasty: a standardized computer model study,” *J. Shoulder Elb. Surg.*, vol. 30, no. 4, pp. 763–771, 2021, doi: 10.1016/j.jse.2020.07.026.
- [49] U. Sheth and M. Saltzman, “Reverse Total Shoulder Arthroplasty: Implant Design Considerations,” *Curr. Rev. Musculoskelet. Med.*, vol. 12, no. 4, pp. 554–561, 2019, doi: 10.1007/s12178-019-09585-z.
- [50] B. J. Erickson, R. M. Frank, J. D. Harris, N. Mall, and A. A. Romeo, “The influence of humeral head inclination in reverse total shoulder arthroplasty: A systematic review,” *J. Shoulder Elb. Surg.*, vol. 24, no. 6, pp. 988–993, 2015, doi: 10.1016/j.jse.2015.01.001.
- [51] M. Frankle, S. Siegal, D. Pupello, A. Saleem, M. Mighell, and M. Vasey, “The reverse shoulder prosthesis for glenohumeral arthritis associated with severe rotator cuff deficiency: A minimum two-year follow-up study of sixty patients,” *J. Bone Jt. Surg. - Ser. A*, vol. 87, no. 8, pp. 1697–1705, 2005, doi: 10.2106/JBJS.D.02813.
- [52] N. J. Stroud et al., “Initial glenoid fixation using two different reverse shoulder designs with an equivalent center of rotation in a low-density and high-density bone substitute,” *J. Shoulder Elb. Surg.*, vol. 22, no. 11, pp. 1573–1579, 2013, doi: 10.1016/j.jse.2013.01.037.
- [53] J. W. Giles, G. D. G. Langohr, J. A. Johnson, and G. S. Athwal, “Implant Design Variations in Reverse Total Shoulder Arthroplasty Influence the Required Deltoid Force and Resultant Joint Load,” *Clin. Orthop. Relat. Res.*, vol. 473, no. 11, pp. 3615–3626, 2015, doi: 10.1007/s11999-015-4526-0.

- [54] G. D. G. Langohr, J. W. Giles, G. S. Athwal, and J. A. Johnson, “The effect of glenosphere diameter in reverse shoulder arthroplasty on muscle force, joint load, and range of motion,” *J. Shoulder Elb. Surg.*, vol. 24, no. 6, pp. 972–979, 2015, doi: 10.1016/j.jse.2014.10.018.
- [55] A. Terrier, A. Reist, F. Merlini, and A. Farron, “Simulated joint and muscle forces in reversed and anatomic shoulder prostheses,” *J. Bone Jt. Surg. - Ser. B*, vol. 90, no. 6, pp. 751–756, 2008, doi: 10.1302/0301-620X.90B6.19708.
- [56] ASTM, “F1378 - 18; Standard Specification for Shoulder Prostheses,” ASTM B. Stand., no. C, pp. 16–20, 2012, doi: 10.1520/F1378-12.2.
- [57] ASTM, “ASTM F2028-17 Standard Test Methods for Dynamic Evaluation of Glenoid Loosening or Disassociation,” pp. 1–15, 2018, doi: 10.1520/F2028-17.Copyright.
- [58] ASTM, “F1839 - 97: Standard Specification for Rigid Polyurethane Foam for use as a Standard Material for Testing Orthopaedic Devices and Instruments,” ASTM B. Stand., vol. 13.01, no. October, pp. 6–11, 2014, doi: 10.1520/F1839-08R12.Copyright.
- [59] P. M. Kurowski, *Engineering Analysis with Solidworks Simulation 2013*. Mission, KS: Stephen Schröff, 2013.
- [60] M. A. Sutton, J.-J. Orteau, and H. W. Schreier, *Image Correlation for Shape, Motion and Deformation Measurements*. New York: Springer Science+Business Media, 2009. doi: 10.1007/978-0-387-78747-3.
- [61] R. Ghosh, S. Gupta, A. Dickinson, and M. Browne, “Verification of the Digital Image Correlation Technique for Bone Surface Strain Measurements,” *J. Biomech.*, vol. 45, no. 1, p. S277, 2012, doi: 10.1016/s0021-9290(12)70278-6.
- [62] W. F. Zimmerman, M. A. Miller, R. J. Cleary, T. H. Izant, and K. A. Mann, “Damage in total knee replacements from mechanical overload,” *J. Biomech.*, vol. 49, no. 10, pp. 2068–2075, 2016, doi: 10.1016/j.jbiomech.2016.05.014.
- [63] K. A. Mann, M. A. Miller, P. A. Costa, A. Race, and T. H. Izant, “Interface micromotion of uncemented femoral components from postmortem retrieved total hip replacements,” *J. Arthroplasty*, vol. 27, no. 2, pp. 238-245.e1, 2012, doi: 10.1016/j.arth.2011.04.018.

- [64] M. Hackl et al., “Plate Osteosynthesis of Proximal Ulna Fractures—A Biomechanical Micromotion Analysis,” *J. Hand Surg. Am.*, vol. 42, no. 10, pp. 834.e1–834.e7, 2017, doi: 10.1016/j.jhsa.2017.05.014.
- [65] P. Favre et al., “In vitro assessments of reverse glenoid stability using displacement gages are misleading - Recommendations for accurate measurements of interface micromotion,” *Clin. Biomech.*, vol. 26, no. 9, pp. 917–922, 2011, doi: 10.1016/j.clinbiomech.2011.05.002.
- [66] P. Favre et al., “In vitro initial stability of a stemless humeral implant,” *Clin. Biomech.*, vol. 32, pp. 113–117, 2016, doi: 10.1016/j.clinbiomech.2015.12.004.

Chapter 2

2 Orthogonal vs Tangential Interface Micromotion in Stemless Shoulder Implants: A Technical Note

OVERVIEW

Evaluating the effects of implant design is essential to their ongoing development. A major focus relates to the nature of interface load transfer, and in particular implant-bone relative motion (micromotion), particularly for implants designed for fixation via osseointegration. However, it is still not fully known what the most appropriate evaluation protocol is for the optimization of stemless humeral implant components. It is therefore important to determine the micromotion outcome measure most appropriate to utilize in the comparative evaluation of orthopaedic implant fixation. Additionally, there seems to be some disparity in the quoted limits of micromotion, and the commonly utilized experimental outcome measure of micromotion. This following technical note focuses on the differentiation of tangential and orthogonal implant-bone relative motion to ascertain a significant model for stemless humeral shoulder implants.

2.1 Introduction

Although there is no formal ASTM protocol for the evaluation of humeral component reverse total shoulder arthroplasty (RTSA) implants, many existing studies evaluating the fixation of humeral components utilize implant-bone relative motion (termed “micromotion”) as the primary outcome measure of implant performance [1]–[4]. However, there is some disparity between the reported micromotion values and the intended reasoning for the use of this metric. Micromotion is an outcome variable most associated with osseointegration, but existing literature rarely differentiates between tangential (shear) and orthogonal (distractive) micromotion, as shown in Figure 2-1. Most studies employ the commonly accepted 150 μm [4]–[13], or the more conservative 30 μm [11], [14] of implant-bone tangential micromotion as the limit before effective implant osseointegration is negatively affected, without isolating tangential micromotion from the measured total micromotion. However, the importance of treating tangential and orthogonal micromotions as discrete outcome measures has previously been indicated explicitly; as those micromotion components likely do not experience the same osseointegrative behaviour [15]. In fact, when evaluating the mechanical interface strength of osseointegrating coatings, it is common to distinguish between tangential and orthogonal loading directions (Figure 2-1), as the failure thresholds are markedly different in the shear and tensile directions [16]; a practice still infrequently applied to studies of primary implant stability. This is extremely important, as implants evaluated will undoubtably experience a combination of both tangential and orthogonal micromotion; with one likely more relevant than the other and consequently be more influential to overall implant fixation.

Although tangential and orthogonal micromotion (Figure 2-1) are both measures of implant-bone relative motion, their effect on osseointegration is markedly different, particularly in the early postoperative period. Tangential micromotion, the more commonly referenced of the two measures as stated, is initially resisted by friction phenomena [17] or mechanical interlocking [18] before bony ingrowth has commenced. Therefore, during the first six weeks postoperatively [19], micromotion is resisted by frictional forces which are imposed by the tangential loading component which may also depend on the press-fit of the implant. Interface damage, changes to bone or implant roughness, or changes to contact

pressure due to tissue relaxation would also then affect the fixation of tangentially resisted micromotion.

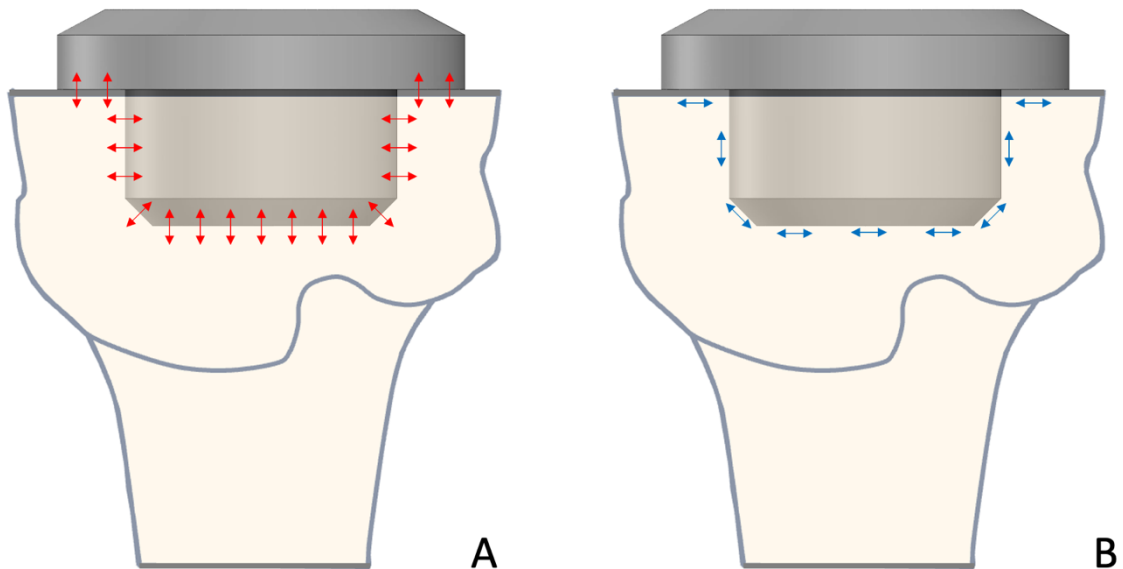


Figure 2-1: Orthogonal vs Tangential Micromotion in a Stemless Humeral Implant
A depiction of the (A) orthogonal micromotion and the (B) tangential micromotion at the bone-implant interface.

Conversely, orthogonal micromotion is resisted by a different mechanism. Orthogonal micromotion in the distractive direction is reliant on the magnitude of osseointegration [17]. Additionally, the effects of mechanical interlocking are nearly eliminated with pure orthogonal loading, and therefore do not significantly enhance fixation in the distractive direction before osseointegration has occurred [18]. This emphasizes the importance of maximizing the rate of osseointegration during the early postoperative period (first six weeks) in order to establish a level of bony ingrowth and bone maturation commensurate with maximal osseointegration [19]. Unlike the tangential micromotion limit of 150 μm , there appears to be no consensus or data on similar limits for distractive orthogonal micromotion.

Before continuing to an evaluation of any specific stemless humeral component design, it is thus important to quantify and compare tangential and orthogonal micromotion in stemless humeral shoulder implants. The purpose of this basic finite element evaluation was to determine the most defining micromotion direction in these implants during simulated physiological loading.

2.2 Methods

A computed tomography (CT) scan of a single left humerus (male, age: 79, height: 173 cm, weight: 71 kg) was acquired using a clinical scanner. A cortical bone surrogate (SB3 model 450; GAMMEX, Middleton, WI, USA), and a distilled water phantom were used to calculate the apparent density in g/cm³ from the recorded Hounsfield units (HU). A three-dimensional model of the humerus was then created from the CT scan with isolated trabecular and cortical sections. The humerus model was imported into SolidWorks (Dassault Systèmes, Waltham, MA, USA) for resection and implant positioning. A board-certified orthopaedic surgeon (GSA) resected the humerus at a neck-shaft angle of 135° and positioned two clinically available stemless humeral implants into the bone model. The Tornier Perform® Stemless Reverse Humeral System (Stryker, Kalamazoo, MI, USA), and Tornier Simpliciti® Stemless Reverse Humeral System (Stryker, Kalamazoo, MI, USA) were utilized for this evaluation. Two distinctly different designs of implant were assessed in order to evaluate the generalizability of the results.

Each positioned implant and bone model was imported into Abaqus CAE 2021 (Dassault Systèmes Corp), and meshed with 1.2 mm quadratic tetrahedral elements, according to mesh convergence. Trabecular bone was assigned inhomogeneous elastic properties according to the Morgan *et al.* density-elasticity relationship [20], and cortical bone was assigned a homogenous elasticity of 20 GPa [21], [22]. The implants were assigned an elastic modulus of 110 GPa to represent titanium [23]. All components were ascribed a Poisson's ratio of 0.3 [8], [21]. A frictional contact condition with $\mu = 0.6$ [12] was imposed at the bone-implant interface to represent a titanium plasma sprayed surface on bone. A 700N load at an angle of 58° from the resection plane was applied to each implant at the

centre of rotation of the glenosphere in the posteroinferior direction; representative of the most aggressive physiological loading conditions experienced by the shoulder, according to data previously collected using telemetrized TSA implants (Figure 2-2)[24]. Encastre boundary conditions were applied to the model at a point 50 mm distal to the humeral head; in accordance with results of an analysis of boundary condition distalization.

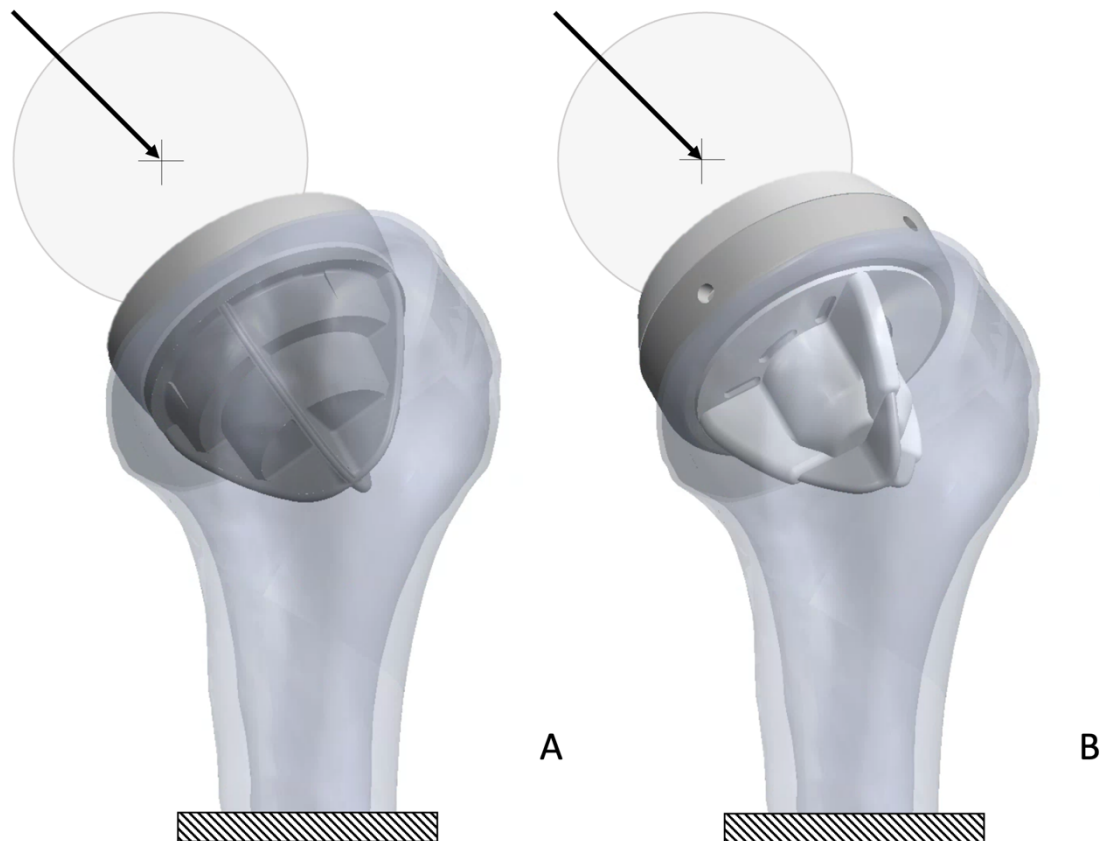


Figure 2-2: Perform and Simpliciti Implants Positioned in a Humeral Model

An anterior view of the (A) Perform and (B) Simpliciti stemless RTSA humeral implants positioned in a 3D humeral model. A representation of the glenosphere is pictured, with the applied loading vector drawn in the posteroinferior direction, and the encastre boundary condition is indicated by the hatched boxes.

2.3 Outcome Variables and Analysis

Maximum bone-implant micromotions were extracted and separated into orthogonal and tangential components. These components were filtered into 180 separate sections; split by 36 circumferential slices and five slices of increasing depth (Figure 2-3).

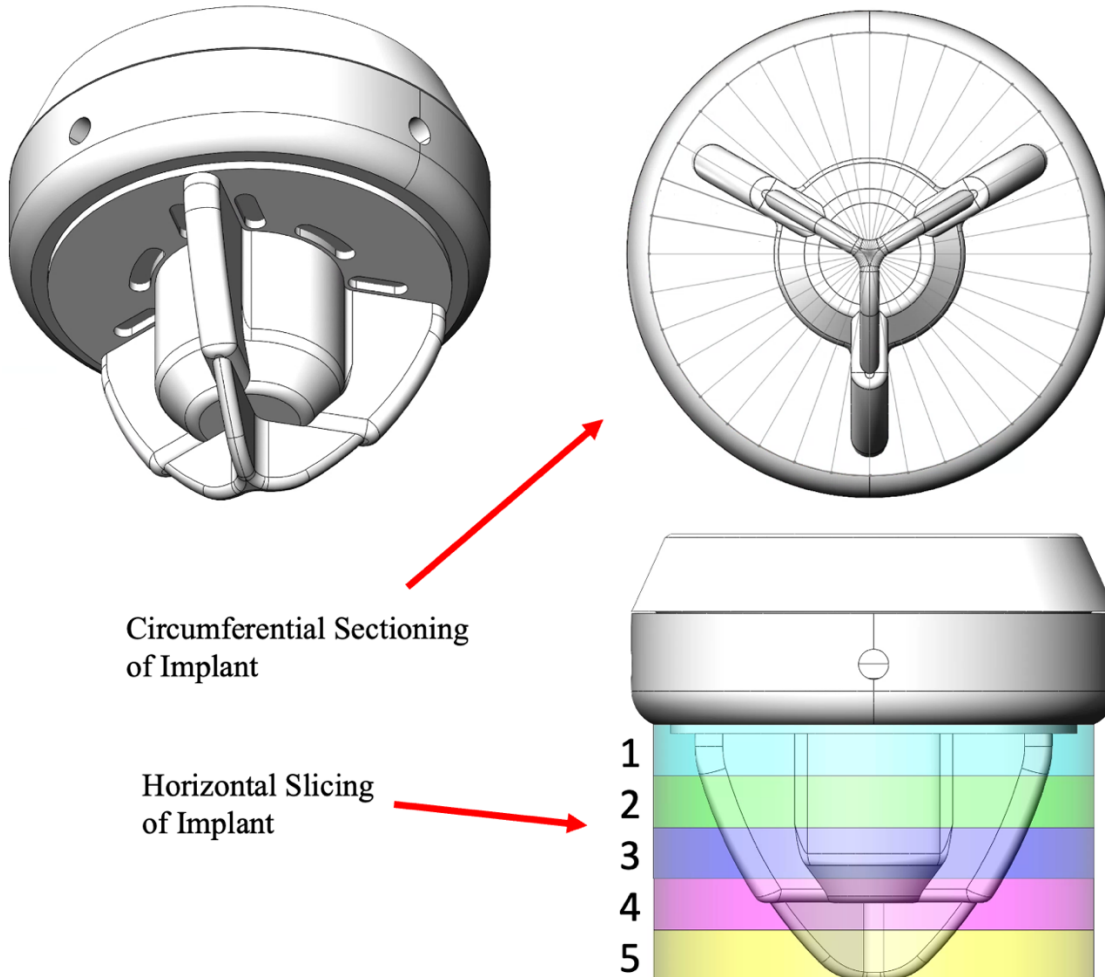


Figure 2-3: The Tornier Simpliciti® Implant Split into Regions of Interest

A depiction of the implant sectioning leveraged. Implants were split into 36 circumferential slices at five slices of increasing depth to investigate micromotion components throughout the implant geometry. For this figure, the Tornier Simpliciti® implant was used as an example.

2.4 Results

It was found that in the stemless humeral implant geometries evaluated, the most defining micromotion component was orthogonal micromotion, which appeared to be largest on the side of the implant opposite to the direction of loading. Conversely, tangential micromotion appeared to be greatest on the side similar to the direction of loading (Figure 2-4). The mean micromotions detected were 13 μm in the orthogonal direction, and 5 μm in the tangential direction in the Perform[®] implant, and 36 μm orthogonal, and 6 μm tangential in the Simpliciti[®] implant. Maximum micromotions were 67 μm orthogonal and 43 μm tangential, and 126 μm orthogonal and 64 μm tangential for the Perform[®] and Simpliciti[®] implants, respectively. These results were intended to guide the design of a protocol for the evaluation of stemless humeral components that is most appropriate to the driving mechanism of fixation.

2.5 Discussion

For the two implants evaluated, implant-bone distraction was the more defining micromotion metric. These results agree with previous findings of previous total ankle replacement design evaluations, which have indicated that shorter pegged tibial implants experience proportionally higher levels of orthogonal micromotions when compared to stemmed implant variants [25]. This is noteworthy, as the findings presented herein suggest not only that the bone-implant relative motion of stemless humeral implants is driven by orthogonal implant micromotion, but that the geometry of the implant evaluated influences the proportion of orthogonal and tangential micromotions expressed. While not evaluated here, it is likely that tangential micromotions are more prevalent for intramedullary stemmed devices responding to the axial component of loading.

Although there are apparently no studies that have specifically evaluated the effect of purely distractive micromotion on the primary fixation, it is not unreasonable to postulate, as the mechanism of osseointegrative bonding is different between tangential and orthogonal loading, that the effect of distractive micromotion is similarly different to that of tangential micromotion. It is also logical to postulate that any distraction, even in the

range up to 10 μm will likely pose a barrier to osseointegration and impede successful long-term fixation. In future studies it will be essential to perform a thorough analysis of micromotions in both orthogonal and tangential directions before a comprehensive understanding of implant primary fixation can be achieved. As the two stemless implants evaluated were radically different in geometrical design, it is likely that these observations may be extended to additional designs of stemless humeral implant. As noted, these results appear to be specific to stemless implant designs, as it has been previously suggested that increasing stem length may shift the defining micromotion from the orthogonal direction to the tangential direction [25].

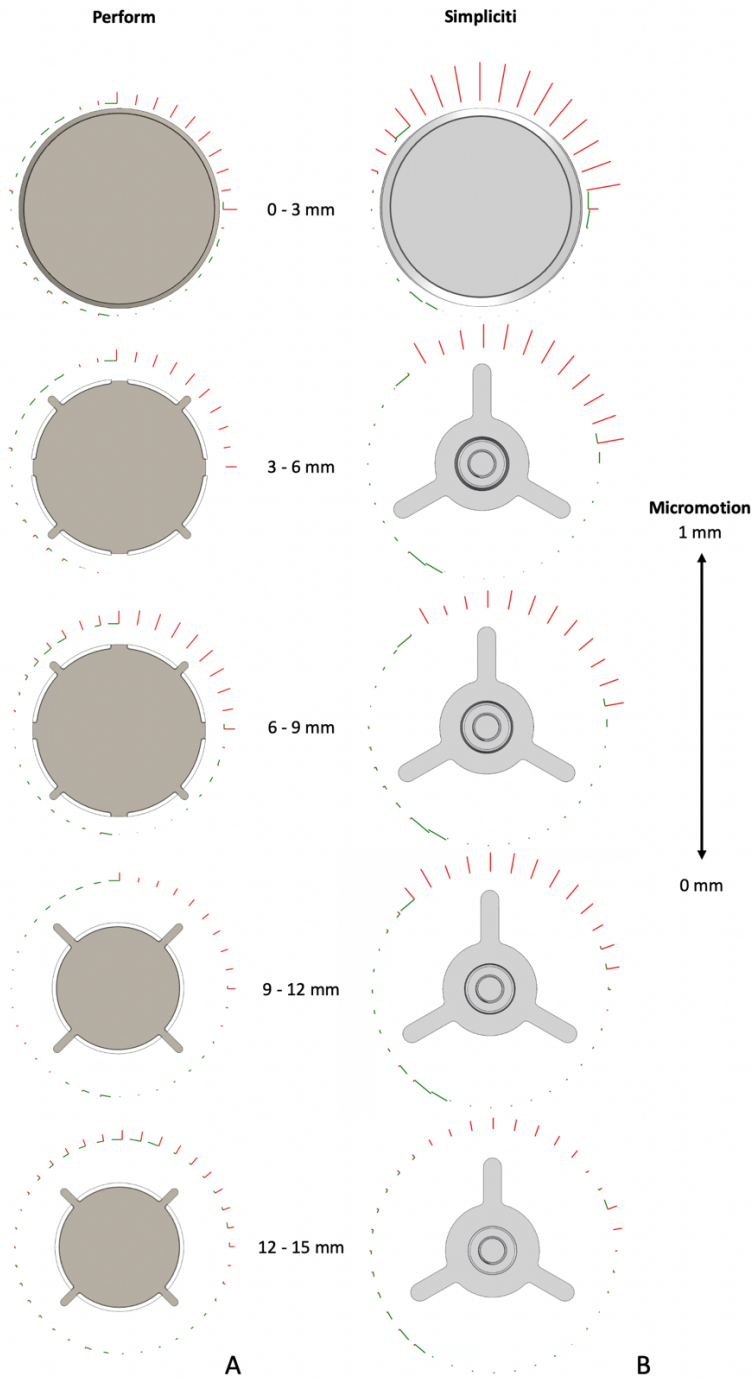


Figure 2-4: Tangential and Orthogonal Micromotion in Tornier Perform and Tornier Simpliciti Implants

A depiction of the relative orthogonal and tangential micromotions developed during loading of the (A) Perform and (B) Simpliciti implants. Red orthogonal lines indicate distractive micromotion magnitude (derived from Abaqus CAE COPEN field output), and green tangential lines indicate shear micromotion magnitude (from CSLIP field output).

2.6 Conclusion

This investigation has provided insight into the appropriate methodologies for the evaluation of humeral components. More specifically, it has stressed the importance of distinguishing between tangential and orthogonal micromotion measurements when assessing implant primary fixation, as the magnitude of each was markedly different. Therefore, for the remainder of this treatise, distractive orthogonal micromotion will be isolated as the metric measured and reported, as not to confound the inferential conclusions on the effects of implant and surgical design variables.

2.7 References

- [1] P. Favre *et al.*, “In vitro initial stability of a stemless humeral implant,” *Clin. Biomech.*, vol. 32, pp. 113–117, 2016, doi: 10.1016/j.clinbiomech.2015.12.004.
- [2] T. S. Bae, E. E. Ritzer, W. Cho, and W. Joo, “Effect of fin length and shape of stemless humeral components in a reverse shoulder implant system: a FEA study,” *J. Mech. Sci. Technol.*, vol. 35, no. 1, pp. 417–422, 2021, doi: 10.1007/s12206-020-1241-x.
- [3] R. E. Chen, E. Knapp, B. Qiu, A. Miniaci, H. A. Awad, and I. Voloshin, “Biomechanical comparison of stemless humeral components in total shoulder arthroplasty,” *Semin. Arthroplast. JSES*, pp. 1–9, 2021, doi: 10.1053/j.sart.2021.08.003.
- [4] P. Favre and A. D. Henderson, “Prediction of stemless humeral implant micromotion during upper limb activities,” *Clin. Biomech.*, vol. 36, pp. 46–51, 2016, doi: 10.1016/j.clinbiomech.2016.05.003.
- [5] ASTM, “ASTM F2028-17 Standard Test Methods for Dynamic Evaluation of Glenoid Loosening or Disassociation,” pp. 1–15, 2018, doi: 10.1520/F2028-17.Copyright.
- [6] W. F. Zimmerman, M. A. Miller, R. J. Cleary, T. H. Izant, and K. A. Mann, “Damage in total knee replacements from mechanical overload,” *J. Biomech.*, vol. 49, no. 10, pp. 2068–2075, 2016, doi: 10.1016/j.biomech.2016.05.014.
- [7] N. T. Formaini *et al.*, “The effect of glenoid bone loss on reverse shoulder arthroplasty baseplate fixation,” *J. Shoulder Elb. Surg.*, vol. 24, no. 11, pp. e312–e319, 2015, doi: 10.1016/j.jse.2015.05.045.
- [8] N. Bonnevialle, L. Geais, J. H. Müller, and J. Berhouet, “Effect of RSA glenoid baseplate central fixation on micromotion and bone stress,” *JSES Int.*, vol. 4, no. 4, pp. 979–986, 2020, doi: 10.1016/j.jseint.2020.07.004.
- [9] J. Tobar-Reyes, L. Andueza-Castro, A. Jiménez-Silva, R. Bustamante-Plaza, and J. Carvajal-Herrera, “Micromotion analysis of immediately loaded implants with Titanium and Cobalt-Chrome superstructures. 3D finite element analysis,” *Clin. Exp. Dent. Res.*, vol. 7, no. 4, pp. 581–590, 2021, doi: 10.1002/cre2.365.
- [10] M. W. Hast, M. Chin, E. C. Schmidt, and A. F. Kuntz, “Central screw use delays

- implant dislodgement in osteopenic bone but not synthetic surrogates: A comparison of reverse total shoulder models,” *J. Biomech.*, vol. 93, pp. 11–17, 2019, doi: 10.1016/j.jbiomech.2019.06.004.
- [11] N. Kohli, J. C. Stoddart, and R. J. van Arkel, “The limit of tolerable micromotion for implant osseointegration: a systematic review,” *Sci. Rep.*, vol. 11, no. 1, pp. 1–11, 2021, doi: 10.1038/s41598-021-90142-5.
 - [12] C. Quental, J. Folgado, M. Comenda, J. Monteiro, and M. Sarmento, “Primary stability analysis of stemless shoulder implants,” *Med. Eng. Phys.*, vol. 81, pp. 22–29, 2020, doi: 10.1016/j.medengphy.2020.04.009.
 - [13] R. M. Pilliar, H. U. Cameron, R. P. Welsh, and A. G. Binnington, “Radiographic and morphologic studies of load-bearing porous-surfaced structured implants,” *Clin. Orthop. Relat. Res.*, vol. 156, no. C, pp. 249–257, 1981, doi: 10.1097/00003086-198105000-00037.
 - [14] H. Kawahara, D. Kawahara, M. Hayakawa, Y. Tamai, T. Kuremoto, and S. Matsuda, “Osseointegration under immediate loading: Biomechanical stress-strain and bone formation-resorption,” *Implant Dent.*, vol. 12, no. 1, pp. 61–68, 2003, doi: 10.1097/01.ID.0000034394.75768.E3.
 - [15] R. Branemark, L. O. Ohrnell, R. Skalak, L. Carlsson, and P. I. Branemark, “Biomechanical characterization of osseointegration: An experimental In Vivo investigation in the beagle dog,” *J. Orthop. Res.*, vol. 16, no. 1, pp. 61–69, 1998, doi: 10.1002/jor.1100160111.
 - [16] Y. T. Sul, D. H. Kwon, B. S. Kang, S. J. Oh, and C. Johansson, “Experimental evidence for interfacial biochemical bonding in osseointegrated titanium implants,” *Clin. Oral Implants Res.*, vol. 24, no. A100, pp. 8–19, 2013, doi: 10.1111/j.1600-0501.2011.02355.x.
 - [17] K. Immel, V. H. Nguyen, G. Haiyat, and R. A. Sauer, “Modeling the debonding process of osseointegrated implants due to coupled adhesion and friction,” *Biomech. Model. Mechanobiol.*, vol. 22, no. 1, pp. 133–158, 2023, doi: 10.1007/s10237-022-01637-7.
 - [18] H. J. Rønold and J. E. Ellingsen, “The use of a coin shaped implant for direct in situ measurement of attachment strength for osseointegrating biomaterial

- surfaces,” *Biomaterials*, vol. 23, no. 10, pp. 2201–2209, 2002, doi: 10.1016/S0142-9612(01)00353-2.
- [19] H. J. Rønold, J. E. Ellingsen, and S. P. Lyngstadaas, “Tensile force testing of optimized coin-shaped titanium implant attachment kinetics in the rabbit tibiae,” *J. Mater. Sci. Mater. Med.*, vol. 14, no. 10, pp. 843–849, 2003, doi: 10.1023/A:1025622407727.
- [20] E. F. Morgan, H. H. Bayraktar, and T. M. Keaveny, “Trabecular bone modulus-density relationships depend on anatomic site,” *J. Biomech.*, vol. 36, no. 7, pp. 897–904, 2003, doi: 10.1016/S0021-9290(03)00071-X.
- [21] J. M. Reeves, G. D. G. Langohr, G. S. Athwal, and J. A. Johnson, “The effect of stemless humeral component fixation feature design on bone stress and strain response: a finite element analysis,” *J. Shoulder Elb. Surg.*, vol. 27, no. 12, pp. 2232–2241, 2018, doi: 10.1016/j.jse.2018.06.002.
- [22] N. Razfar, J. M. Reeves, D. G. Langohr, R. Willing, G. S. Athwal, and J. A. Johnson, “Comparison of proximal humeral bone stresses between stemless, short stem, and standard stem length: A finite element analysis,” *J. Shoulder Elb. Surg.*, vol. 25, no. 7, pp. 1076–1083, 2016, doi: 10.1016/j.jse.2015.11.011.
- [23] S. Synnott, “The Effect of Implant Girth and Implant Collar on the Degree of Bone to Implant Contact and Bone Stresses in the Proximal Humerus,” The University of Western Ontario, 2018.
- [24] P. Damm and J. Dymke, “Orthoload Database,” *Julius Wolff Institute*, 2021. <https://orthoload.com/database/> (accessed Jul. 26, 2021).
- [25] R. S. Sopher, A. A. Amis, J. D. Calder, and J. R. T. Jeffers, “Total ankle replacement design and positioning affect implant-bone micromotion and bone strains,” *Med. Eng. Phys.*, vol. 42, pp. 80–90, 2017, doi: 10.1016/j.medengphy.2017.01.022.

Chapter 3

3 Developing a System for the Evaluation of Novel Shoulder Implant Designs

OVERVIEW

Evaluating the efficacy of orthopaedic implant designs is essential in the protection of patients and the optimization of implant development. A significant clinical concern is the fixation of the implant to bone and hence the subject of a number of biomechanical investigations. Precedent literature investigating the influence of design variables in the development of orthopaedic shoulder implants have employed linear variable differential transformers (LVDTs), idealized loading conditions, and other methods to quantify fixation of implants to bone. However, in this ever-evolving field, it is essential to update the industry-accepted protocols for the evaluation of implant designs. Although previous evaluations of shoulder implants have satisfactorily replicated some of the general load magnitudes that may be experienced by an implant during an abduction motion in-vivo, they have not replicated the wide array of loading magnitudes and directions that are commonly experienced by shoulder implants during activities of daily living. This chapter describes the design of a novel loading apparatus and implant-fixation tracking system; created to accurately replicate the loading magnitudes and directions that are experienced by the shoulder joint during common activities of daily living. The systems described herein are likely to improve the validity of biomechanical assessments of implant performance and thus the value of the conclusions obtained in those works.

3.1 Introduction

The glenohumeral joint possesses the largest range of motion of any joint in the body, largely due to its soft-tissue constraint mechanism [1], [2]. However, the greater degree of freedom experienced by the shoulder joint also makes the construct susceptible to instability and dysfunction [3]. Due to the large range of motion experienced by the shoulder joint, many force magnitudes and directions are experienced at the articulation; making it important to evaluate not only the forces developed during the simple abduction motion, but those developed during activities commonly performed throughout the day. In order to obtain experimentally-valid *in-vitro* data, it is necessary to employ a testing method capable of replicating real life forces in a repeatable, objective, and quantifiable way. This requires the development of a quasi-static simulator that can repeatably apply three-dimensional loads to a bone-implant construct, thereby permitting the accurate evaluation of time-zero implant stability.

Past investigators have developed a number of designs of static loading simulators to enable the evaluation of implant performance [4]–[9]. However, each of these systems have been limited in the variety of loading scenarios investigated. Many existing evaluations of shoulder implant stability have employed single axis loading methods, which are limited in their ability to replicate physiologically accurate conditions. Although newer, computational evaluations, of shoulder implant performance have begun to investigate the influence of physiologically-relevant loading direction and magnitude [10], [11], few experimental investigations have evaluated more than a single loading scenario. This is, in part, due to the ASTM F2028 standard testing methods for the “Dynamic Evaluation of Glenoid Loosening or Disassociation”, which references only the humeral abduction motion when describing the suggested protocol for the evaluation of implant fixation [12].

Therefore, the objective of this work was to develop a loading apparatus capable of applying a complex array of physiologically relevant loads to investigate the degree of primary fixation in stemless orthopaedic implants. Additionally, this apparatus was designed with integrated best-practice digital methods for the measurement of bone-implant initial stability at the interface. It was hypothesized that the implementation of these

methods would improve the validity of performing evaluations of implant performance, while improving the accuracy of existing industry-accepted protocols for the evaluation of shoulder implant designs.

3.2 Methods

The following sections describe the design, development, and validation of the Comprehensive Evaluation for the Realistic Biomechanical Examination and Repair of Upper-limb Systems (CERBERUS) apparatus.

3.2.1 Design Problem and Requirements

The design of CERBERUS was guided by a base problem statement: orthopaedic researchers investigating the primary fixation of humeral implants require a method of applying physiologically relevant forces to bone-implant systems, as existing planar testing approaches are unable to thoroughly investigate the behaviors of novel implant designs.

The requirements for the physical design were: (1) all components were required to interface with the lab's existing data acquisition system; (2) the apparatus must be able to apply three-dimensional loads to a fully assembled and installed total shoulder arthroplasty implant; and (3) the apparatus must not interfere in the acquisition of bone-implant micromotion measurements when using digital tracking methods. For the digital image collection system, the requirements were: (1) to meet the industry standard for an accuracy of five microns distraction when collection bone-implant relative motion measurements; and (2) to improve upon the existing linear displacement measuring method utilized by the orthopaedic design industry. The primary constraint of this design was to avoid altering the design of a reversed total shoulder arthroplasty humeral component during the evaluation of said component.

3.2.2 Three-Dimensional Force Application

Precedent testing methods used in the evaluation of novel osseointegrated prosthetics predominantly employ uniaxial loading protocols. Specifically, in the evaluation of reversed total shoulder arthroplasty implants, these industry-accepted methods are intended to stimulate the “rocking horse” phenomenon in the bone-implant construct; where a compressive-eccentric load (intended on replicating the maximum force magnitude and direction developed during an unweighted abduction motion) is applied to the implant, causing bone-implant distraction on the opposite end (Figure 3-1). The bone-implant relative motion is then quantified using linear variable differential transformers (LVDTs), or a similar linear displacement measurement device. This aforementioned method is currently supported by the ASTM F2028 standard testing method for the Dynamic Evaluation of Glenoid Loosening or Disassociation [12]; although the standard does indicate that additional discretionary testing may be required. However, investigations utilizing load-sensing total shoulder arthroplasty implants in patients have more recently reported that the shoulder articulation experiences a wide range of loading vectors that are not thoroughly encompassed by the simple abduction motion (Figure 3-2)[13]. In light of the foregoing, it is therefore necessary to supersede the uniaxial loading method with a triaxial apparatus to apply more clinically relevant loading states to the shoulder articulation.

The design of this apparatus was generated around the driving principal of avoiding changes to the form, fit, or function of the implant under investigation. This principal design consideration translated to producing a device that could test a fully assembled shoulder implant while the implant was surgically installed into a humerus without changing the biomechanical function of the implant. In the reversed total shoulder arthroplasty procedure, the centre of rotation of the reconstructed glenohumeral joint is restricted to the centre of the glenosphere [1] and thus, this was chosen as the point of force transmission for the bone-implant construct (Figure 3-3).

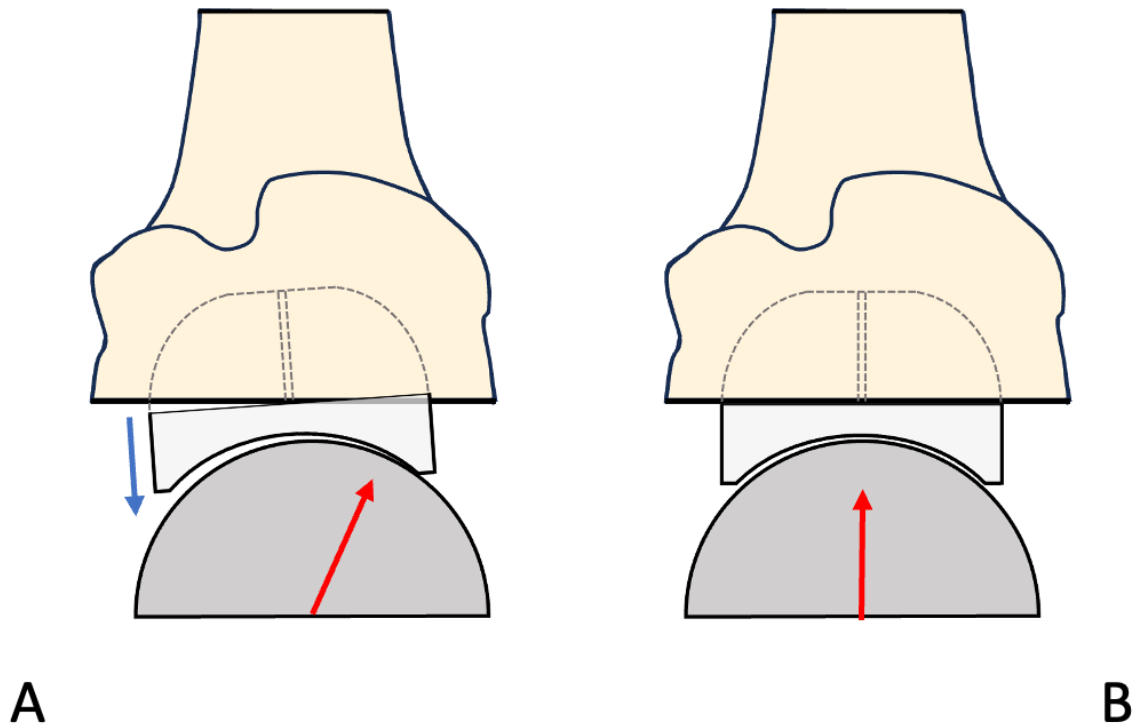


Figure 3-1: Rocking Horse Phenomenon Depicted on a Reversed Total Shoulder Arthroplasty

Superior-lateral view of the right humerus, depicting (A) an eccentric load (red arrow) stimulating implant distraction on the opposite side to loading (blue arrow) via the rocking horse phenomenon, and (B) a purely compressive load with a stable implant.

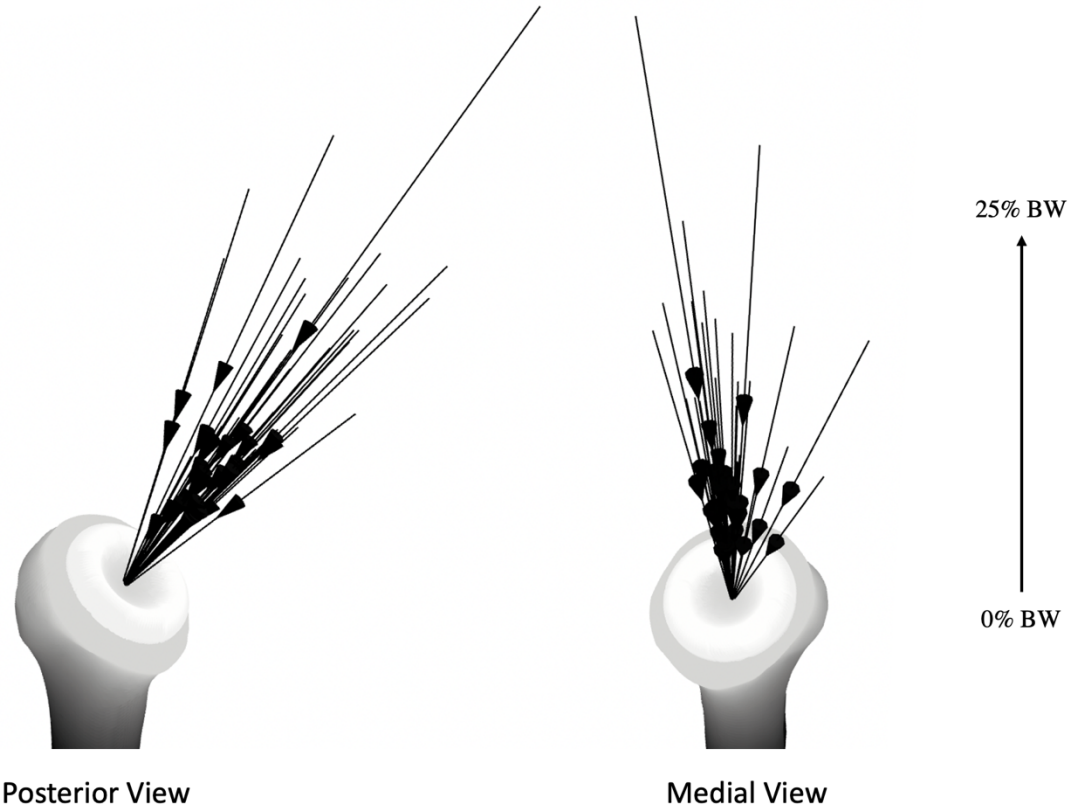


Figure 3-2: Vector Representation of all Relevant Loading Conditions available in OrthoLoad

Posterior and medial views of the loading vectors, overlayed onto a humeral model, that might reasonably be experienced postoperatively. Loading directions and magnitudes were retrieved from the OrthoLoad database [13].

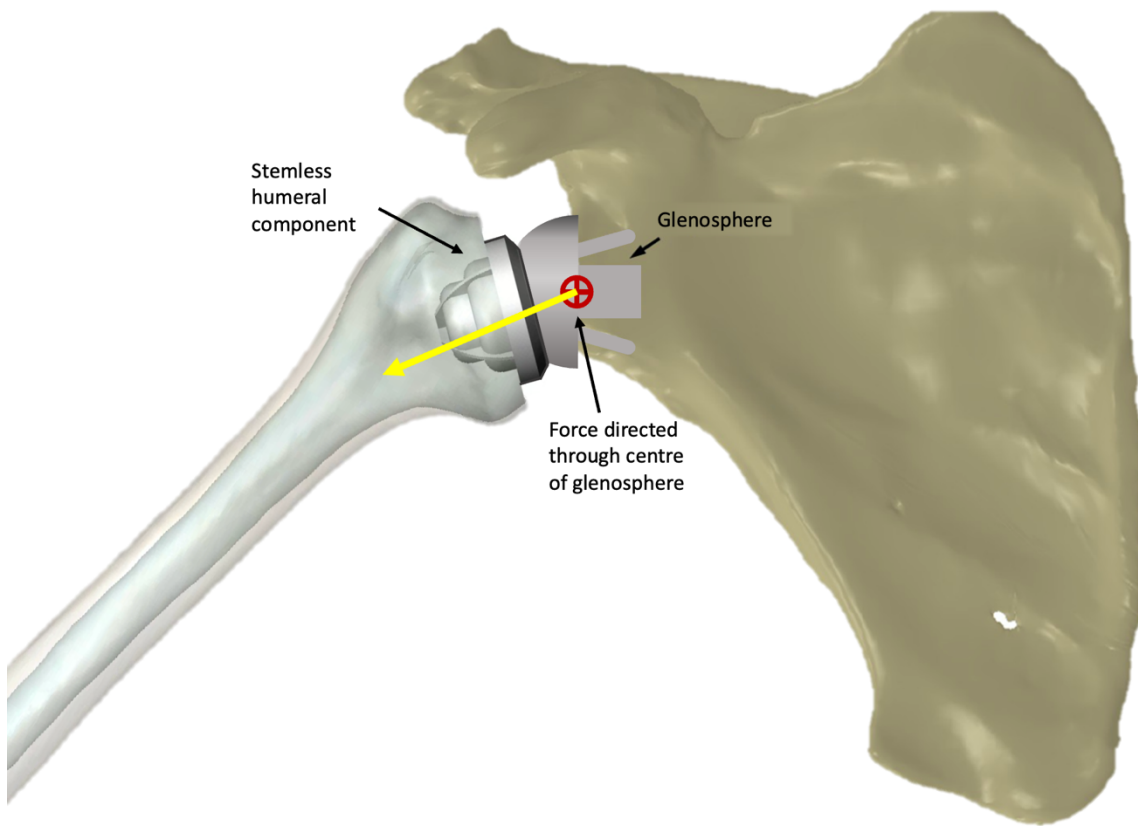


Figure 3-3: Reverse Total Shoulder Arthroplasty Glenosphere Reaction Force

Reverse total shoulder arthroplasty articular force, passing through the spherical centre of the glenosphere component.

Accurately replicating the force transmission from the glenoid component onto the humeral component of a total shoulder arthroplasty, while maintaining the full geometry of an assembled humeral component, required that three-dimensional forces be applied using a mock articulation. As the present work was focused on the reversed humeral component design, this was facilitated by using a large ball-bearing with the same diameter of the clinical glenosphere as a loading intermediary. This setup facilitated the simulation of a full RTSA assembly by maintaining a similar centre of rotation for application of articular forces (Figure 3-3). Polished force application pads were designed to isolate and apply orthogonal forces to the glenosphere without imposing an additional moment (Figure 3-4). This consideration has not been previously implemented into existing loading apparatuses,

which generally apply articular forces with a fixed actuator, thereby potentially complicating the load application procedure [4], [9], [14].

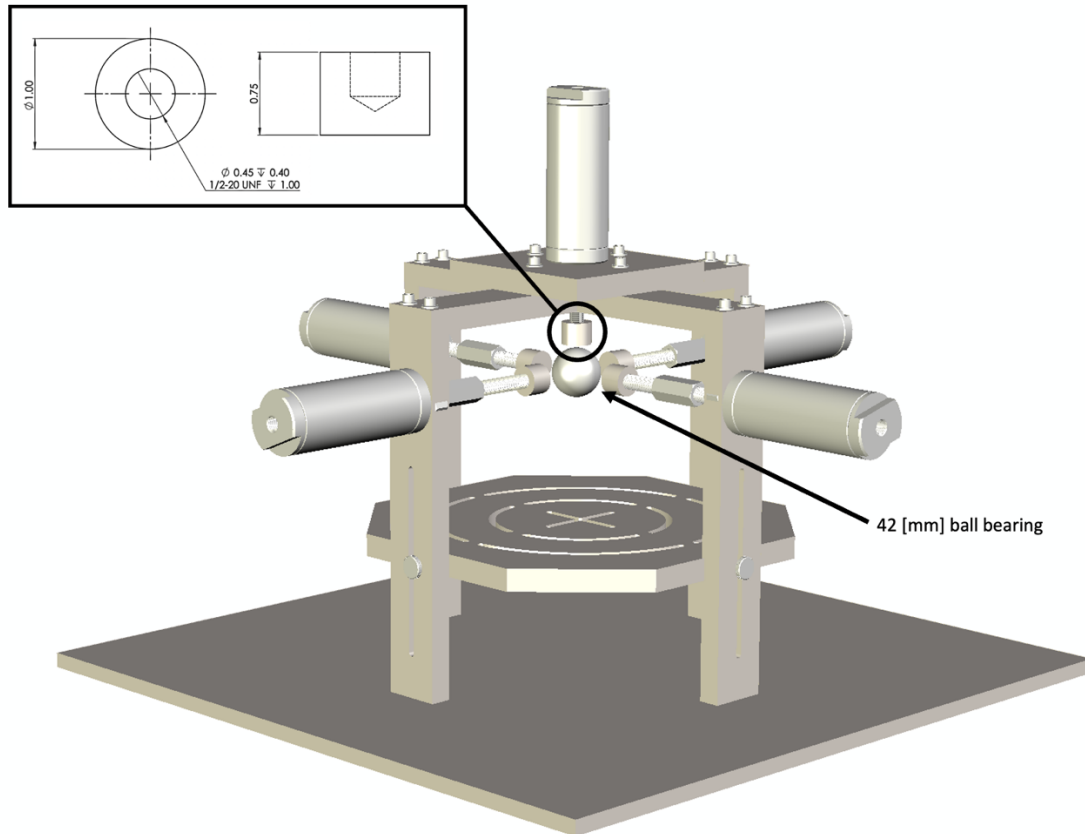


Figure 3-4: Triaxial Loading Apparatus and Polished Force Application Pad Detail

Novel triaxial loading apparatus, with five orthogonally oriented force application pads, shown in drawing-format in the top left.

A target loading limit (1250 [N]) was identified from the OrthoLoad *in-vivo* telemetrized shoulder implant database [13]. Utilizing the laboratory-supplied air system with an operating pressure of 100 psi, five double-acting universal-mount round body air cylinders (6498K558, McMaster-Carr, Douglasville, GA, USA) were positioned orthogonally to facilitate the application of a full array of resolved compressive force vectors. A loading limit of 1380 [N] was identified as the upper range for each actuator, given the 100 [psi]

laboratory pressure limit. Five proportional pressure controllers (PPC5C-AAA-AGCB-BBB-JB, MAC Valves, Wixom, MI, USA) with closed loop feedback were employed to control actuator load.

AISI 304 stainless steel was chosen for the apparatus material due to its high strength and corrosion resistant properties. As human body fluids may corrode metals, and the purpose of the loading apparatus was to test cadaveric specimens, a bioinert material was necessary for the structure of the apparatus. All additional hardware for the apparatus was also chosen with bioactivity considered. For more details on the design of the CERBERUS apparatus, please refer to Appendix B.

3.2.3 Digital Micromotion Tracking

A severe limitation of existing *in-vivo* primary fixation studies has been the usage of linear variable differential transformers (LVDTs) during the evaluation of implant stability [4], [15]. It has been previously found that LVDT-driven micromotion measurements consistently overreport bone-implant relative motion when compared to direct-measurement using digital tracking technology [4], [15], and it has therefore been suggested that the use LVDTs may be inferior to digital tracking methods when evaluating precise micromotion at the interface [15]. Given these findings, it was decided that a digital tracking setup be adopted for the triaxial loading apparatus design.

The primary method for achieving fixation in press fit orthopedic designs is through osseointegration (via bony ingrowth) of the implanted structure. It is generally accepted that for this bone-implant bonding to occur, bone-implant surfaces are required to maintain less than 150 μm of relative motion (termed “micromotion”) [6], [16], although some studies have suggested that osseointegration requires tangential micromotions of less than 50 μm , and any micromotion between 50 μm and 150 μm yields indeterminate activity [17]. This was the driving limit behind the choice of digital tracking system, as it was therefore necessary to confidently track micromotion with a sensitivity of less than 50 μm . Additionally, although the industry standard protocol still references linear digital tracking

methods which do not provide an accurate measurement of micromotion due to systemic limitations [15], the ASTM F2028 standard specification for testing of shoulder prostheses currently suggests an accuracy of less than 5 μm during the evaluation of bone-implant relative motion.

Due to the testing requirements of the digital tracking system discussed above, it was identified that a system be designed with a sensitivity and accuracy of less than 5 [μm] to meet the requirements of the ASTM F2028 standard. Ultimately, a 9MP high-resolution mono-chrome digital machine vision camera (acA4096-30uc, Basler AG, Ahrensburg, SH, Germany) with a pixel size of $3.45 \times 3.45 \mu\text{m}$ was paired with a high-resolution, low distortion lens (FL-BC3518-9M, Ricoh Canada, Missisauga, ON, Canada) with a pixel pitch of 3.45 μm . For three-dimensional digital image tracking purposes, the software package ProAnalyst (Xcitex Inc., Woburn, MA, USA) [18] was procured.

3.2.4 Apparatus Control and Digital Image Collection

A custom controller program was created for synchronized apparatus control and digital image collection. The program was developed with Python 3.10.

To interface with the existing lab data acquisition system (DAQ), the custom controller takes advantage of python dictionaries and the National Instruments NI-DAQmx 0.6 Python library (National Instruments, Austin, TX)[19] for the simultaneous loading of all actuators. It was critical to ensure that forces were applied simultaneously instead of loading each actuator individually, as the intent of this apparatus was to mimic the physiological loading of the shoulder articulation as closely to the *in-vivo* case as was possible. This method for loading of the apparatus made it possible to evaluate the effects of loading on the fixation of shoulder implants without potentially confounding the results by loading each actuator individually.

To facilitate synchronized digital image collection, the Python Balser pypylon 1.8 library (PyPylon, Basler AG, Ahrensburg, SH, Germany)[20] was leveraged. It was essential that the same program be used when applying forces and collecting image data, as this

facilitated the collection of synchronized application/response data, which substantially expedited postprocessing of the results.

Coding of the custom loading software also took advantage of the Tkinter 8.6 python library [21] for the generation of a user interface (UI). Implementing a formal UI added convenience to the process of running an evaluation using the novel loading apparatus. The implementation of a UI also ensured that the controller software could be utilized by others in the laboratory without any coding experience.

3.3 Outcome Variables and Statistical Analysis

3.3.1 Apparatus Design Evaluation

3.3.1.1 Loading Apparatus Evaluation

Once the loading apparatus was fully designed and assembled, it was necessary to evaluate its performance. Therefore, both the implant loading apparatus and the high-resolution digital tracking system were evaluated using the outcome variables relevant to their function. The loading apparatus was evaluated on its mechanical performance during loading. Actuator function was verified using a calibrated load cell (Mini 45, ATI Industrial Automation, NC, USA) at varied loading levels of between 100 N and 350 N in 50 N increments.

3.3.1.2 Digital Tracking System Evaluation

The digital tracking system was evaluated at both a micro and macro scale. This was to determine the performance in the context of both large and small displacements. To determine the accuracy of the digital tracking system at a macro scale, a digital micrometer (Model H-2780, Mitutoyo, Mississauga, ON, Canada) with a resolution of 1.27 μm was utilized. The micrometer was outfitted with a 3D printed calibration fixture, outfitted with a generic 5 mm eyepiece graticule ruler slide, with subdivisions every 0.05 mm (Figure 3-5) was used for calibration.



Figure 3-5: Custom 3D-Printed Calibration Fixture

Custom calibration fixture outfitted with an eyepiece graticule with a 5 mm eyepiece ruler and index values every 5 μm .

For the macro-evaluation, the digital micrometer was opened in regular increments of 25.4 μm for nine increments. After each incrementation, the system was allowed to reach equilibrium for 5 seconds, thereby decreasing the potential for vibration artifact to affect the results. The micrometer was opened for four 3 trials, and then the process was reversed for an additional two trials.

For the micro-evaluation, it was not possible to open the micrometer at sufficiently small regular increments. Therefore, the micrometer was incrementally opened in approximately 5 μm increments, up to an approximate displacement of 20 μm ; after which the same process was reversed until fully closed. After each incrementation, the system was allowed to reach equilibrium for 5 seconds. Three repeated trials were completed with both opening and closing cycles to identify if any hysteresis effects were present in the system.

3.3.1.3 Comparison to Existing Tracking Methods

The digital tracking system was then compared to linear variable differential transformers (LVDTs) in its application to orthopaedic implant tracking. An LVDT (Model 0236-0000, Trans-Tek Incorporated, Ellington, CT, USA) was compared with the digital tracking system to detect and measure the relative motion between metal and bone during the eccentric loading of a stainless-steel implant beam (35.00 mm x 19.02 x 2.32 mm) which was employed as an implant surrogate. A bovine tibial bone was milled to a flat surface to provide a generous trabecular bone bed for testing. The implant beam was positioned on the bovine tibial bone bed and loaded with an incrementally increasing eccentric load of 10 N -160 N on one end. Loads were increased in 10 N increments in a stepwise manner. The relative bone-implant distraction was measured on the opposite end to loading, using both the LVDT and digital tracking systems to measure the motions simultaneously. Differences in bone-implant relative motions were evaluated over five trials via testing at different locations across the cancellous bone surface. Average percent difference between LVDT and digital tracking micromotion measurements were calculated at all loading increments.

3.4 Results

3.4.1 Loading Apparatus Evaluation

The results of the load application system evaluation reflected good loading application performance (Figure 3-6). The average percent difference for all loading levels was 0.7% \pm 0.66% [100 N: -4.29% \pm 1.47%, 150 N: -0.98% \pm 0.87%, 200 N: -0.45% \pm 0.64%, 250

N: $0.16\% \pm 0.30\%$, 300 N: $0.49\% \pm 0.43\%$, 350 N: $0.91\% \pm 0.25\%$] from the intended load, reflecting substantial accuracy in load application.

3.4.2 Digital Tracking System Evaluation

The macro-scale evaluation of the digital tracking system (Figure 3-7) exhibited an average percent difference of 2.18% when compared to the digital micrometer, indicating acceptable accuracy by industry standards. The mean squared error was calculated at 0.14, signifying a considerable level of accuracy. The R^2 value was reported at 0.96, reflecting an excellent fit to the micrometer curve. The precision, measured by the standard deviation of the digital tracking values, was 0.37; indicating that there was a low variation in measurements between trials. No significant hysteresis effects were identified in the system.

The results of the micro digital tracking system evaluation also reflected considerable agreement between the digital system and the digital micrometer (Figure 3-8). Indeed, at the maximum caliper displacement of 0.02 mm, the 1.45% difference in average measurement was resolved into less than 1 micron of difference between the two systems. No significant hysteresis error was identified in the digital system. A coefficient of variation of 0.047 was computed for the percent differences calculated across all separate trials, reflecting acceptable repeatability in the digital system and verification method.

3.4.3 Comparison to Existing Tracking Methods

When comparing the digital system to the industry-accepted method of utilizing linear variable differential transformers, the average micromotion via LVDTs was $158 \pm 65\%$ that of the average micromotion via digital tracking (Figure 3-9). These results were consistent with the values previously reported in the literature [4], [15]. Overall, these results show that the digital system provides a more contextually accurate and repeatable method for the evaluation of fixation in orthopaedic implants than LVDTs.

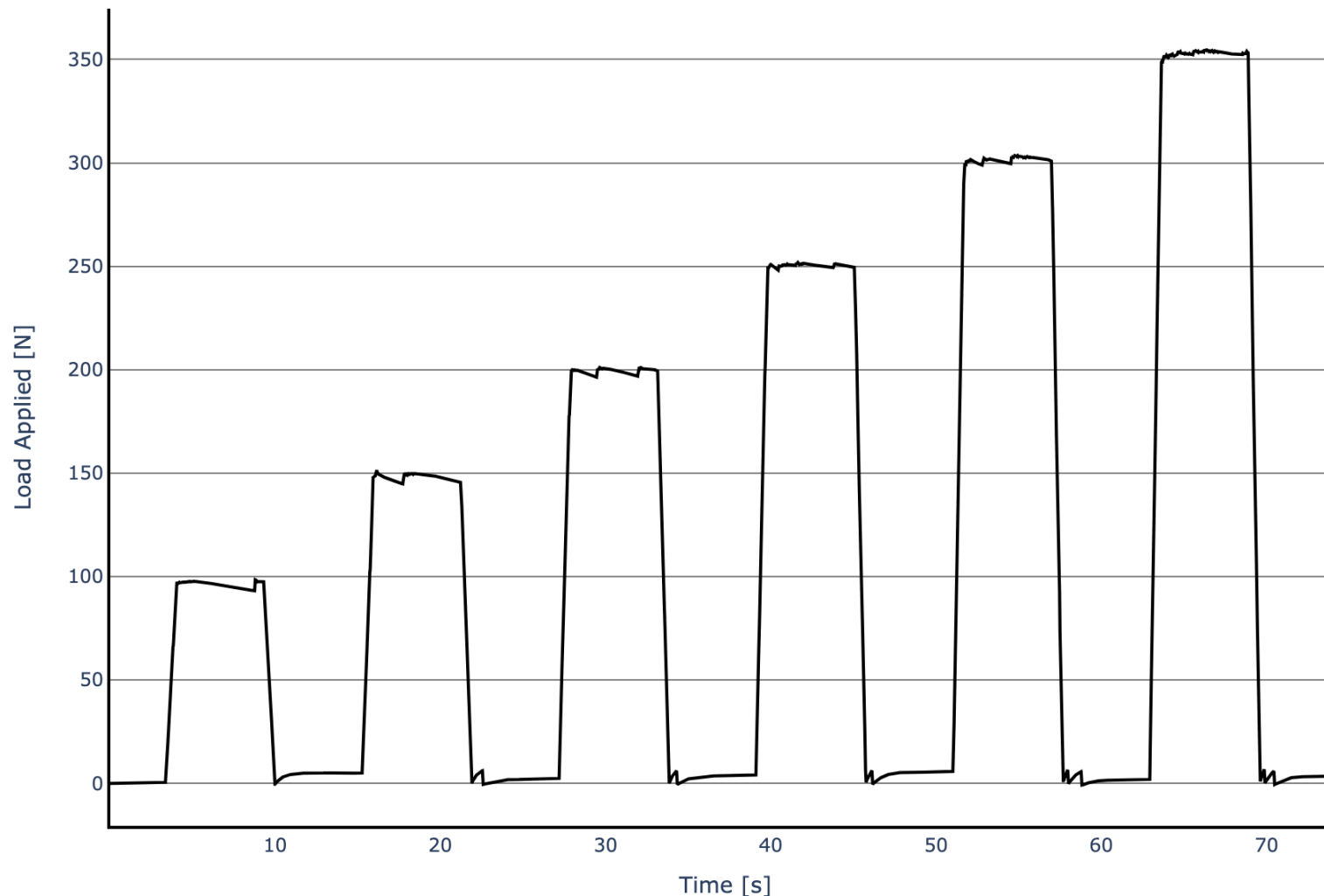


Figure 3-6: Cyclical Loading of a CERBERUS Actuator, Increasing Load from 100 [N] to 350 [N]

Plot of a cyclical loading profile applied by the CERBERUS actuator system, measured using a calibrated load cell.

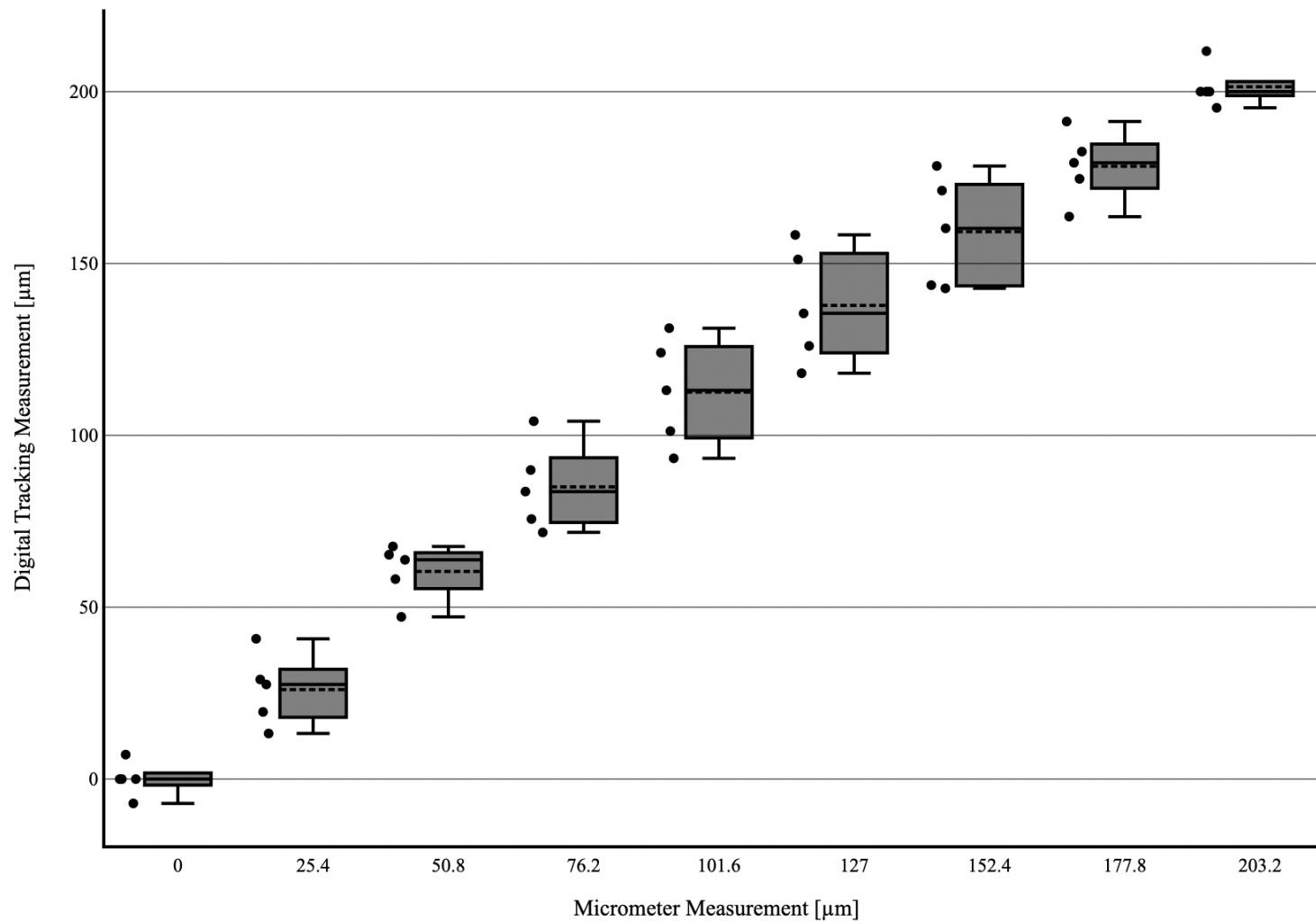


Figure 3-7: Macro Digital Tracking Calibration Curve

Calibration curves range from 0 μm to 203 μm. The test was repeated in increasing and decreasing tests.

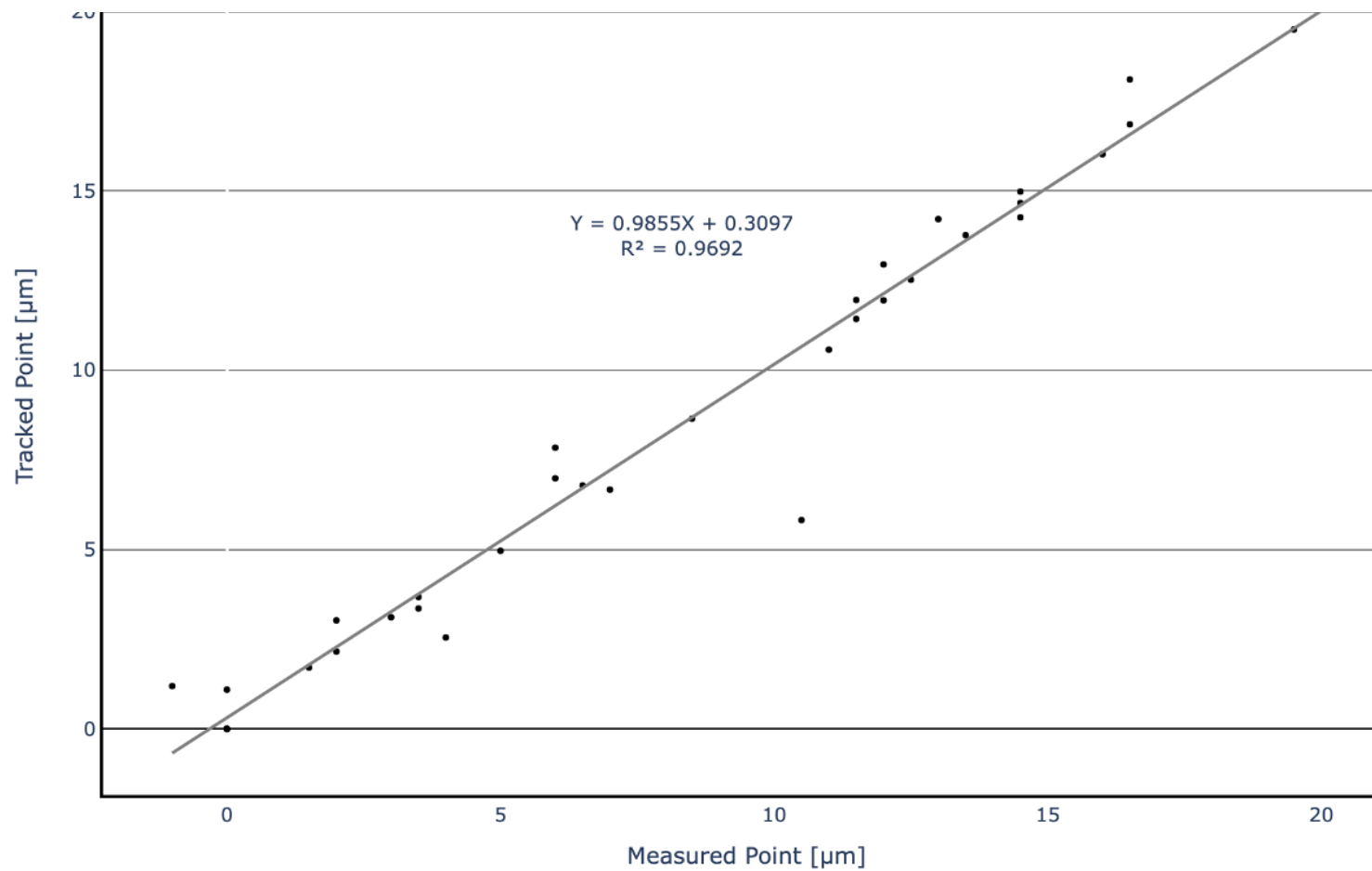


Figure 3-8: Micro Digital Tracking Calibration Curve

Results of the digital tracking system evaluation, reflecting a 1.45% average difference between the caliper and digital tracking system measurements. At the maximum value measured (0.02 mm), the difference in measurements was less than 1 micron.

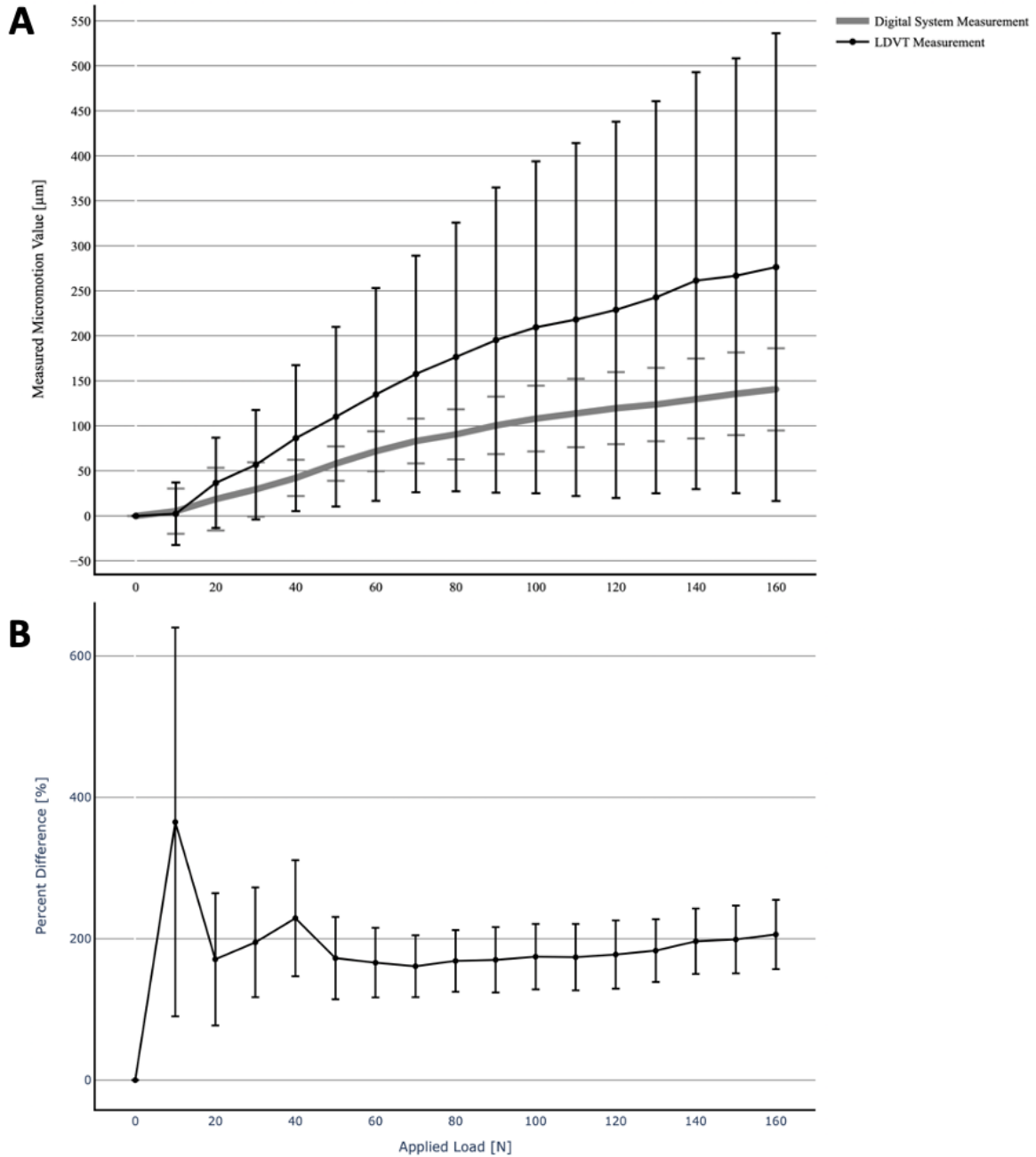


Figure 3-9: Comparison Between LVDT and Digital Tracking Measurements as a Function of Load

Results of comparing the digital tracking system to the LVDT tracking method. The first plot indicates the system measurements recorded, and the second shows the percent difference between the two systems. On average, LVDT measurements were $194\% \pm 69\%$ that of the average micromotion calculated using digital tracking methods.

3.5 Discussion

Previously developed *in-vitro* shoulder loading devices have utilized non-physiological, idealized, forces during the evaluation of shoulder prosthetic designs. However, in many cases, these devices are unable to provide thorough insight into the effectiveness of novel implant designs due to their inability to simulate real-world loading conditions. Additionally, these experimental approaches have frequently utilized linear variable differential transformers or other linear displacement measuring devices which have been shown to overreport bone-implant relative motion. The simulator described above was intended to address these limitations by providing a method by which clinically relevant forces might be imposed at the shoulder articulation in a controlled environment, and by which micromotion could be evaluated using digital methods. By achieving these goals, data produced in the future will be able to investigate implant performance more thoroughly, thereby providing a more informed insight into the biomechanical factors affecting implant performance.

The novel implant loading system described above was intended to be an improvement on the technology currently used for the evaluation of the primary fixation of orthopaedic implants. This apparatus interfaces with the lab's existing data acquisition system (DAQ) when applying three-dimensional loads simultaneously, all while avoiding interfering with the capture of high-resolution imaging data. The systems developed above were designed to improve upon these forementioned goals; however, it was necessary to validate the design of the apparatus and measuring system in terms of their ability to achieve their purpose.

The effect of the loading system was first assessed, and it was found to meet the design requirements as indicated. The control system implemented was able to interface with the lab's existing DAQ system and was able to apply three-dimensional loads simultaneously while collecting synchronized digital imaging data. For the digital tracking system, both goals of meeting the industry standard of $5\mu\text{m}$ for accuracy and improving upon the existing methods of measuring bone-implant relative motion were achieved. These results

suggested that this apparatus would meet all the design requirements outlined and is therefore likely to improve the validity of biomechanical assessments focused on the primary fixation of shoulder implants.

3.6 Conclusion

The replication of physiological loading profiles is important in the evaluation of implant performance. Similarly important is the accurate measurement of implant responses to those physiological loads. This chapter focused on the design and development of a novel triaxial loading simulator and paired data acquisition system capable of synchronously applying loads and collecting high-resolution digital image data. The goal of this design was to represent an improvement to the legacy loading protocols and micromotion measurement systems currently leveraged in the orthopaedics design industry. The testing device's design, described herein, was evaluated for its load application capabilities, and the paired digital tracking system was thoroughly compared to the established traditional technologies commonly used. The findings of this work confirm the successful design and implementation of the novel system, effective in the application of loads in three-dimensions, as well as the efficacious implementation of high-resolution digital tracking methods for the evaluation of implant distractive micromotion. Although not the main focus of the CERBERUS apparatus development, this device could be used equally for investigations at the elbow, wrist, hip, knee, or other joints with similar implant fixation approaches.

3.7 References

- [1] G. D. Langohr, “Fundamentals of the Biomechanical Characteristics Related to the Loading of Reverse Total Shoulder Arthroplasty Implants and the Development of a Wear Simulation Strategy,” 2015. [Online]. Available: https://ir.lib.uwo.ca/etd/3436/?utm_source=ir.lib.uwo.ca%2Fetd%2F3436&utm_medium=PDF&utm_campaign=PDFCoverPages
- [2] T. Millett, Peter J;van der Meijden, Olivier A.J.; Gaskill, “Surgical Anatomy of the Shoulder,” *Instructional Course Lectures*, 2012. <https://link-gale-com.proxy1.lib.uwo.ca/apps/doc/A453291476/AONE?u=lond95336&sid=AONE&xid=3ed1353e> (accessed Nov. 09, 2019).
- [3] J. W. Giles, “Development of an In-Vitro Passive and Active Motion Simulator for the Investigation of Shoulder Function and Kinematics,” University of Western Ontario, 2014.
- [4] P. Favre *et al.*, “In vitro initial stability of a stemless humeral implant,” *Clin. Biomech.*, vol. 32, pp. 113–117, 2016, doi: 10.1016/j.clinbiomech.2015.12.004.
- [5] N. J. Stroud *et al.*, “Initial glenoid fixation using two different reverse shoulder designs with an equivalent center of rotation in a low-density and high-density bone substitute,” *J. Shoulder Elb. Surg.*, vol. 22, no. 11, pp. 1573–1579, 2013, doi: 10.1016/j.jse.2013.01.037.
- [6] E. J. Martin, T. R. Duquin, and M. T. Ehrensberger, “Reverse total shoulder glenoid baseplate stability with superior glenoid bone loss,” *J. Shoulder Elb. Surg.*, vol. 26, no. 10, pp. 1748–1755, 2017, doi: 10.1016/j.jse.2017.04.020.
- [7] S. W. Chae, S. Y. Kim, H. Lee, J. R. Yon, J. Lee, and S. H. Han, “Effect of baseplate size on primary glenoid stability and impingement-free range of motion in reverse shoulder arthroplasty,” *BMC Musculoskelet. Disord.*, vol. 15, no. 1, pp. 1–7, 2014, doi: 10.1186/1471-2474-15-417.
- [8] J. K. Anderson, “Glenoid Baseplate Micromotion in Reverse Total Shoulder Arthroplasty,” Clemson, 2016. [Online]. Available: https://pdfs.semanticscholar.org/ffaf/5961a40283d75e1ffb96a0fbb6758e53cfb0.pdf?_ga=2.67772441.942403469.1591136784-737171972.1591136784

- [9] R. E. Chen, E. Knapp, B. Qiu, A. Miniaci, H. A. Awad, and I. Voloshin, “Biomechanical comparison of stemless humeral components in total shoulder arthroplasty,” *Semin. Arthroplast. JSES*, pp. 1–9, 2021, doi: 10.1053/j.sart.2021.08.003.
- [10] C. Quental, J. Folgado, M. Comenda, J. Monteiro, and M. Sarmento, “Primary stability analysis of stemless shoulder implants,” *Med. Eng. Phys.*, vol. 81, pp. 22–29, 2020, doi: 10.1016/j.medengphy.2020.04.009.
- [11] P. Favre and A. D. Henderson, “Prediction of stemless humeral implant micromotion during upper limb activities,” *Clin. Biomech.*, vol. 36, pp. 46–51, 2016, doi: 10.1016/j.clinbiomech.2016.05.003.
- [12] ASTM, “ASTM F2028-17 Standard Test Methods for Dynamic Evaluation of Glenoid Loosening or Disassociation,” pp. 1–15, 2018, doi: 10.1520/F2028-17.Copyright.
- [13] P. Damm and J. Dymke, “Orthoload Database,” *Julius Wolff Institute*, 2021. <https://orthoload.com/database/> (accessed Jul. 26, 2021).
- [14] C. Tavares, “Development of a two-axis cyclic loading device for mechanical testing of glenoid component fixation,” University of Western Ontario, 2022.
- [15] P. Favre *et al.*, “In vitro assessments of reverse glenoid stability using displacement gages are misleading - Recommendations for accurate measurements of interface micromotion,” *Clin. Biomech.*, vol. 26, no. 9, pp. 917–922, 2011, doi: 10.1016/j.clinbiomech.2011.05.002.
- [16] N. T. Formaini, N. G. Everding, J. C. Levy, B. G. Santoni, A. N. Nayak, and C. Wilson, “Glenoid baseplate fixation using hybrid configurations of locked and unlocked peripheral screws,” *J. Orthop. Traumatol.*, vol. 18, no. 3, pp. 221–228, 2017, doi: 10.1007/s10195-016-0438-3.
- [17] A. R. Hopkins, U. N. Hansen, A. M. J. Bull, R. Emery, and A. A. Amis, “Fixation of the reversed shoulder prosthesis,” *J. Shoulder Elb. Surg.*, vol. 17, no. 6, pp. 974–980, 2008, doi: 10.1016/j.jse.2008.04.012.
- [18] Xcitex, “ProAnalyst Motion Analysis Software,” *ProAnalyst User Guides*, vol. 13. 2020.
- [19] National Instruments, “NI-DAQmx,” 2022.

- [20] Basler, “pypylon,” 2022. <https://github.com/basler/pypylon> (accessed Jan. 09, 2023).
- [21] L. Fredrik, “An Introduction to Tkinter,” 1999, [Online]. Available: www.pythonware.com/library/tkinter/introduction/index.htm

Chapter 4

4 An Assessment of Cadaveric vs Synthetic Cancellous Bone Models for the Quantification of Normal Micromotion using Press-Fit as a Clinical Variable

OVERVIEW

As press-fit prosthetics become more popular, the benchtop testing of these humeral component designs has also increased. This necessary measure is important to the ongoing optimization of humeral prosthetics, however, the commonly utilized methods of evaluating time-zero fixation have not been thoroughly evaluated; particularly in stemless humeral prostheses. This distinct paucity to the degree of insight into the effectiveness of testing protocol is certainly a limit to ongoing implant development, as optimization approaches will always be driven by the accuracy of the data utilized for design guidance. Currently, many works evaluating the performance of press-fit implants have utilized the ASTM-F2028 standard testing methodology for the dynamic evaluation of glenoid loosening or disassociation, as well as the ASTM F2839 standard specification for the use of rigid polyurethane foam as a bone substitute during the testing of orthopaedic devices and instruments. However, there is insufficient evidence that the use of bone substitute materials is effective in truly replicating the fixation behaviour of implants in trabecular bone. The following chapter aims to compare the performance of stemless prostheses in animal tissue and in commonly utilized foam surrogate materials to determine the appropriateness of utilizing bone analogues for the evaluation of primary fixation.

4.1 Introduction

The evaluation of fixation in orthopedic devices is an essential step in the ongoing development and optimization of osseointegrated implants. However, not many stemless humeral component design variables have been thoroughly evaluated. Fundamental understanding of geometry variations and implantation design choices are extremely relevant to the development of high-performance implants, and it is therefore vital to meticulously determine the effect of each design choice on implant performance. Likewise, it is essential to evaluate the efficacy of the evaluation protocols chosen for the quantification of implant performance, as test design errors can severely diminish the applicability of the conclusions taken from implant design studies.

Existing evaluations of shoulder prostheses have commonly utilized polyurethane foam bone substitutes as surrogates for biological bone specimens [1]–[5]; however, works have noted that the material properties of bone substitute materials, although similar in failure stress, may not exhibit similar energy dissipation properties to harvested bone [6]. Indeed, the ASTM F1839 Standard Specification for Rigid Polyurethane Foam for Use as a Standard Material for Testing Orthopaedic Devices and Instruments [7] indicates that the original purpose of the standard was to provide a uniform and consistent material as a testing medium for medical bone screw pullout, however, the ASTM F2028 Standard Test Methods for Dynamic Evaluation of Glenoid Loosening or Disassociation [8], perhaps injudiciously, calls for the use of these foam surrogate materials when performing micromotion testing. This erroneous reference to the ASTM F1839 standard has, in part, resulted in the common use of polyurethane bone in lieu of cadaveric or animal testing; a practice which may not lead to an accurate understanding of implant performance.

Press-fit, or interference fit, is a bone-implant configuration where the bone cavity is slightly smaller than the implant by design. This design choice is particularly relevant to the choice of foundation substrate, as the implantation procedure of a press-fit implant is dependent on both the elastic and failure properties of the implant and bone materials. When an implant has surface roughness, this press-fit imposes a residual contact pressure which, in turn, creates frictional forces which hold the implant in place. Accordingly, it

stands to reason that increasing press-fit design would influence immediate postoperative implant fixation and early stage effective osseointegration. Indeed, previous evaluations have found that increasing the magnitude of the interference fit also increases the primary fixation of stemmed implants [9], however, no literature is currently available on the effect of press-fit magnitude in stemless humeral components.

This present investigation, therefore, was intended to compare the results of fixation analyses using biological vs synthetic bone models while using the effects of press-fit in stemless implants and resultant micromotion as a metric for degree of fixation.

4.2 Methods

Eight porcine tibial specimens were potted and milled to a flat surface using a mini milling/drilling machine (KC-15VS, King Canada, Dorval, QC, Canada), before a $\varnothing 20$ mm blind hole was drilled to a depth of 10 mm in the centre of the exposed trabecular bone bed. Each prepared specimen was scanned using Computed tomography and imported into Mimics v23.0 (Materialise, Leuven, Belgium). A 3D model of each prepared porcine specimen was developed, and the bone mineral density (BMD)/Young's modulus plot of each specimen was created (Figure 4-1) using cortical bone surrogate (SB3 model 450; GAMMEX, Middleton, WI, USA) and distilled water phantoms. All Young's moduli were computed using the Morgan *et al.* bone density-elasticity relationship [10]. It was found that the moduli of the bone segments adjacent to the implant surface ranged from 169 MPa to 260 MPa.

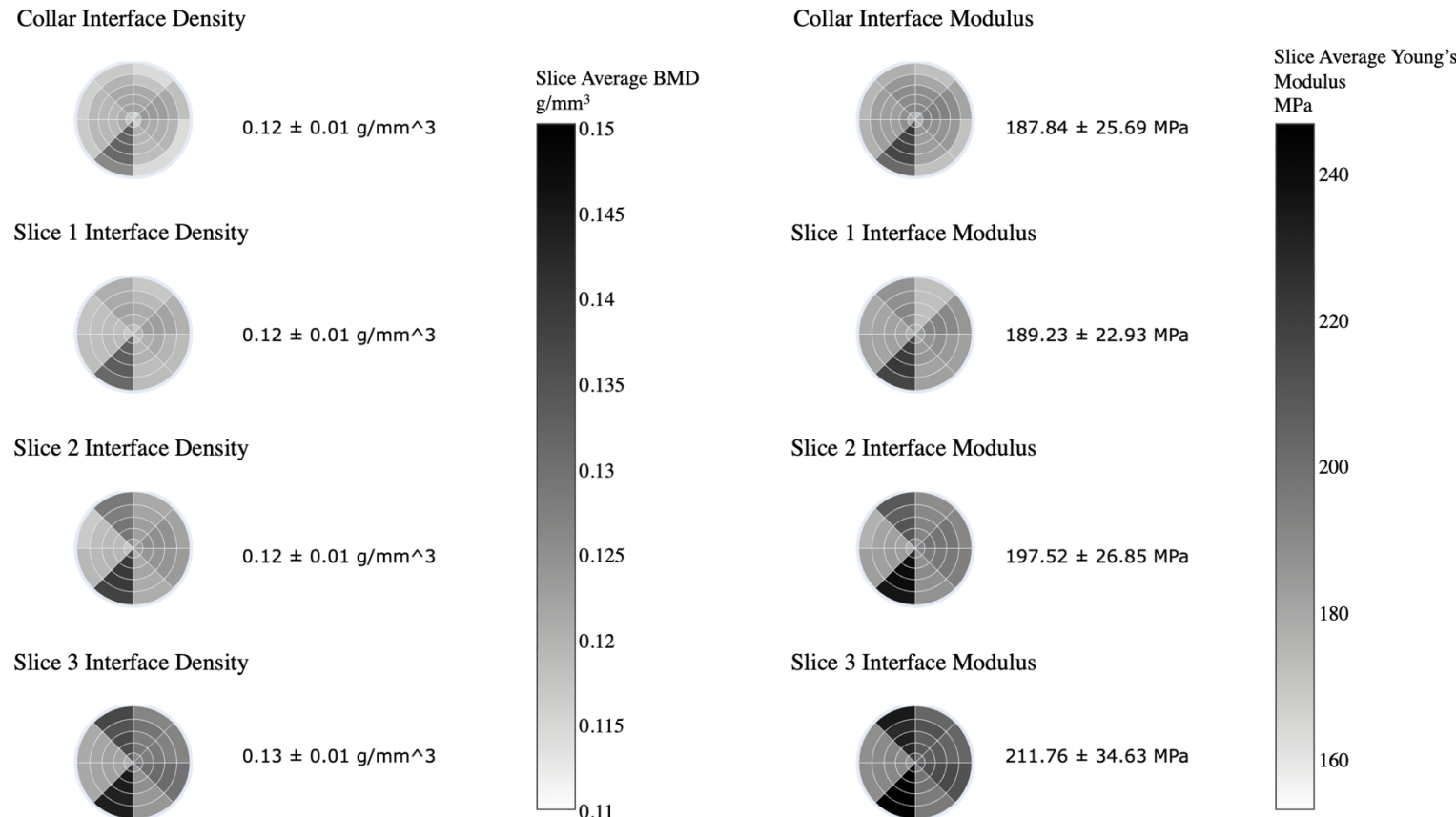


Figure 4-1: BMD and Young's Modulus of Bone Slices at Interface

Bone mineral density (BMD) and Young's Modulus heatmaps showing variation as the sample slice moves from the resection surface (Collar Interface) to the stem tip (Slice 3 Interface), and as the position of the sample moves from the centre of the bone bed to the cortex. Due to the porcine fibula specimen geometries used, the collar interface was most proximal (farthest from the talocrural joint articulation (TJA)), whereas the Slice 3 Interface was most distal (closest to the TJA). Each polar heatmap shows eight specimens.

Three rigid polyurethane foam blocks of varying densities (15 PCF, 20 PCF, 25 PCF) (Sawbones® Rigid Cellular Foam; Pacific Research Laboratories, Vashon, WA, USA) were drilled in three places to a depth of 10 mm at regular intervals. The specimens procured had nominal densities of 0.24 g/cm^3 , 0.32 g/cm^3 , and 0.40 g/cm^3 , respectively, with corresponding nominal compressive moduli of 173 MPa, 284 MPa, and 399 MPa; similar to that of the forementioned porcine specimens and those utilized in previous biomechanical works [1], [2], [11]–[13].

A generic simplified humeral implant was created using the parametric design software CadQuery [96]. This generic design (collar radius: 15 mm, collar thickness: 4 mm, barrel radius: 10 mm, barrel thickness: 10 mm) was regenerated at varied diametral press fits (0.175 mm, 0.35 mm, 0.525 mm, 0.70 mm, and 0.875 mm) on the barrel component. The generic implant was fabricated from 312 Stainless Steel with a dull surface polish (Figure 4-2).

The CERBERUS apparatus, as presented in Chapter 3, was utilized to apply a cyclical load of 150 N at an angle of 45 degrees eccentric to the resection surface for 60 cycles. Implant-bone distractive micromotion was measured using a single optical machine vision USB3 camera (acA4096-30uc, Basler AG, Ahrensburg, SH, Germany), outfitted with a c-mount premium lens (FL-BC3518-9M, Ricoh, Tokyo, Kanto, Japan) (resultant pixel size of $3.45 \mu\text{m}$). The camera was focused on the implant-bone interface with tracking points positioned on the implant and bone surfaces (Figure 4-3). Bone-implant distractive micromotion was calculated from the collected high-resolution digital images using ProAnalyst (Xcitex Inc., Woburn, MA, USA).

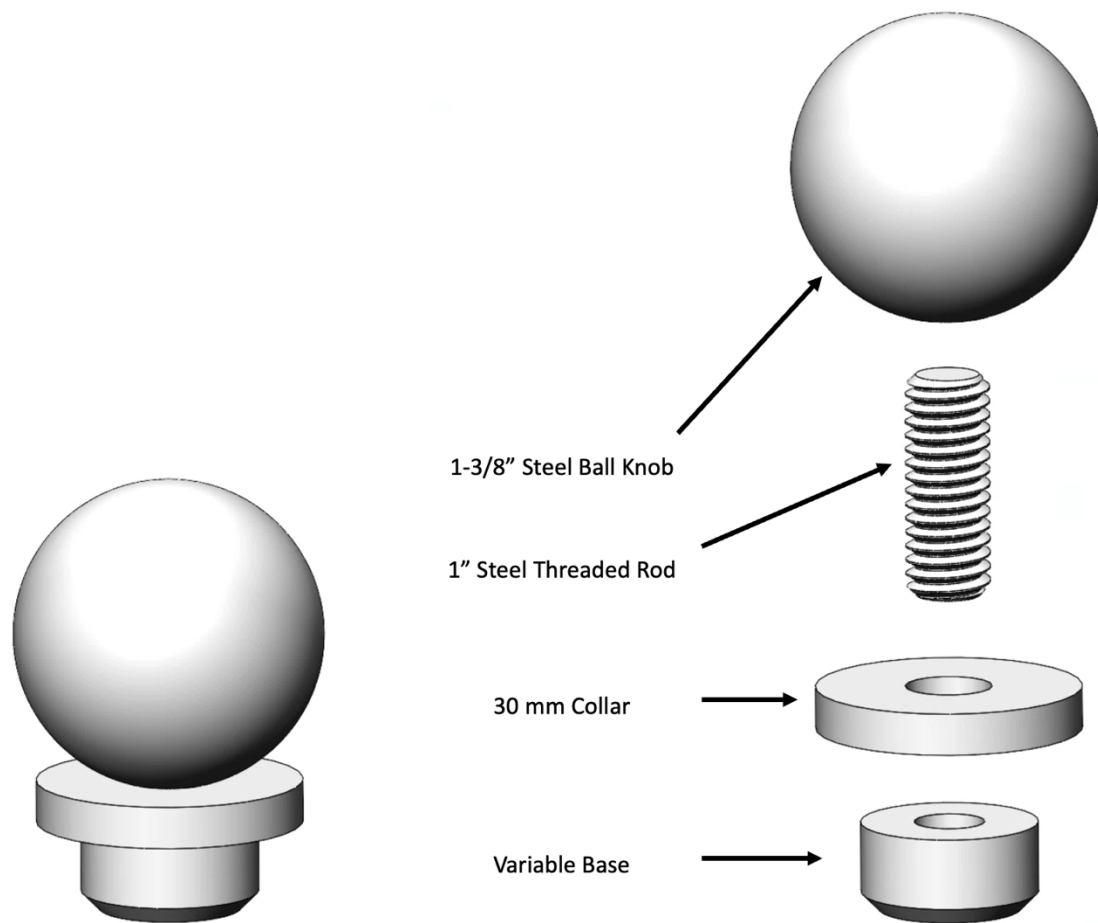


Figure 4-2: Modular Generic Press-Fit Implant

A modular design of generic press-fit implant, with a variable base size, was utilized for the experimental evaluation of effect of press-fit.

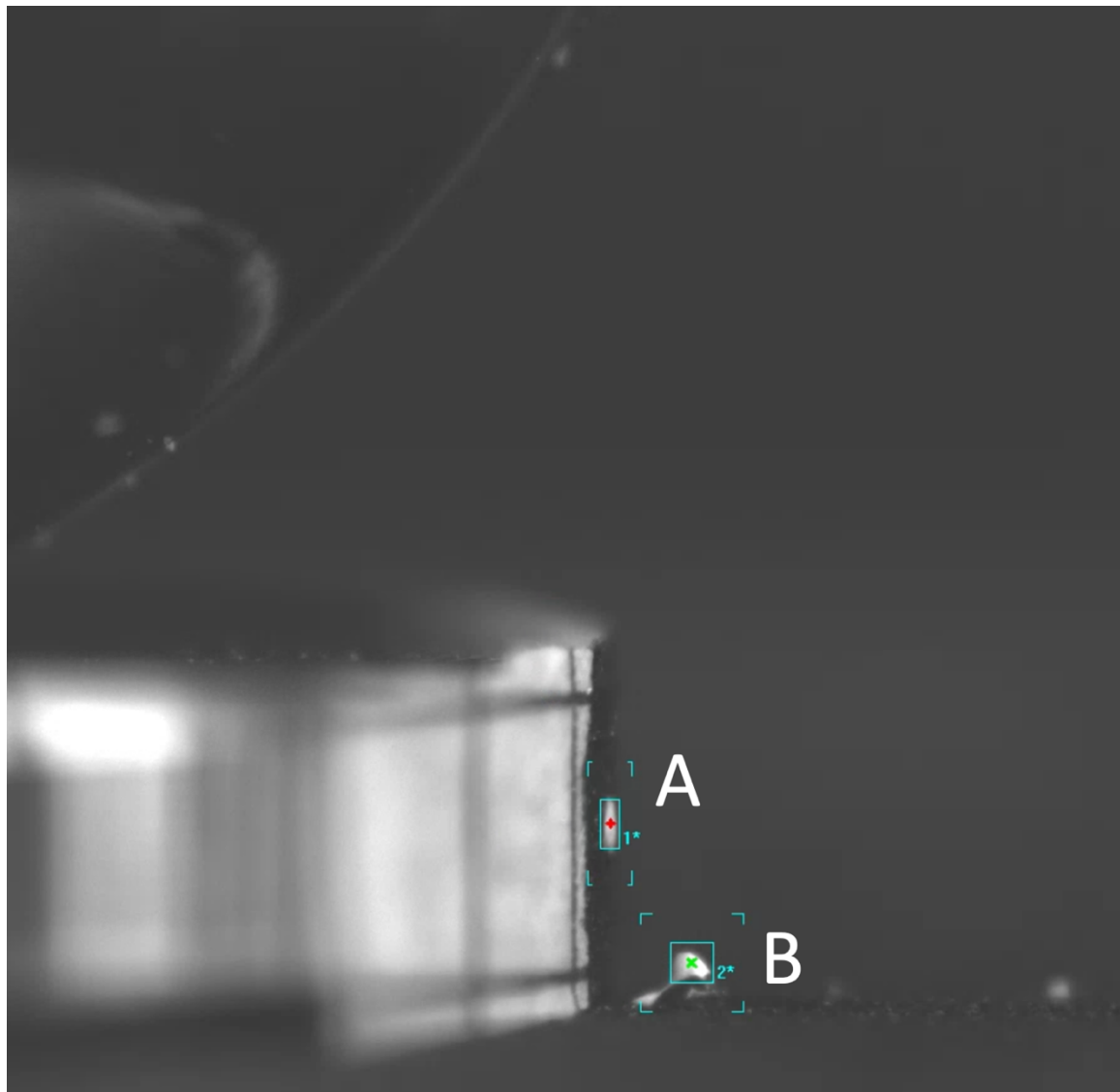


Figure 4-3: High Resolution Digital Image Tracking

A high-resolution image of the implant-bone interface opposite to the direction of loading. White markings on the implant (A) and bone (B) serve as tracking points during quantification of micromotion.

4.3 Outcome Variables and Analysis

Fixation of the generic stemless implant was evaluated as the maximum bone-implant distraction detected during the cyclical loading protocol. Micromotions were calculated while the implant was unloaded, in order to remove the confounding variable of elastic deformation. Initially, a one-way repeated measures analysis of variance (ANOVA) was conducted on the dependent variable of diametral press-fit magnitude in the porcine specimens. Second, a two-way ANOVA was conducted to determine the effect of PCF and press-fit magnitude on the foam specimens. Lastly, t-tests were conducted to compare each press-fit/PCF pairing to the collected data of the porcine specimens. All statistical analyses were computed using SciPy 1.9.1 [14] with a significance set at $P < 0.05$. A Bonferroni correction with an adjusted alpha level of 0.025 (0.05/2) per test was utilized for the two-way ANOVA test.

4.4 Results

Diametral press-fit magnitude was identified to have a significant effect on fixation in the porcine specimens ($p < 0.01$). Foam density and diametral press-fit magnitude also had a significant effect on fixation in the foam analogue specimens ($p < 0.01$, $p < 0.01$)(Figure 4-4).

It was found that the 15 PCF foam analogue differed the most when compared to the porcine specimens at sliding fit conditions ($66.8 \mu\text{m} \pm 8.9 \mu\text{m}$ vs $36.2 \mu\text{m} \pm 9.4 \mu\text{m}$) $(p = 0.02)$. However, at sliding fit conditions, there was no significant difference in the micromotions detected in the 20 PCF and 25 PCF foam analogues when compared to the animal model. These comparative relationships were not constant at higher magnitudes of press fit. Conversely, at press fit magnitudes greater than 0.525 mm, the 15 PCF foam blocks reflected more consistent fixation with the porcine specimens, whereas the 20 PCF and 25 PCF foam blocks exhibited significantly lower micromotion magnitudes than the porcine specimens under the same press-fit conditions (20 PCF: [0.7 mm: $p = 0.021$, 0.875 mm: $p = 0.026$], 25 PCF: [0.7 mm: $p = 0.043$, 0.875 mm: $p = 0.046$]).

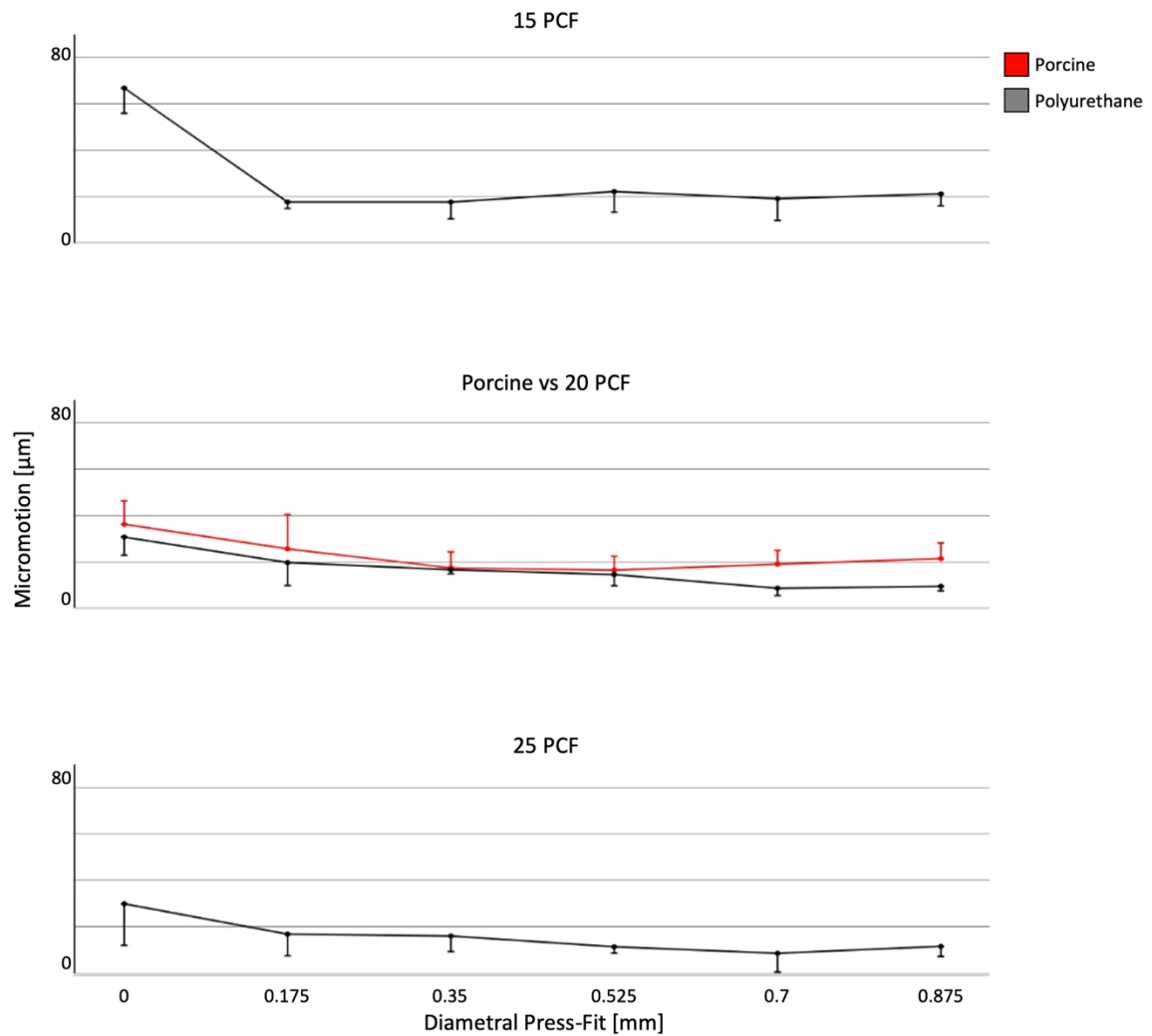


Figure 4-4: Porcine vs Polyurethane Foam Micromotion

Micromotion developed in porcine bone samples (red) vs polyurethane foam (grey) analogue blocks during cyclic eccentric loading. For discussion, the porcine bone specimens are overlayed on the 20 PCF foam press fit vs micromotion plot.

4.5 Discussion

The two objectives of this work were to (1) identify if bone surrogate models could accurately replicate the fixation behaviour of bone tissue samples when evaluating press-fit implants, and to (2) assess the influence of press-fit magnitude in stemless uncemented implants. We specifically hypothesized that (1) foam analogue materials would not appropriately reflect the fixation behaviour of press-fit implants, and that (2) increasing press-fit would elicit a more favourable level of implant stability than lower diametral press-fits.

Our results identified inconsistencies in the results obtained while using foam analogue materials when comparing implant primary fixation to the animal model. Lower PCF foams overreported implant micromotion at sliding fits, whereas higher PCF foams underreported implant micromotion at larger diametral press-fit magnitudes. We postulate that this is due to different failure thresholds in cancellous bone vs rigid cellular polyurethane foam, as it has been previously been proposed that the presence of lubricating bone debris, left behind after the implant insertion, may reduce the level of primary implant fixation [15]. As rigid polyurethane foam porosities are produced through a gaseous method, they would not experience the same micro-strut failure mechanism as cancellous bone – likely causing the fixation differences at larger press-fit magnitudes. This behavior is hypothesized to be exacerbated in highly porous implants, which are likely to produce more bone tissue fragments during insertion [15].

The fixation of press-fit implants in bone specimens were nonlinear with increasing press-fit magnitude. As diametral press-fit increased, the porcine specimen fixation achieved a maximum threshold at 0.35 mm press-fit, before gradually decreasing as a larger amount of bone fragmentation occurred. Most clinically available press-fit implants are not purely cylindrical and regularly have porous surfaces commensurate with bony ingrowth [16], however, it is not unreasonable to posit that most press-fit implant will reflect a similar behaviour, where a maximum threshold of press-fit will be present before fixation begins to be compromised and fixation in bone tissue diverges from fixation in bone surrogate

materials. This suggests that, at minimum, the viability of utilizing polyurethane bone surrogates should be evaluated on an implant-to-implant basis to determine if the differing micro-failure mechanism will introduce a confound to the experimental protocol.

There are several limitations present with this present work. Primarily, a generic stemless design without notable surface roughness was utilized; disparate with clinically available stemless implants which exhibit more complex geometries and intentionally roughened surfaces. This may lessen the clinical significance of these findings. As noted, future investigations should continue to assess different implant designs that correspond with clinically relevant implant designs. Another possible limitation of this work is the small porcine sample size utilized. Due to the limited variability in the bone densities of the sample set, we were not able to infer the effect of bone density on fixation. This would be a good topic for future work. However, the use of 8 specimens is higher than typically employed for studies of this nature on implant-bone fixation analyses. This evaluation was also focused on time-zero fixation, and the results of this work may not be applicable to implants after sufficient osseointegration has occurred.

Strengths of this work include the repeated measures design when evaluating the influence of press-fit in porcine specimens. This produced greater statistical power during the comparative study. Additionally, the standard deviations recorded in the foam analogue blocks were low ($\pm 7 \mu\text{m}$ on average) when compared to the industry standard accuracy of $\pm 5 \mu\text{m}$, which was expected due to the homogeneity of the foam analogue blocks. This reflects good performance from the novel CERBERUS loading apparatus.

4.6 Conclusion

Although bone substitutes may exhibit similar nameplate material properties to cancellous bone, the conclusions derived from fixation studies utilizing polyurethane foam analogue materials may be inconsistent to those using harvested bone when evaluating press-fit orthopaedic implants. Additionally, implant press fit is a modifiable parameter that has a significant effect on time zero implant stability. Although increasing press fit from a sliding fit is likely to increase implant fixation, there appears to be a limit of press-fit magnitude

before the residual bone material damaged during the installation procedure begins to impede implant fixation. It is therefore suggested that (1) press-fit magnitude be carefully considered during the design of novel orthopaedic prostheses as not to over-damage periprosthetic bone tissue, and (2) that animal or cadaveric bone tissue be utilized whenever possible for the comparative evaluation of implant design when comparing press-fit orthopaedic implants, as the added confound of analogue bone material may be a source of erroneous conclusion in press-fit implant design studies.

4.7 References

- [1] D. R. Suárez, W. Nerkens, E. R. Valstar, P. M. Rozing, and F. van Keulen, “Interface micromotions increase with less-conforming cementless glenoid components,” *J. Shoulder Elb. Surg.*, vol. 21, no. 4, pp. 474–482, 2012, doi: 10.1016/j.jse.2011.03.008.
- [2] E. J. Martin, T. R. Duquin, and M. T. Ehrensberger, “Reverse total shoulder glenoid baseplate stability with superior glenoid bone loss,” *J. Shoulder Elb. Surg.*, vol. 26, no. 10, pp. 1748–1755, 2017, doi: 10.1016/j.jse.2017.04.020.
- [3] N. T. Formaini *et al.*, “The effect of glenoid bone loss on reverse shoulder arthroplasty baseplate fixation,” *J. Shoulder Elb. Surg.*, vol. 24, no. 11, pp. e312–e319, 2015, doi: 10.1016/j.jse.2015.05.045.
- [4] M. W. Hast, M. Chin, E. C. Schmidt, and A. F. Kuntz, “Central screw use delays implant dislodgement in osteopenic bone but not synthetic surrogates: A comparison of reverse total shoulder models,” *J. Biomech.*, vol. 93, pp. 11–17, 2019, doi: 10.1016/j.jbiomech.2019.06.004.
- [5] C. Tavares, “Development of a two-axis cyclic loading device for mechanical testing of glenoid component fixation,” University of Western Ontario, 2022.
- [6] P. S. D. Patel, D. E. T. Shepherd, and D. W. L. Hukins, “Compressive properties of commercially available polyurethane foams as mechanical models for osteoporotic human cancellous bone,” *BMC Musculoskelet. Disord.*, vol. 9, pp. 5–11, 2008, doi: 10.1186/1471-2474-9-137.
- [7] ASTM, “F1839 - 97: Standard Specification for Rigid Polyurethane Foam for use as a Standard Material for Testing Orthopaedic Devices and Instruments,” *ASTM B. Stand.*, vol. 13.01, no. October, pp. 6–11, 2014, doi: 10.1520/F1839-08R12.Copyright.
- [8] ASTM, “ASTM F2028-17 Standard Test Methods for Dynamic Evaluation of Glenoid Loosening or Disassociation,” pp. 1–15, 2018, doi: 10.1520/F2028-17.Copyright.
- [9] M. R. Abdul-Kadir, U. Hansen, R. Klabunde, D. Lucas, and A. Amis, “Finite element modelling of primary hip stem stability: The effect of interference fit,” *J.*

- Biomech.*, vol. 41, no. 3, pp. 587–594, 2008, doi: 10.1016/j.jbiomech.2007.10.009.
- [10] E. F. Morgan, H. H. Bayraktar, and T. M. Keaveny, “Trabecular bone modulus-density relationships depend on anatomic site,” *J. Biomech.*, vol. 36, no. 7, pp. 897–904, 2003, doi: 10.1016/S0021-9290(03)00071-X.
 - [11] M. Königshausen *et al.*, “Bone grafting in oblique versus prepared rectangular uncontained glenoid defects in reversed shoulder arthroplasty. A biomechanical comparison,” *Clin. Biomech.*, vol. 50, no. June, pp. 7–15, 2017, doi: 10.1016/j.clinbiomech.2017.09.011.
 - [12] N. T. Formaini, N. G. Everding, J. C. Levy, B. G. Santoni, A. N. Nayak, and C. Wilson, “Glenoid baseplate fixation using hybrid configurations of locked and unlocked peripheral screws,” *J. Orthop. Traumatol.*, vol. 18, no. 3, pp. 221–228, 2017, doi: 10.1007/s10195-016-0438-3.
 - [13] T. S. Lung, D. Cruickshank, H. J. Grant, M. J. Rainbow, T. J. Bryant, and R. T. Bicknell, “Factors contributing to glenoid baseplate micromotion in reverse shoulder arthroplasty: a biomechanical study,” *J. Shoulder Elb. Surg.*, vol. 28, no. 4, pp. 648–653, 2019, doi: 10.1016/j.jse.2018.09.012.
 - [14] P. Virtanen *et al.*, “SciPy 1.0: fundamental algorithms for scientific computing in Python,” *Nat. Methods*, vol. 17, no. 3, pp. 261–272, 2020, doi: 10.1038/s41592-019-0686-2.
 - [15] X. Gao, M. Fraulob, and G. Haïat, “Biomechanical behaviours of the bone-implant interface: A review,” *J. R. Soc. Interface*, vol. 16, no. 156, 2019, doi: 10.1098/rsif.2019.0259.
 - [16] H. J. Rønold and J. E. Ellingsen, “The use of a coin shaped implant for direct in situ measurement of attachment strength for osseointegrating biomaterial surfaces,” *Biomaterials*, vol. 23, no. 10, pp. 2201–2209, 2002, doi: 10.1016/S0142-9612(01)00353-2.

Chapter 5

5 Stemless Reverse Shoulder Arthroplasty Neck-Shaft Angle Influences Humeral Component Time-Zero Fixation and Survivorship: A Cadaveric Biomechanical Assessment

OVERVIEW

This work has now been published in the Journal of Shoulder and Elbow Surgery - International. Additionally, components of this work have been presented at the International Society for Technology in Arthroplasty, the Canadian Operational Research Society, and the Canadian Orthopaedic Association Annual Conferences.

Although the evaluation of implant design variables such as press fit, stem length, or fixation method is essential to the ongoing development of novel prostheses, the influence of implant positioning is just as important to the performance of said implants. Particularly in the context of primary fixation, there remains little to no information on the effects of surgical implantation decision. When installing a humeral prosthesis, surgeons must decide on such implantation variables as lateralization, version, and inclination (referred to as neck shaft angle). This study focused on the surgical implantation variable of neck shaft angle, and its effect on primary fixation and survivorship of stemless reversed humeral implants.

5.1 Introduction

(Much of this background was addressed in Chapter 1. The literature discussed in this introduction remains consistent with the content of the submitted manuscript.)

In recent years, stemless reverse shoulder arthroplasty (RSA) humeral prostheses have been introduced to preserve healthy bone stock, to minimize periprosthetic humeral fractures, and to simplify future revision surgeries [1], [2]. Additionally, these shorter humeral implants have been shown to better-mimic the natural force-transmission properties of the shoulder joint, thereby reducing risk of stress shielding in periprosthetic bone [3]. However, stemless humeral implants rely primarily on metaphyseal bone press-fit for stability and fixation and are therefore vulnerable to poor initial fixation or loosening depending on implantation and/or metaphyseal bone properties and morphology [1], which often may be compromised by disuse osteopenia or osteoporosis [4].

Surgeons must decide on the surgical variable of resection inclination (or neck shaft angle) of the humeral head. Currently, most standard RSA systems vary the neck shaft angle (NSA) between 135° and 155°. Previously, it has been reported that decreasing NSA may reduce the risk of scapular notching [5] and may increase total impingement-free range of motion [5]. With respect to implant fixation, a recent computational finite element study reported that decreasing NSA may also significantly decrease the initial fixation of stemless RSA humeral components, potentially leading to increased incidence of premature failure in these implants [4]. This was commensurate to the results of a previous retrospective clinical study, which found that in a small series RSA humeral component loosening was more prevalent in 135° NSA stemmed implants when compared to 155° NSA stemmed implants [6]; although the data was not statistically significant due to the small numbers. At present, there is little clinical data available on failure modes of stemless RSA implants.

Currently, no in-vitro studies are available that have evaluated the effect of NSA in stemless RSA humeral components during physiological loading. This present investigation compared 135° and 145° NSA stemless RSA humeral component performance and its effect on primary implant stability and early survivorship. We hypothesized that humeral

components implanted at 145° NSA would exhibit better primary biomechanical stability and improved implant survivorship when compared to those implanted at 135° NSA.

5.2 Methods

5.2.1 Specimen Preparation

Twelve paired cadaveric humeral specimens (height: 71 ± 4 cm, weight: 57 ± 20 kg) aged 57 ± 12 years (mean \pm standard deviation) were implanted with metaphyseal filling two-tiered round stemless RSA humeral components (Tornier Perform® Stemless Reverse Humeral System, Stryker, Kalamazoo, MI, USA) by three board-certified orthopedic surgeons (GSA, AH, FU). The implant evaluated was of press-fit design, with a combination of 3D printed and plasma sprayed titanium surface finishes. Nominal barrel and fin interferences of 1.5 mm and 0.75 mm were present, respectively. The bone mineral density (BMD) of the local periprosthetic bone was calculated using a clinical CT Scanner (GE 750HD Discovery Scanner; GE Healthcare, Chicago, IL, USA), and cortical bone surrogate (SB3 model 450; GAMMEX, Middleton, WI, USA) and distilled water phantoms. The average periprosthetic BMD of the specimens evaluated was 0.106 ± 0.003 g/mm³.

Each bilateral specimen pair (L/R) was randomized to receive a 135° NSA and a 145° NSA implantation, and a single surgeon positioned both components in each pair. Each neck shaft angle cut was prepared using an intramedullary diaphyseal referencing cut-guide (Figure 5-1). Two stemless reverse humeral implant sizes were utilized, sized based on individual patient geometry. A constant size was utilized between each bilateral 135°/145° NSA pair to remove the independent variable of sizing. After the humeral head resection, the metaphyseal bone was reamed with an appropriately sized reamer, followed by insertion of the stemless trial implant. After which, the trial implant was removed, and the final implant was impacted in and press-fit into the prepared humerus.

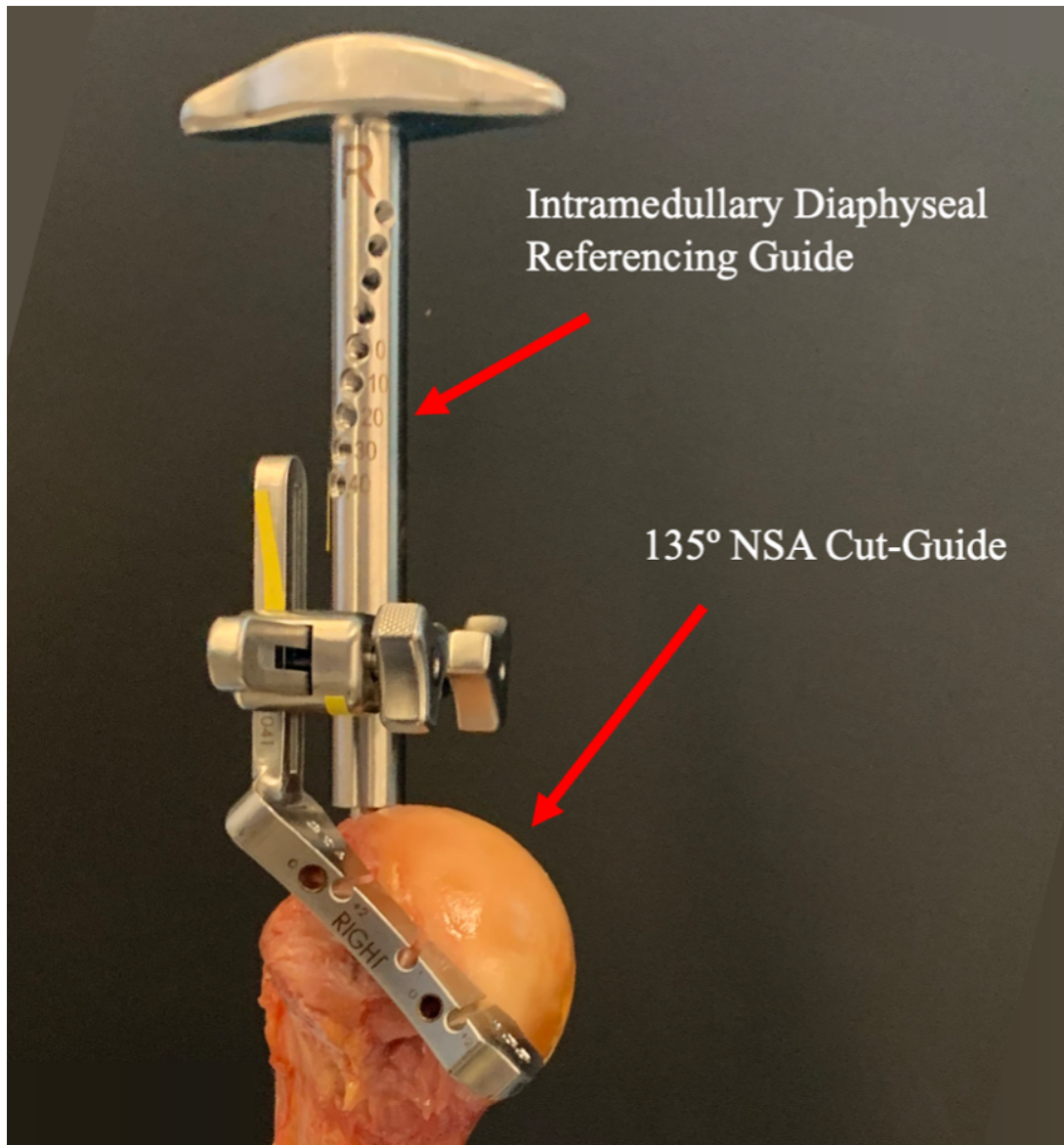


Figure 5-1: NSA Cut Guide

An intermedullary diaphyseal referencing guide and 135° NSA cut-guide attachment used to control resection inclination.

5.2.2 *In-Vitro* Loading Protocol

A custom loading apparatus (Figure 5-2) was used to apply three loading conditions representative of aggressive boundary loading (extreme physiological loads) that a humeral implant might reasonably experience in the early postoperative period. This boundary loading envelope was calculated to represent the 95% percentile of all the relevant loads from instrumented humeral implants that were available on the OrthoLoad database [7] (Figure 5-3) – a database with records of the articular forces generated from telemetrized humeral implants during common upper limb motions. This envelope was developed by plotting all relevant articular load vectors into the humeral coordinate system, then establishing limits based on the upper and lower values ± 2 standard deviations from the mean in a spherical coordinate system.

Loads with vectors pointed most superior-inferiorly were predominantly 90° abduction motions, whereas loads with vectors pointed most anterior-posteriorly included steering a steering wheel or arm elevation motions. Most OrthoLoad [7] loads were directed along the anterosuperior - posteroinferior vector direction. These included combing hair, 2 kg waist-height lifting, and some elevation and abduction motions [7]. Loads with the largest magnitude/eccentricity combination, and therefore most challenging to implant fixation, included a 2 kg head-height lifting motion, a single hand steering motion, and an unweighted 90-degree abduction motion. The aforementioned boundary loads were reconverted into the humeral coordinate system for load application (Figure 5-4). For each trial, the order of loading direction was randomized. Each loading set (Superior, Anterosuperior, and Anterior) was applied for 30 cycles at a frequency of 1 Hz at 20%, 40%, 60%, 80%, and 100% of the physiological magnitude.

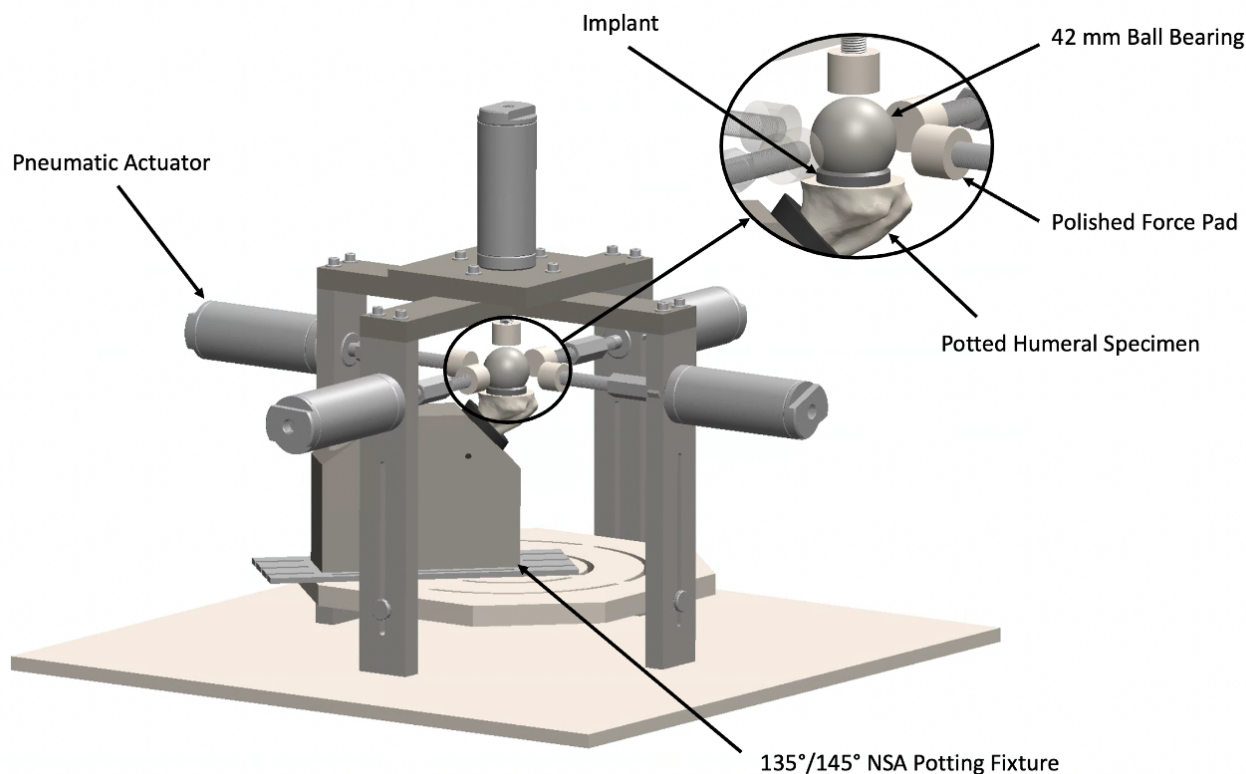


Figure 5-2: CERBERUS Apparatus with a Potted Humeral Specimen Positioned

A custom three-dimensional loading apparatus used to apply physiological loads to a stemless humeral RSA implant. For the purposes of the figure, a 135° NSA specimen has been positioned for loading. Loads were applied using an array of (5) pneumatic actuators, which articulated pistons with polished force pads. Combinations of loads on each actuator applied resolved physiological loads to the 42 mm ball bearing, which was utilized as a proxy for the glenosphere component of the RSA. The potted humeral specimen was positioned at using a custom adaptable potting fixture to facilitate a static boundary condition during loading.

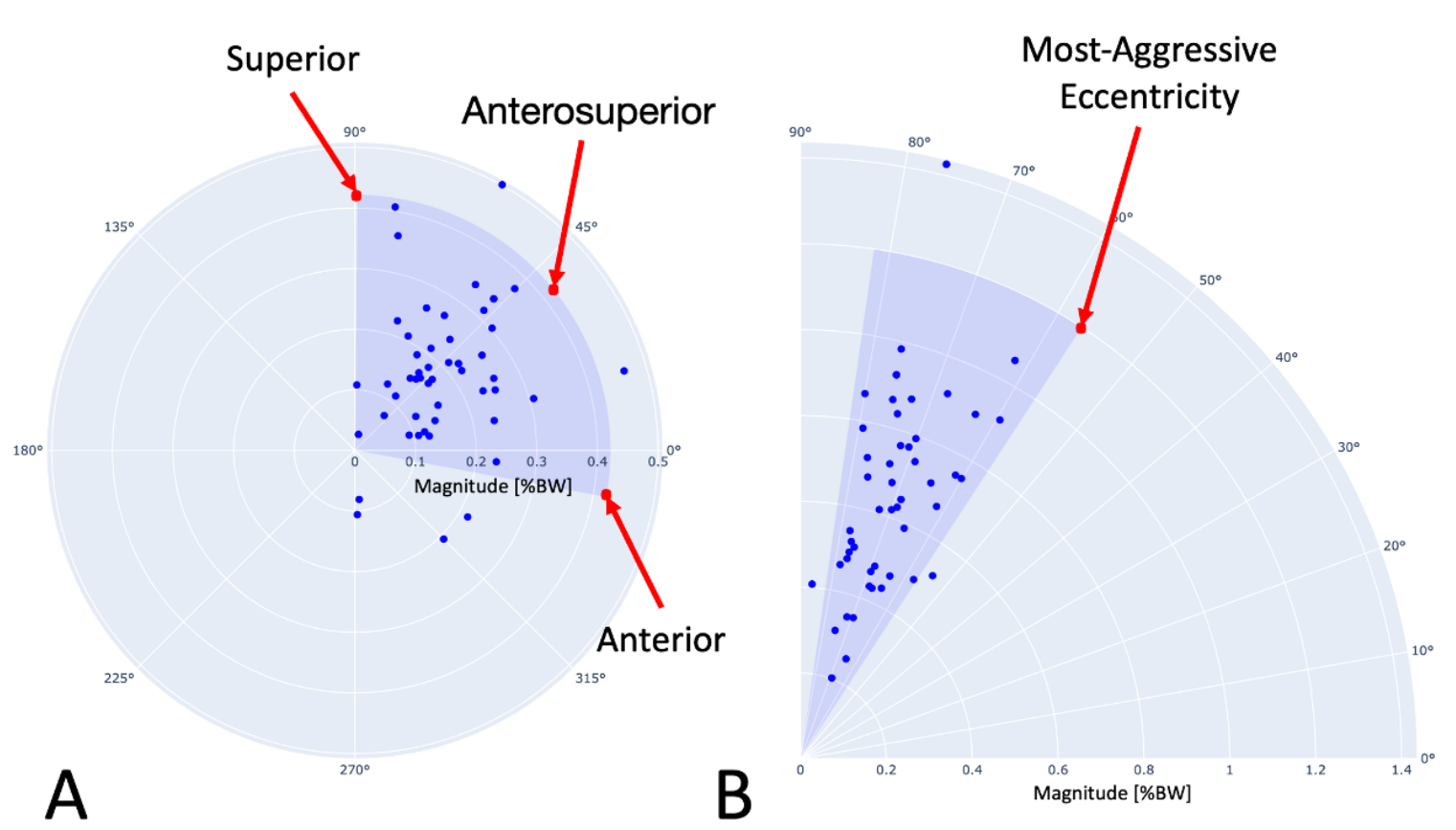


Figure 5-3: OrthoLoad Boundary Load Vectors

Scatter plots of relevant OrthoLoad [7] load vectors relative to the local resection coordinate system. (A) represents a summary of all vector tails orthogonal to the resection plane, whereas (B) indicates the relevant loads' eccentricities relative to the resection plane. The Superior, Anterosuperior, and Anterior simulated loads are indicated by the red arrows and dots. All loading directions were evaluated at the most aggressive eccentricity experienced in order to simulate the most challenging loading profile to implant stability.

Physiological Boundary Forces

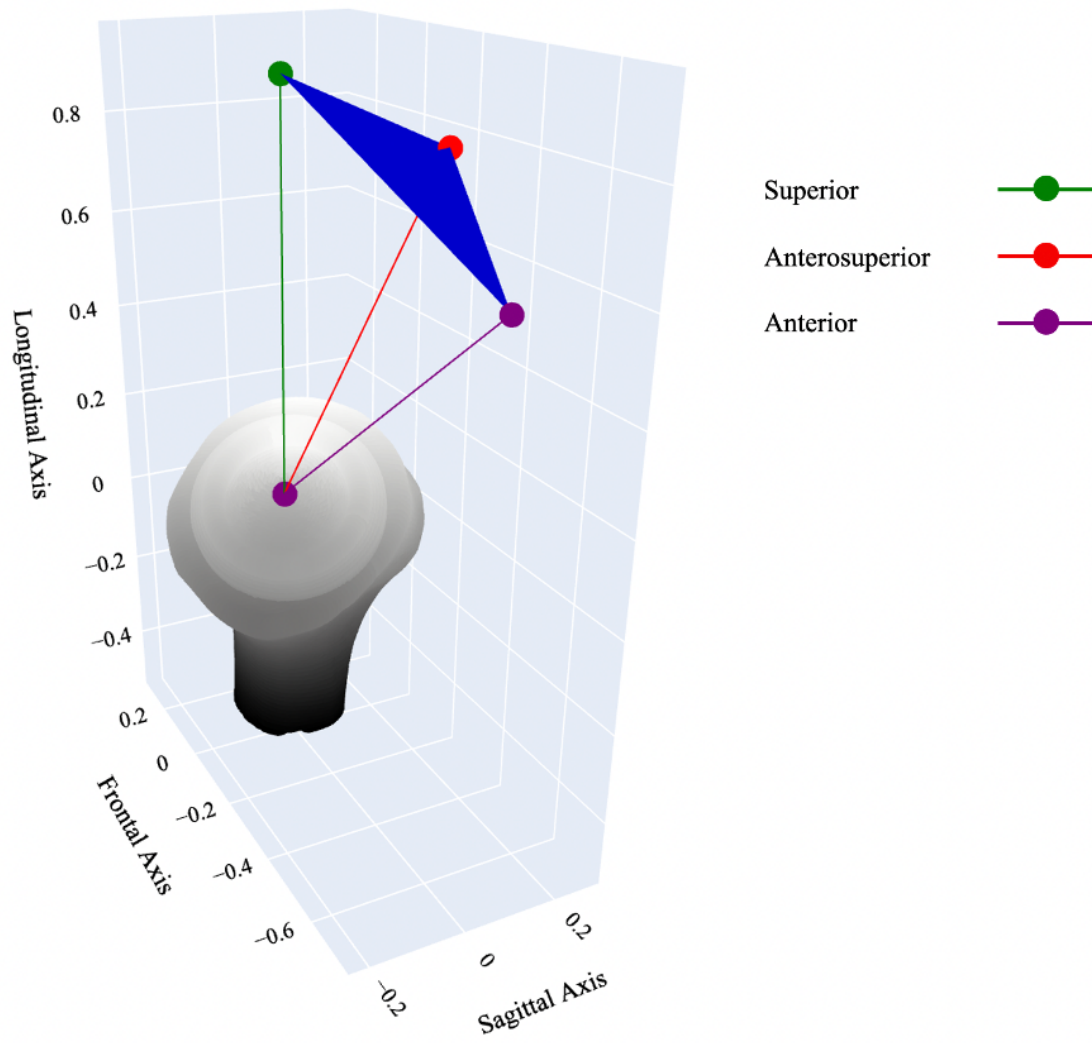


Figure 5-4: Boundary Loads on a Humeral Model

Boundary loads representing 95% of loading scenarios available on the OrthoLoad [7] database. The humerus represented in the figure is a left side specimen resected at 135° NSA.

5.2.3 Measurement of Implant Stability

Implant-bone micromotion (i.e. implant distraction orthogonal to the bone surface) was used as the primary outcome. Three optical machine vision USB3 cameras (acA4096-30uc, Basler AG, Ahrensburg, SH, Germany) were outfitted with c-mount premium lenses (FL-BC3518-9M, Ricoh, Tokyo, Kanto, Japan) (resultant pixel size of 3.45 μm) and focused on the implant-bone interface to collect micromotion measurements at the superior, anterosuperior, and anterior edges of each implant (Figure 5-5). Micromotion data was extracted from the collected high-resolution digital images using ProAnalyst (Xcitex Inc., Woburn, MA, USA) motion analysis software. All images were collected and stored in Tagged Image File Format (.TIFF). Implant survivability (defined as maximum micromotion of less than 350 μm during the cyclical test), was used as the secondary outcome measure for this study. A limit of 350 μm was utilized, as this was the observed threshold of micromotion before critical macro-failure of the bone or disassociation of the implant occurred.

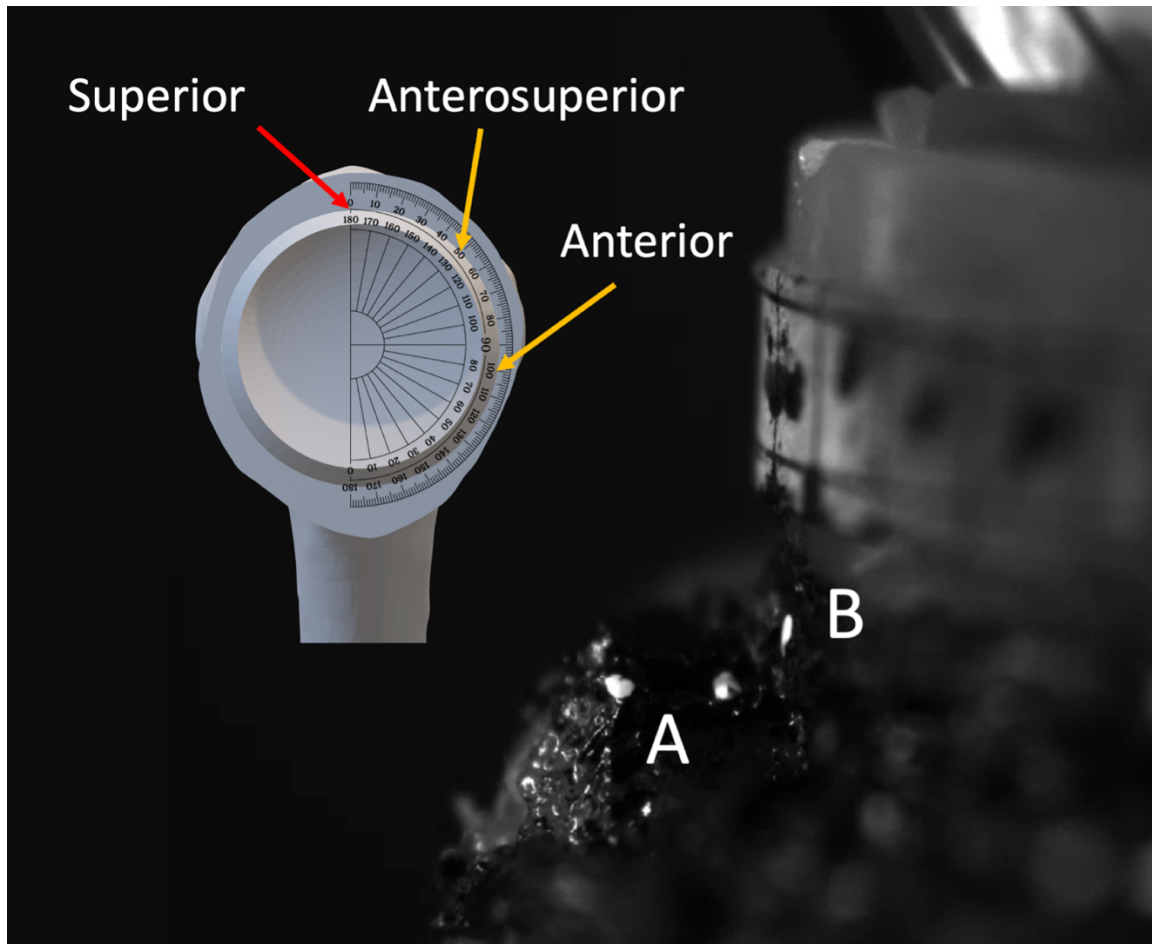


Figure 5-5: High Resolution Image of the Bone-Implant Interface

A high-resolution image of the implant-bone interface on the superior periphery (position depicted by red arrow on the resection view in the top left) of the stemless humeral implant with respect to the humeral resection plane on a 135° NSA model. White markings on the bone (A) and implant (B) served as tracking points during micromotion measurement. The Anterosuperior and Anterior regions of interest relative to the resection plane view are indicated by yellow arrows.

5.3 Outcome Variables and Analysis

A two-way paired repeated measures analysis of variance (ANOVA) was conducted for the dependent variables of neck shaft angle and loading scenario, and a one-way paired repeated measures ANOVA was conducted for the dependent variable of survivability. All statistical analyses were computed using SciPy 1.9.1[8], with the threshold of significance set at $p < 0.05$ and Bonferroni correction with an adjusted alpha level of 0.025 (0.05/2) per two-way test.

5.4 Results

At a 145° NSA, all implants experienced significantly lower time-zero micromotions ($P = 0.001$) and better survivorship ($P < 0.001$) when compared to the 135° NSA implantations. For all loading scenarios, maximum micromotion was detected on the implant edge that was opposite to the direction of loading. Micromotions detected were significantly higher in the 135° NSA implantations (Table 5-1)($P = 0.001$)(Figure 5-6), and the catastrophic failure rate was also significantly higher in the 135° NSA implantations ($P < 0.001$) (135° NSA failures: total n = 6 [at load levels: 20%: 0, 40%: 0, 60%: 1, 80%: 3, 100%: 2], 145° NSA failures: total n = 3 [at load levels: 20%: 0, 40%: 0, 60%: 1, 80%: 0, 100%: 2]) (Figure 5-7).

	Direction	20%	40%	60%	80%	100%
135°	Average	11 ± 4	35 ± 27	118 ± 93	100 ± 9	153 ± NaN
	Superior	16 ± 7	40 ± 18	138 ± 99	53 ± 16	74 ± NaN
	Anterior	10 ± 6	74 ± 103	80 ± 72	181 ± 205	None Survived.
145°	Average	8 ± 6	23 ± 19	36 ± 27	69 ± 39	134 ± 114
	Superior	10 ± 3	25 ± 22	45 ± 47	85 ± 76	139 ± 100
	Anterior	6 ± 2	31 ± 27	37 ± 29	122 ± 76	234 ± 128

Table 5-1: Micromotion Data during Increasing Cyclical Load Tests

Micromotion developed at each load level for each loading direction (mean ± standard deviation). Both 135° NSA and 145° NSA are shown.

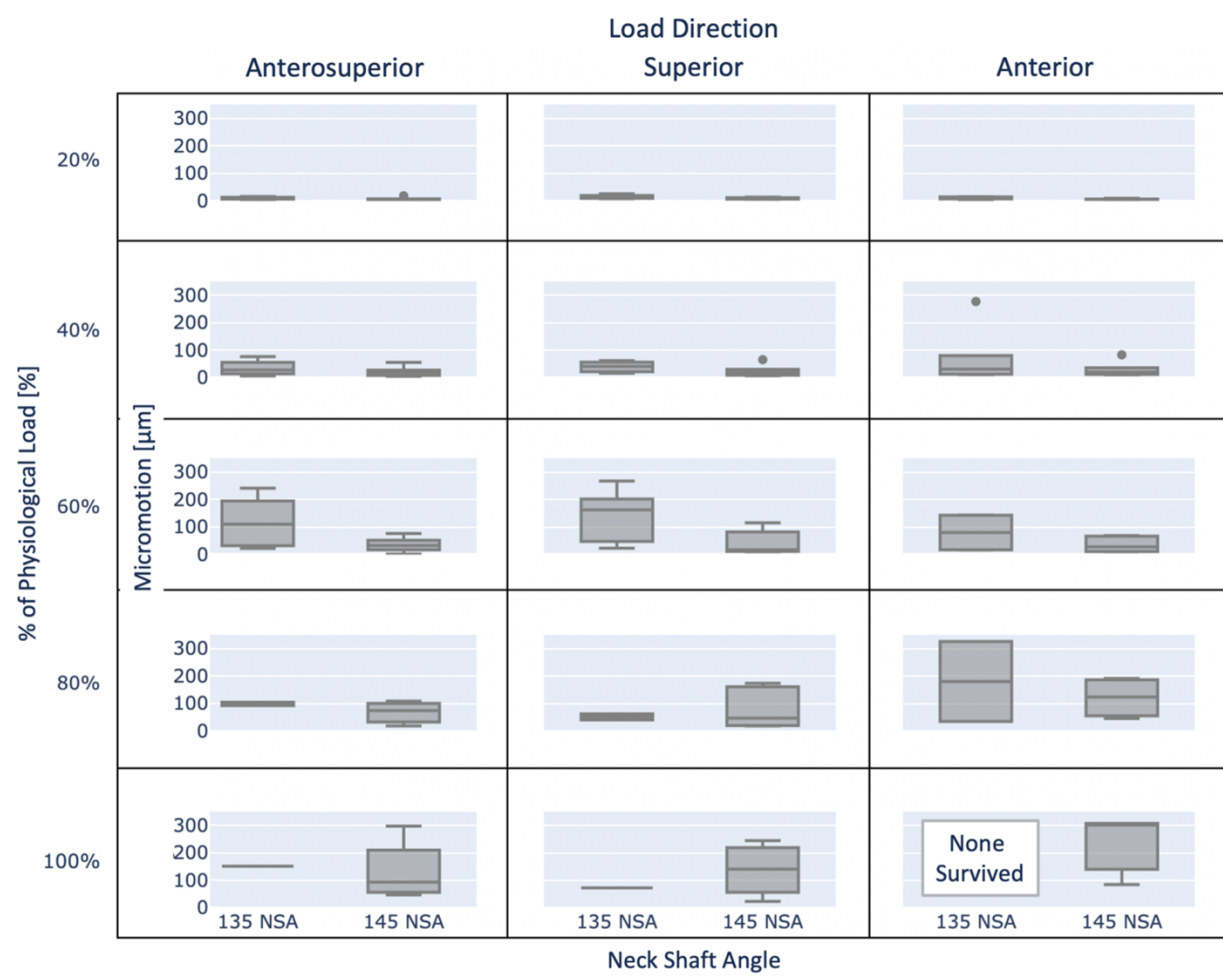


Figure 5-6: Micromotions in Stemless Implants based on Neck Shaft Angle

Micromotions developed in stemless reversed implants based on loading magnitude, NSA, and loading direction. Where an implant did not survive during a trial, it was given a micromotion of N/A and is not shown on the plot.

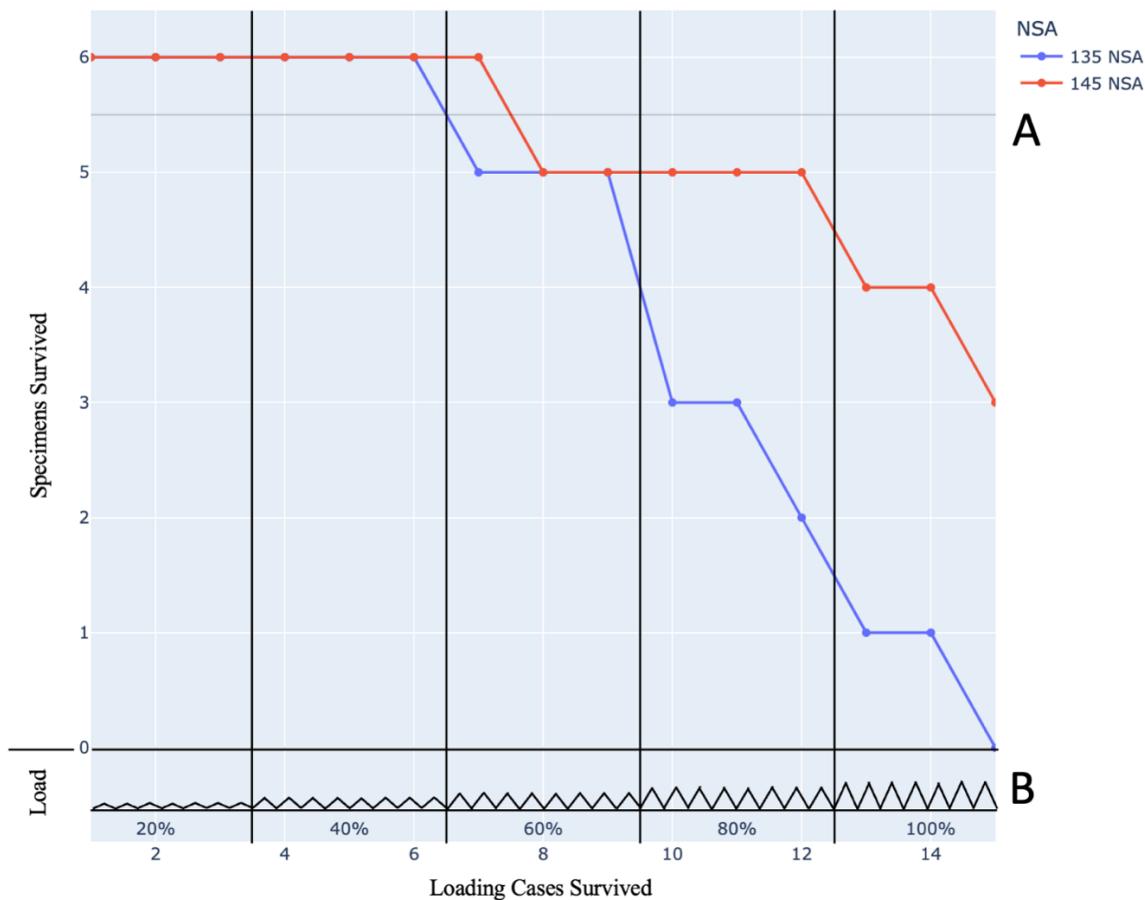


Figure 5-7: Implant Survivability at 135° and 145° NSA

Survivability of stemless reversed implants based on NSA and cycles survived at increasing load magnitudes. The above plot [A] shows the number of specimens surviving at each loading case, whereas the below plot [B] shows a representation of the cyclical loading at increasing magnitudes. Please note that the plot in [B] is a representation of the cyclical loading, and in actuality, each specimen underwent a total of 90 cycles at each load level.

5.5 Discussion

The principal objective of this work was to evaluate the comparative biomechanical performance of a metaphyseal filling two-tiered round stemless RSA humeral component implanted at 135° NSA and 145° NSA. We hypothesized that 145° NSA stemless pressfit implants would exhibit better primary fixation and biomechanical survivorship when compared to 135° NSA stemless pressfit implants. Our results identified that increasing NSA from 135° to 145° substantially increased time-zero stemless implant fixation and biomechanical survivorship. Additionally, the results indicated that when stemless humeral components are subjected to cyclical loading, critical implant fixation failure may occur when single-load distractive micromotions are well below the previous referenced limit of 150 μm for successful osseointegration [2], [9]–[11].

The osseointegrative potential of porous humeral stemless implants has not yet been thoroughly investigated, and existing studies evaluating the primary fixation of press-fit implants have defaulted to the literature, accepting the 150 μm threshold for osseointegration without fibrous tissue formation [2], [9]–[11]. However, this threshold appears to be relevant to shear or tangential micromotion, commensurate with axially-loaded stemmed implant designs. Indeed, previous reports have indicated that for ideal osseointegration, full contact between the implant and bone should be maintained, and any level of shear or distractive micromotion may potentially negatively influence the success of primary and secondary fixation [12], [13]. The micromotions observed in this work show this threshold of long-term fixation surpassed even at 40% physiological load, which supports the directive of postoperative immobilization to increase the probability of successful long-term fixation.

Measurement of implant stability is a commonly utilized assessment method when evaluating the osseointegrative potential of different orthopedic implants [1], [2], [9], [10], [14]–[16]. The use of high-resolution digital tracking methods for the quantification of implant stability (viz micromotion) is becoming more widely utilized [2], [14]. This technique is able to evaluate the implant-bone interface during the application of loads that

may realistically be experienced postoperatively during activities of daily living [7], [17]–[19]. Although the use of Linear Variable Digital Transformers (LVDTs) has been commonly utilized in the experimental evaluation of shoulder implants [9], it has previously been found that LVDT methods may overreport implant-bone relative motion [14], so a high-resolution digital tracking system was used.

Given the interface changes that were observed due to the loading states simulated, it is logical to postulate that loading of this nature may be an impediment to osseous integration and may contribute to early migration or subsidence if it were to occur postoperatively. When interpreting the telemetized implant data available, there are only a limited number of activities that maintained load magnitudes of less than 40% of the physiological boundary load (53% body-weight), and those activities of daily living (ADLs) identified as “safe” were limited to physiotherapist-assisted external rotation motions (in 1/1 patient(s)) and controlled unweighted 90° abduction motions (in 4/17 patient(s))[7] (Figure 5-8). It is therefore reasonable to postulate that immobilization during the first four to six weeks after surgery may serve to decrease implant-bone micromotion, thereby increasing the potential for bone on-growth with resultant increased long-term fixation in stemless humeral implants. However, four to six weeks of sling use may result in increased joint stiffness, which may take longer to resolve. Previous investigations on the effect of modifying NSA have reported comparable results; indicating that lower, more varus, NSAs exhibit lower levels of stability [4]; therefore also supporting the position that when implant stability is of concern, higher neck-shaft angles may improve early implant stability in stemless reverse humeral components [4]. Although both the 135° NSA and 145° NSA cohorts experienced failures, it is important to note that the conservative loads utilized for this work were intended to represent the worst-case conditions that a shoulder implant might experience postoperatively, before any osseointegration had occurred.

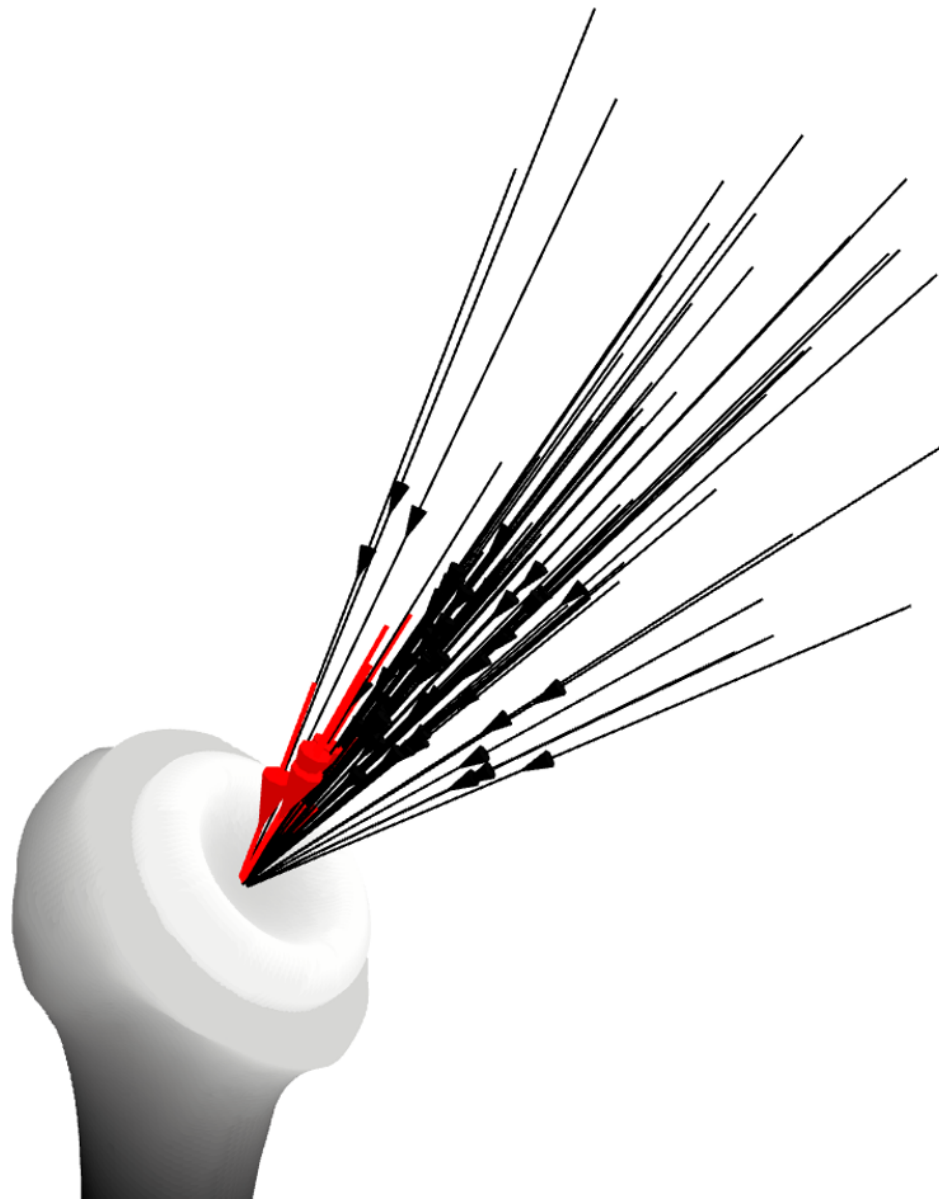


Figure 5-8: A 3D Plot of "Safe" OrthoLoad Activities

A 3D plot of the proximal humerus, showing all relevant OrthoLoad [7] activities used in the calculation of boundary loading limits in vector format. All black arrows represent ADLs that exceed the 40% physiological load survivorship limit determined by the study. The red arrows show the ADLs that were below the 40% limit. Only No-Weight Abduction and External Rotation in 90° Elbow Flexion, supported by a physiotherapist were determined as "safe" activities in a few of the patients.

Increasing humeral component NSA, however, may have important negative implications; including decreased impingement-free range of motion in adduction [20], increased risk of scapular notching [5], increased humeral distalization, and possibly reduced internal/external rotation [5], [21]. As such, it is important to consider all these factors when selecting an appropriate NSA. When using a traditional stemmed implant with diaphyseal or meta-diaphyseal fixation, the effect of NSA on primary implant stability is likely less pronounced.

Implant fixation has frequently been studied in the shoulder, however, most studies have focused on glenoid components [9]; as such, there are limited protocols currently available for the evaluation of humeral component implant performance. In a clinical setting, humeral implants are subjected to a wide range of loading [7], and hence, it is reasonable to postulate that testing should include a comprehensive protocol. Most recently, studies have employed cyclical loading protocols to better mimic the early performance of uncemented devices [16], [19], [22]; a strategy that was also employed herein. Additionally, due to the diverse array of loading states that are experienced by the shoulder postoperatively, this study utilized a novel loading protocol that was designed to examine the fixation of implants using an increasingly aggressive loading protocol. This was important, as this study also aimed to assess the survivability of humeral implants during loading that best attempted to mimic the physiological state.

As discussed, one of the outcome measures leveraged in this work was distractive micromotion magnitude. This metric is most commonly associated with osseointegration, as bony ingrowth is generally more successful when implant micromotion is limited [2], [9]–[11]. However, existing literature rarely differentiates between tangential (shear) and orthogonal (distractive) micromotion. In fact, to the authors' knowledge, there are no studies that examine the influence of cyclical loading on the osseointegration of surfaces resisting load in the distractive direction. As it has been proposed that the mechanism of implant-bone distractive fixation is dependent on the osseointegrated surface area and level of osseointegration [23], this would imply that when the level of osseointegration is negligible, any loads resulting in distractive micromotions would not be resisted in the

orthogonal direction by adhesion phenomena [24], and hence osseous ingrowth in the distractive direction may be compromised by comparatively small micromotion magnitudes. This is noteworthy, as for implant geometries that rely on fixation to a primarily cancellous bone foundation, eccentric loading is known to cause “lift-off” and hence analyses of fixation in these constructs requires assessment of implant micromotion orthogonal to the interface. Previous finite element studies for the evaluation of micromotion in humeral implants found the primary mode of micromotion at the interface to be distractive micromotion for a similar implant geometry investigated [19]. Hence, distractive micromotion was utilized as the outcome measure of this work, but 150 μm was not purposed as a hard limit as knowledge on the relevance of that value is disputed. The experimental approaches employed herein have also been widely employed for tibial and glenoid implants [9], [11], [15].

There are limitations with the present study. Primarily, boundary loading limits were established using in-vivo telemetized data for anatomic implants. This is noteworthy, as reversed implants are likely to experience lower magnitudes of articular force at potentially higher eccentricities due to the medialized centre of rotation and increased deltoid moment arm [25]. However, for the purposes of this work, a conservative approach using larger magnitude loading was used as telemetized data for RSA implants is not yet available [4]. This evaluation also focused on time-zero (directly after implantation) implant behaviours. As trabecular bone is a mechanoresponsive material and press-fit implants rely on osseointegration for fixation, stability during the postoperative rehabilitation period may differ in a clinical setting. Lastly, this evaluation only investigated one design of stemless RSA humeral implant. Future works should assess additional implant designs with a large variation in fixation geometry to provide a more thorough evaluation of the effect of neck shaft angle.

5.6 Conclusion

Neck shaft angle in stemless reverse humeral components is a modifiable intra-operative parameter that significantly effects the time-zero stability and early survivorship of the stemless reverse humeral component implant design tested. The results demonstrate that a metaphyseal filling round two-tiered stemless implant inserted at an NSA of 145° exhibits better primary stability than when inserted at 135° during simulated early post-operative physiological loading scenarios. It is suggested, therefore, with conditions of poorer humeral bone quality, that a higher, more valgus, neck shaft angle may be considered to maximize time zero stemless implant fixation. Alternatively, sling immobilization to limit provocative activities of daily living in the early postoperative period will decrease undesirable bone-implant micromotions.

5.7 References

- [1] C. Quental, J. Folgado, M. Comenda, J. Monteiro, and M. Sarmento, “Primary stability analysis of stemless shoulder implants,” *Med. Eng. Phys.*, vol. 81, pp. 22–29, 2020, doi: 10.1016/j.medengphy.2020.04.009.
- [2] P. Favre et al., “In vitro initial stability of a stemless humeral implant,” *Clin. Biomech.*, vol. 32, pp. 113–117, 2016, doi: 10.1016/j.clinbiomech.2015.12.004.
- [3] N. Razfar, “Finite Element Modeling of the Proximal Humerus to Compare Stemless , Short and Standard Stem Humeral Components of Varying Material Stiffness for Shoulder Arthroplasty,” University of Western Ontario, 2014. [Online]. Available: <https://ir.lib.uwo.ca/etd/2431>
- [4] D. E. Cunningham, G. W. Spangenberg, G. D. G. Langohr, G. S. Athwal, and J. A. Johnson, “Stemless Reverse Humeral Component Neck Shaft Angle has an Influence on Initial Fixation,” *J. Shoulder Elb. Surg.*, 2023, doi: 10.1016/j.jse.2023.06.035.
- [5] B. K. Jeon et al., “Combined effect of change in humeral neck-shaft angle and retroversion on shoulder range of motion in reverse total shoulder arthroplasty - A simulation study,” *Clin. Biomech.*, vol. 31, pp. 12–19, 2016, doi: 10.1016/j.clinbiomech.2015.06.022.
- [6] R. Gobezie, Y. Shishani, E. Lederman, and P. J. Denard, “Can a functional difference be detected in reverse arthroplasty with 135° versus 155° prosthesis for the treatment of rotator cuff arthropathy: a prospective randomized study,” *J. Shoulder Elb. Surg.*, vol. 28, no. 5, pp. 813–818, 2019, doi: 10.1016/j.jse.2018.11.064.
- [7] P. Damm and J. Dymke, “Orthoload Database,” Julius Wolff Institute, 2021. <https://orthoload.com/database/> (accessed Jul. 26, 2021).
- [8] P. Virtanen et al., “SciPy 1.0: fundamental algorithms for scientific computing in Python,” *Nat. Methods*, vol. 17, no. 3, pp. 261–272, 2020, doi: 10.1038/s41592-019-0686-2.
- [9] American Society for Testing and Materials, “ASTM F2028-17 Standard Test Methods for Dynamic Evaluation of Glenoid Loosening or Disassociation,” ASTM, pp. 1–15, 2018, doi: 10.1520/F2028-17.Copyright.

- [10] N. Bonnevialle, L. Geais, J. H. Müller, and J. Berhouet, “Effect of RSA glenoid baseplate central fixation on micromotion and bone stress,” *JSES Int.*, vol. 4, no. 4, pp. 979–986, 2020, doi: 10.1016/j.jseint.2020.07.004.
- [11] N. Kohli, J. C. Stoddart, and R. J. van Arkel, “The limit of tolerable micromotion for implant osseointegration: a systematic review,” *Sci. Rep.*, vol. 11, no. 1, pp. 1–11, 2021, doi: 10.1038/s41598-021-90142-5.
- [12] M. Viceconti, G. Brusi, A. Pancanti, and L. Cristofolini, “Primary stability of an anatomical cementless hip stem: A statistical analysis,” *J. Biomech.*, vol. 39, no. 7, pp. 1169–1179, 2006, doi: 10.1016/j.jbiomech.2005.03.024.
- [13] E. Sánchez et al., “The effect of different interference fits on the primary fixation of a cementless femoral component during experimental testing,” *J. Mech. Behav. Biomed. Mater.*, vol. 113, no. September 2020, 2021, doi: 10.1016/j.jmbbm.2020.104189.
- [14] P. Favre et al., “In vitro assessments of reverse glenoid stability using displacement gages are misleading - Recommendations for accurate measurements of interface micromotion,” *Clin. Biomech.*, vol. 26, no. 9, pp. 917–922, 2011, doi: 10.1016/j.clinbiomech.2011.05.002.
- [15] D. R. Suárez, W. Nerkens, E. R. Valstar, P. M. Rozing, and F. van Keulen, “Interface micromotions increase with less-conforming cementless glenoid components,” *J. Shoulder Elb. Surg.*, vol. 21, no. 4, pp. 474–482, 2012, doi: 10.1016/j.jse.2011.03.008.
- [16] R. E. Chen, E. Knapp, B. Qiu, A. Miniaci, H. A. Awad, and I. Voloshin, “Biomechanical comparison of stemless humeral components in total shoulder arthroplasty,” *Semin. Arthroplast. JSES*, vol. 32, no. 1, pp. 145–153, 2021, doi: 10.1053/j.sart.2021.08.003.
- [17] M. Masjedi and G. R. Johnson, “Glenohumeral contact forces in reversed anatomy shoulder replacement,” *J. Biomech.*, vol. 43, no. 13, pp. 2493–2500, 2010, doi: 10.1016/j.jbiomech.2010.05.024.
- [18] W. F. Zimmerman, M. A. Miller, R. J. Cleary, T. H. Izant, and K. A. Mann, “Damage in total knee replacements from mechanical overload,” *J. Biomech.*, vol.

- 49, no. 10, pp. 2068–2075, 2016, doi: 10.1016/j.jbiomech.2016.05.014.
- [19] P. Favre and A. D. Henderson, “Prediction of stemless humeral implant micromotion during upper limb activities,” *Clin. Biomech.*, vol. 36, pp. 46–51, 2016, doi: 10.1016/j.clinbiomech.2016.05.003.
- [20] B. S. Werner, J. Chaoui, and G. Walch, “The influence of humeral neck shaft angle and glenoid lateralization on range of motion in reverse shoulder arthroplasty,” *J. Shoulder Elb. Surg.*, vol. 26, no. 10, pp. 1726–1731, 2017, doi: 10.1016/j.jse.2017.03.032.
- [21] A. Arenas-Miquelez, R. J. Murphy, A. Rosa, D. Caironi, and M. A. Zumstein, “Impact of humeral and glenoid component variations on range of motion in reverse geometry total shoulder arthroplasty: a standardized computer model study,” *J. Shoulder Elb. Surg.*, vol. 30, no. 4, pp. 763–771, 2021, doi: 10.1016/j.jse.2020.07.026.
- [22] T. Freitag, K. P. Kutzner, R. Bieger, H. Reichel, A. Ignatius, and L. Dürselen, “Biomechanics of a cemented short stem: a comparative in vitro study regarding primary stability and maximum fracture load,” *Arch. Orthop. Trauma Surg.*, vol. 141, no. 10, pp. 1797–1806, 2021, doi: 10.1007/s00402-021-03843-x.
- [23] H. J. Rønold and J. E. Ellingsen, “The use of a coin shaped implant for direct in situ measurement of attachment strength for osseointegrating biomaterial surfaces,” *Biomaterials*, vol. 23, no. 10, pp. 2201–2209, 2002, doi: 10.1016/S0142-9612(01)00353-2.
- [24] X. Gao, M. Fraulob, and G. Haïat, “Biomechanical behaviours of the bone-implant interface: A review,” *J. R. Soc. Interface*, vol. 16, no. 156, pp. 13–17, 2019, doi: 10.1098/rsif.2019.0259.
- [25] G. D. Langohr, “Fundamentals of the Biomechanical Characteristics Related to the Loading of Reverse Total Shoulder Arthroplasty Implants and the Development of a Wear Simulation Strategy,” 2015. Accessed: May 01, 2023. [Online]. Available: https://ir.lib.uwo.ca/etd/3436/?utm_source=ir.lib.uwo.ca%2Fetd%2F3436&utm_medium=PDF&utm_campaign=PDFCoverPages

Chapter 6

6 Stemless Reverse Humeral Component Neck-Shaft Angle has an Influence on Initial Fixation

OVERVIEW

This work has previously been published in the Journal of Shoulder and Elbow Surgery [1], but has been adapted to include additional imaging based analyses to enhance our interpretation of the findings. Additionally, components of this work have been presented at the International Society for Technology in Arthroplasty, the Canadian Operational Research Society, and the Canadian Orthopaedic Association Annual Conferences.

*Finite element analysis is an effective tool in the evaluation of the designs of orthopaedic implants. Finite element models can be used to determine the level of fixation *in-silico*, thereby providing a means to evaluate the efficacy of different orthopaedic implant designs without the need for cadaveric specimens or the physical manufacturing of each implant iteration. This investigation will employ a three-dimensional modelling approach, using finite element analysis to improve the understanding of the surgical implantation variable of neck shaft angle. While the influence of neck shaft angle has been investigated in stemmed implants, there remains a need to further evaluate the comparative effectiveness of this variable in the context of more novel reverse total shoulder arthroplasty designs.*

6.1 Introduction

(Much of this background was addressed in Chapter 1. The literature discussed in this introduction remains consistent with the content of the published manuscript.)

Reverse shoulder arthroplasty (RSA) implants have undergone a variety of design modifications since first introduced. Some modifications include press-fit stems, modularity, adjustments in neck shaft angle, and onlay/inlay design features. One design feature, focused on decreasing stress shielding and simplifying future revisions, has been the gradual shortening of the humeral stem [2].

Although anatomical stemless shoulder arthroplasty implants are steadily becoming more popular, the use of stemless RSA implants is still limited, with very few published works reporting on the clinical and biomechanical performance of these novel implants [3]. Shorter humeral stem lengths have been shown to decrease stress shielding in periprosthetic bone by better mimicking natural force-transmission properties [4]. Stemless designs also benefit from the preservation of humeral bone stock, reduction of risk of periprosthetic fractures, and simplification of surgical technique [5]. However, these designs of humeral implant also pose several risks that emphasize the importance of primary fixation. Ultra-short implants or stemless humeral implants are more vulnerable to poor initial fixation, instability, or loosening than their stemmed counterparts, due to the reduced bone-implant contact area and lack of cortical bone contact [3], [5].

The primary method of achieving fixation in existing stemless RSA implants is via osseointegration (viz. bony ingrowth). In order for this bone-implant bonding to occur, the two surfaces are required to maintain limited relative motion (termed “micromotion” [6], [7]) during the healing phase following surgery [8]. The tolerable threshold of tangential micromotion is often quoted as 150 μm [5], [9]–[12]. However, the threshold of tolerable micromotion has also been reported as a range of between 30 μm [12], [13] and 750 μm [12], [14]. Additionally, it is rational to postulate that any lift-off or distraction micromotion may well impede bone contact and hence ingrowth.

One modifiable technical factor with stemless RSA humeral implants is the resection inclination angle (or neck shaft angle) of the humeral head. RSA systems with varied neck shaft angles (NSA) of between 127.5° and 155° are currently used. It has been found that decreasing NSA reduces the risk of scapular notching [15], and that modifying NSA results in no significant differences in scapular spine strain [16]. In addition, it has previously been found that decreasing NSA significantly increases impingement-free range of motion [17], providing incentive to decreasing NSA. However, there remains a lack of knowledge regarding the effect of NSA on primary implant fixation.

Computational methods have gained popularity in orthopedics due to their ability to estimate post-operative physical phenomena that are difficult to measure *in-vivo* [8], [37], [65], [67], [71], [83], [84], [107]. Numerous computational studies evaluating implant designs are available [40], [67], [83], [84], [108], however, little to no literature has evaluated the effect of neck shaft angle on primary reverse humeral implant fixation *in-silico*. The present investigation, therefore, determined the effect of stemless reverse humeral component insertion neck shaft angles on the primary time-zero stability of the implants. We hypothesized that increasing neck shaft angle would result in better implant stability and decreased micromotion at the implant bone interface.

6.2 Methods

6.2.1 Developing 3D Models using Computed Tomography

Computed tomography (CT) scans of eight shoulders from male cadaveric specimens (height: 177 ± 4 cm, weight: 69 ± 10 kg) aged 70 ± 21 years (mean \pm standard deviation) were collected using a clinical CT Scanner (slice thickness: 0.5 mm, pixel spacing: 0.961 x 0.961 mm, exposure time: 750 ms, kVp: 120) (GE 750HD Discovery Scanner; GE Healthcare, Chicago, IL, USA). A cortical bone surrogate (SB3 model 450; GAMMEX, Middleton, WI, USA), and distilled water were purposed as phantoms to calibrate the apparent density in g/cm³ from CT attenuation in Hounsfield units (HU) [18]. Three-dimensional models of the humerus (NSA: $139^\circ \pm 6^\circ$, retroversion: $22^\circ \pm 13^\circ$) and cortical shell were created in Mimics v23.0 (Materialise, Leuven, Belgium). A 3D solid model of

the humerus was created in trabecular and cortical parts (Figure 6-1). The cortical bone region was first created first by using threshold-based segmentation of the DICOM images. Further refinement of the model mask was performed manually in a slice-by-slice method until a full mask of the cortical bone had been created, free from excessive pixilation and void.

Trabecular bone was isolated using an islanding approach, where an unrestricted mask was first created to encompass the entire CT image portfolio. This mask was cropped to the approximate size of the relevant anatomy, and a Boolean subtraction operation was performed to separate all space on the outside of the cortical shell from the remainder on the inside of the cortical shell. These separations were then split into separate masks and a 3D model was created from the cortical shell and the remaining internal space under the intention that all volume internal to the cortical shell was to be treated as trabecular bone during material property assignment. Please see Appendix C for a full description on the generation of 3D bone models using Mimics v23.0. Models were exported as non-uniform rational basis spline (NURBS) models instead of stereolithography (STL) models since they can model complex surfaces on the bony anatomy with greater accuracy.

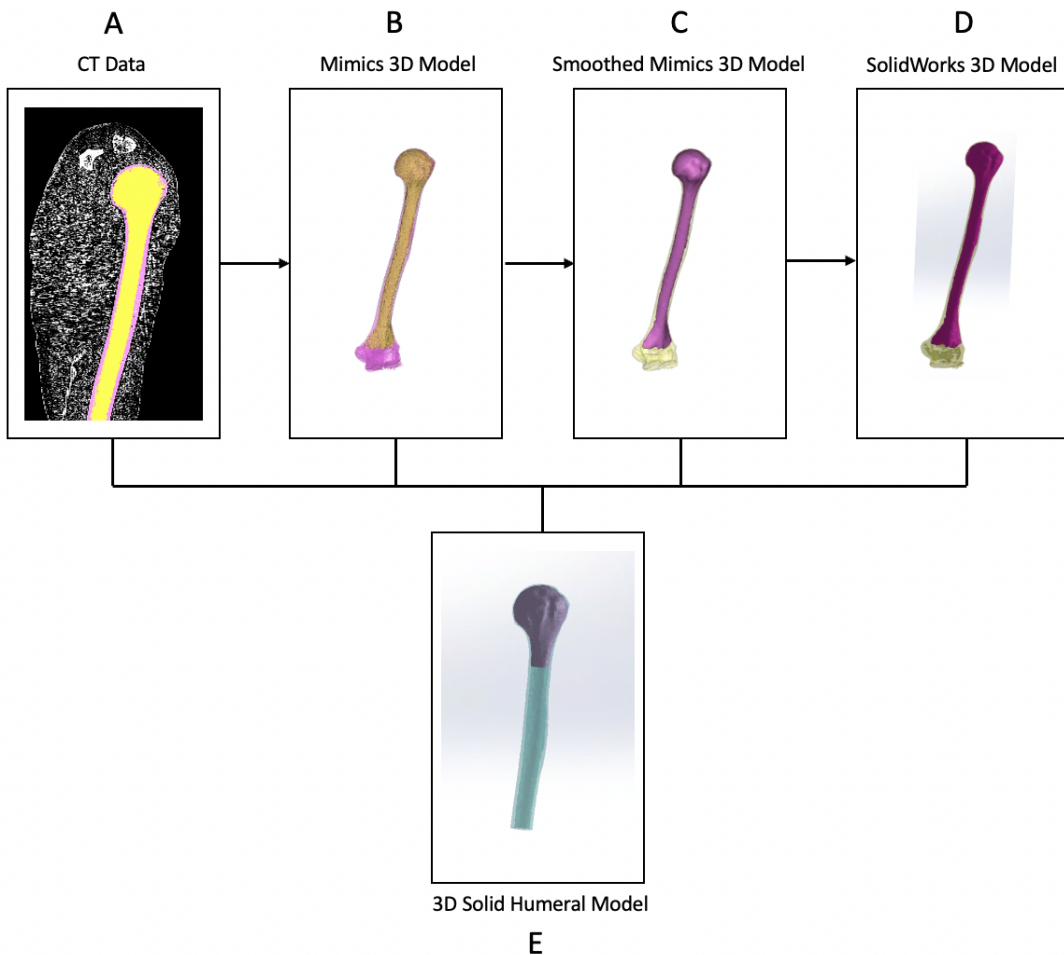


Figure 6-1: Development of 3D SolidWorks Humeral Model with Trabecular and Cortical Regions from CT Scan Data

Steps illustrating the process required for converting CT DICOM images of the humerus to a smoothed and wrapped 3D SolidWorks model with division of cortical and trabecular bone. Figure A shows the unmodified CT scan data with the full humerus masked and isolated. Figure B shows the raw 3D Mimics model without reduction and Figure C Shows the smoothed and wrapped Mimics 3D model after removal of sharp edges and pixilation. Figure D shows the same model exported in SolidWorks, and Figure E shows the completed humeral solid model with the length of the cortical bone resected to 180 mm distally from the humeral head resection surface, and the length of the trabecular bone shortened to 40 mm distally from the resection surface [19].

6.2.2 Implant Development and Positioning

A generic stemless reverse implant design was developed using CadQuery, a 3D parametric design Python library [20] (Figure 6-2). This generic implant design was chosen as a general representation of a stemless boundary-crossing generic implant [2], [21]; an amalgamation of the Reeves *et al.* Quad-Peg boundary crossing generic implant [2], as well as the Stryker Tornier, Zimmer Biomet, and Lima Corporate stemless designs currently available clinically. Anatomic generator implant examples were utilized due to the lack of stemless reversed implants available clinically. A single size of generic implant (glenosphere diameter: 40 mm, collar diameter: 36 mm, penetrating volume: 6.2 cm³) was found to be an acceptable fit for all humeral models used.

The generic implant model was positioned by a board-certified surgeon (GSA) in SolidWorks CAD software (Dassault Systèmes Corp., Waltham, MA, USA) at a 135° neck shaft angle. This procedure was designed to replicate the process by which an implant would be positioned in the surgical suite. A full description of the implant positioning process may be viewed in Appendix D. Implant cut planes were identified using the distal border of the humeral head and the diaphyseal long axis as primary bony landmarks during resection. The border of the humeral head, directly adjacent to the anatomical neck, and two points at locations of 50 mm and 100 mm distal to the most proximal aspect of the humeral head on the diaphyseal long axis was utilized to determine consistent retroversion and lateralization across patient models. The diaphyseal long axis of the humerus was also utilized to determine the 135° neck shaft angle as is consistent with surgical procedure.

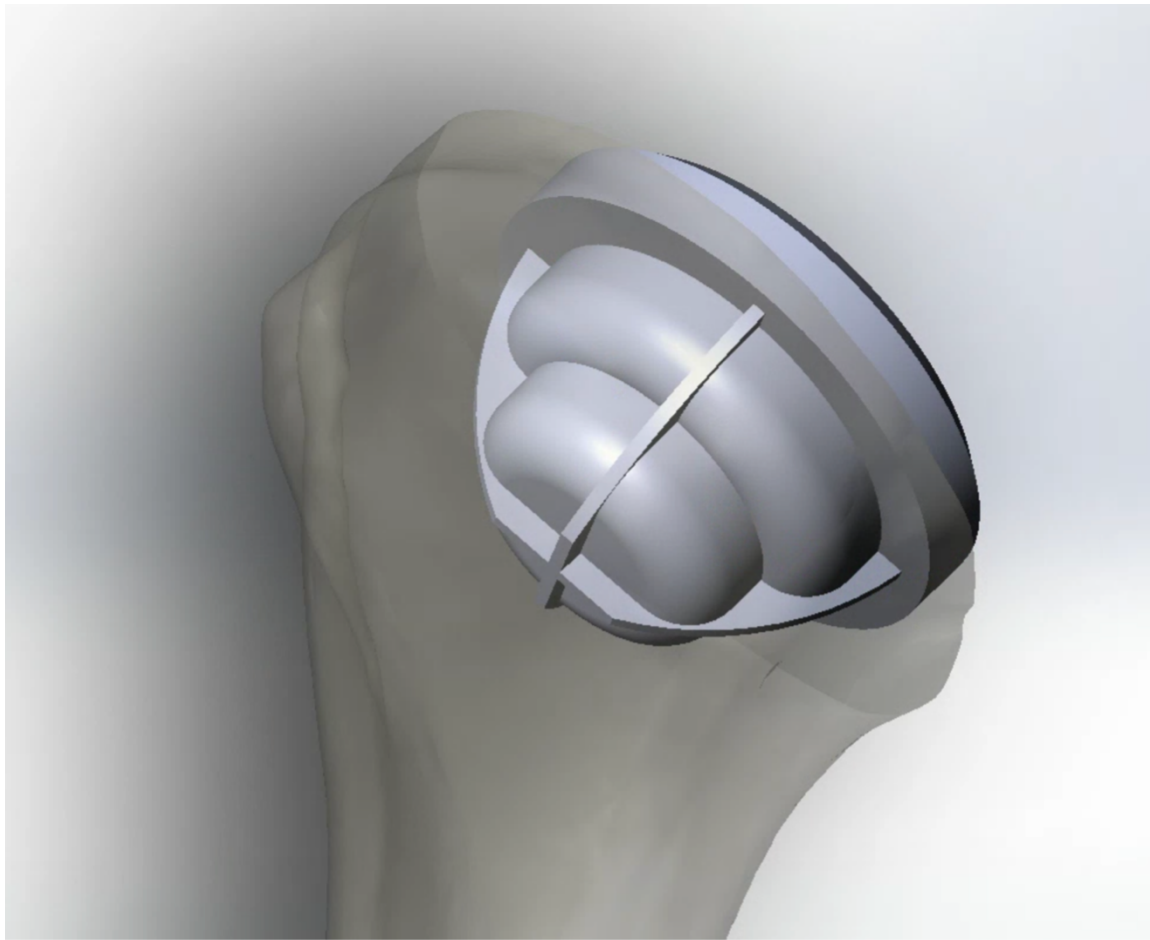


Figure 6-2: A Generic Stemless Reversed Humeral Component Inserted into a Proximal Humerus (Left)

A posterior-lateral view of the left humerus implanted with a generic boundary-crossing implant, designed using variable-driven parametric design software. The implant was repetitively positioned into all 3D humeral models, developed from patient CT scans, at each neck shaft angle.

In order to maintain inclination consistency between specimens, the 135° implantation case was first positioned as a control, and a computational matrix transformation was utilized to vary inclination angle (at 130°, 135°, 140°, 145°, and 150° neck-shaft angles). A constant centre of rotation, positioned at the most superior-lateral apex of the anatomical humeral neck in each specimen, was identified in the 135° control resection and utilized for NSA variation. Each humeral model was re-evaluated at every implantation condition. All implants were fully positioned in humeral trabecular bone, and no cortical contact was detected.

The cut plane was used to shorten the length of trabecular bone models to 40 mm distally to the resection surface [22]. Similarly, the cortical bone models were shortened to 50 mm distally to the resection surface. The 50 mm cut plane was determined from a preliminary step which evaluated the effect of distal cut plane proximity. Both cuts were performed normal to the long axis of the humerus for consistency.

6.2.3 Finite Element Model Generation

Finite element models were developed in Abaqus CAE 2021 software (Dassault Systèmes Corp) using a previously validated approach [4], [19], [23]. All components were meshed with 1.2 mm quadratic tetrahedral elements, according to mesh convergence. Cortical bone was assigned a constant Young's modulus of 20 GPa [2], [23]–[26], and trabecular bone was assigned elastic moduli that varied in accordance to the Morgan *et al.* density-elasticity relationship [2], [18], [23]–[25], [27]. Mimics CT software was utilized to apply all inhomogeneous material properties to trabecular bone models ($0.11 \pm 0.01 \text{ g/cm}^3$, Pearson skew: 1.87). The cortical and trabecular bone models were both assigned a Poisson's ratio of 0.3 [11], [23]. The generic implant was assigned an elastic modulus of 110 GPa, representing titanium [24], [28], and a Poisson's ratio of 0.3 [2], [11], [23]. Implant-bone contact was assumed as frictional and modelled to represent the behaviour of a titanium plasma sprayed surface on bone ($\mu = 0.6$) [5]. Further detail of the trabecular bone material property assignment may be found in Appendix E.

We employed four different loading scenarios [30° shoulder abduction with neutral forearm rotation, 30° shoulder abduction with forearm supination, a head-height lifting motion, and a single-arm steering motion] built from Orthoload patient-based measurements [23] to encompass a range of activities, particularly those known to produce eccentric loading, and therefore challenges to implant-bone fixation (Figure 6-3). These aforementioned activities were chosen as they represent a diverse array of loading states that a patient may experience immediately postoperatively while adhering to standard postoperative instruction. Loading data was extracted and corrected for the individual body weight of each subject [2], [23], [29]. The joint force line-of-action was directed through the centre of rotation of the simulated reverse arthroplasty joint, and the humeral models were assigned encastre boundary conditions on a plane 50 mm distal to the neck shaft angle centre of rotation (Figure 6-3).

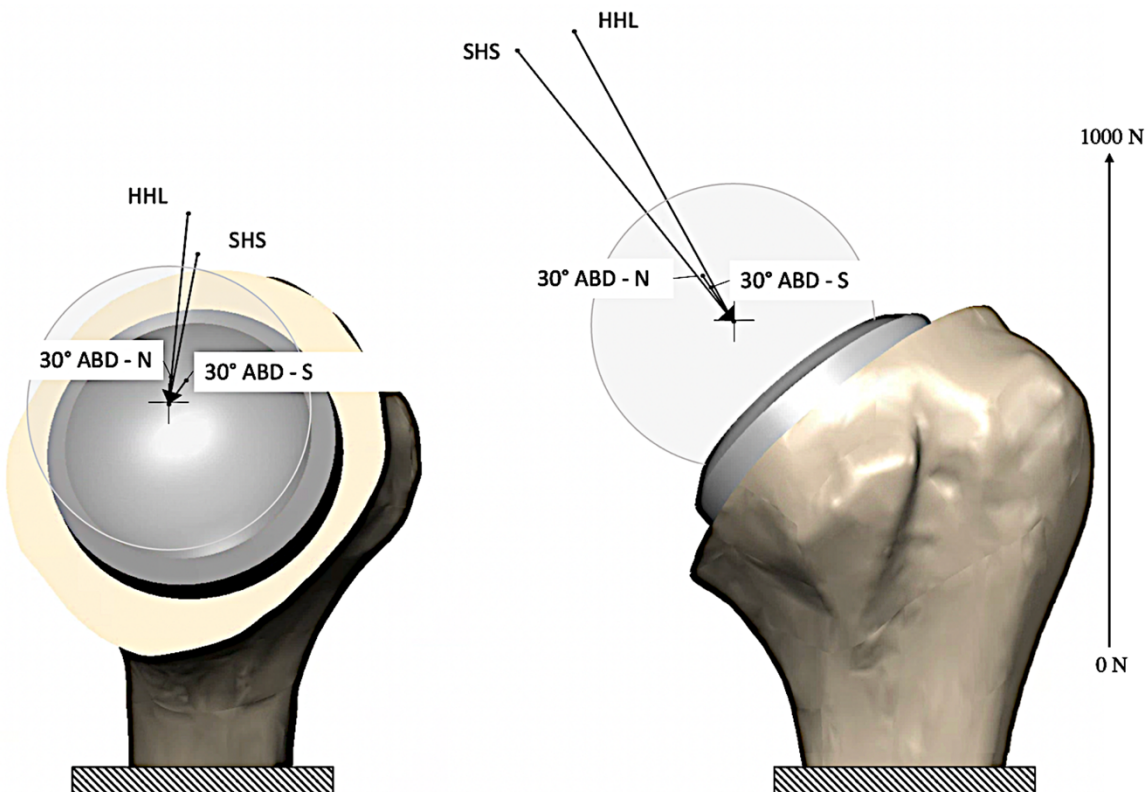


Figure 6-3: Force Vectors for Four Activities of Daily Living and Projected onto a Humeral Model (Left)

Four loading scenarios representing common activities of daily living that a patient might experience postoperatively (30° shoulder abduction with neutral forearm rotation (30° ABD – N), 30° shoulder abduction with forearm supination (30° ABD – S), a head-height lifting motion (HHL), and a single-arm steering motion (SHS)). Each load was applied to a point consistent with the centre of the glenosphere in the total reversed total shoulder arthroplasty reconstruction. Encastre boundary conditions are depicted at the distal humeral resection surface using striped boxes.

6.3 Outcome Variables and Analysis

In order to quantify the initial fixation of each implantation case, the maximum normal bone-implant distraction (micromotion) was assessed. A one-way repeated measures analysis of variance (ANOVA), and a supplementary two-way repeated measures ANOVA

with Bonferroni correction were conducted for the dependent variable of neck shaft angle for each loading scenario. All statistical analyses were computed using SciPy 1.9.1 [30], with the threshold of significance set as $p < 0.05$.

6.4 Results

Stemless humeral implants exhibit greater stability when implanted at higher neck-shaft angles. At higher neck shaft angles, a larger portion of the implant maintained contact with the cancellous epiphyseal and metaphyseal bone (Figure 6-4 A) when compared to lower, more vertical, neck shaft angles (Figure 6-4 B). For all loading cases, the maximum micromotion was detected on the periphery of the implant baseplate opposite to the direction of loading, while a greater portion of the implant maintained contact with bone at higher, more horizontal, neck shaft angles (Figure 6-5). The repeated measures ANOVA analysis revealed that the maximum micromotion developed at the implant-bone interface was significantly higher for the 130° neck shaft angle implantation conditions (30° shoulder abduction with neutral forearm rotation: $p = 0.0192$, 30° shoulder abduction with forearm supination: $p < 0.0001$, single handed steering motion: $p = 0.0002$, head-height lifting motion: $p = 0.0038$) (Figure 6-6)(Table 6-1). During a supplementary two-way repeated measures ANOVA, Bonferroni correction with an adjusted alpha level of 0.025 ($0.05/2$) per test was utilized to further investigate the significance of neck-shaft angle. Results suggest that across all loading scenarios, neck-shaft angle significantly affected initial implant stability ($p < 0.0001$).

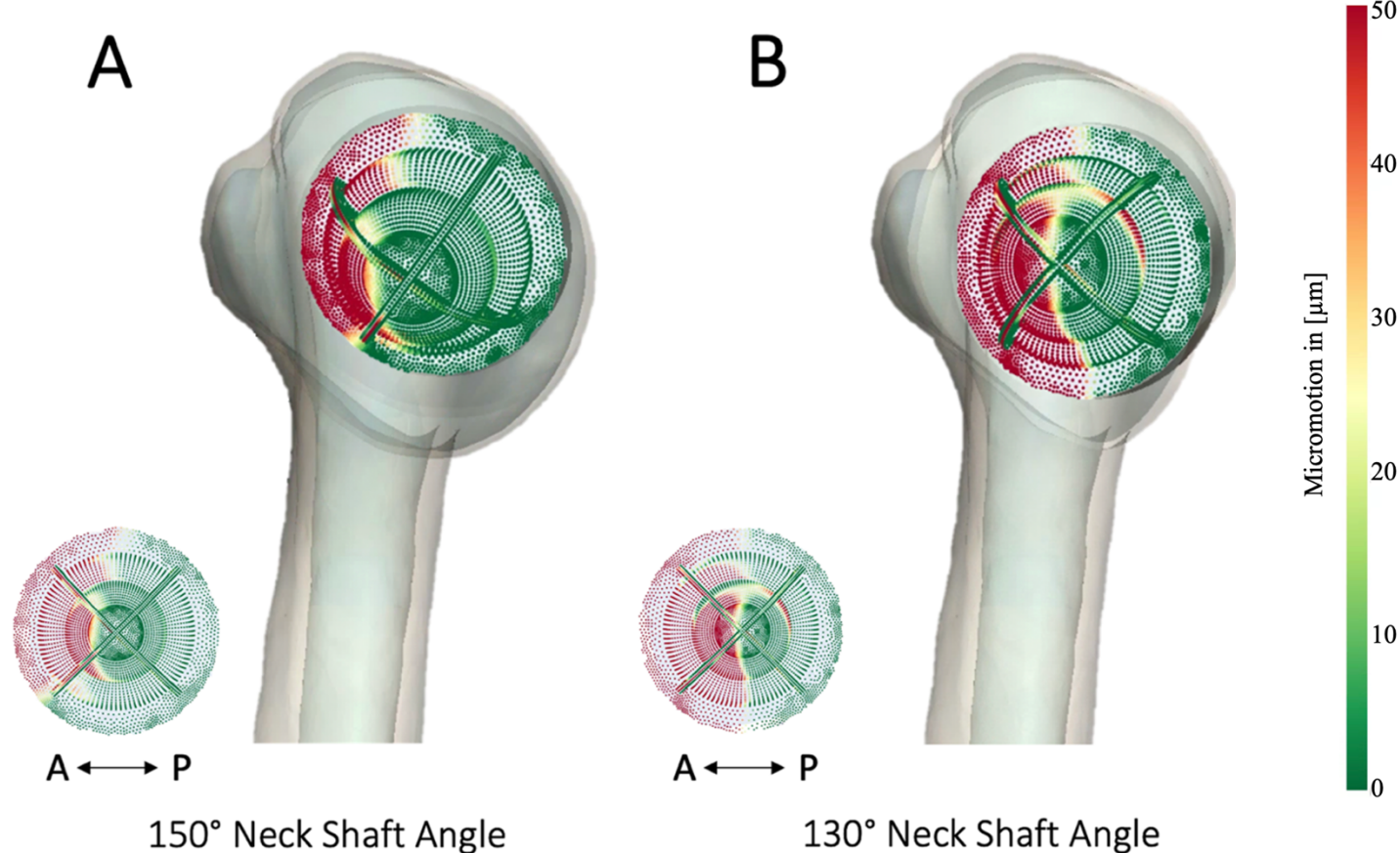


Figure 6-4: Heatmaps of Bone-Implant Distraction, Projected onto a Left Humerus

Posterior-Lateral view of the left humerus, implanted with a generic stemless implant at 150° (A) and 130° (B), with a heatmap of bone-implant distraction magnitude overlayed. A lateral resection-view is also displayed in the bottom left corner of each subplot. For illustration purposes, the micromotion heatmap resulting from a single hand steering motion is shown.

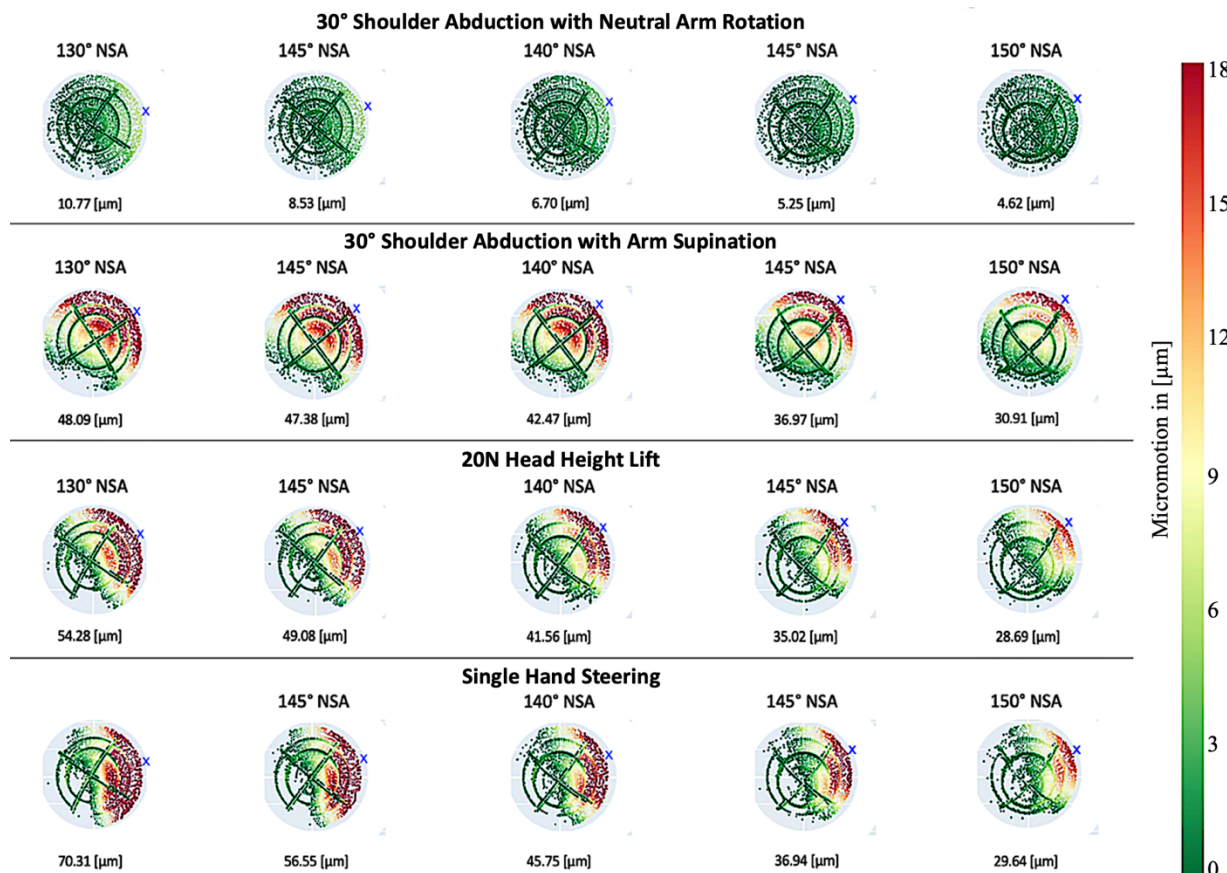


Figure 6-5: Heatmaps of Implant-Bone Distraction Micromotion for Four Activities of Daily Living at Five NSAs

Heatmaps of the micromotions developed at the bone-implant interface ($N = 1$). All plots shown above are visualized medial-laterally at a view normal to the 135° neck shaft angle resection surface. Maximum micromotions were detected at the bone-implant interface at a position opposite to the direction of loading, indicated by the blue cross markings. Areas without coloured nodes did not move relative to bone throughout the analysis.

	Micromotion (μm)									
	130°		135°		140°		145°		150°	
	Mean (SD)	Range	Mean (SD)	Range	Mean (SD)	Range	Mean (SD)	Range	Mean (SD)	Range
30° shoulder abduction with neutral forearm rotation	4.19 (2.77)	2.29 - 10.77	3.40 (1.99)	2.21 - 8.53	3.05 (1.43)	2.20 - 6.70	2.83 (1.07)	1.76 - 5.25	2.59 (0.80)	1.80 - 4.62
30° shoulder abduction with forearm supination	33.71 (8.01)	24.08 - 48.09	31.06 (8.36)	21.74 - 47.38	27.66 (7.86)	19.11 - 42.47	23.32 (7.15)	16.60 - 36.97	18.80 (6.50)	12.06 - 30.91
Single handed steering motion	26.66 (19.94)	6.74 - 70.31	19.79 (15.16)	7.05 - 56.55	16.23 (11.70)	7.42 - 45.75	13.81 (9.12)	7.51 - 36.94	11.68 (6.92)	7.72 - 29.64
Head-height lifting motion	17.39 (15.96)	4.28 - 54.28	14.33 (14.12)	3.53 - 49.08	12.11 (11.71)	3.95 - 41.56	11.17 (9.79)	4.56 - 35.02	9.47 (7.45)	5.24 - 28.69

Table 6-1: Summary of Micromotions Developed During Activities of Daily Living at Varied NSAs

A tabular format description of the micromotions, standard deviations, and ranges of micromotion developed during 30° shoulder abduction with neutral forearm rotation, 30° shoulder abduction with forearm supination, single handed steering, and head height lifting motions.

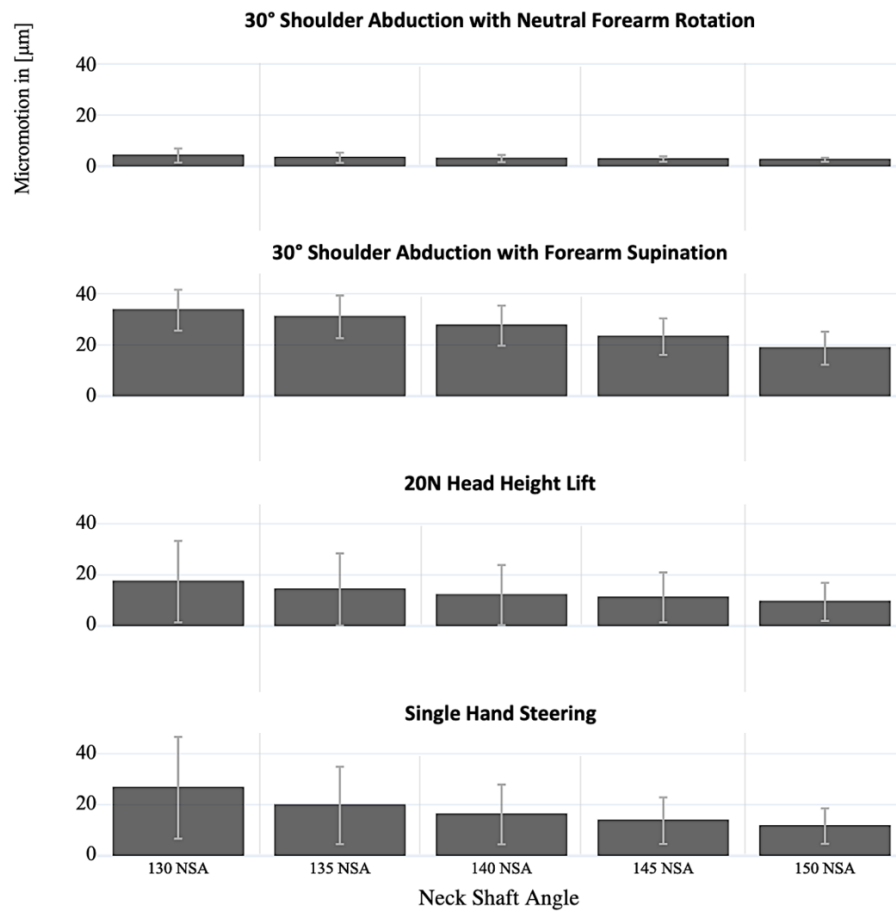


Figure 6-6: Maximum Micromotion (mean \pm 1 SD) Levels for the Four Simulated Activities at Five Neck Shaft Angles.

A bar graph showing the relative micromotions for each activity of daily living at 130°, 135°, 140°, 145°, and 150° NSA.

With every 5° increase in neck shaft angle, there was an average 14% decrease in the micromotion (30° shoulder abduction with neutral forearm rotation: 11.2%, 30° shoulder abduction with forearm supination: 13.5%, single handed steering motion: 18.5%, head-height lifting.

6.5 Discussion

The principal objective of this work was to assess how humeral resection inclination (or neck shaft angle) may affect the primary stability of stemless reverse humeral implants. We specifically hypothesized that increasing neck shaft angle, thereby decreasing implant inclination, would elicit a more favorable level of implant stability than is experienced at lower neck shaft angles. Our results identified that variations in the neck shaft angle substantially influence time zero stemless implant fixation and stability.

From the results of this investigation, we postulate that increasing the neck shaft angle and the potential improvement for stemless implant fixation may in part be attributed to the line-of-action of the joint loading vector relative to the implant-bone interface. With a more horizontal (higher neck shaft angle) the joint loading vector passes closer to the center of the interface, reducing eccentric loading. Hence, the implant experiences a greater amount of compression into the proximal humeral bone and less distraction or lift-off. With a more vertical neck shaft angle, the implant does also experience compression, however, there is also a greater amount of eccentric loading. These eccentric loads, with a lower neck shaft angle, result in substantially greater amount of distraction of the implant anteriorly. Distraction, as a mechanism of failure, would clinically present as lift off of the implant anteriorly or flipping out of the implant.

We also postulate that bone quality may be influential, as altering the neck shaft angle affects the native bone stock present at the bone-implant interface. Reeves *et al.* [19] have shown that the best quality bone in the proximal humerus is located peripherally in the metaphysis and in the humeral head. As such, we hypothesized that a higher neck shaft angle resection preserves a wedge of higher quality bone behind at the medial calcar region [19] (Figure 6-7). This was verified in a post-experimental evaluation, where five cadaveric

specimens were evaluated in a similar manner as that leveraged in Chapter 4. The BMD of each specimen was plotted at regions adjacent to the implant positioned first at 135° NSA and then at 145° NSA. It was found that 145° NSA stemless humeral implants are installed in better quality bone than their 135° NSA counterparts ($p < 0.01$)(Figure 6-8). Therefore, a stemless humeral implant placed at a higher neck shaft angle is typically inset into better quality bone in the medial calcar area than it would be at a lower neck shaft angle. In addition to improved primary fixation, this increase in BMD is also likely to contribute to enhanced long-term implant stability, due to the increased incidence of positive bone remodelling and therefore better osseointegration in the higher quality periprosthetic bone [31]. A full description of this aforementioned BMD analysis can be found in Appendix G.

Alterations in neck shaft angle do have other important ramifications. Higher neck shaft angles result in greater humeral distalization, adduction impingement, possible notching, reduced abduction impingement and reduced internal/external rotation [15], [22]. In contrast, lower neck shaft angles result in greater humeral offset, improved adduction motion and rotation, and a higher potential for abduction impingement [22], [32]. All of the above factors should be considered when selecting a particular neck shaft angle.

There are limitations with the present work. A generic stemless implant design was assessed instead of implants currently available in the global market, which may lessen the clinical significance of these findings. The use of a generic implant ensured that full control over implant variables could be maintained and could therefore align with the initial hypothesis. This provided unbiased insight into how neck shaft angle may affect primary stability of stemless humeral implants. Future investigations should continue to assess additional implant designs in order to provide a more thorough evaluation on the load transfer effects of varying neck shaft angle.

Another possible limitation of this work is the small sample size utilized. Future investigations should use a larger cohort of patient CTs in order to better represent the global population. A larger cohort would provide valuable insights into diverse populations,

including variations across sex, broader age ranges, and different geographic regions, thereby enhancing the generalizability and applicability of the findings.

However, the use of 8 specimens is higher than typically employed for computational studies of this nature on implant-bone stress analyses. Additionally, this evaluation was focused on time-zero (directly after implantation) implant behaviours. This is noteworthy, as trabecular bone is mechanoresponsive, and the differences in loading postoperatively may result in changes to the osseointegration responses in bone during the postoperative rehabilitation period. Specifically, in press-fit implants, experimental analyses focused on the effect of cyclical loading may provide valuable insight into the failure mechanisms of stemless humeral implants.

Strengths of this work include the repeated measures study design, with each specimen reconstructed repeatedly with varying neck shaft angles. This produced a more robust statistical power. The loads applied were also based on *in-vivo* telemetized data. While this data was collected for an anatomical total shoulder arthroplasty implant, *in-vivo* data for RSA does not yet exist. The same general loading scenarios adapted for RSA kinematics, should not be markedly different.

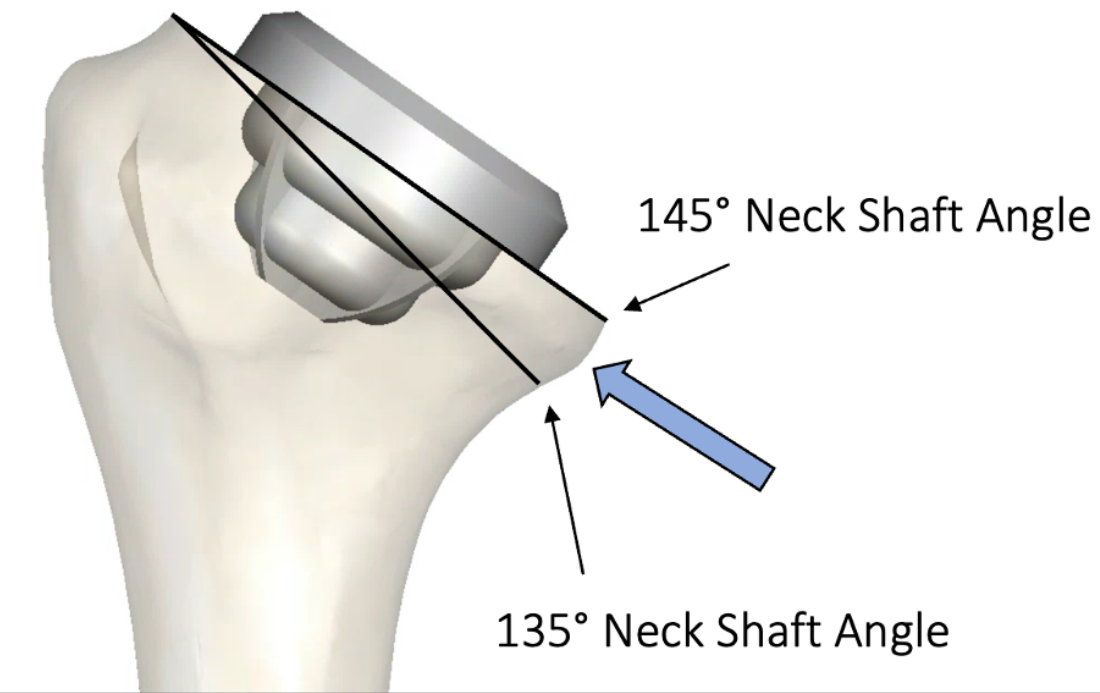


Figure 6-7: Depiction of a Wedge of High-Quality Bone, Removed by a 135° NSA Resection

An implant placed at a 145° neck shaft angle. The resultant resection at 145° leaves a wedge of higher quality medial calcar bone behind (blue arrow) for improved implant stability and fixation when compared with the 135° neck shaft angle resection.

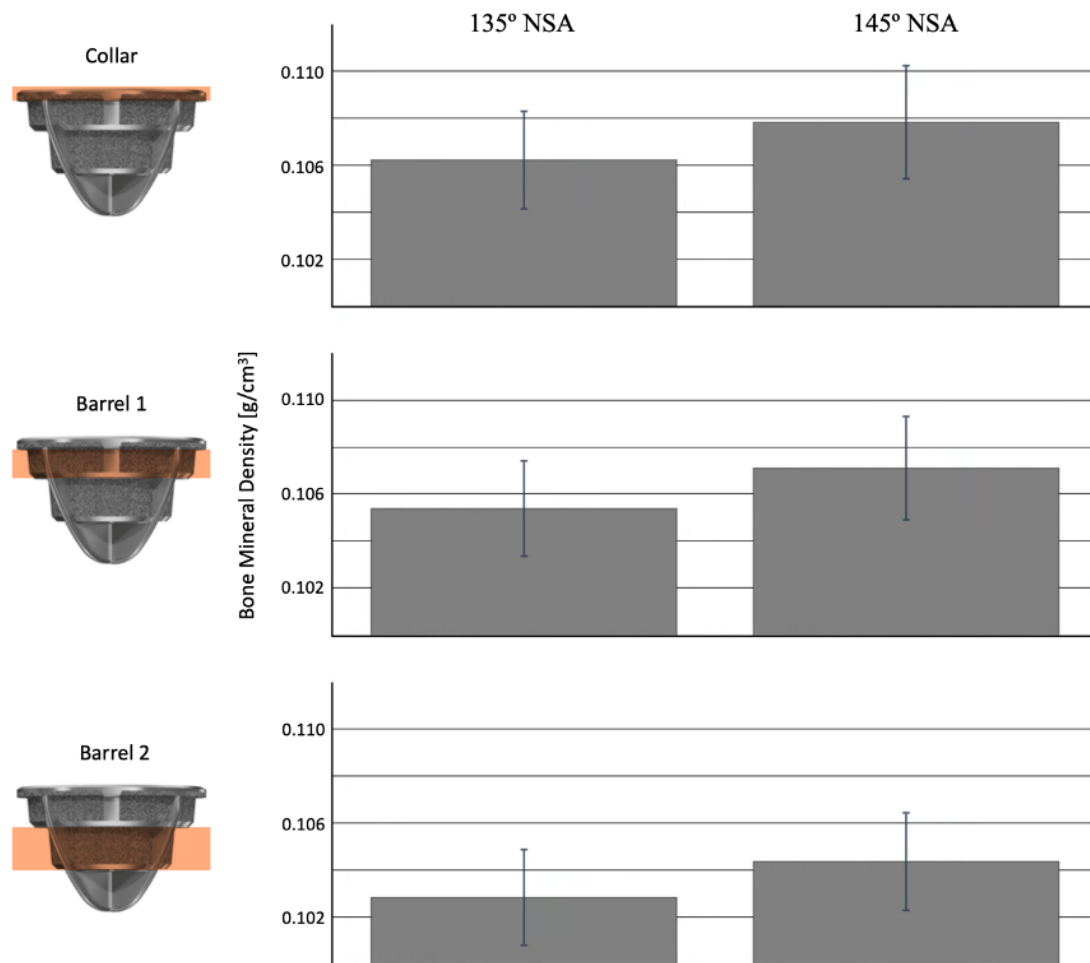


Figure 6-8: Interface BMD of 135° NSA and 145° NSA Stemless Humeral Implants

Periprosthetic bone mineral density in 135° NSA (left) and 145° NSA (right) stemless humeral implants. Each specimen was evaluated at three separate periprosthetic regions: at the collar-adjacent interface, and adjacent to the two osseointegrating barrels.

6.6 Conclusion

The neck shaft angle of implantation for a stemless reverse humeral component is a modifiable parameter that has a substantial effect on time zero implant stability. Lower, more varus, neck shaft angles increase bone-implant distractions with simulated activities of daily living. It is therefore suggested that in cases where primary reverse stemless implant stability is to be maximized for fixation, humeral head osteotomies at a higher neck shaft angle may be beneficial.

6.7 References

- [1] D. E. Cunningham, G. W. Spangenberg, G. D. G. Langohr, G. S. Athwal, and J. A. Johnson, “Stemless Reverse Humeral Component Neck Shaft Angle has an Influence on Initial Fixation,” *J. Shoulder Elb. Surg.*, 2023, doi: 10.1016/j.jse.2023.06.035.
- [2] J. M. Reeves, G. D. G. Langohr, G. S. Athwal, and J. A. Johnson, “The effect of stemless humeral component fixation feature design on bone stress and strain response: a finite element analysis,” *J. Shoulder Elb. Surg.*, vol. 27, no. 12, pp. 2232–2241, 2018, doi: 10.1016/j.jse.2018.06.002.
- [3] D. A. Ajibade, C. X. Yin, H. S. Hamid, B. P. Wiater, A. Martusiewicz, and J. M. Wiater, “Stemless reverse total shoulder arthroplasty: a systematic review,” *J. Shoulder Elb. Surg.*, vol. 31, no. 5, pp. 1083–1095, 2022, doi: 10.1016/j.jse.2021.12.017.
- [4] N. Razfar, “Finite Element Modeling of the Proximal Humerus to Compare Stemless , Short and Standard Stem Humeral Components of Varying Material Stiffness for Shoulder Arthroplasty,” University of Western Ontario, 2014. [Online]. Available: <https://ir.lib.uwo.ca/etd/2431>
- [5] C. Quental, J. Folgado, M. Comenda, J. Monteiro, and M. Sarmento, “Primary stability analysis of stemless shoulder implants,” *Med. Eng. Phys.*, vol. 81, pp. 22–29, 2020, doi: 10.1016/j.medengphy.2020.04.009.
- [6] N. T. Formaini, N. G. Everding, J. C. Levy, B. G. Santoni, A. N. Nayak, and C. Wilson, “Glenoid baseplate fixation using hybrid configurations of locked and unlocked peripheral screws,” *J. Orthop. Traumatol.*, vol. 18, no. 3, pp. 221–228, 2017, doi: 10.1007/s10195-016-0438-3.
- [7] E. J. Martin, T. R. Duquin, and M. T. Ehrensberger, “Reverse total shoulder glenoid baseplate stability with superior glenoid bone loss,” *J. Shoulder Elb. Surg.*, vol. 26, no. 10, pp. 1748–1755, 2017, doi: 10.1016/j.jse.2017.04.020.
- [8] P. Favre and A. D. Henderson, “Prediction of stemless humeral implant micromotion during upper limb activities,” *Clin. Biomech.*, vol. 36, pp. 46–51,

- 2016, doi: 10.1016/j.clinbiomech.2016.05.003.
- [9] ASTM, “ASTM F2028-17 Standard Test Methods for Dynamic Evaluation of Glenoid Loosening or Disassociation,” pp. 1–15, 2018, doi: 10.1520/F2028-17.Copyright.
 - [10] P. Favre *et al.*, “In vitro initial stability of a stemless humeral implant,” *Clin. Biomech.*, vol. 32, pp. 113–117, 2016, doi: 10.1016/j.clinbiomech.2015.12.004.
 - [11] N. Bonnevialle, L. Geais, J. H. Müller, and J. Berhouet, “Effect of RSA glenoid baseplate central fixation on micromotion and bone stress,” *JSES Int.*, vol. 4, no. 4, pp. 979–986, 2020, doi: 10.1016/j.jseint.2020.07.004.
 - [12] N. Kohli, J. C. Stoddart, and R. J. van Arkel, “The limit of tolerable micromotion for implant osseointegration: a systematic review,” *Sci. Rep.*, vol. 11, no. 1, pp. 1–11, 2021, doi: 10.1038/s41598-021-90142-5.
 - [13] H. Kawahara, D. Kawahara, M. Hayakawa, Y. Tamai, T. Kuremoto, and S. Matsuda, “Osseointegration under immediate loading: Biomechanical stress-strain and bone formation-resorption,” *Implant Dent.*, vol. 12, no. 1, pp. 61–68, 2003, doi: 10.1097/01.ID.0000034394.75768.E3.
 - [14] S. Goodman, J. -S Wang, A. Doshi, and P. Aspenberg, “Difference in bone ingrowth after one versus two daily episodes of micromotion: Experiments with titanium chambers in rabbits,” *J. Biomed. Mater. Res.*, vol. 27, no. 11, pp. 1419–1424, 1993, doi: 10.1002/jbm.820271109.
 - [15] B. K. Jeon *et al.*, “Combined effect of change in humeral neck-shaft angle and retroversion on shoulder range of motion in reverse total shoulder arthroplasty - A simulation study,” *Clin. Biomech.*, vol. 31, pp. 12–19, 2016, doi: 10.1016/j.clinbiomech.2015.06.022.
 - [16] A. M. Kerrigan, J. M. Reeves, G. D. G. Langohr, J. A. Johnson, and G. S. Athwal, “The influence of reverse arthroplasty humeral component design features on scapular spine strain,” *J. Shoulder Elb. Surg.*, vol. 30, no. 3, pp. 572–579, 2021, doi: 10.1016/j.jse.2020.06.011.
 - [17] B. S. Werner, J. Chaoui, and G. Walch, “The influence of humeral neck shaft angle

- and glenoid lateralization on range of motion in reverse shoulder arthroplasty,” *J. Shoulder Elb. Surg.*, vol. 26, no. 10, pp. 1726–1731, 2017, doi: 10.1016/j.jse.2017.03.032.
- [18] N. K. Knowles, J. M. Reeves, and L. M. Ferreira, “Quantitative Computed Tomography (QCT) derived Bone Mineral Density (BMD) in finite element studies: a review of the literature,” *J. Exp. Orthop.*, vol. 3, no. 1, 2016, doi: 10.1186/s40634-016-0072-2.
 - [19] J. M. Reeves, “An In-Silico Assessment of Stemless Shoulder Arthroplasty: from An In-Silico Assessment of Stemless Shoulder Arthroplasty: from CT to Predicted Bone Response CT to Predicted Bone Response.” 2018. [Online]. Available: <https://ir.lib.uwo.ca/etdhttps://ir.lib.uwo.ca/etd/5398>
 - [20] Parametric Products, “CadQuery.” Github, 2022. [Online]. Available: <https://github.com/CadQuery/cadquery>
 - [21] T. S. Bae, E. E. Ritzer, W. Cho, and W. Joo, “Effect of fin length and shape of stemless humeral components in a reverse shoulder implant system: a FEA study,” *J. Mech. Sci. Technol.*, vol. 35, no. 1, pp. 417–422, 2021, doi: 10.1007/s12206-020-1241-x.
 - [22] A. Arenas-Miquelez, R. J. Murphy, A. Rosa, D. Caironi, and M. A. Zumstein, “Impact of humeral and glenoid component variations on range of motion in reverse geometry total shoulder arthroplasty: a standardized computer model study,” *J. Shoulder Elb. Surg.*, vol. 30, no. 4, pp. 763–771, 2021, doi: 10.1016/j.jse.2020.07.026.
 - [23] N. Razfar, J. M. Reeves, D. G. Langohr, R. Willing, G. S. Athwal, and J. A. Johnson, “Comparison of proximal humeral bone stresses between stemless, short stem, and standard stem length: A finite element analysis,” *J. Shoulder Elb. Surg.*, vol. 25, no. 7, pp. 1076–1083, 2016, doi: 10.1016/j.jse.2015.11.011.
 - [24] S. Synnott, “The Effect of Implant Girth and Implant Collar on the Degree of Bone to Implant Contact and Bone Stresses in the Proximal Humerus,” The University of Western Ontario, 2018.

- [25] E. F. Morgan, H. H. Bayraktar, and T. M. Keaveny, “Trabecular bone modulus-density relationships depend on anatomic site,” *J. Biomech.*, vol. 36, no. 7, pp. 897–904, 2003, doi: 10.1016/S0021-9290(03)00071-X.
- [26] N. Knowles, “Improving Material Mapping in Glenohumeral Finite Element Models: A Multi-Level Evaluation,” *Electron. Thesis Diss. Repos.*, 2019, [Online]. Available: <https://ir.lib.uwo.ca/etd/6100>
- [27] M. D. Mahaffy, “Examining Reverse Total Shoulder Arthroplasty Baseplate Fixation in Patients with E2-type Glenoid Erosion Keywords,” University of Western Ontario, 2018.
- [28] M. Navarro *et al.*, “Biomaterials in orthopaedics Biomaterials in orthopaedics,” *J. R. Soc. Interface*, vol. 5, pp. 1137–1158, 2008, doi: 10.1098/rsif.2008.0151.
- [29] P. Damm and J. Dymke, “Orthoload Database,” *Julius Wolff Institute*, 2021. <https://orthoload.com/database/> (accessed Jul. 26, 2021).
- [30] P. Virtanen *et al.*, “SciPy 1.0: fundamental algorithms for scientific computing in Python,” *Nat. Methods*, vol. 17, no. 3, pp. 261–272, 2020, doi: 10.1038/s41592-019-0686-2.
- [31] S. Sunil and P. Dhatrak, “Biomechanical consideration of bone density and its influence on stress distribution characteristics of dental implants,” *Mater. Today Proc.*, vol. 46, pp. 478–483, 2021, doi: 10.1016/j.matpr.2020.10.368.
- [32] D. M. Kim *et al.*, “Loosening and revision rates after total shoulder arthroplasty: A systematic review of cemented all-polyethylene glenoid and three modern designs of metal-backed glenoid,” *BMC Musculoskelet. Disord.*, vol. 21, no. 1, pp. 1–16, 2020, doi: 10.1186/s12891-020-3135-6.

Chapter 7

7 Thesis Closure

OVERVIEW

This final chapter reiterates the objectives and hypotheses investigated herein, and discusses the works performed to accomplish those aforementioned objectives. The findings of the studies will be highlighted, as well as their strengths and limitations, and future directions regarding the evaluation of stemless reverse humeral prosthetic designs will be proposed.

7.1 Summary

To quantify the relative performance of varied implant designs, it is essential to study the primary fixation effects of individual surgical and design variables. By using a combination of computational and experimental methodologies, it is possible to provide detailed insights into the performance of implants; both strategies that have been leveraged in this thesis. A high-fidelity computational framework for the evaluation of parametric implant models was developed, and micromotion phenomena were investigated for the implant geometries and surgical variables of interest. A novel loading apparatus and digital tracking system was designed for the evaluation of distractive micromotion; the driving fixation variable identified in the computational analyses. These systems were then adroitly deployed to thoroughly investigate the influence of cadaveric bone surrogate choice, as well as the surgical parameter of neck shaft angle in the context of primary fixation.

The first objective of this work was to quantify both tangential and orthogonal micromotion in stemless humeral component implants. A computational analysis was performed in order to identify the driving implant-specific metric to be used in the evaluation of implant primary fixation. This work is detailed in Chapter 2, which describes the identification of orthogonal distractive micromotion as the most effective measure for the quantification of primary fixation in stemless humeral prostheses.

The results of this primary work are leveraged in Chapter 3, where the second objective of this work was tackled: to develop a loading apparatus capable of applying a complex array of physiologically relevant loads to investigate the degree of primary fixation in stemless orthopaedic implants. Herein, the Comprehensive Evaluation for the Realistic Biomechanical Examination and Repair of Upper-limb Systems (CERBERUS) apparatus was developed to replicate the anatomical loading profiles imposed on the shoulder joint during realistic activities of daily living that a patient might experience during the early postoperative window. High-resolution digital tracking was utilized to facilitate the accurate measurement of relative implant performance, and a comprehensive software was developed to enable synchronized loading and collection of high-resolution images and strain gauge data. In Chapter 3, the successful development of a novel loading apparatus

and data collection suite was described; a system specifically designed to target the measurement of distractive micromotion during physiological loading.

The CERBERUS evaluation technology was then employed in the works detailed in Chapter 4, where the third objective, to compare the results of fixation analyses using biological vs synthetic bone models while using the effects of press-fit in stemless implants and resultant micromotion as a metric for degree of fixation., was beset.

At lower foam densities, fixation was significantly underreported when compared to the biological bone tissue model at sliding fit conditions ($p = 0.02$). At higher press-fit magnitudes, models utilizing higher density foams overreported stemless component fixation when compared to the biological model ($p \leq 0.046$). Secondly, it was found that press-fit has a significant effect on the primary fixation of stemless humeral components ($p < 0.01$). Therefore, the null hypotheses (i) there is no significant difference in the micromotion of implants installed in biological bone tissue vs when installed in polyurethane foam substitute materials and (ii) press-fit magnitude does not have a significant effect on the primary fixation of stemless components, were rejected. The work described in Chapter 4 also identified the important note that the production of bone tissue fragments during the insertion of the press-fit implant may impose lubrication phenomena at the implant-bone interface, thereby compromising the optimal primary fixation of the press-fit implant. This phenomenon was not replicated in the foam analogue materials.

The fourth objective of this thesis was to experimentally evaluate the performance of 145° and 135° neck shaft angle stemless humeral components using micromotion as a metric for degree of fixation. This was detailed in Chapter 5, where the CERBERUS apparatus was employed to replicate the loading environment of the shoulder post-surgery.

The conclusion of the fourth work of this dissertation found that increasing neck shaft angle provided better primary fixation during experimental physiological loading. Therefore, the null hypothesis (iii) there is no significant difference in micromotion developed at the implant-bone interface between 145° and 135° neck shaft angle in stemless reverse

shoulder arthroplasty humeral components *in-vitro*, was rejected, as statistically significant ($p = 0.001$) differences in normal micromotion were detected at the implant-bone interface. This was noteworthy, as clinicians are generally enticed to decrease the neck shaft angle of reversed humeral prostheses due to the previously reported benefits to postoperative range of adduction motion and rotation, a greater humeral offset distance, and decreased risk of scapular notching. However, the work contained herein has identified that the possible benefits to reducing neck shaft angle may be offset due to the increased risk of premature failure in stemless humeral implants.

This same surgical variable of neck shaft angle was then re-evaluated *in-silico* in Chapter 6 to exhaustively investigate the fixation of stemless humeral prostheses at other varying clinically relevant neck-shaft angles; thereby completing the fifth objective of this work: to develop a three-dimensional finite element model of the proximal humerus to evaluate the comparative degree of fixation of stemless reverse shoulder arthroplasty humeral components at varying neck shaft angles.

This work is detailed in Chapter 6, where a program was developed and leveraged to create a parametrically designed generic stemless reversed humeral implant which was then evaluated for primary fixation at varying neck shaft angles ranging between 130° and 150° . The results of this work were in agreement with the results of the experimental testing outlined in Chapter 5; also indicating that increasing implant neck shaft angle provided better primary stability than lower, more varus, neck shaft angles. These results rejected null hypothesis (iv), that there is no significant difference in micromotion at the implant-bone interface when comparing reverse shoulder arthroplasty stemless humeral components at varying neck shaft angles *in silico*, as statistically significant ($p < 0.001$) differences were detected between neck shaft angles.

The consistent observation of improving fixation at higher neck shaft angles then led to an additional null hypothesis which was discussed in Chapter 5: that the bone quality at the bone-implant interface is not better in stemless implants installed at higher neck shaft angles when compared to their more varus counterparts. It was found that statistically

significant differences in average BMD were present when comparing 135° NSA and 145° NSA implant prosthetic bone quality, and thus, the additional null hypothesis (v) there is no significant difference in the bone mineral density of peri-prosthetic bone in 135° NSA and 145° NSA implants, was also rejected.

The present work represents the continued expanse to the current breadth of knowledge regarding stemless implants, and in particular, the fixation effects of implant design and surgical implantation variables. It was curious to note that although decreasing neck shaft angle is a popular surgical decision in order to increase postoperative range of motion and reduce adduction impingement [1]–[3], those benefits may come at the expense of initial fixation of the implant.

7.2 Strengths and Limitations

The implementation of 3D physiological loading into the evaluation of RTSA humeral components represents a step forward for the *in-vitro* biomechanical evaluation of humeral components. The development of the CERBERUS apparatus enabled a much more thorough evaluation of the performance of stemless implants than has previously been achievable. Additionally, the incorporation of high-resolution digital quantification of implant-bone relative motion is a marketable improvement on the precedent use of physical linear displacement measuring devices. Because physiological boundary loading of the shoulder articulation was directly evaluated in a population of cadaveric shoulders, the experimental data obtained can be considered to be representative of what could be reasonably expected in stemless shoulder prostheses during common activities of daily living.

The loads applied during experimental evaluation of neck shaft angle in this present thesis were produced in a procedure intended on identifying the worst-case boundary forces that an implant might experience postoperatively. Alternatively, the loads utilized during the evaluation of neck shaft angle could have been less conservative; more demonstrative near-perfect patient compliance to a restrictive surgeon-suggested postoperative protocol. Another strength of this work was the implementation of a cyclic loading protocol. By

investigating the behaviour of press-fit implants over a period of cycled loading, a more reasonable representation of the fixation of stemless implants was derived than would have been consequent of unistatic loading protocol. Overall, the results of the experimental work contained herein are commensurate with the implant failure mechanisms observed clinically.

The investigation of RTSA humeral component performance using a finite element model facilitated the measurement and visualization of the bone-implant interfacial mechanics that would not be measurable using laboratory methods without obtaining an artifact-less x-ray; something that is not possible using existing technologies. This also allowed for the simulation of a large distribution of the loads developed during true activities of daily living to be compared across a variety of neck-shaft angles.

There are some limitations of the present work. First, the finite element model employed assumptions regarding the material properties and contact interaction properties of the implants and bone. These included modelling of isotropic trabecular bone, when in reality trabecular bone is highly anisotropic. With respect to the bone-implant interface, a realistic implant would be press-fit into place; a procedure that was not included in the present work. Second, constant friction properties were assumed about the implant interface, whereas many clinically utilized implants commonly exhibit a variety of different surface treatments within a single component. Additionally, in the neck shaft angle evaluations, telemetrized data from anatomic humeral components was used. This introduced some discrepancy in the loading protocol when applied to reversed humeral component designs, as previous works have found that RTSA articular loads are lower than their anatomic TSA counterparts [4]. In reality, the loading magnitudes experienced by an RTSA would likely be lower, which may influence the micromotion magnitudes detected. However, it is reasonable to assume that the comparative results of this investigation are still applicable, as the 135° NSA eccentricities in the reversed loading environment would still be larger than those at 145° NSA resections.

Although these assumptions employed are consistent with other finite element simulations of orthopaedic prostheses, they may have influenced the micromotion magnitudes reported. While these limitations certainly promote direction for future works, it is not unreasonable to accept the experimental and computational protocols described herein as movements in a positive direction to a more thorough and accurate simulation of the fixation behaviours of stemless press-fit orthopaedic implants.

7.3 Future Investigations

The fixation evaluation strategy employed herein was effective in achieving the specific objectives of this work; however, there still exists the opportunity to further investigate the fixation of press-fit implants.

Future work should focus on determining articular loads in reversed total shoulder arthroplasty constructs. This was a potential limitation of the works in Chapter 5 and 6 focused on the fixation behaviour of reversed implants. This would involve the design of a telemetrized reversed shoulder implant, and the collection of load data during various activities of daily living; similar to the previous works of the Julius Wolff Institute [5].

Another topic of ample research would be a more thorough investigation into the press-fit mechanics of osseointegrating prostheses. As discussed in Chapter 4, understanding the press-fit fixation behaviours of a larger variety of common implant geometries could provide much-needed insight into the effects of different implant parametric variables. Further, investigating the micro-failure mechanisms of trabecular bone during the press-fit of implants would provide clarity on the influence of lubricating bone debris, and its impact on primary fixation. An effective method for evaluating these variables would be through leveraging micro-CT techniques to obtain data on the inhomogenous failure of periprosthetic bone.

Finally, factors that contributed to the limitations of this work were the computational assumptions made during the evaluation of implant fixation. To date, evaluations on the fixation and load transfer properties of osseointegrating prostheses have not considered the

press-fit in complex implant geometries; which would require an explicit press-fit analysis before evaluating the behaviour of a loaded implant. This is a factor that heavily influences the initial contact pressure at the implant-bone interface, and therefore the friction force resisting movement of the implant. In addition, some studies have indeed employed heterogeneous trabecular bone properties through the application of CT-derived elastic material properties, but have not commonly utilized anisotropic material properties. This is noteworthy as trabecular bone is highly anisotropic and, especially in the context of press-fit, would likely behave differently with the dissimilar material properties in the secondary or tertiary directions.

7.4 Significance and Conclusions

As the innovation of RTSA continues to accelerate, the accuracy and clinical relevance of implant evaluation methodologies has become much more important. With greater implant design refinement comes a greater requirement for reliable testing procedures to drive the direction of that optimization. This present work shows the importance, and the possibility, of accurately replicating the articular loads achieved by the shoulder joint postoperatively, as well as the dangers of utilizing simplified or potentially less costly materials and evaluation equipment during the quantification of implant primary fixation. The relevance of considering micromotion as two distinct metrics (*viz.* normal vs. tangential), and the focus on normal mode due to its prominence for the stemless implant designs was also raised in this work.

The ability to confidently assess the performance of implants *in-vitro* will help improve the current state of implant technology by allowing implant fixation to easily be evaluated under different loading conditions. Having a thorough understanding of implant performance under clinically-relevant conditions will ultimately result in an overall improvement in RTSA implant technology, as well as a greater understanding of the clinical performance of these designs before risking patient well-being in clinical trials.

The ability to confidently assess the performance of implants *in-vitro* will help improve the current state of implant technology by allowing implant fixation to easily be evaluated

under different loading conditions. Having a thorough understanding of implant performance under clinically-relevant conditions will ultimately result in an overall improvement in RTSA implant technology, as well as a greater understanding of the clinical performance of these designs before risking patient well-being in clinical trials.

7.5 References

- [1] A. Arenas-Miquelez, R. J. Murphy, A. Rosa, D. Caironi, and M. A. Zumstein, “Impact of humeral and glenoid component variations on range of motion in reverse geometry total shoulder arthroplasty: a standardized computer model study,” *J. Shoulder Elb. Surg.*, vol. 30, no. 4, pp. 763–771, 2021, doi: 10.1016/j.jse.2020.07.026.
- [2] B. K. Jeon *et al.*, “Combined effect of change in humeral neck-shaft angle and retroversion on shoulder range of motion in reverse total shoulder arthroplasty - A simulation study,” *Clin. Biomech.*, vol. 31, pp. 12–19, 2016, doi: 10.1016/j.clinbiomech.2015.06.022.
- [3] D. M. Kim *et al.*, “Loosening and revision rates after total shoulder arthroplasty: A systematic review of cemented all-polyethylene glenoid and three modern designs of metal-backed glenoid,” *BMC Musculoskelet. Disord.*, vol. 21, no. 1, pp. 1–16, 2020, doi: 10.1186/s12891-020-3135-6.
- [4] G. D. Langohr, “Fundamentals of the Biomechanical Characteristics Related to the Loading of Reverse Total Shoulder Arthroplasty Implants and the Development of a Wear Simulation Strategy,” 2015. [Online]. Available: https://ir.lib.uwo.ca/etd/3436/?utm_source=ir.lib.uwo.ca%2Fetd%2F3436&utm_medium=PDF&utm_campaign=PDFCoverPages
- [5] P. Damm and J. Dymke, “Orthoload Database,” *Julius Wolff Institute*, 2021. <https://orthoload.com/database/> (accessed Jul. 26, 2021).

Appendices

Appendix A: Glossary of Medical and Engineering Terminology

Anisotropic: Exhibiting different properties in different directions.

Anterior: Toward the front or the front side of the body.

ANOVA: Statistical analysis technique used to compare means of multiple groups to determine if there are significant differences among them.

Arthritis: Inflammation of the joints, causing pain, swelling, and stiffness.

Arthroplasty: Surgical procedure involving the reconstruction or replacement of a joint, typically to relieve pain or improve joint function.

Articular: Relating to the joints, where bones connect and allow movement.

CERBERUS: Comprehensive Evaluation for the Realistic Biomechanical Examination and Repair of Upper-limb Systems

Composite Material: A substance made by combining two or more different materials to leverage the material properties of both.

Distal: Farther away from the center or point of origin in the body.

Extension: Straightening or increasing the angle between body parts.

External Rotation: Outward movement or rotation of a body part away from the center of the body.

Fibrocartilaginous: Composed of or relating to tissue that has characteristics of both fibrous and cartilaginous tissues.

Finite Element Analysis (FEA): A numerical technique used to predict and analyze the behavior of structures or materials by dividing them into smaller, simpler elements

Fixation: Stabilizing or immobilizing a medical device.

Flexion: Bending or decreasing the angle between body parts.

Heterogeneous: Varied or diverse in composition, containing differences or irregularities.

Homogeneous: Uniform or consistent in composition, lacking variations or differences.

In-silico: Performed on a computer or using computer simulations.

In-vitro: Conducted outside the living organism, typically a benchtop study.

In-vivo: Occurring or performed within a living organism or natural setting.

Inclination: The angle or slope of a surface, the tilt or deviation from the horizontal plane.

Internal Rotation: Inward movement or rotation of a body part toward the center of the body.

Isotropic: Having the same properties in all directions.

Lateral: Away from the midline or toward the sides of the body.

Medial: Toward the midline or center of the body.

Moment: A turning force or rotational effect, calculated as the product of a force and its distance from a reference point.

Moment Arm: The perpendicular distance between the line of action of a muscle's force and the axis of rotation at a joint,

Musculoskeletal: Relating to the muscles and bony skeleton.

Orthogonal: Mutually perpendicular to a surface.

Orthopaedics: The medical specialty focused on the diagnosis and treatment of conditions related to the musculoskeletal system, including bones, joints, ligaments, tendons, and muscles.

Osseous: Pertaining to bone tissue or composed of bone.

Physiological Motion: Normal and natural movements or actions of the body, typically associated with the functioning and health of living organisms.

Posterior: Toward the back side of the body.

Posterosuperior: Located toward the back and upper part of a structure or body.

Posterolateral: Positioned toward the back and to the side of a structure or body.

Prosthetic: Artificial body part or device designed to replace or enhance natural functions.

Proximal: Closer to the center or point of origin in the body.

Range of Motion: The extent and direction of movement that a joint or a group of joints can achieve.

Scapulothoracic Rotation: Movement involving the rotation of the shoulder blade (scapula) in relation to the thoracic (ribcage) region.

Tangential: Direction along a tangent, sharing the same instantaneous slope as the surface.

Viscoelastic: Having both viscous and elastic properties.

Appendix B: Loading Apparatus Design and Control

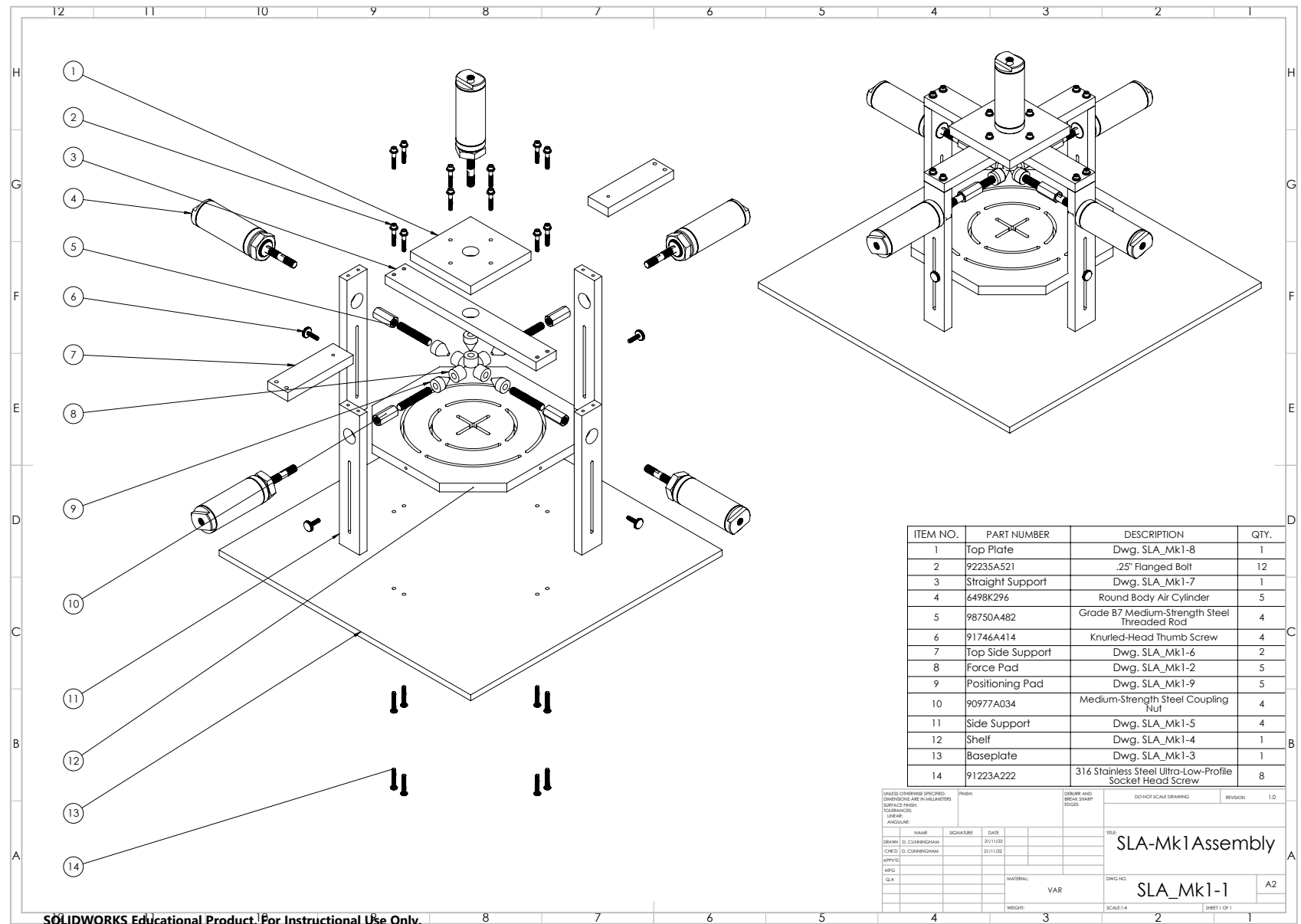
The following section presents the detailed design of the Comprehensive Evaluation for the Realistic Biomechanical Examination and Repair of Upper-limb Systems (CERBERUS) apparatus and controller software.

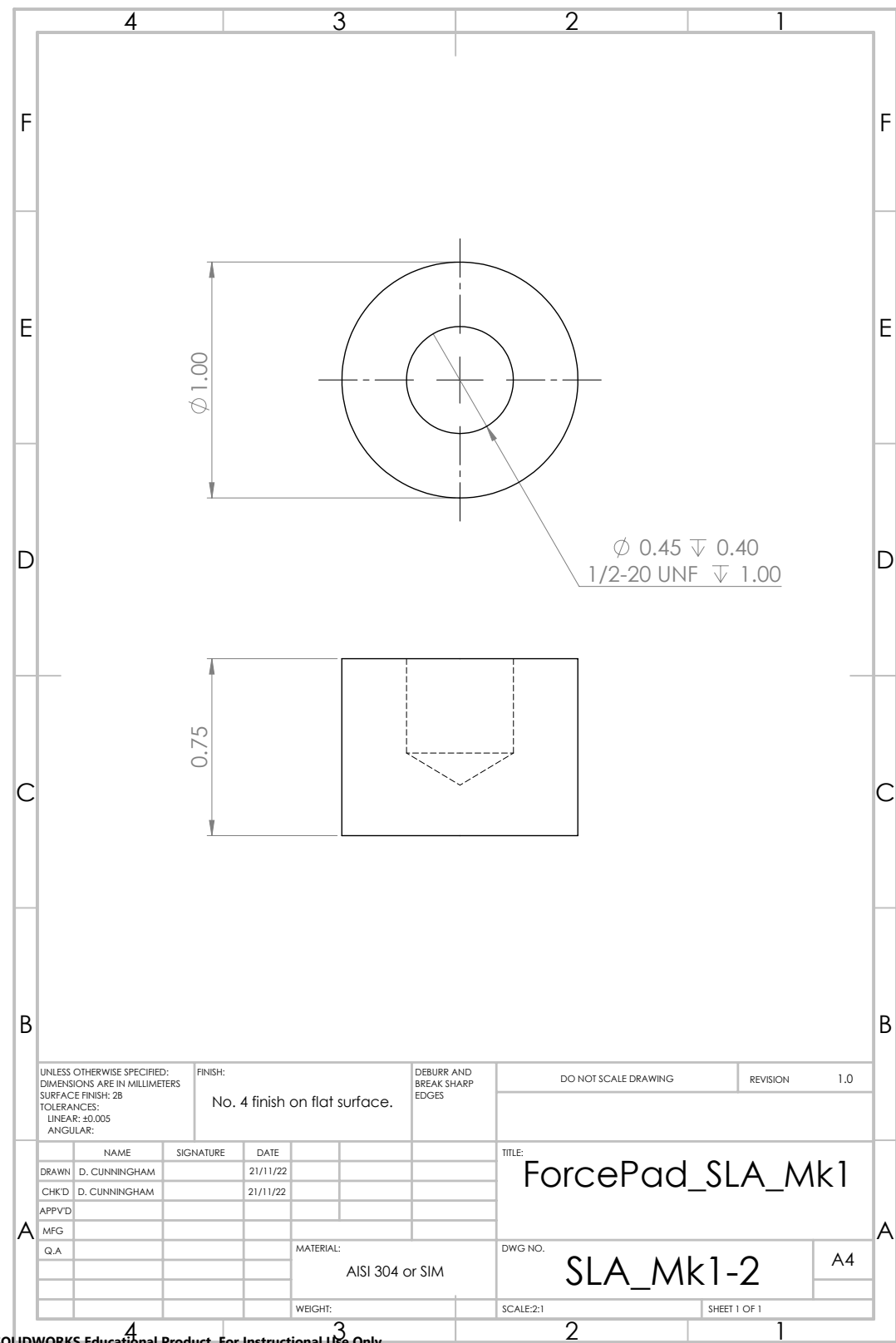
B.1 Introduction

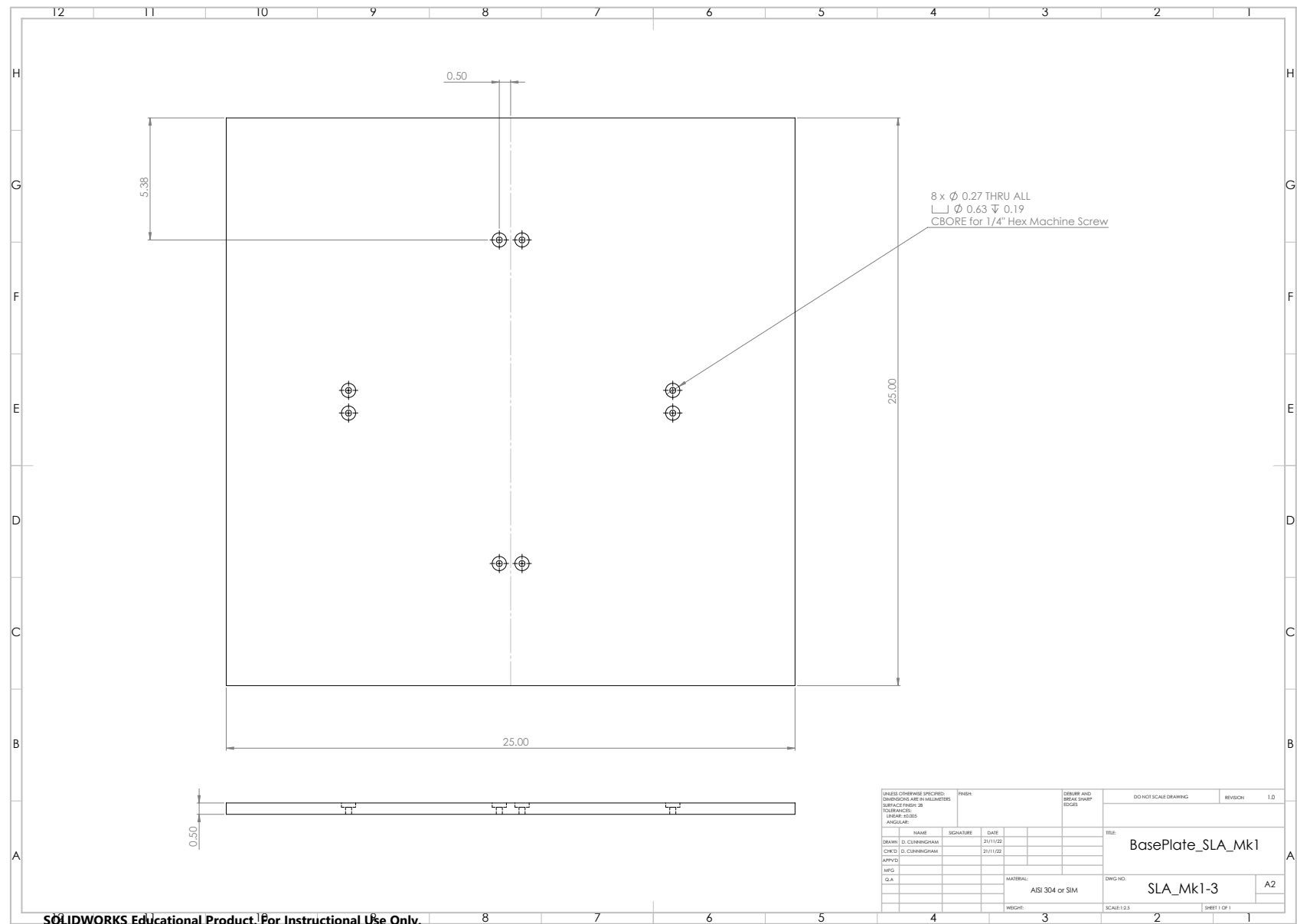
The development and evaluation of a simulator, capable of replicating the true loading environment of the shoulder, is crucial for the ongoing advancement of orthopaedic shoulder implants. In response to this technological gap, a specialized testing platform dedicated to assessing the stability and fixation of these implants was designed. This innovative system utilizes high-resolution machine-vision cameras to measure implant stability, can collect synchronized analogue input data from proxy measurement devices (strain gauges/force sensors), and can apply loads to all actuators simultaneously. This work creates the possibility of including anatomically relevant loading states in our protocols, increasing the robustness of these evaluations compared to conventional techniques employing simplistic planar force loading scenarios. The collected output data is synchronized with loading input values and readily exported for streamlined statistical analysis.

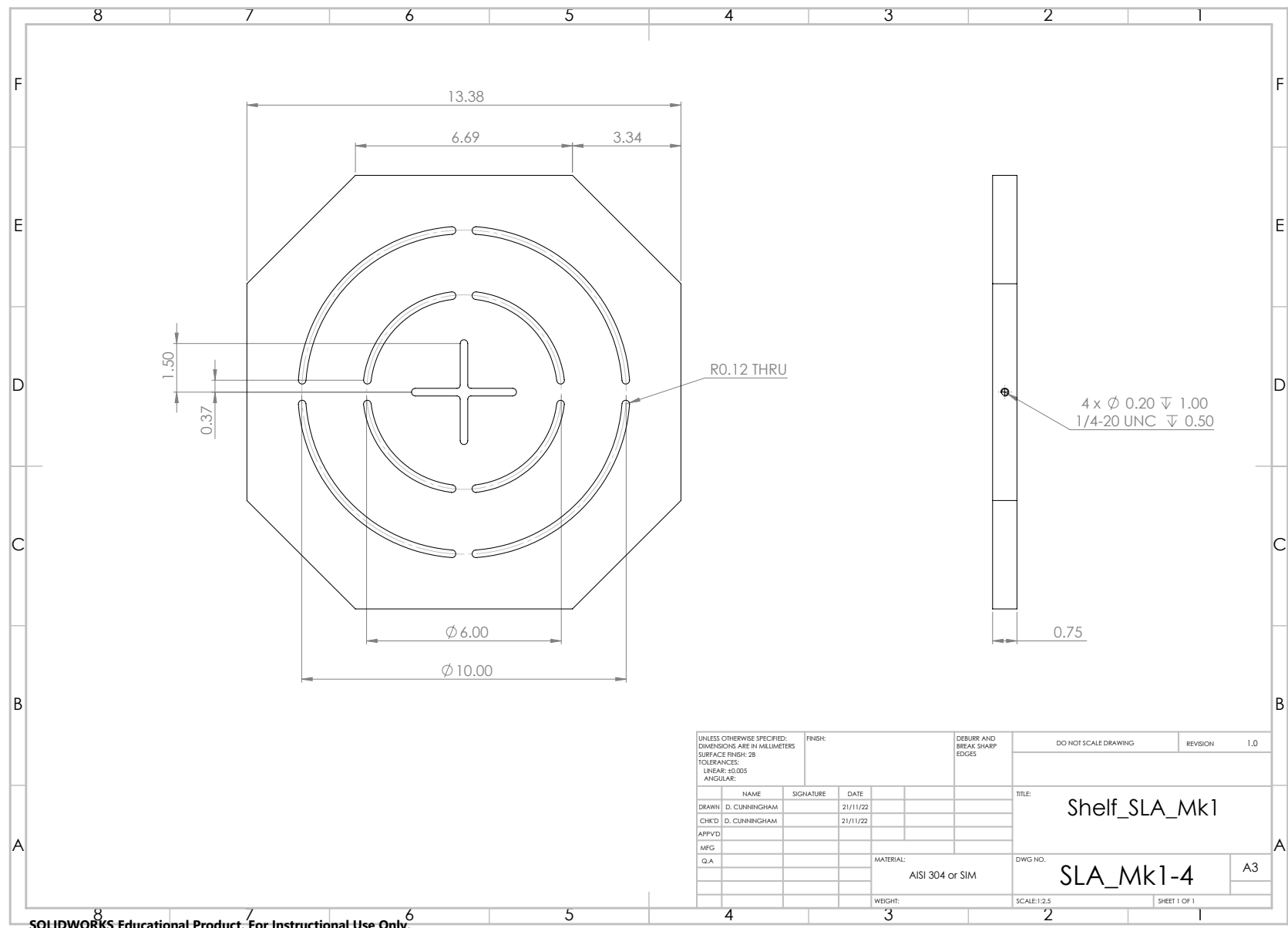
B.2 Physical Design

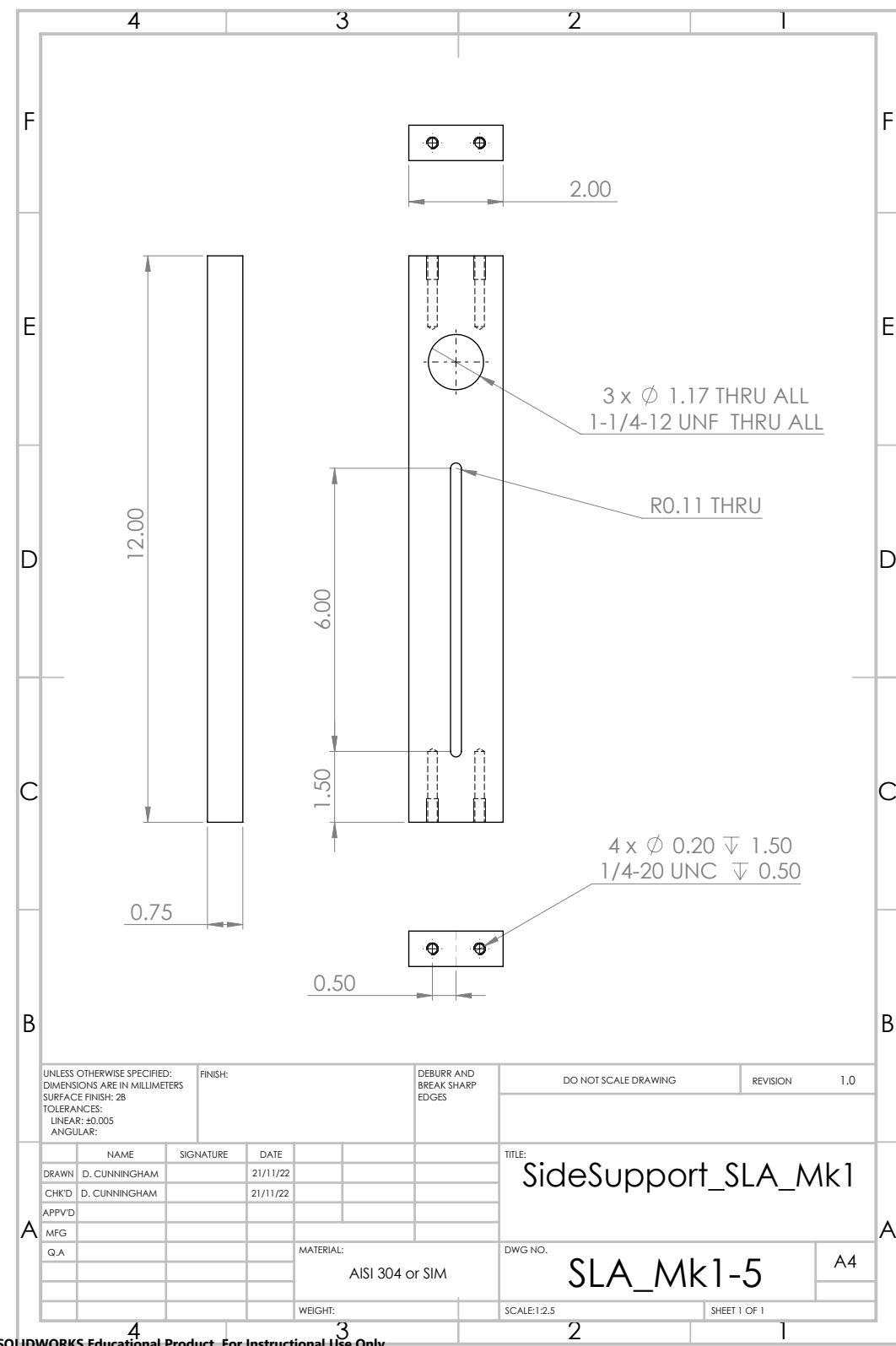
The basic physical design of the CERBERUS apparatus has been described in Chapter 3 of this work. The following pages include the detailed design drawings of each of the components, as well as the structural analyses performed to evaluate said design. Following the detailed design drawings of the apparatus, the detailed design drawings of the humeral specimen holder. Detailed drawing images are not separately titled.

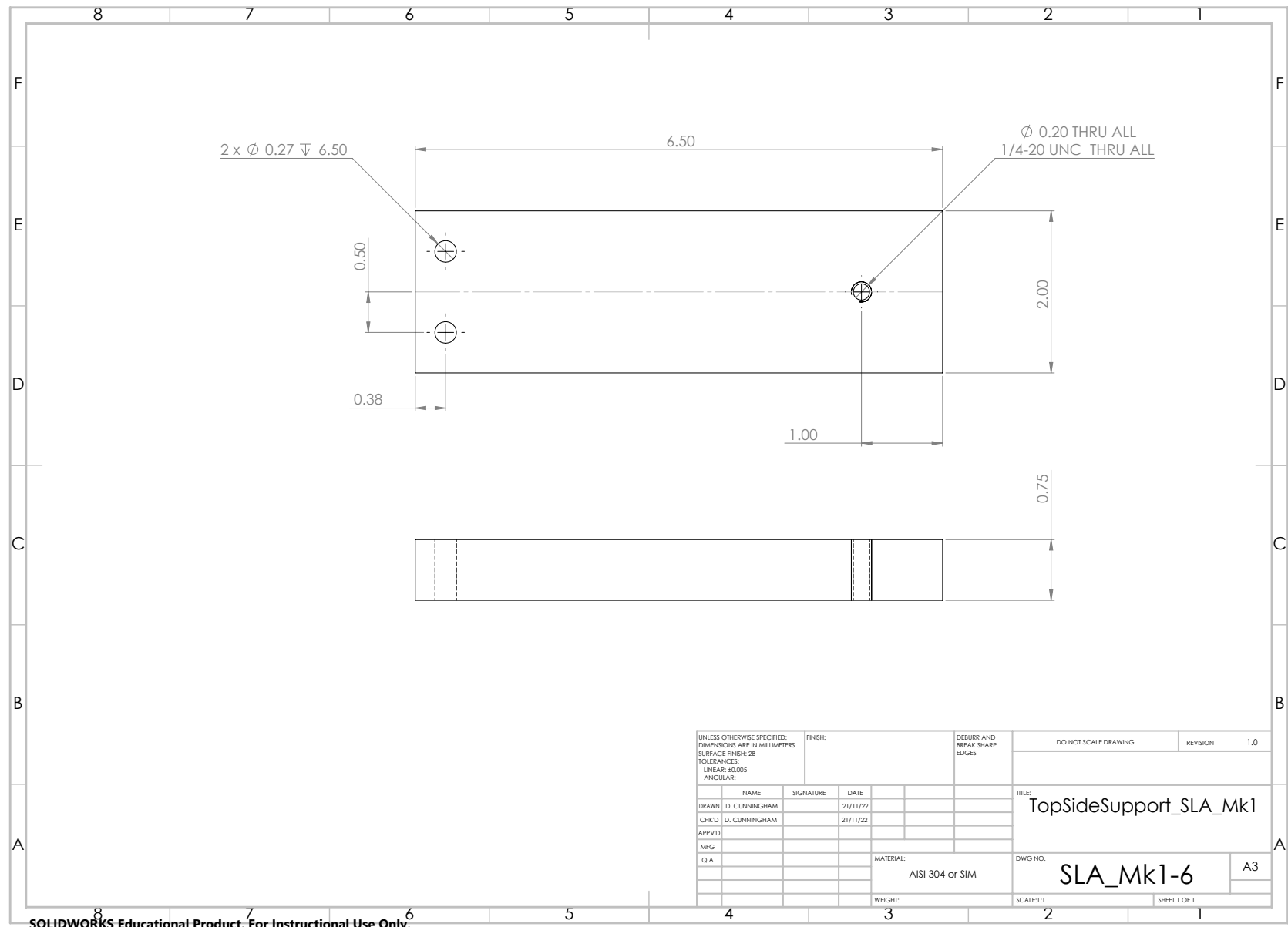


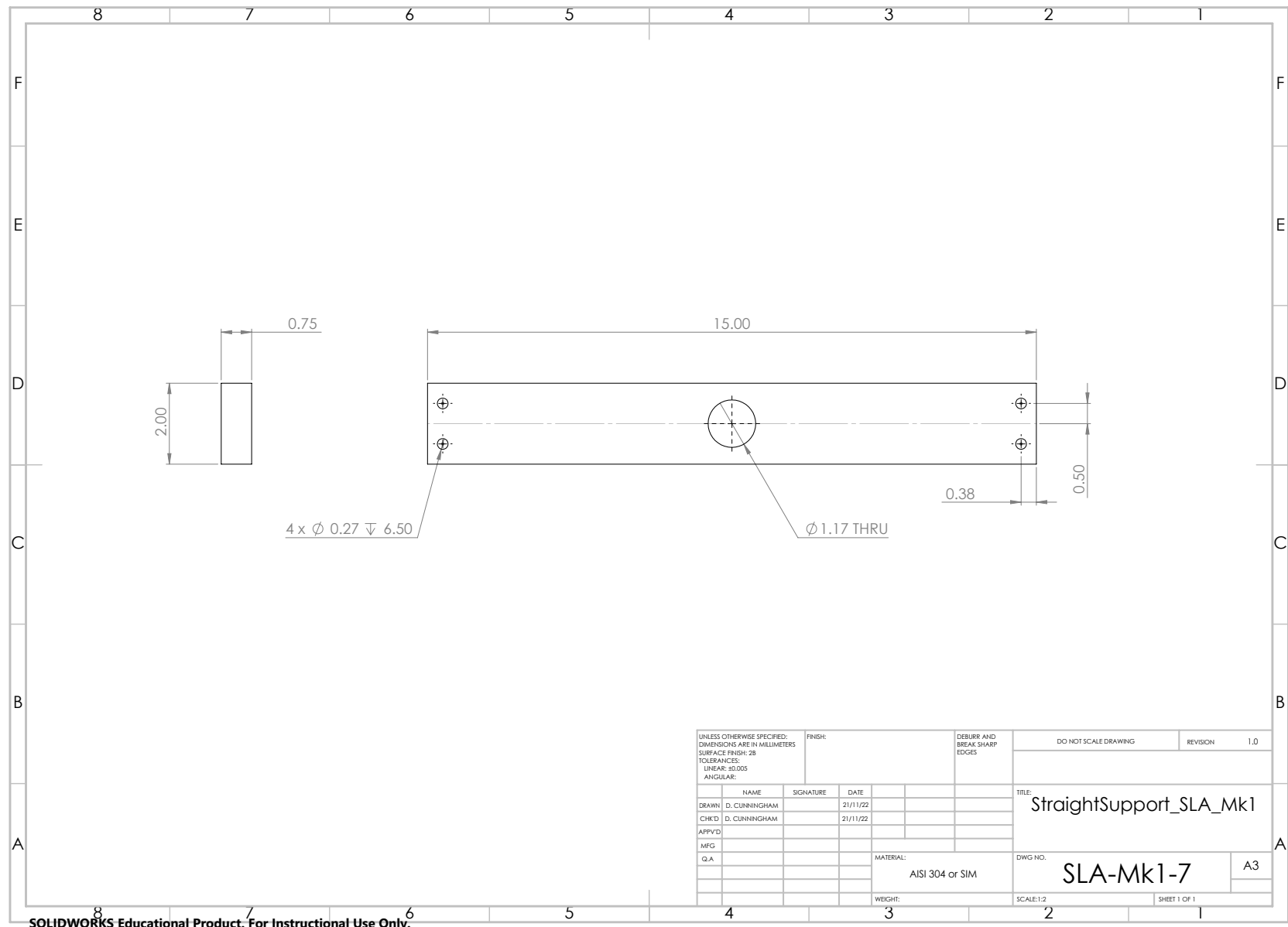


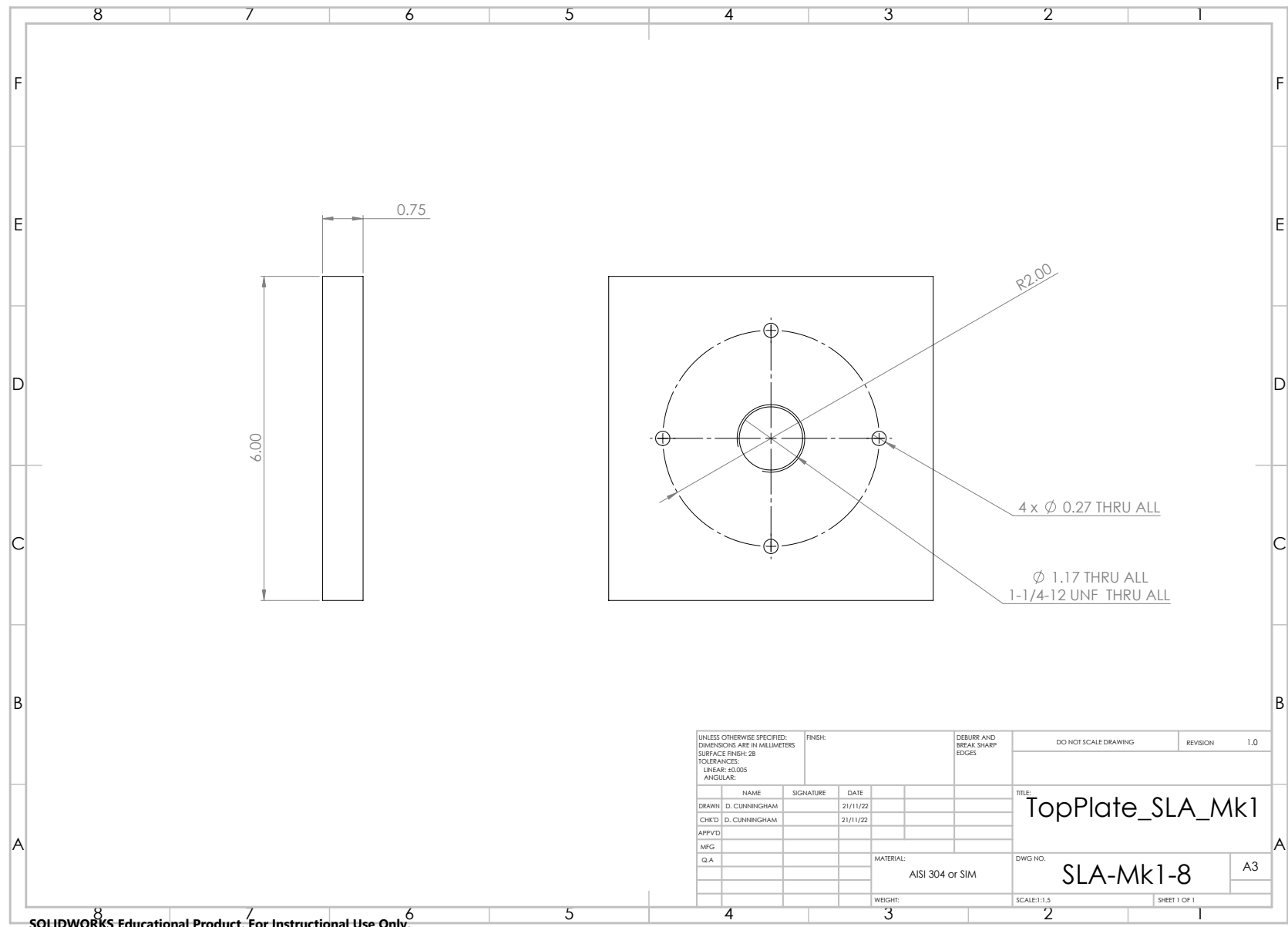


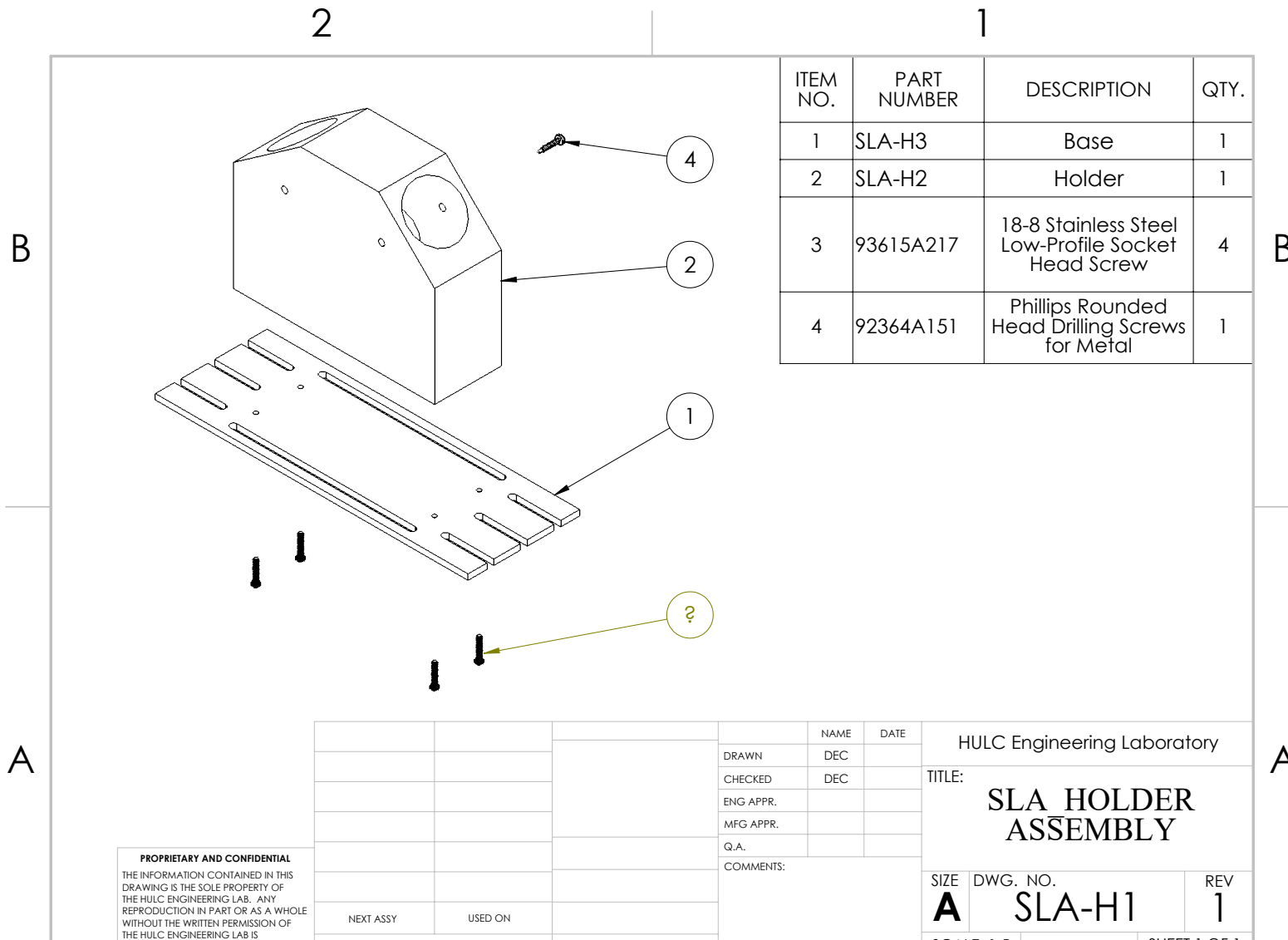


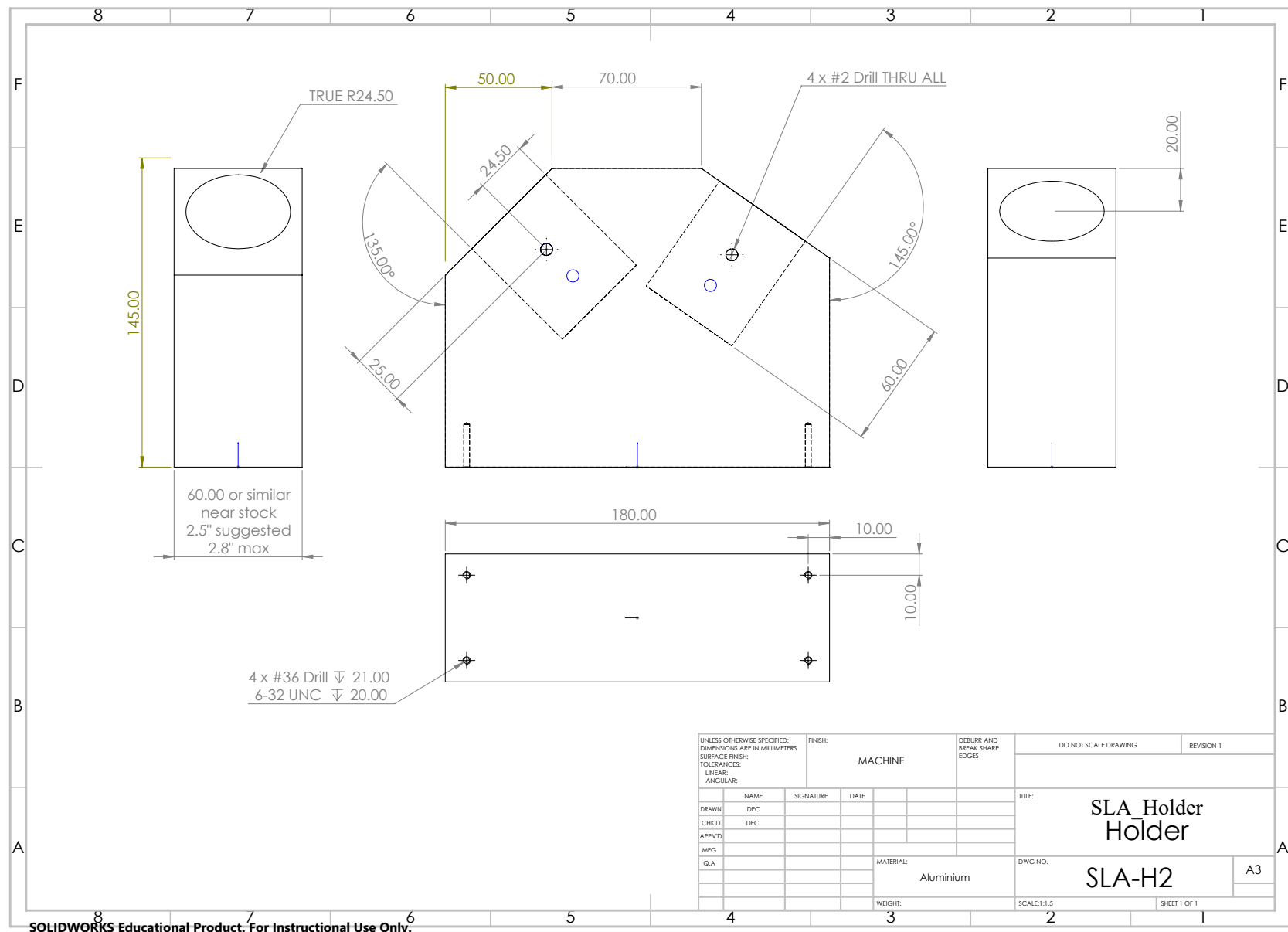


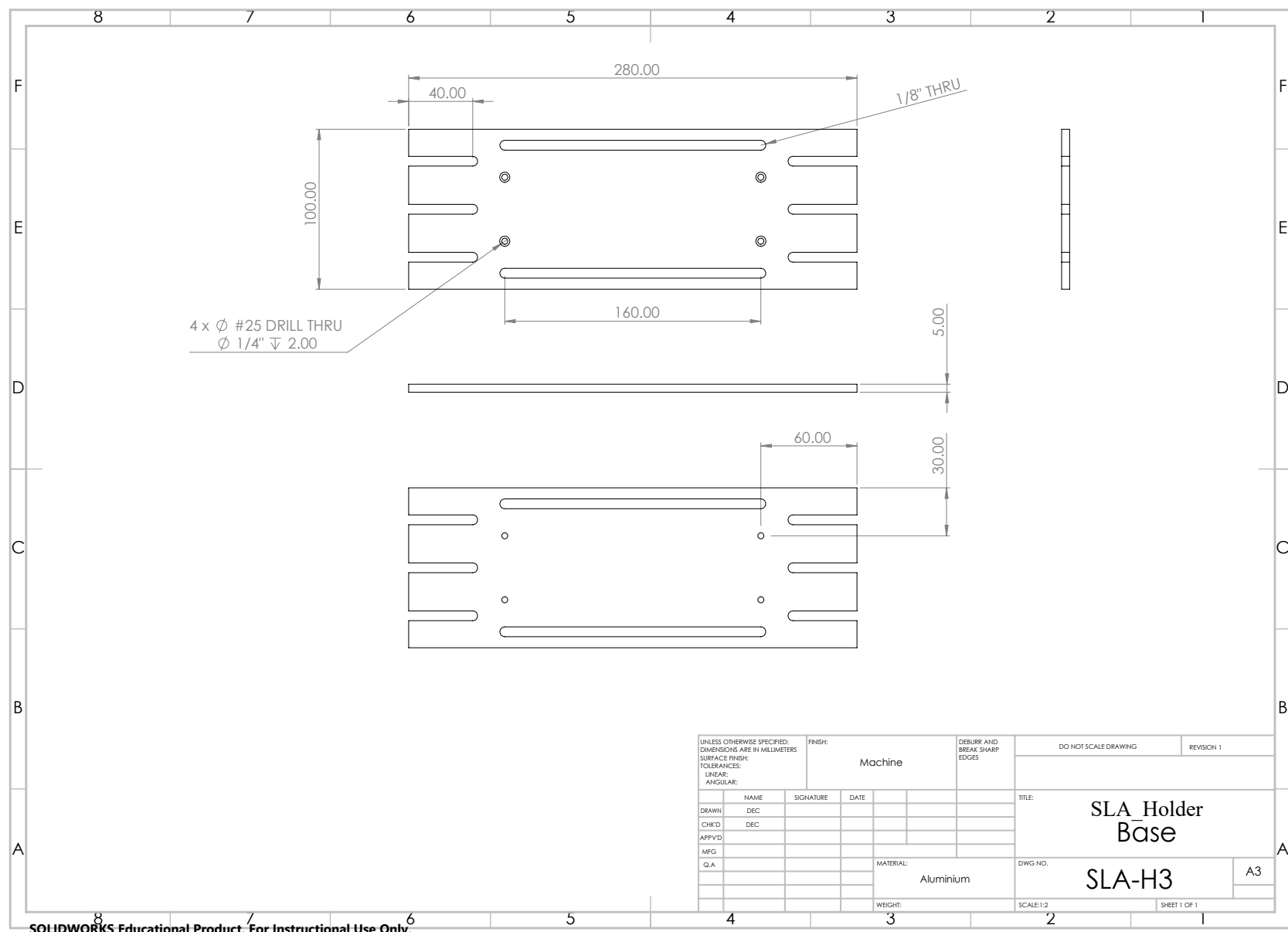












Structural analysis was done through a finite element evaluation of the side supports of the apparatus to investigate the maximum deflection and angulation developed during loading. These components were identified through a failure modes and effects analysis as the parts with the highest risk score, as excessive deformation of the side supports would result in a change to the loading component directions applied to the ball bearing. To ensure safety of the user, it was also necessary to confirm that the force application surfaces would not slip from the ball bearing under maximum loading conditions. The top support was not evaluated due to its symmetry. A nonlinear finite element evaluation was employed to determine displacement of the side support during maximum loading, assuming fixed boundary conditions at the top and bottom of the side supports. The side support model was meshed with high quality 3.5 mm quadratic tetrahedral elements, according to mesh convergence.

The displacement results were differentiated to determine the deflection angle. It was found that the maximum loading, assuming a maximum possible loading state of 1380 [N], the maximum deflection developed was 0.013 mm, well within previously accepted limits. It was also identified that the angle of deflection present at the loading point was only 0.31° (Figure B - 1). Given this maximum angle, at the ball bearing surface, the displacement of the force application pad was 0.81 mm; only 3.2% of the diameter of the force pad. These deflection results indicate that during the maximum loading conditions possible, the loading apparatus will not slip from the ball bearing surface. Overall, these results reflected that the loading apparatus would perform safely and effectively, even under the maximum loading conditions possible by the pneumatic system.

Beam Deflection Behaviour of Side Support

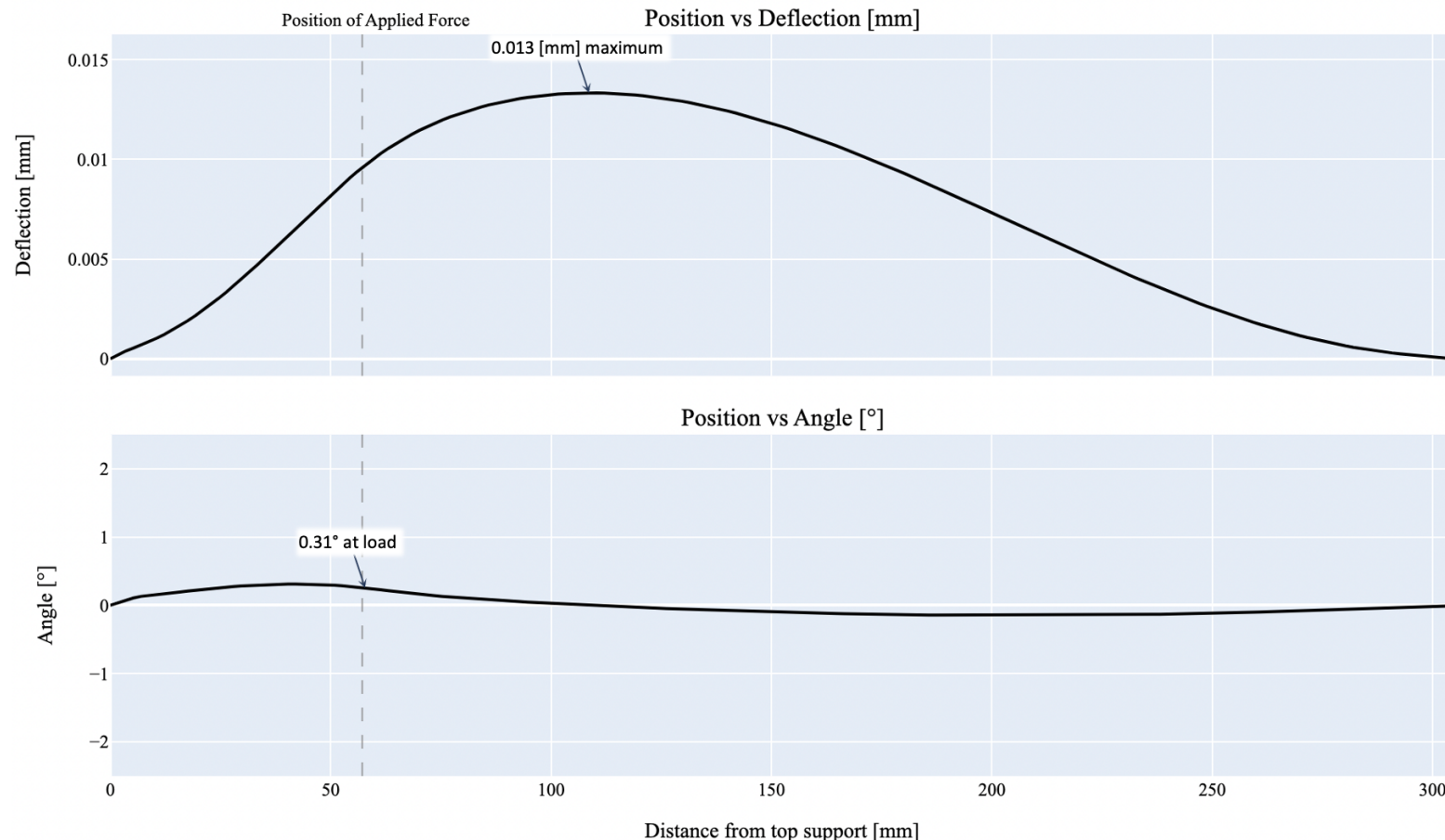


Figure B - 1: Fixed Beam Analysis of Side Support

Results of the finite element deflection analysis during maximum loading of the triaxial loading apparatus side support component.

B.3 Software Design

The software design of this apparatus had three main objectives: (1) to simultaneously load all actuators at once, as not to introduce unnecessary delay to loading, (2) to capture and save high-resolution digital images in a method that could be triggered by the same software., and (3) to collect strain gauge analogue input data for synchronized strain recording throughout the course of the loading plan.

In order to control the loading of the actuators, the National Instruments nidaqmx package [1] was leveraged. This process was complicated by the first objective; defining the requirement that all actuators be loaded simultaneously. This was accomplished by using a list of voltage values as the primary argument of the nidaqmx write task function, instead of a singular value (Figure B - 2). Collection of digital image data was facilitated through the use of the Basler pypylon [2] and Pillow [3] packages (Figure B - 3).

```
#import nidaqmx package
import nidaqmx

#initialize a dictionary of analogue output channels and the voltages
#to be applied to each channel
voltage_dict = {'Dev1/ao0' : 1, 'Dev1/ao1' : 1, 'Dev1/ao2' : 1}

#create a continuous writing task
with nidaqmx.Task() as writeTask:

    #initialize all the analogue output channels
    for i in voltage_dict.keys():
        writeTask.ao_channels.add_ao_voltage_chan(i)

    #simultaneously write to all the analogue output channels
    writeTask.write(list(voltage_dict.values()),auto_start=True)
```

Figure B - 2: Simultaneous Loading of Triaxial Loading Apparatus Actuators

Python code snippet showing the loading of the triaxial loading apparatus actuators simultaneously. This method ensured that the ball bearing would not dissociate from the polyurethane liner component during ramp loading.

```

import numpy as np
from pypylon import pylon
from PIL import Image, ImageTk

#create an generic instance for the camera acquisition
tl_factory = pylon.TlFactory.GetInstance()
l = 0

#enumerate the connected pylon-compatible devices
devices = tl_factory.EnumerateDevices()

#Loop through the connected pylon devices to create an array of camera names
for device in devices:
    if l == 0:
        #creating the array of the cameras detected
        cameraoptions = np.array([device.GetFriendlyName()])
        l=l+1
    else:
        #append to the camera options array for the remaining cameras
        cameraoptions = np.append(cameraoptions, [device.GetFriendlyName()])

    #create a camera object array, 3 camera maximum identified
    cameras = pylon.InstantCameraArray(min(len(cameraoptions),3))

#initialize each camera and set the format of all cameras to Mono12
for i, cam in enumerate(cameras):
    cam.Attach(tl_factory.CreateDevice(devices[i]))
cameras.Open()
cameras.Pixelformat = "Mono12"
cameras.StartGrabbing()

#attempt to capture images
try:
    #attempt capture for each camera
    for s in range(len(cameraoptions)):
        while cameras.IsGrabbing():
            result = cameras[s].RetrieveResult(5000, pylon.TimeoutHandling_ThrowException)
            if result.GrabSucceeded():
                try:
                    #saving an image for each camera as a .tiff file
                    filename = 'camera' + str(s+1) + "_image.tiff"
                    Image.fromarray(result.Array).save(filename)
                finally:
                    result.Release()
                    break
    finally:
        cameras.StopGrabbing()
        cameras.Close()

```

Figure B - 3: Capturing High-Resolution Digital Images using Python

Python code snippet showing the use of the Basler pypylon library when capturing high-resolution digital images.

Lastly, collection of analogue input data was similarly facilitated through the use of the National Instruments nidaqmx package. As this system was designed for rosette strain gauges a minimum of three strain gauge channels were initialized. In this case, four separate channels were initialized in order to provide a backup in case rosette troubleshooting was required (Figure B – 4).

```
#import nidaqmx package
import nidaqmx

#define the analogue input channels
channel_to_read = 'Dev1/ai0'

#set acquisition parameters
sample_rate = 1000 # Set the desired sample rate in samples per second
number_of_samples = 5 # Duration of data acquisition in seconds

with nidaqmx.Task() as readTask:
    #iterate over the channels
    for analogue_input in channels_to_read:
        #add analogue input channels for the four rosette inputs on the specified device
        readTask.ai_channels.add_ai_strain_gage_chan(f'{analogueinput}/ai0:3',
                                                    min_val=-0.015, max_val=0.015,
                                                    strain_config=nidaqmx.constants.StrainGageBridgeType.HALF_BRIDGE_I,
                                                    voltage_excit_val=2.5, gage_factor=4.0,
                                                    initial_bridge_voltage=0.0, nominal_gage_resistance=350.0,
                                                    poisson_ratio=0.30, lead_wire_resistance=0.1,
                                                    custom_scale_name="")

    #configure the sample clock rate and number of samples
    readTask.timing.cfg_samp_clk_timing(rate=sample_rate, samps_per_chan=number_of_samples)

    #read all initialized channels in readTask at once
    data = readTask.read(number_of_samples_per_channel=numberofsamples, timeout=0.1)
    #average the data collected by column
    averages = [sum(channel_data) / len(channel_data) for channel_data in data]

    #print averages
    print(averages)
```

Figure B – 4: Collecting Analogue Input Data from Rosette Strain Gauges
Python code snippet showing the collection of strain gauge data for a rosette strain gauge.

Appendix C: Mimics Bone Model Generation

The following figures and instructions detail the method of creating 3D bone models from CT scans in Mimics. A step-by-step, video-formatted version of this appendix has also been created for the purposes of knowledge transfer in the HULC [4].

C.1 Introduction

This appendix outlines a Standard Operating Procedure to develop a consistent level of accuracy when developing 3D bone models while using Mimics v23.0. This approach has been developed in an effort to increase the validity of bone models developed for stress analysis using the humerus as an example bone model. This method employs a strategy focused on creating a complete cortical shell prior to filling the remaining void with a secondary mask in order to approximate the geometry of the remaining trabecular bone and marrow cavity. It is important to note that this method assumes that trabecular bone and marrow follow the same density-modulus relationship as expressed in Morgan et al. [5]. In addition, this method has been developed to maximize compatibility with SolidWorks and Abaqus/CAE 2021.

When developing and employing 3D models from CT scan data, it is important to distinguish cortical and trabecular bone into independent regions. During finite element analysis of bone models, way may apply global anisotropic Young's modulus values to the cortical shell [6], however, all trabecular bone models must account for the apparent density/elastic modulus relationship similar to that which has been discussed in Morgan *et al.* [5]. This measure serves the purpose of reflecting the anatomically varying nature of trabecular bone. There are many relationships used in literature used to quantify the mechanical properties of trabecular bone, however, the most prevalent relationship accepted in literature today is the Young's modulus-bone density estimation, which has been employed in this work [7], [8].

Application of the Young's modulus-bone density estimation noted above is achieved through the use of the Mimics FEA tool and Abaqus CAE. These two programs use

compatible file types and can be used to achieve near-perfect material property distribution after SolidWorks implant positioning and bone reaming procedures are complete.

C.2 Bone Model Isolation

C.2.1 Development of the Cortical and Trabecular Bone Masks

1. Using the New Project tool, CT DICOM image folders may be imported directly.
 - a. By selecting the DICOM tags tab in the Import Wizard, patient ID and phantom location should be accessible for file naming purposes.
2. To manipulate the CT slice images, the mouse and keyboard may be used.
 - a. RMB-drag left/right increases/decreases the level of the gray scale, darkening and lightening the soft tissue .
 - b. RMB-drag up/down increases/decreases the width of the gray scale, decreasing/increasing contrast within the soft tissue.
 - c. SHIFT-RMB-drag will pan over the selected DICOM image.
 - d. CTRL-RMB-drag will zoom in and out on the selected DICOM image.
 - e. Mouse wheel scrolling will go to the previous/next slice.
 - f. Spacebar will maximize the plane windows for more accurate tracing.
3. For effectively isolating bone, it is suggested that you do not use the Mimics default ‘bone’ settings (Figure C – 1).
 - a. Using the gray scale controls listed above, decrease the width of the gray scale, and increase the contrast of the gray scale until only cortical bone is visible on the coronal plane. Note that it is preferable to undershoot rather than overshoot the cortical shell visible.
 - b. Under the ‘Segment’ tab, select ‘draw profile line’ to automatically create a mask and draw a profile line through the region of interest. For example, the humeral head.
 - c. Using the slider, increase the maximum Hounsfield Unit value until only the previously isolated cortical bone pixels are highlighted.

4. Using the ‘Crop Mask’ tool, crop the masked region to the area of interest. This is necessary, as Mimics will not be able to split the mask later on if the area is too large.
5. Using the ‘Split Mask’ tool, isolate the bone of interest and select any adjacent bone to be ‘Region B’. This will reduce the model to the isolated region of interest. It is suggested that the CT slices be scrolled through using the mouse wheel so that only a small region of the relevant bone is still visible, as it will reduce the split time and possibility of human error due to incorrect highlighting.
 - a. Name this new mask “<patient id>_cortical”.
6. Using the gray scale settings, modify the contrast until the new bone mask is superimposed over a visible outline of the CT bone image.
7. Using the ‘Edit Mask’ tool, fill in the voids of the existing cortical shell model on the coronal, sagittal, and axial planes until a solid and “watertight” cortical model has been developed.
 - a. It is suggested that a mouse, and not a trackpad is used for this procedure.
 - b. Verify the completeness of the shell model by rendering the 3D model by selecting ‘Part’ under the ‘Calculate’ heading.
 - c. Trace over the DICOM CT images smoothly with an appropriately-sized rectangular or circular brush that is smaller than the thickness of the cortical shell.
8. Using the ‘New Mask’ tool, create a globally unrestricted mask (Figure C – 2).
 - a. Crop this new mask using the same crop regions used for the original bone mask.
9. Under the ‘Modify’ heading, use the ‘Boolean Operations’ tool to subtract the new mask minus “<patient id>_cortical”.
10. Use the ‘Split Mask’ tool to split the interior of the new mask from the exterior of the new mask.
 - a. Name the interior bone mask “<patient id>_trabecular”.

C.2.2 Rendering and Refining the 3D Bone Model

1. Using the ‘Part’ tool in the ‘Calculate’ heading under the ‘Segment’ tab, render both the trabecular and cortical bone 3D parts.
2. Select the ‘3D Tools’ tab.
 - a. Use the ‘Wrap’ tool with Smallest Detail = 0.5 mm, Gap Closing Distance = 1 mm to start.
 - i. These settings will vary on a case-by-case basis but are a good starting point.
 - b. Use the ‘Smooth’ tool with Iterations = 20, Smooth Factor = 0.1.
 - c. Repeat smoothing and wrapping and modify masks until there is no exterior visible surface penetration of the trabecular bone model on the cortical shell model.
3. Using the ‘Boolean’ tool under the ‘3D Tools’ tab, perform a “<patient id>_trabecular” minus “<patient id>_cortical” subtraction operation.
4. Visually inspect the model and adapt as needed.
5. Under the ‘File’ tab, export the “<patient id>_trabecular” and “<patient id>_cortical” parts as ASCII STL (*.STL) files, specifying output directory and making sure to ‘add’ both files to the operation. Optionally, one can export the full humerus model instead of the cortical shell and create the cortical shell through performing a Boolean subtraction using the full humerus and trabecular models.

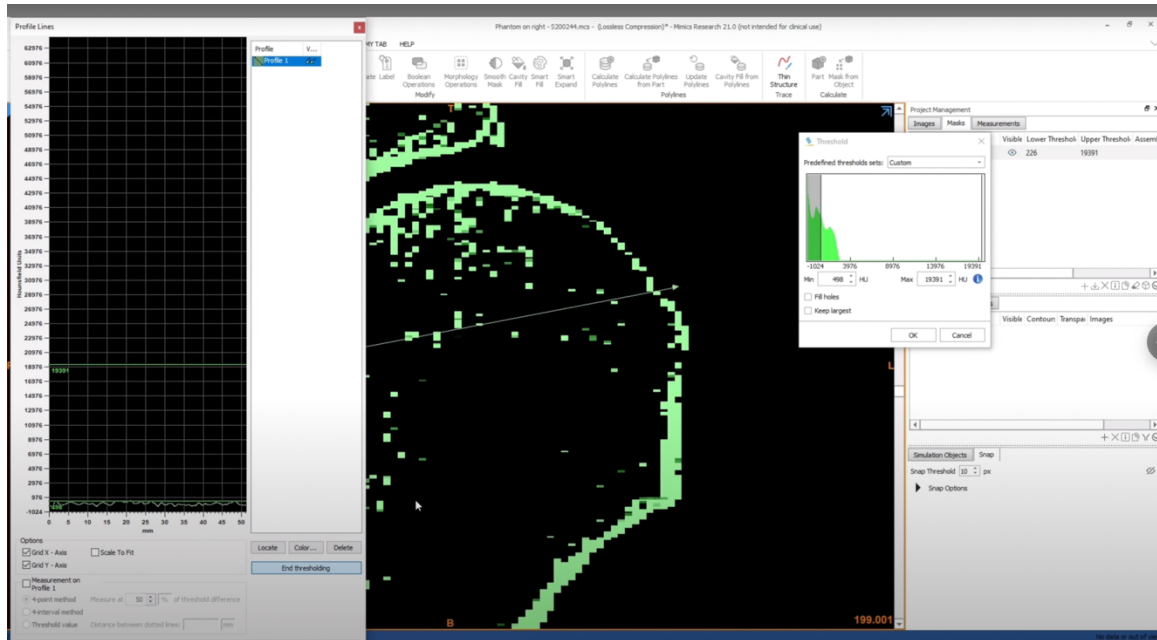


Figure C – 1: Mimics Baseline Mask Threshold

Gray scale and threshold values for isolation of cortical bone in a proximal humerus example.

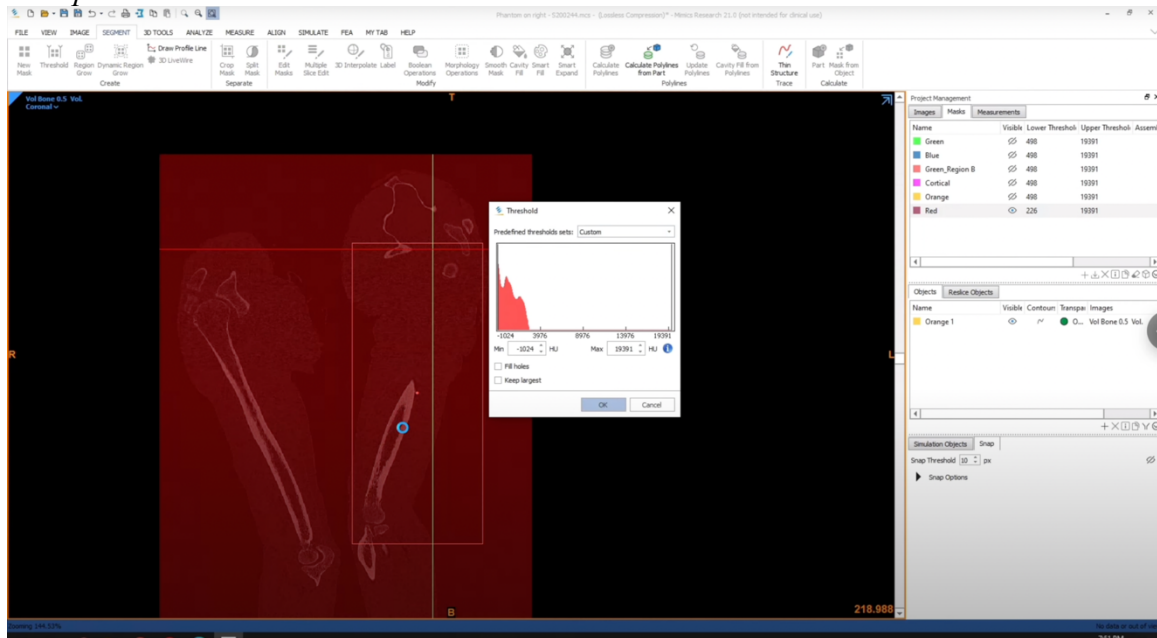


Figure C – 2: Mimics Unrestricted Baseline Mask for Trabecular Bone Model

Unrestricted mask for negative filling of a cortical shell bone model in a proximal humerus.

Appendix D: SolidWorks Bone Reaming and Implant Positioning

The following pages describe the standard operation for reaming of bone and positioning of humeral implants in a SolidWorks assembly. A step-by-step, video-formatted version of this appendix is available for the purposes of ongoing training and transfer of knowledge in the HULC laboratory [9].

D.1 Introduction

This appendix outlines the process by which a reverse total shoulder arthroplasty humeral prosthetic may be positioned in SolidWorks 2020. The recorded approach has been developed as a standard operating procedure for the positioning of humeral head implants while maintaining consistency across patient bone models. When positioning orthopaedic implants *in-silico*, it is essential to maintain orientation consistency relative to the natural geometry of the local bony anatomy. This procedure was developed under the guidance of an experienced orthopaedic surgeon specializing in shoulder and elbow reconstruction and upper extremity trauma.

When determining any implant positioning, it is essential to first isolate coordinate systems with reference to the local anatomy. For the purposes of this work, a method has been developed for implant positioning that can be completed solely in SolidWorks 2020 without any additional software packages. It is noted, however, that more exact methods may be employed using analytical best-fit methodologies via third-party software.

When positioning implants across patient groups, it is essential to maintain consistency in the orientation of the resection planes and implant geometries. In an *in-silico* medium, it is possible to maintain a much higher regularity in positioning than is reasonably achievable in a surgical suite. The implant positioning method contain herein outlines a procedure that is designed to be translated into an automated process by which implants may be positioned without excessive user intervention in the future.

D.2 *In-Silico* Humeral Head Reaming

1. After opening SolidWorks 2020, close the file wizard and open the cortical bone model ASCII STL file as developed in Appendix E.
 - a. When opening the ASCII STL, while in the open file tool, select “options” and ensure that the “Import as” selection textbox has the “Solid Body” import setting selected.
 - b. It is suggested that you use either a resource monitor application or Windows Task Manager to monitor memory usage during this process. SolidWorks may show as “Not Responding” during this process.
 - c. If the ASCII STL is taking over ten minutes to open, reopen Mimics and using the “Reduce” tool under the “3D Tools” tab, reduce the model complexity using the “Advanced edge” approach with tolerance = 0.03 mm, edge angle = 15°, and iterations = 10. Repeat as necessary after attempting to reopen the new ASCII STL in SolidWorks.
2. Delete any superfluous or disassociated solid bodies from the imported bone model and save to a relevant folder as “<patient id>_cortical”.
3. Close the cortical SolidWorks model to increase number of available cores and threads, and repeat the process with the trabecular bone model, using the naming convention “<patient id>_cortical”.
4. Close the trabecular bone model and open a new assembly. Name this new assembly “<patient id>_<identifier>”.
5. Import the cortical bone model and mate the origin of the cortical bone model with the origin of the assembly, ensuring that the “align axis” option is selected.
6. Import the trabecular bone model and mate origins to position the trabecular bone model in the empty volume of the trabecular bone model.
7. Optionally, save this assembly separately to use as the “intact state”.
8. Isolate the central axis of the humerus.
 - a. Using the “Section View” tool, identify a section plane approximately normal to the long axis of the humerus.

- b. Identify a plane position at the most proximal aspect of the humeral head and note down the relative position in perpendicular offset to the assembly reference plane.
- c. Move the section view distally by 50 mm and under “tools”, use the “evaluate” tool to calculate the centroid of the exposed trabecular cross section, noting these values down relative to the assembly origin (Figure D – 1).
- d. Continue to move the section view distally by another 50 mm and repeat the process, noting the new coordinates.
 - i. Under “sketch”, create a 3D sketch and mark points at the two noted centroidal points found in steps 11 and 12.
 - e. Create a line of infinite length using the centroid points. This will serve as the long axis of the humerus.
9. Using another 3D sketch, draw three points on the crest of the humeral head, directly adjacent to the anatomical neck. Use these three points to draw a plane which will be used to determine the natural retroversion (Figure D – 2).
10. Identify the cut plane inclination.
 - a. Create a plane orthogonal to the natural retroversion plane and coincident to the central axis of the humerus as developed previously. This will be referred to as the neck shaft angle plane.
 - b. On the neck shaft angle plane, draw a line orthogonal to the long axis of the humerus at an intersection point at the location most inferior on the humeral head. At the intersection location, draw a point.
 - c. Using this point at the most inferior aspect of the crest of the humeral head and the “smart dimension” tool, draw another line to identify the inclination of the cut. In the case of the reverse total shoulder arthroplasty implant, this may be identified using the neck shaft angle specification metric.
11. Draw the cut plane coincident to the neck shaft angle line and orthogonal to the neck shaft angle plane.

12. Draw a sketch on the cut plane that is sufficiently large to resect the humeral head.
13. Under the “Insert” tab, create an “Assembly Feature” and perform the cut. Make sure to only include the trabecular and cortical bone models in the feature scope and optionally propagate the feature to the parts.
14. Optionally, shorten the cortical and trabecular bone models.
 - a. Using the “Section View” tool, identify a plane orthogonal to the central axis of the humerus that intersects with the point drawn on the inferior aspect of the humeral head.
 - b. Move the new plane distally by 40 mm and draw a plane. Using the “Assembly Feature-Cut” tool, remove the distal volume of the trabecular bone model.
 - c. Move the section view to 180 mm distal to the forementioned point and using a similar method, shorten the cortical bone.
 - d. Save the assembly.

D.2 Implant Positioning

For implant positioning, it is suggested that a master implant be used on each patient model and other implant revisions to be positioned concentrically to the master implant. All implants with similar bone resection requirements may be stored in a common assembly and exported individually at a later stage.

1. If necessary, create an implant SLDPRT from the Parasolid part files.
 - a. Open the implant Parasolid component part files in SolidWorks
 - b. Save each component as a SLDPRT.
 - c. Create a new assembly and assemble implant.
 - d. Under “Save As”, save the implant assembly as a SLDPRT and name accordingly.
 - e. Open the implant SLDPRT and sketch a relevant coordinate system that may be used for positioning. Set the sketch to be visible.
2. Bring the implant SLDPRT file into the cortical/trabecular bone assembly.

3. Position the implant coincident to the cut plane, using the neck shaft angle line to orient the implant posteriorly-anteriorly on the cut plane.
4. Use the previously identified implant coordinate sketch to orient the implant rotationally.
5. Draw a line on the neck shaft angle plane, orthogonal to the long axis of the humerus.
6. Using a landmark on the stem of the master implant, choose the lateralization of the implant in reference to the central axis of the humerus to maintain consistency across patient models.
7. Save the SolidWorks assembly.
8. Export each part as a STEP AP214 file.
 - a. Suppress everything but the cortical bone model.
 - b. Under “Save As”, save the implant as a STEP AP214 file. When asked to resolve suppressed components, select “No”.
 - c. Repeat with both the trabecular bone and the positioned implant.

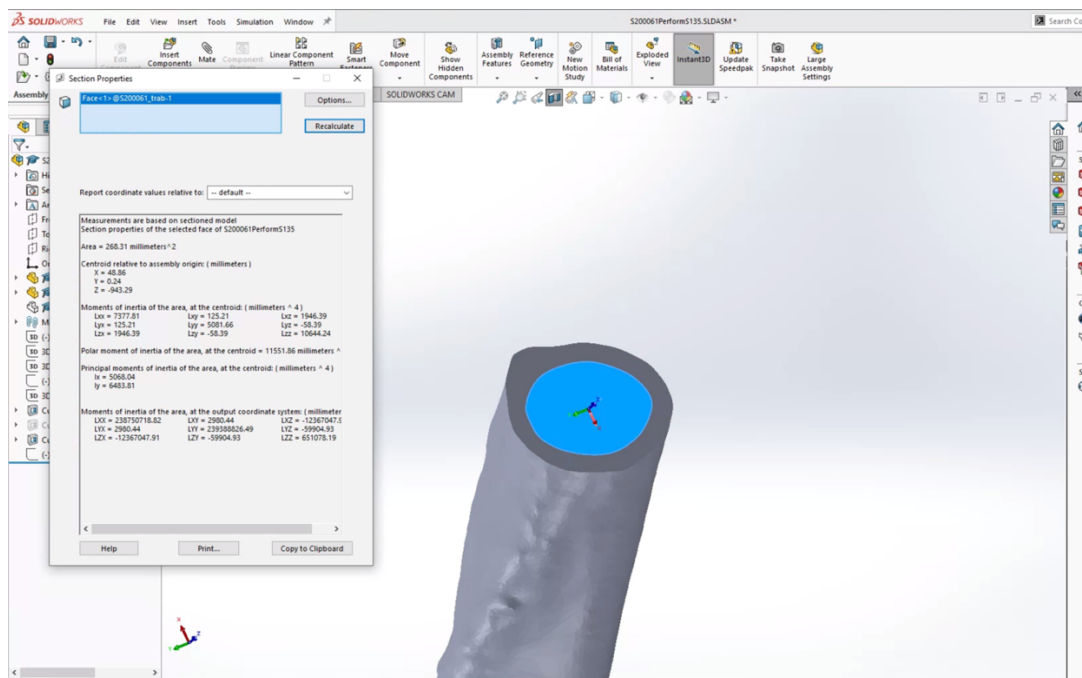


Figure D – 1: Determining the Centroid of the Humeral Canal
Using the “Section Properties” tool to determine the centroid of the diaphyseal humeral canal at a cross section 100 mm distal to the most proximal aspect of the humeral head.

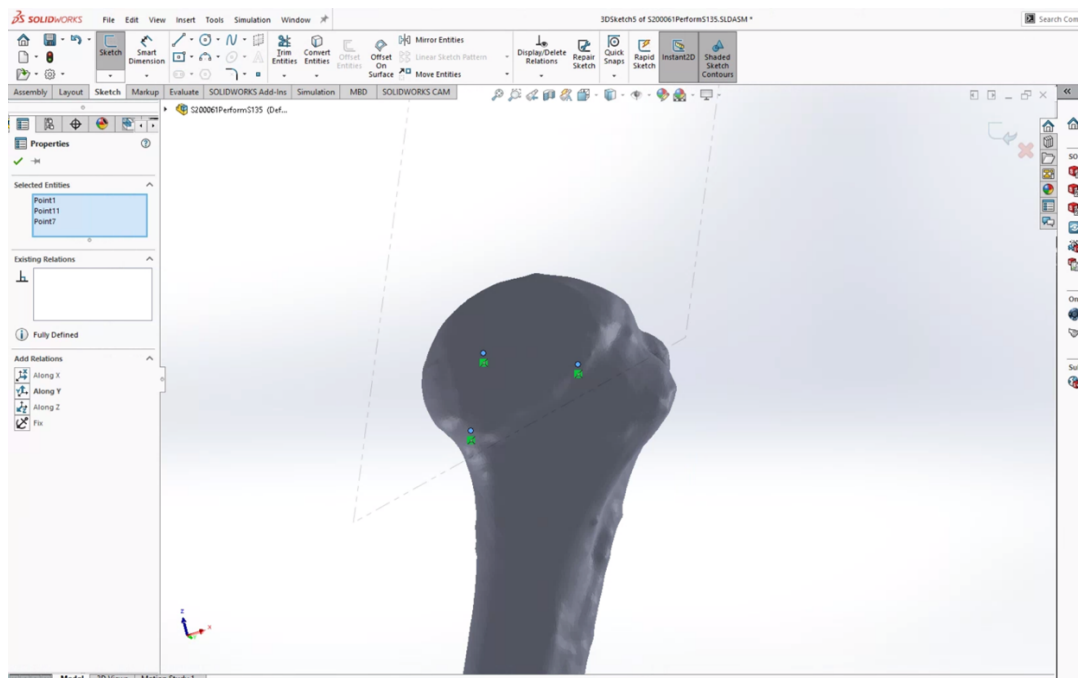


Figure D – 2: Determining Natural Retroversion

Three reference points used in determining the natural retroversion of the humeral head to be used in positioning of the resection plane.

Appendix E: Material Property Assignment using Mimics 2021

The following pages describe the standard operation for the application of material properties for trabecular bone in Abaqus/CAE 2021, using Mimics v23.0.

E.1 Introduction

This appendix outlines the procedure by which density-based material properties may be applied to Abaqus/CAE 2021 bone models. This approach has been outlined to establish consistency when applying the Young's modulus-bone density estimation as developed by Morgan *et al.* [5]. When applying material properties to cortical bone, it has been found that Young's modulus can be approximated at between 12-14 Gpa in the transverse axis, and at 20-22 Gpa in the longitudinal axis [6]. The application of the anisotropic material properties of cortical bone can be performed locally in Abaqus/CAE 2021. However, in the case of trabecular bone, there is a much larger degree of location-based variation in mechanical properties. For the purposes of this work, the standard Young's modulus-bone density estimation will be used [5], [7], [8] (Equation E – 1).

$$E = 8920 \rho_{app}^{1.83}$$

Equation E – 1

Where E references Young's modulus, and ρ_{app} references the apparent density of the trabecular bone at the location of interest. Due to the high level of variation in trabecular bone density through the humerus, individual materials must be developed across the model to reflect the variation in Young's modulus through the cross section. This procedure is completed through using the Mimics v23.0 'Assign Material' tool.

E.2 Material Property Assignment

E.2.1 Developing an Orphan Mesh

1. After all bone and implant models have been positioned in Abaqus/CAE 2021, ensure that sets have been created for both trabecular and cortical bone parts.
2. Create instances for cortical and trabecular bone and using the 'Merge/Cut Instances' tool, merge the cortical and trabecular bone geometries, suppressing

original instances and retaining the intersecting boundaries. If necessary, cut the total bone model with the relevant implant/cut tool.

3. Assign tetrahedral mesh control to merged bone instance and assign element type to quadratic, keeping default values (standard, quadratic elements).
4. Mesh part.
5. Under ‘Analysis’, create a new job and name it “MeshWash”, using the relevant model and retaining the default job settings.
6. Under the new job, select ‘WriteInput’ and navigate to the working directory to retrieve the .inp file.
7. Under ‘Models’, import the newly created .inp file.
8. Rename the new part “<patient id>_trabecular”.
9. Copy the new part and rename as “<patient id>_cortical” and under ‘Parts’, double click on the part mesh to make current.
10. Select ‘Edit Mesh’ and delete elements, selecting the ‘trabecular’ set to isolate the cortical bone with compatible mesh.
11. Repeat with the “<patient id>_trabecular” part, this time selecting the ‘cortical’ set to be deleted, thereby isolating the trabecular bone with compatible mesh.
12. Create an instance for the “<patient id>_trabecular” part and create another .inp file by creating a new job named “MaterialApplication” and selecting ‘WriteInput’.

E.2.2 Correlating Density and Material Properties in Mimics

1. Open the original .mcs file for the patient in Mimics v23.0.
2. Under the ‘File’ tab, import the newly created ‘MaterialApplication’ .inp file.
3. Using the ‘Segment’ tab, isolate the imaged phantoms and measure the densities of each known value in Hounsfield Units (Figure E – 1).
4. Navigate to the ‘FEA’ tab and select ‘Assign Material’.
5. Select ‘Gray value based’ under the ‘Material assignment method’, and select ‘Density’, ‘Young’s Modulus’, and Poisson Coefficient’.
6. Using the measured Hounsfield Unit bounds for the phantoms, apply the calibration values obtained.

7. Under Young's modulus, input values associated with the Young's modulus-bone density estimation (Figure E – 1).
8. Under 'Poisson Coefficient', use a constant value of 0.3.
9. Toggle 'Number of materials' to an acceptable value.
10. Apply material properties and export the mesh to the working folder under the name “<patient id>_<implant identifier>”.

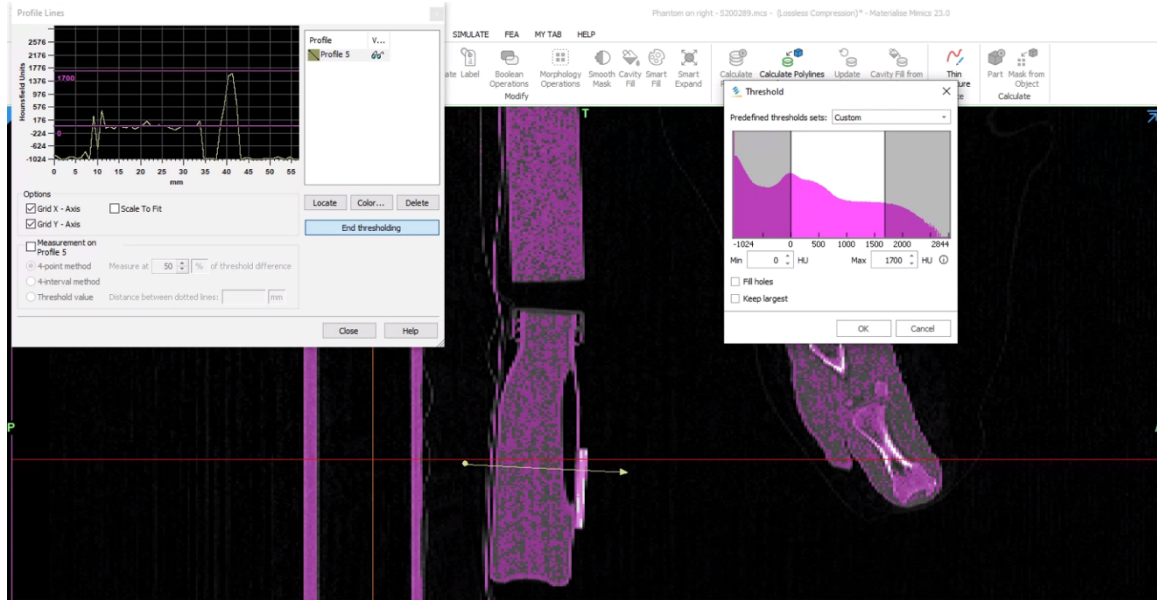


Figure E – 1: Measuring HU Density of Phantom

Process to measure the density of the SB3 cortical bone and water phantoms scanned alongside the patient.

E.2.3 Importing/Applying Material Properties

1. Open Abaqus/CAE 2021 and under ‘Models’, import the newly created mesh .inp file.
2. Rename the new part “<patient id>_trabecular”.
3. Under ‘Models’, copy objects from the ‘MeshWash’ model. Copy the “<patient id>_cortical” to the “<patient id>_<implant identifier>” model. Copy the positioned implant part from the original model.
4. If applying anisotropic material properties, under the ‘Property’ module, assign material orientation to maintain the ‘3’ direction parallel to the long axis of the humerus.
5. Make the cortical bone part current. Select ‘Edit Material’ and name the new material “CorticalBone”. Under ‘Mechanical’, apply the relevant material properties to the part.
6. For orthotropic behaviour, as is exhibited by cortical bone, input the nine independent elastic stiffness parameters. For isotropic behaviour approximations, input Young’s modulus and Poisson’s ratio directly. For isotropic cortical bone, precedent literature suggests applying a Young’s modulus of 20,000 MPa, and a Poisson’s ratio of 0.3 [10].

7. Copy the implant part from the original model. Make current.
8. Select ‘Edit Material’ and assign relevant material properties to the implant. For cobalt-chrome implants, precedent literature has used a Young’s modulus of 210,000 MPa and a Poisson’s Ratio of 0.3 [10].

Appendix F: Finite Element Analysis using Abaqus/CAE 2021

The following pages describe the process by which boundary conditions and forces may be simulated using Abaqus/CAE 2021, after implant positioning and material assignment has been completed.

F.1 Introduction

This appendix describes a standard procedure by which contact conditions, boundary conditions, and forces may be simulated using Abaqus/CAE 2021. This approach was developed to increase the validity of future work by incorporating press-fit behaviour, varying surface contact conditions, and both trabecular and cortical bone models into the finite element analysis of orthopaedic implants. Prerequisite steps are outlined in Appendix C, Appendix D, and Appendix E. When applying boundary conditions to the implant-bone system, it is important to ensure that surfaces are compatible, and that the manufacturer specifications on press-fit geometries are accurately applied to the model before running analysis.

F.2 Implant/Bone Contact

F.2.1 Defining Contact Surfaces

1. As indicated in Appendix E, bone material properties have been applied to the bone part models. However, in order to simulate the no-translation bonding between cortical and trabecular bone, the bone meshes must be remerged with their compatible meshes.
 - a. In the “Assembly” module, create an instance for both the cortical and trabecular bone part models.
 - b. Using the “Merge/Cut Instances” tool, create a new part called “<patient id>_bone” and merge using mesh, supressing the original instances, and merging all nodes. Use a tolerance of 1E-03. Be sure to remove duplicate elements.
2. Resume the implant assembly instance.
3. Under the “Parts” module, open the implant model and assign element type to quadratic using a tetrahedral mesh control. Keep default values.

4. Under the part surface dropdown, create a surface for all different contact conditions expected in the model. Individual surfaces should be made for each interference fit/surface roughness combination.
5. Make the merged bone model current and assign contact and boundary condition surfaces.
 - a. Under “surfaces”, create a new surface and name it “bone_fixed”. Select the regions for the surface by angle, selecting the most distal cross section of the cut diaphysis for the first surface.
 - b. Create additional surfaces for each mating surface defined earlier, one for each contact condition combination. It is most efficient to use the “by angle” approach, changing the designated angle and holding shift to select multiple faces at once.
6. Under the “Step” module, create a new step titled “loading_<load identifier>”.
 - a. Set maximum number of increments to 1000 and use an iterative solver.
 - b. Under “Edit Field Output Request”, select contact pressure, strain energy density, von Mises maximum stress, and von Mises stress as outcome measures. Other options may be selected dependent on the outcome measures associated with the individual study.
7. For each contact condition, create an interaction.
 - a. For the selected loading step, create a “surface-to-surface” standard contact.
 - b. Select a relevant surface and choose slave type “surface”, identifying the corresponding mating surface in the region selection window.
 - c. Choose finite sliding, and a surface-to-surface discretization method.
Under contact interaction property, create a new contact interaction.
 - i. Name this contact property to be recognizable to the surfaces identified.
 - ii. Under “Tangential Behaviour”, define the friction formulation as “penalty”, and apply the designated coefficient of static friction to the contact surface.

- iii. Under “Normal Behaviour”, define the “pressure-overclosure” method as “Hard” contact.
- iv. Assign the new contact property and select “interference fit” in the “edit interaction” window.
- v. Select “gradually remove slave node overclosure during the step” and apply the default settings.
- d. Repeat for each surface interaction.

F.2.2 Applying Forces and Boundary Conditions

1. After defining the bone/implant interaction, create a new boundary condition.
2. Name this boundary condition “distal_fixed”, and apply a mechanical encastre boundary condition to the “bone_fixed” surface created in Appendix F.2.1.
3. Select “ENCASTRE (U1 = U2 = U3 = UR1 = UR2 = UR3 = 0)” boundary condition with reference to the CSYS global coordinate system.
4. Define a relevant load to the implant surface.
 - a. Under the “Part” module, make the implant part current.
 - b. Create a new set named “<patient id>_<load id>”, making a node type set and identifying a point at the centre of rotation of the implant.
 - c. Name the new load “<patient id>_<load id>”.
5. Identify your force vector in SolidWorks.
 - a. Open the SolidWorks assembly.
 - b. Draw a line orthogonal to the neck shaft angle plane.
 - c. Insert a “coordinate system” under reference geometry.
 - d. Set the medial-lateral axis, the superior-inferior axis, and the orthogonal to the neck shaft angle plane as the x, y, and z axis’, respectively.
 - e. Verify the load vector in SolidWorks.
6. Apply the force in Abaqus CAE.
 - a. Under the “Load” module, select “Create Load” and apply a “Concentrated Force” to the centre of rotation node set.

Appendix G: Bone Mineral Density Analysis of Peri-Prosthetic Bone

The following pages describe the work performed during the evaluation of implant-adjacent bone-mineral density.

G.1 Introduction

The primary mechanism of stability of osseointegrating prostheses changes as bony ingrowth occurs. As previously discussed in Chapter 3, during the first few weeks postoperatively when osseointegrating bone has not yet fully formed [11], the implant is primarily held in place through press-fit; or rather, the frictional forces between the implant and bone surfaces which is inflated through increased contact pressures at the interacting surfaces. Conversely, as the phenomenon of osseointegration proceeds, the driving variables promoting successful fixation of the prosthetic device multiply to include chemical bonding and mechanical interlocking, in addition to the aforementioned friction [12].

Chemical bonding of implant and bone materials is a process that is frequently leveraged in implants with bioactive coatings – in this fixation design, the bioactive coating allows the deposition of osteoids directly onto the implant coating [13]. This is also known as implant adhesion [12], [14], [15]. Osseointegration in this manner depends on various surface interactions with surrounding bone tissue, and relies on enhanced cell adhesion, proliferation, and osteogenic differentiation to provide direct chemical bonding between implants and bone tissue [15].

Mechanical interlocking, or the physical ingrowth of bone into a porous surface, functions differently. Mechanical interlocking occurs when the bone tissue surrounding the implant grows into the voids of a porous implant surface [16]. This creates a physical barrier to implant-bone relative motion but is not a true bonding between an implant surface and bone tissue. This interlocking effect, as well as the paired friction properties, have been found to be sufficient even in cases where there is no direct contact between implant and bone, however, unlike chemical bonding, these phenomena do not resist tensile forces [12].

Although there are multiple mechanisms to primary implant fixation, each individual method independently relies on the quality of the adjacent bone for sufficient osteogenesis for bone ingrowth and osteoid deposition [15], or the modulus of the surrounding bone to provide sufficient contact pressure and static resistance to motion between implant and bone [17]. This common requirement means that bone mineral density (BMD), as a metric for local bone quality, is an important variable in the short and long term fixation of press-fit prostheses [18], as higher BMD values translate to higher material moduli [5], [17]; thereby providing better initial stability to facilitate mechanical interlocking and chemical bonding, all while assisting with tighter press-fit and thereby higher frictional forces.

In the particular case of stemless humeral prostheses, stemless humeral implants exhibit greater stability when a larger portion of the implant maintains contact with good quality metaphyseal bone [19]. This was discussed in Chapters 5 and 6, where it was postulated that the mechanism of greater stability in implants at higher neck shaft angles (NSAs) was both the decreased loading eccentricity, as well as the better quality of periprosthetic bone. In order to thoroughly investigate this topic, it was therefore prudent to evaluate the accuracy of the latter postulation, as the former has already been supported in the discussion of Chapter 6 where it was identified that loading direction and magnitude had a significant effect on implant micromotion. The resultant purpose of this work to compare the periprosthetic BMD values, and thereby the potential for successful osseointegration of stemless humeral prostheses, in 135° and 145° NSA implantation configurations to determine if there is significant variation in the stabilizing metaphyseal bone resisting implant-bone relative motion.

G.2 Methods

Computed tomography (CT) scans of eight shoulders from male cadaveric specimens (height: 177 ± 4 cm, weight: 69 ± 10 kg) aged 70 ± 21 years (mean \pm standard deviation) were collected using a clinical CT Scanner (slice thickness: 0.5 mm, pixel spacing: 0.961 x 0.961 mm, exposure time: 750 ms, kVp: 120) (GE 750HD Discovery Scanner; GE Healthcare, Chicago, IL, USA). A bottle of distilled water, and a cortical bone surrogate

(SB3 model 450; GAMMEX, Middleton, WI, USA) were purposed as phantoms to calculate the apparent density in g/cm³ from the recorded Hounsfield units (HU). Three-dimensional models of each humerus were generated using Mimics v23.0 (Materialise, Leuven, Belgium). A stemless humeral implant (Tornier Perform® Stemless Reverse Humeral System, Stryker, Kalamazoo, MI, USA) was positioned in each model by a board-certified orthopaedic surgeon (GSA), and local coordinate systems were created for each implant position.

Three ghost rings were created using the parametric design software CadQuery [96]. These ghosts were positioned to occupy the volume of bone directly adjacent to the primary osseointegrating surfaces of the stemless humeral implant at three different positions (Figure G - 1). These query ghosts were then transformed into the positioned implant coordinate systems and meshed using Abaqus CAE 2021 (Dassault Systèmes Corp). Material properties were assigned using Mimics and exported as Abaqus input (.inp) files for evaluation. All ghost nodes were retransformed back into the base coordinate systems and BMD was identified for each element volume centre.

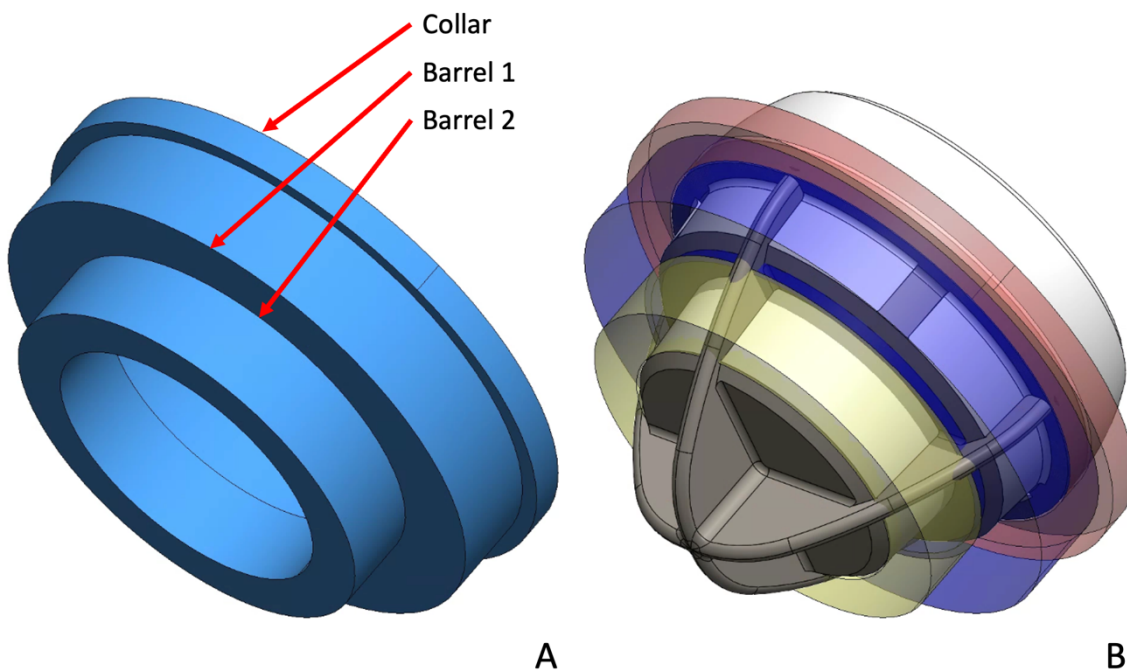


Figure G - 1: Implant BMD Analysis Ghost Primaries
Geometry primary ghost shapes for the location-specific querying of bone mineral density.

G.3 Outcome Variables and Analysis

In order to quantify the local BMD surrounding the implant, each ring was divided circumferentially in 10° segments. A pairwise t-test was performed at each implant level to compare the local BMD values between 135 NSA and 145 NSA resections. A supplementary two-way ANOVA was performed on the independent variables of neck shaft angle and sample position, with the dependent variable of BMD. All statistical analyses were computed using SciPy 1.9.1 [20], with the threshold of significance set as $p < 0.05$.

G.4 Results

Stemless humeral implants are surrounded by more dense (higher BMD) trabecular bone when installed at 145° NSA (Collar: $P = 0.001$, Barrel 1: $P < 0.001$, Barrel 2: $P < 0.001$)(Figure G - 2, Figure G - 3, Figure G - 4). The two-way ANOVA found both that NSA had a significant effect on stabilizing bone BMD ($P < 0.001$), and that the position of the volume sample also had a significant effect on BMD ($P < 0.001$)(Figure G - 5); this was commensurate with previously identified density variations in the humeral head [17].

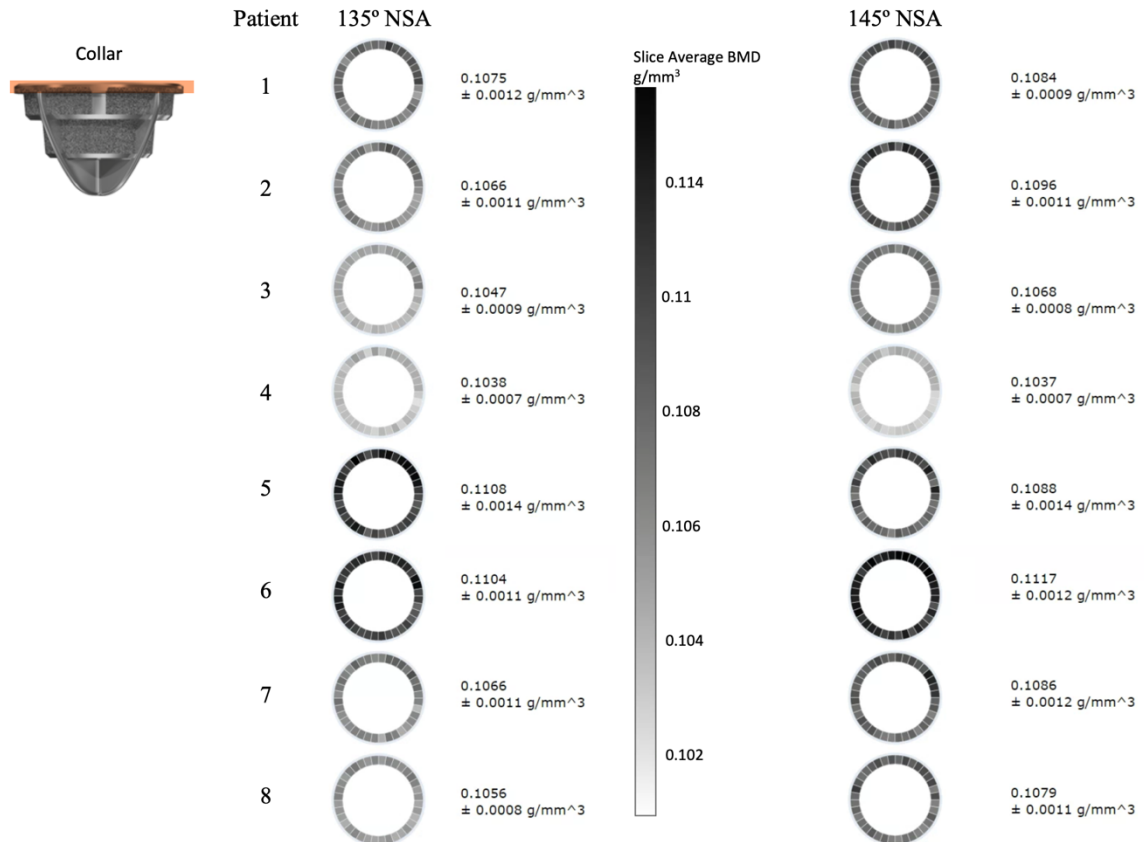


Figure G - 2: Circumferentially Partitioned BMD Plots of the Collar Ghost

Circumferential variation of BMD in eight humeral specimens in the periprosthetic interfacial collar region. Individual circumferential plots for each specimen are depicted as heatmaps, with mean and standard deviation annotated to the right.

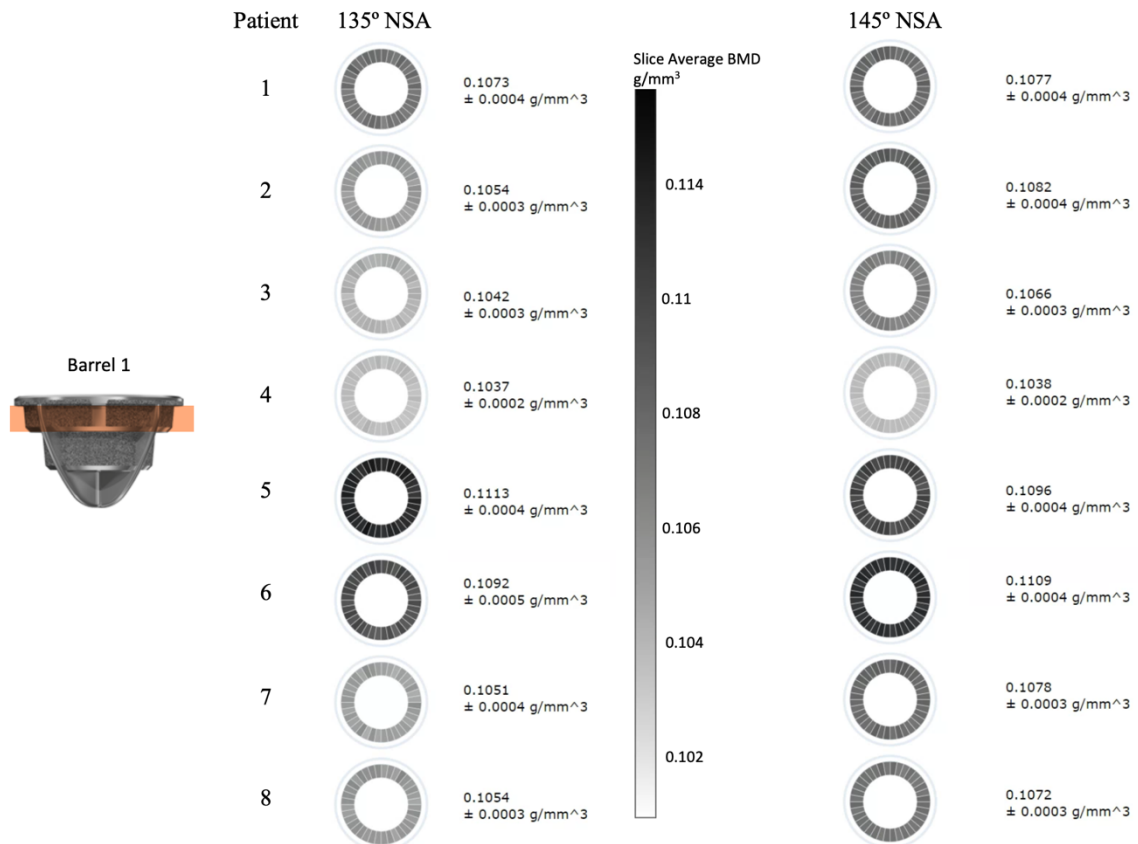


Figure G - 3: Circumferentially Partitioned BMD Plots of the Barrel 1 Ghost

Circumferential variation of BMD in eight humeral specimens in the periprosthetic interfacial barrel 1 region. Individual circumferential plots for each specimen are depicted as heatmaps, with mean and standard deviation annotated to the right.

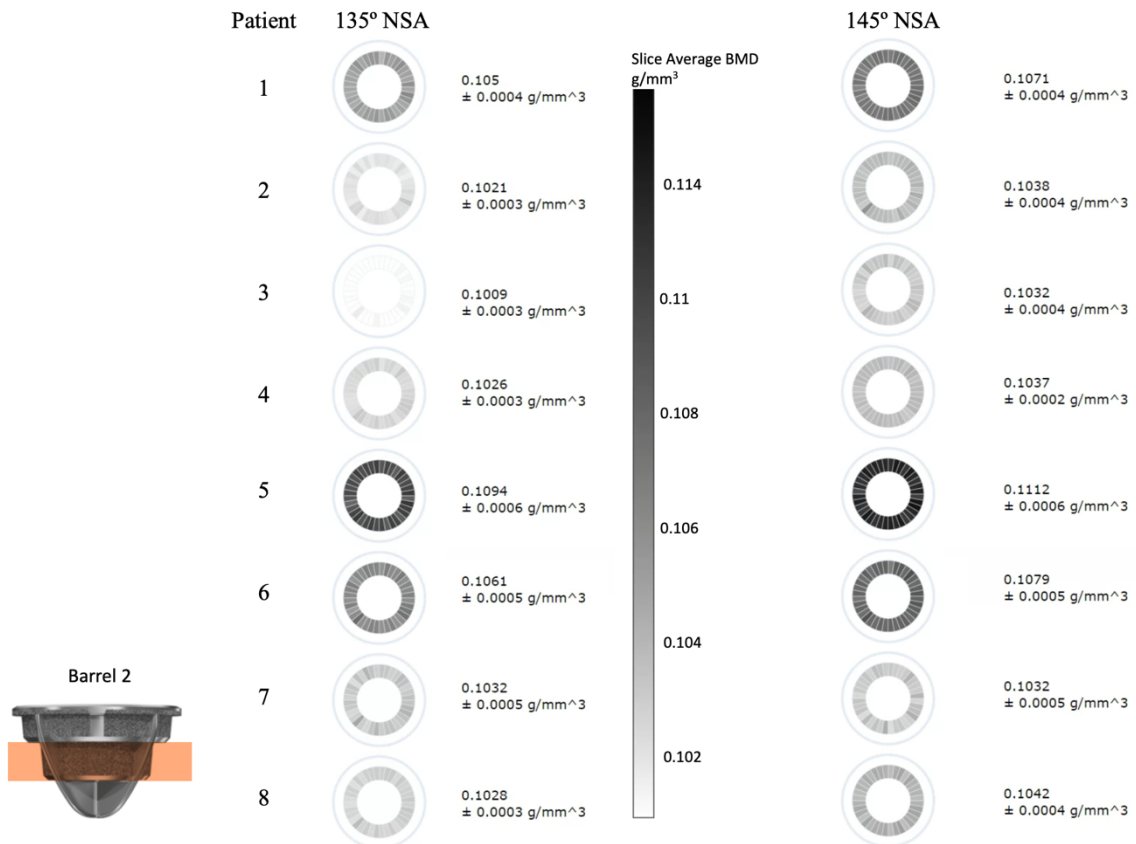


Figure G - 4: Circumferentially Partitioned BMD Plots of the Barrel 2 Ghost

Circumferential variation of BMD in eight humeral specimens in the periprosthetic interfacial barrel 2 region. Individual circumferential plots for each specimen are depicted as heatmaps, with mean and standard deviation annotated to the right.

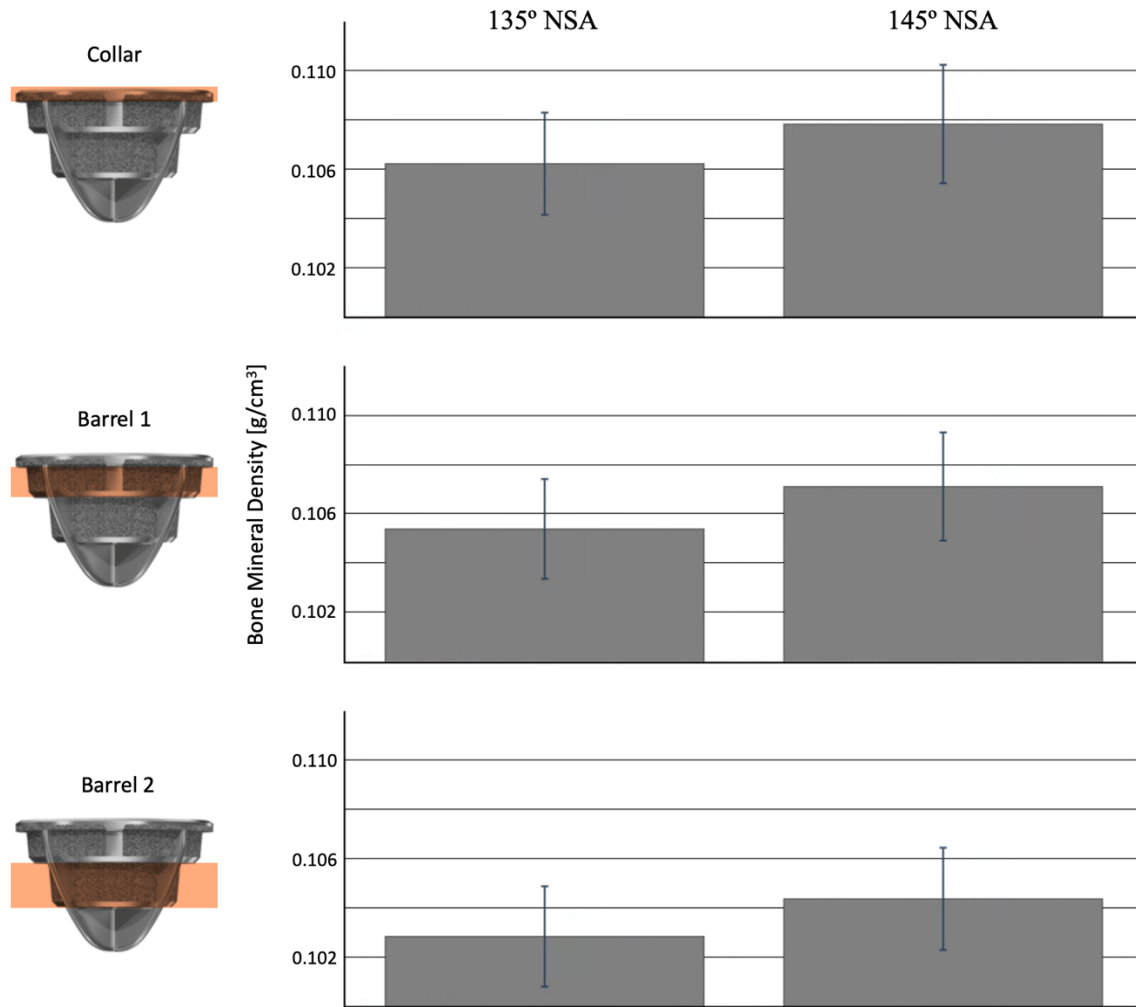


Figure G - 5: Bar plot of BMD at Varying Implant Neck Shaft Angles and Ghost Positions

Variation of BMD at three different locations of periprosthetic interfacial bone at 135° and 145° NSA resections.

G.5 Discussion

The principal objective of this work was to assess how humeral resection inclination (or neck shaft angle) may affect the periprosthetic metaphyseal bone quality. We specifically hypothesized that increasing neck shaft angle would result in better quality interfacial bone. Our results identified that increasing neck shaft angle provided significantly better-quality bone for implant fixation.

From the results of this investigation, we identified other important trends with relation to the metaphyseal bone interfacing with the implant queried. Although it was primarily found that there were consistent increases to the quality of periprosthetic bone at all implant levels when comparing 135° and 145° neck shaft angles, but the variation of bone quality was considerably greater the closer the queried implant surface was to the intermedullary canal. Indeed, the standard deviation increased from a minimum $\pm 0.00265 \text{ g/cm}^3$ at the 135° NSA collar, to a maximum $\pm 0.0088 \text{ g/cm}^3$ at the 145° NSA barrel 2 (Figure G - 5). This is noteworthy, as it indicated that the implant geometry chosen breached to a sufficient depth of bone beneath the resection surface to penetrate the canal; a location which, when devoid of implant cortical contact, would likely provide no additional stability to the implant.

There are limitations with the present work. Primarily, only a single stemless humeral component design was evaluated, which may lessen the clinical significance of these findings. This was assumed as an acceptable limitation, as although the implant geometry may vary, the chosen design was considered to be of similar size to other stemless humeral implants available on the global market. Future investigations should continue to evaluate the interfacial BMD of a larger variety of implant designs to provide a more thorough evaluation on the bone density distribution in metaphyseal-affixing implants.

Another possible limitation of this work is the small sample size utilized. It is suggested that future works evaluate a larger cohort of patient CTs to better represent the global population. However, the sample size utilized for this work is consistent with other investigations of this nature. Additionally, this evaluation was focused on native bone prior

to implantation. Due to the press-fit design of most osseointegrating implant designs, the degree to which press-fit of an implant may affect the interfacial bone density, and whether bone fragmentation may play a role in long-term fixation of implants.

Strengths of this work include the repeated measures design with each specimen being reconstructed at both 135° and 145° NSAs. This increased the statistical power of this investigation. Additionally, the use of implant ghosts at varying interface depths provided a more thorough and implant-specific understanding of periprosthetic interfacial bone than has previously been reported in existing literature.

G.6 Conclusion

The neck shaft angle of implantation in stemless humeral components is a modifiable surgical variable that has a significant effect on the bone substrate in contact with the implant surface. Lower, more varus, neck-shaft angles may result in the implant being inset into lower quality bone. It is therefore suggested that in cases where stemless humeral component stability is to be maximized, that increased installation neck shaft angles may be beneficial.

Appendix References

- [1] National Instruments, “nidaqmx,” *readthedocs*, 2024.
<https://github.com/ni/nidaqmx-python.git> (accessed Jan. 05, 2021).
- [2] Basler, “pypylon,” 2022. <https://github.com/basler/pypylon> (accessed Jan. 09, 2023).
- [3] A. Clarke, “Pillow (PIL Fork),” *readthedocs*, 2015.
<https://buildmedia.readthedocs.org/media/pdf/pillow/latest/pillow.pdf> (accessed Mar. 08, 2024).
- [4] D. Cunningham, “Developing a Mimics 3D Bone Model with Trabecular and Cortical Bone Separated (Prox Humerus Example),” *YouTube*, 2021.
<https://www.youtube.com/watch?v=9MSso3LbgO8>
- [5] E. F. Morgan, H. H. Bayraktar, and T. M. Keaveny, “Trabecular bone modulus-density relationships depend on anatomic site,” *J. Biomech.*, vol. 36, no. 7, pp. 897–904, 2003, doi: 10.1016/S0021-9290(03)00071-X.
- [6] E. Hamed, E. Novitskaya, J. Li, P. Y. Chen, I. Jasiuk, and J. McKittrick, “Elastic moduli of untreated, demineralized and deproteinized cortical bone: Validation of a theoretical model of bone as an interpenetrating composite material,” *Acta Biomater.*, vol. 8, no. 3, pp. 1080–1092, 2012, doi: 10.1016/j.actbio.2011.11.010.
- [7] S. Synnott, “The Effect of Implant Girth and Implant Collar on the Degree of Bone to Implant Contact and Bone Stresses in the Proximal Humerus,” The University of Western Ontario, 2018.
- [8] I. Kalouche, J. Crépin, S. Abdelmoumen, D. Mitton, G. Guillot, and O. Gagey, “Mechanical properties of glenoid cancellous bone,” *Clin. Biomech.*, vol. 25, no. 4, pp. 292–298, 2010, doi: 10.1016/j.clinbiomech.2009.12.009.
- [9] D. Cunningham, “Positioning a Humeral Implant in a Mimics Bone Model, and In-Silico Bone Resection using SolidWorks,” *YouTube*, 2021.
<https://www.youtube.com/watch?v=nXgO-5HkU1w>
- [10] N. Razfar, “Finite Element Modeling of the Proximal Humerus to Compare Stemless , Short and Standard Stem Humeral Components of Varying Material Stiffness for Shoulder Arthroplasty,” University of Western Ontario, 2014. [Online]. Available: <https://ir.lib.uwo.ca/etd/2431>
- [11] N. Kohli, J. C. Stoddart, and R. J. van Arkel, “The limit of tolerable micromotion for implant osseointegration: a systematic review,” *Sci. Rep.*, vol.

- 11, no. 1, pp. 1–11, 2021, doi: 10.1038/s41598-021-90142-5.
- [12] H. J. Rønold and J. E. Ellingsen, “The use of a coin shaped implant for direct in situ measurement of attachment strength for osseointegrating biomaterial surfaces,” *Biomaterials*, vol. 23, no. 10, pp. 2201–2209, 2002, doi: 10.1016/S0142-9612(01)00353-2.
- [13] R. G. Geesink, K. de Groot, and C. P. Klein, “Chemical implant fixation using hydroxylapatite coatings. The development of a human total hip prosthesis for chemical fixation to bone using hydroxylapatite coatings on titanium substrates,” *Clin. Orthop. Relat. Res.*, vol. 225, pp. 147–170, 1987.
- [14] H. Zreiqat *et al.*, “Mechanisms of magnesium-stimulated adhesion of osteoblastic cells to commonly used orthopaedic implants,” *J. Biomed. Mater. Res.*, vol. 62, no. 2, pp. 175–184, 2002, doi: 10.1002/jbm.10270.
- [15] J. Cui *et al.*, “Micro-nano porous structured tantalum-coated dental implants promote osteogenic activity in vitro and enhance osseointegration in vivo.pdf.crdownload,” *J. Biomed. Mater. Res.*, vol. 111, no. 9, pp. 1358–1371, 2023, doi: 10.1002/jbm.a.375381358.
- [16] A. Halldin, M. Ander, M. Jacobsson, and S. Hansson, “Simulation of the mechanical interlocking capacity of a rough bone implant surface during healing,” *Biomed. Eng. Online*, vol. 14, no. 1, pp. 1–13, 2015, doi: 10.1186/s12938-015-0038-0.
- [17] J. M. Reeves, “An In-Silico Assessment of Stemless Shoulder Arthroplasty: from An In-Silico Assessment of Stemless Shoulder Arthroplasty: from CT to Predicted Bone Response CT to Predicted Bone Response.” 2018. [Online]. Available: <https://ir.lib.uwo.ca/etdhttps://ir.lib.uwo.ca/etd/5398>
- [18] S. Sunil and P. Dhatrak, “Biomechanical consideration of bone density and its influence on stress distribution characteristics of dental implants,” *Mater. Today Proc.*, vol. 46, pp. 478–483, 2021, doi: 10.1016/j.matpr.2020.10.368.
- [19] D. E. Cunningham, G. W. Spangenberg, G. D. G. Langohr, G. S. Athwal, and J. A. Johnson, “Stemless Reverse Humeral Component Neck Shaft Angle has an Influence on Initial Fixation,” *J. Shoulder Elb. Surg.*, 2023, doi: 10.1016/j.jse.2023.06.035.
- [20] P. Virtanen *et al.*, “SciPy 1.0: fundamental algorithms for scientific computing in Python,” *Nat. Methods*, vol. 17, no. 3, pp. 261–272, 2020, doi: 10.1038/s41592-019-0686-2.

Curriculum Vitae

David E. Cunningham B.E.Sc.

Lawson Health Research Institute, St. Joseph's Hospital PhD Candidate
Mechanical Engineering Graduate Program, The University of Western Ontario

Education

2020/05 - Present **University of Western Ontario, London, ON, Ph.D. Department of Mechanical and Materials Engineering**

Dissertation Title: An Analysis of Primary Stability of Stemless Humeral Implants in Shoulder Arthroplasty

Dissertation supervisor: Dr. James A. Johnson, P.Eng. PhD

2015/09 - 2020/05 **University of Western Ontario, London, ON, B.E.Sc. Department of Mechanical and Materials Engineering**

Thesis Title: Effectiveness of Analogue Bone Materials in Glenoid Baseplate Fixation Studies

Thesis supervisor: Dr. James A. Johnson, P.Eng. PhD

Grants and Fellowships

2023/05 - Present **Ontario Graduate Scholarship (OGS) - \$15,000**

2020/05 - Present **Western Graduate Research Scholarship (WGRS-MME)**

2020/05 - Present **Western Graduate Research Assistance (WGRA-GMME)**

Awards

2022/04 **Bone and Joint Research – Best Poster Award**

2020/05 **Dean's Honour List**

2018/05 **Dean's Honour List**

2016/05 **Dean's Honour List**

2015/09 **Western Scholarship of Distinction**

Publications

- 2023/12 **Stemless Reverse Shoulder Arthroplasty Neck-Shaft Angle Influences Humeral Component Time-Zero Fixation and Survivorship: A Cadaveric Biomechanical Assessment**
Journal of Shoulder and Elbow Surgery International
<https://doi.org/10.1016/j.jseint.2024.04.001>
- 2023/06 **Stemless Reverse Humeral Component Neck Shaft Angle has an Influence on Fixation**
Journal of Shoulder and Elbow Surgery
<https://doi.org/10.1016/j.jse.2023.06.035>
- 2023/02 **Leveraging Kindness in Canadian Post-Secondary Education: A Conceptual Paper**
College Teaching
<https://doi.org/10.1080/87567555.2023.2181307>
-

Conference Talks and Abstracts Presented

- 2023/09 **International Society of Technology in Arthroplasty 2023 Annual Congress**
Evaluating the Effect of Simulating Extreme Physiological Loads in the Evaluation of Stemless Reverse Humeral Component Fixation
- 2023/09 **International Society of Technology in Arthroplasty 2023 Annual Congress**
Evaluating the Effect of Neck Shaft Angle on Stemless Reverse Humeral Component Fixation
- 2023/06 **Canadian Operational Research Society 2023 Conference**
Evaluating the Effect of Varying Neck Shaft Angle in Reverse Humeral Component Fixation
- 2022/08 **International Society of Technology in Arthroplasty 2022 Annual Congress**
Evaluating the Efficacy of Tracking Methods in the Evaluation of Orthopaedic Implants
- 2022/08 **International Society of Technology in Arthroplasty 2022 Annual Congress**
Evaluating the Effect of Anatomical Loading Scenarios on the Fixation Evaluation of Anatomical Shoulder Glenoid Implants
- 2022/06 **Canadian Operational Research Society 2022 Conference**
Evaluating Micromotion Measurements in Orthopaedic Implants Relative to Bone

- 2022/05 **London Heath Research Day**
 Development of an Automated Test Bed to Assess the Performance of Shoulder
 Implants
-

Teaching Assignments

- 2021/01 – Present **Teaching Assistant, Biomechanics of the MSK System - MME 4469B**
University of Western Ontario
- 2021/01 – Present **Teaching Assistant, Mechanical Components Design - MME 3380B**
University of Western Ontario
- 2021/09 – 2023/12 **Teaching Assistant, Product Design and Development - MME 2259A**
University of Western Ontario
- 2021/05 – 2021/08 **Teaching Assistant, Finite Element Methods - MME 9612L**
University of Western Ontario
- 2021/01 – 2020/05 **Teaching Assistant, Engineering Experimentation – MME 2285B**
University of Western Ontario
- 2020/09 – 2020/12 **Teaching Assistant, Industrial Materials - MME 2260A**
University of Western Ontario
-

Design Experience

- 2021/05 – 2021/08 **Novel Triaxial Implant Testing Apparatus, Ph.D. HULC**
Roth McFarlane Hand and Upper Limb Centre
Design title: Triaxial Implant Loading Apparatus
 A loading simulator for the in-vitro evaluation of novel reversed total shoulder arthroplasty humeral prosthetics. Custom Python code design of a synchronized pneumatic loading, digital tracking, and sensor feedback control application and paired user interface compatible with the NI DAQ interface. Extended functionality of loading and sensory software to all equipment in HULC biomechanics laboratory.
- Design supervisor:** Dr. James A. Johnson, P.Eng. PhD
- 2021/01 – 2020/05 **Mechanical BEsc Capstone Design Project**
Department of Mechanical and Materials Engineering
Design title: Proximal Phalanx Actuated Finger Prosthetic
 Design of a 3D printed actuated prosthetic for the functional replacement of the proximal phalanx of an amputee. Code design and incorporation of surface electromyography technology using an Arduino controller and micromotors to facilitate flexion/extension actuations.
- Design supervisor:** Dr. George K. Knopf, PEng PhD

Professional Appointments

2021/09 – **Research and Development Engineer (EIT)**
present *Roth McFarlane Hand and Upper Limb Clinic, London, ON*

2020/05 - **Ricky Ratchets Auto Repair Mechanical Assistant**
present *Ricky Ratchets Auto Repair, London, ON*

2019/01 - **Mechanical Reliability Engineer (EIT)**
2019/08 *NOVA Chemicals, Corunna, ON*

2018/05 - **Polyethylene Engineering and Capital Engineer (EIT)**
2018/12 *NOVA Chemicals, Mooretown, ON*
